Molecular photodissociation dynamics studied by photoion and photoelectron imaging

Hideki Katayanagi

DOCTOR OF PHILOSOPHY

Department of Functional Molecular Science
School of Mathematical and Physical Science
The Graduate University for Advanced Studies

2002

Contents

Chapter 1

General introduction

One of the ultimate experimental approaches for obtaining the knowledge of chemical reaction dynamics is to behold the reactions directly with our eyes. If we were able to visualize the reaction --- the motion of associating or dissociating atoms in collisions or unimolecular reactions of energized isolated molecules ---, we would be able to achieve utmost understanding on chemical reaction dynamics.

Perhaps, this is a general consensus among chemists, and it is indeed the ultimate objective of this study. Yet, we need to examine here " the knowledge of chemical reaction dynamics" and "visualize the reaction" more precisely, in order to clarify the scope of this dissertation.

In this dissertation, we focus on photodissociation of small molecules, because it is one of the simplest chemical reactions. When photodissociation occurs on a single electronic potential energy surface, the final state distributions of photofragments can be predicted and understood by classical mechanics semiquantitatively [1]. This is due to the famous Born-Oppenheimer principle: the nuclei in a molecule are much heavier than the electrons, and so the nuclei move on a potential energy surface solely determined by the electronic motions. The classical mechanics, which is established by Newton based on observation of mechanics in a macroscopic scale, is known to be approximately valid even in the scale of molecules. What is remarkable, in the regnum of classical mechanics, is that the photodissociation mechanism on a single surface is not more complex than the mechanics of a rolling ball on a slope [2]. Then, what are more complex and important features of chemical reactions to be investigated?

When a number of potential energy surfaces are involved in a photodissociation process, the product state distributions are not always simple sums of photodissociation on each surface due to quantum mechanical effects. Two prominent examples are the non-adiabatic transitions [3] and interference between different dissociation pathways [4]. In this dissertation, we will discuss the effects of the non-adiabatic transitions in the ultraviolet photodissociation of carbonyl sulfide (OCS) mainly in Chapter 4 and 5. As a result, photodissociation of small molecules can have diverse and complex product state distributions according to parent species and electronic states photoexcited. Generation of diversity from simple systems makes the photodissociation of small molecules to be a versatile experimental apparatus for a variety of quantum mechanical events, even beyond chemical interests.

Another kind of complexity arises from multi-dimensionality of the potential energy surface. This is true even for the systems investigated in this dissertation ("small and isolated" molecules of at most six atoms). As the vibrational degrees of freedom increases, characteristic dynamical behavior tends to be washed out by statistical or thermal behavior even in such "small and isolated" systems [5]. The border between dynamical and thermal regimes generally lies in the systems with a few atoms. In Chapters 7 and 8, photodissociation of a penta-atomic molecule, ketene (CH_2=CO), and a hexa-atomic molecule, vinyl bromide (CH_2=CHBr), will be discussed.

Once photodissociation occurs, products are scattered with various speeds and scattering angles in the three-dimensional (3D) space. In addition, the directionality (orientation of fragments and/or the direction of rotational and electronic angular momentum vectors) of product species is created, and they usually have dynamical correlation to each other. If we are able to capture this entire event in a movie, the dynamics will be completely clear. Needless to say, however, position and speed of an atom cannot be determined simultaneously owing to the uncertainty principle. Hence, we cannot cinematograph the photodissociation event verbatim. Visualization of chemical reaction may be defined here as simultaneous observation and determination of good quantum numbers of products that are highly correlated to each other during the reaction.

The photoion [6] and photoelectron [7] imaging employed in this study are the experimental methods that ionize neutral photofragment selectively using tunable lasers and project the 3D distribution of charged particles onto a two-dimensional (2D) position sensitive detector. Using this method, the angular and speed distributions of photofragments are examined from intensity profiles in the 2D image. In addition, a well defined polarization of laser light allows us to observe the directionality of the vector property of the photofragments. The measurement of anisotropy of angular momentum vectors provides us valuable information on stereochemical aspects of the photodissociation. As described in Chapter 3, simultaneous determination of scattering distribution and polarization of angular momentum, so-called vector correlation measurements of atomic fragments, were made possible in this work for the first time.

References

[1] R. Schinke, “Photodissociation Dynamics” (Cambridge University Press, 1993).

[2] R. Bluemel, W. P. Reinhardt, “Chaos in Atomic Physics” (Cambridge University Press, 1997).

[3] H. Nakamura, “Nonadiabatic Transitions: Concepts, Basic Theories and Applications ” (World Scientific, 2002)

[4] T. P. Rakitzis, S. A. Kandel, A. J. Alexander, Z.-H. Kim, R. N. Zare, Science **281**, 1346 (1998).

[5] T. Baer, W. L. Hase, “Unimolecular Reaction Dynamics, Theory and Experiments” (Oxford University Press, 1996)

[6] D. W. Chandler, P. L. Houston, J. Chem. Phys. **87**, 1445 (1987).

[7] M. Tsubouchi, B. Whitaker, L. Wang, H. Kohguchi, T. Suzuki, J. Chem. Phys. **115**, 8810 (2001).

Chapter 2

223 nm photodissociation of OCS: Two components in S ($^1D_2$) and S($^3P_2$) channels [a]

[a] Published on *Chemical Physics Letters* **247**, 571-576 (1995)

2.1. Introduction

The electronic structures and photodissociation mechanisms of CO_2, N_2O, and OCS are interesting subjects for molecular spectroscopy and dynamics. These problems are somewhat complicated due to the Renner-Teller effect that causes complex topographies of the excited state potential energy surfaces and non-adiabatic transitions between them. Furthermore, as one of the common features of the photodissociation mechanisms of these 16 valence electron systems, not only spin-allowed (~95%) but also spin-forbidden (~5%) dissociation occurs. Therefore, excited triplet states also play some roles in the dissociation dynamics.

The UV photodissociation of OCS has been studied by Houston and co-workers by VUV laser spectroscopy [1,2]. They observed a bimodal CO ($X\ ^1\Sigma^+$) rotational distribution and the anisotropy parameter changing from b = 0 to 1.9 as a function of the rotational quantum number of CO [1]. Considering the predominant branching ratio 0.95 of the spin-allowed channel, the bimodal rotational distribution of CO suggests that two velocity components are expected for the $S(^1D)$ photofragments. Similar observation has also been reported by Sato *et al.* [9]. On the other hand, the translational energy distribution of $S(^3P_2)$ atoms has been found to be a single distribution by Doppler spectroscopy [2]. In addition, the beta parameter observed for $S(^3P)$ was much smaller than that for $S(^1D_2)$. From these results, it is not yet clear whether the singlet and triplet products originate from the same spin-allowed electronic transition(s) to the singlet state(s). Clearly, more detailed investigation on OCS, especially on the triplet channel, is necessary. In the case of CO_2, for instance, the anisotropy parameters observed for $O(^1D_2)$ and $O(^3P_J)$ channels have been determined to be b = 0 (singlet) and 2 (triplet), from which Stolow and Lee have concluded that the triplet channel arises from direct triplet$\leftarrow S_0$ absorption [3].

In this chapter, ultraviolet photodissociation dynamics of OCS is described. Two dimensional ion imaging method [4,5] is employed to map out the velocity distributions in the center-of-mass frame with complete separation of the singlet and triplet channels, which provides more comprehensive picture of the dissociation dynamics of OCS than previous studies.

2.2. Experimental

A supersonic molecular beam of OCS was generated using a pulsed valve (General Valve series 9, 0.8 mmϕ) and two skimmers (0.5 mmϕ). The molecular beam 1 mm in diameter was introduced parallel to the electric field vector of a time-of-flight mass spectrometer through the second skimmer embedded in the repeller plate [6]. The concentration of OCS seeded in He was 10% for $O(^1D)$ and 2.5 % for $O(^3P_2)$ measurements. The latter was intentionally diluted to minimize cluster formation in the supersonic expansion. The stagnation pressure was 600 - 1200 Torr relative to the vacuum. The molecular beam intersected with the photolysis (223 nm) and probe laser beams at 79 mm downstream from the nozzle. Both of the laser beams were focused by axisymmetric lenses (f = 300 for photolysis and f = 250 for probe). The time delay between the photolysis and probe laser pulses was kept within 20 ns. Sulfur atoms were ionized by (2+1) REMPI using the resonance of $^1F_3 \leftarrow\leftarrow {}^1D_2$ at 288.19 nm and of $^3P_1$ and $^3P_2 \leftarrow\leftarrow {}^3P_2$ at 308.20 nm. Since the absorption lines are broadened by the Doppler effects due to the hyperthermal recoil velocities, the probe laser frequency was scanned over the entire Doppler-broadened absorption lines during integration of images. In the measurement of $^3P_2$, the laser frequency was scanned to cover both of closely lying lines of $^3P_1 \leftarrow\leftarrow {}^3P_2$ and $^3P_2 \leftarrow\leftarrow {}^3P_2$. The ions were accelerated and projected onto a microchannel plate detector (Hamamatsu, 38 mm in effective diameter) backed by a phosphor screen (P20). At the time when S^+ ions (m/e=32) arrived at the microchannel plate (MCP), a high voltage pulse 1700 - 1800 V in height and 200 - 500 ns in duration was applied to the MCP, raising the gain up to 10^6 - 10^7. The high voltage pulse was generated by a home-made power supply using a transistor switch (Behlke HTS31-06). Signals due to the scattered light of laser beams and background ions with different masses were thus discriminated. The transient image on the phosphor screen was monitored by a CCD camera (Sony XC77CE, 756(H) x 581(V) pixels), and the video signal from the camera was fed into a monitor screen for real-time display and into an image capture board (Hamamatsu, IQ-V50) for integration. Images were accumulated for 125,000 – 127,000 laser shots. The entire system was operated at 25 Hz of the CCIR video rate. Typical background pressures in the beam source and the main chamber were 2 x 10^{-5} Torr and 2 x 10^{-7} Torr, respectively, when the molecular beam was operated.

The second harmonic of the output of a XeC1-pumped dye laser (Lambda Physik, LPX105i/LPD3002; coumarin 440) generated in a BBO crystal was used for photolysis, while the second harmonic of the output of a YAG-pumped dye laser (Spectra Physics GCR 230-25 / Lumonics HD-500; sulforhodamine 640) generated in a KD*P crystal was used for probing the fragments. A double Fresnel rhomb was used to rotate the laser polarization. The typical laser intensities used for the measurements were 0.2 mJ pulse^{-1} for photolysis, 0.1 mJ pulse^{-1} for probing $^1D_2$, and 0.4 mJ pulse^{-1} for probing $^3P_2$. The spatial resolution of the image is mainly limited by the ratio between the size of the beam-laser interaction region and that of an ion image (~20 mm in diameter). Although the diameter of the molecular beam is 1 mm (fwhm), the effective beam-laser interaction width is estimated to be much smaller, since [2+1] REMPI occurs most efficiently in the waist of the focused probe laser beam.

2.3. Results and Discussion

Figure 2-1 shows (a) the observed 2D ion image of S($^1D_2$) and (b) its inverse Abel transform. The areas of interest, 256 x 256 pixels, were selected from the larger sizes of the data. The 2D image in Fig. 2-1 (a) was measured with the photolysis and probe laser polarization vertically aligned in the figure. This polarization configuration ensures cylindrical symmetry for the 3D ion distribution, which is the prerequisite for an inverse Abel transform to reconstruct the section of the 3D distribution. In both of the figures, it is clearly seen that the velocity distribution consists of a high speed component with negligible anisotropy and a low speed component with high anisotropy. The difference in anisotropy between the slow and fast components was quantitatively evaluated for the speed ranges of 600 – 800 and 1100 - 1400 m s^{-1}. The two speed ranges correspond to the center-of-mass (C.M.) translational energy release of 3.1 - 5.5 and 10.6 - 16.9 kcal mol^{-1}; these energy ranges are indicated in Fig. 2-2 as shaded areas. The effective anisotropy parameters, b_{eff}, for these two ranges were determined to be 1.1 and 0.1, respectively, using the following formula,

$$I(q) \sim 1 + b_{\mathrm{eff}} P_2(\cos q) \qquad (1)$$

where $P_2(x)$ is the second order Legendre polynomial and q is the angle between the photolysis laser polarization and the recoil velocity of a fragment, respectively. The large

positive b_{eff} value of the slow component indicates that this arises from the transition to ^{1}A' state. The b_{eff} value for the fast component is very small but is slightly positive.

It is noted here that laser detection of atoms and molecules is sensitive to their alignment. In fact, this is one of the greatest advantages of laser-based technique that enables us to investigate into the stereochemical aspects of reactions. In the present case, REMPI detection is sensitive to electron orbital alignment in the S(^{1}D$_2$) fragment, so that b_{eff} is determined by the anisotropy (b) of the recoil velocity and also the alignment of J vector of the S atom. Lengthy description of the analysis on the alignment is not described here, as it is fully described elsewhere [7], but the result of the detailed analysis provides the 'true' values of b to be 1.8 (slow component) and 0.6 (fast component). The magnitude of b (0.6) of the fast component is large enough to conclude that the transition is dominated by ^{1}A'←^{1}A', although the overlap of ^{1}A"←^{1}A' cannot be excluded at this point as a cause of low anisotropy.

The speed distribution of S(^{1}D$_2$) was obtained by integrating the velocity distribution of S(^{1}D$_2$) for all scattering angles, then it was converted to the center-of-mass translational energy release by considering momentum conservation between the S and CO fragments. The translational energy release, $P(E_{\mathrm{T}})$, thus calculated is shown in Fig. 2-2. Since the branching ratio of the singlet channel is 0.95 [2], the distribution is directly converted to the internal state distribution of CO by using E_{rovib} (CO) = E_{avl} - E_{T}(C.M.). By VUV-LIF of CO, Sivakumar *et al.* have found that the vibrational excitation in CO is negligible; the ratio of the vibrational states of CO has been determined to be $N(v=1)$ / $N(v=0)$ < 0.02 for 222 nm photodissociation [1]. Therefore, our $P(E_{\mathrm{T}})$ can be directly related to the rotational distribution of CO (v=0). The corresponding rotational quantum numbers of CO are indicated in the figure. The peaks in the rotational distribution of CO are estimated from our data to be J = 54-55 and 66-67, which is in excellent agreement with the result of VUV-LIF of CO [1]. The $P(E_{\mathrm{T}})$ can be fitted with two Gaussian distributions as showed in the figure.

Figure 2-3 (a) shows the 2D image of S(^{3}P$_2$) observed for the same photodissociation wavelength (223 nm). Again the photolysis and probe laser beams are aligned vertically in the figure. The image was obtained by subtracting a weak background signal produced by the probe beam from the original S(^{3}P$_2$) data. It is seen that S(^{3}P$_2$) is predominantly scattered along the photolysis laser polarization, indicating that it arises from the transition to the A' state. On the other hand, there exists a very weak and nearly isotropic distribution outside of the intense signal that is not visible in this color image. In order to display this hint of the fast

and isotropic component, the surface plot of the velocity contour map is show in Fig. 2-3 (b). The anisotropy of the slow and fast components were examined quantitatively for the C.M. translational energy ranges of 16.1 - 23.8 and 40.3 - 56.0 kcal mol^{-1}, and the b_{eff} parameters were determined to be 1.1 and 0.2. The result clearly indicates that there are two components in S(^{3}P$_2$) channel, just like the singlet channel.

The C.M. translational energy release is shown in Fig. 2-4 (a). The separation of the two components is not as clear as the singlet channel, but the distribution can be reasonably well fitted by two Gaussian functions. In Fig. 2-4 (b), the distribution is compared with the shifted Boltzmarm distribution assumed by Nan *et al.* in their analysis [2]. It is seen that although the width of their distribution is much larger than ours, the shifted-Boltzmann function resembles our distribution in the peak position and in the tail extending towards higher energies. Our result provides the anisotropy for the overall translational energy distribution to be 1.0 which is much larger than 0.3 $\pm$ 0.2 reported by Nan *et al.* [2]. The discrepancy in anisotropy is mainly attributed to the different rotational temperature of the sample; Nan *et al.* used OCS vapor at room temperature, while we used OCS in a supersonic molecular beam.

The speed and angular distributions of S(^{1}D$_2$) and S(^{3}P$_2$) fragments suggest that both channels arise from the same singlet$\leftarrow$S$_0$ transition(s). The photoexcitation process is either (1) a single optical transition followed by two different (singlet) dissociation pathways or (2) two overlapping optical transitions. In any case, each of these two singlet dissociation pathways with larger and smaller kinetic energy releases undergo intersystem crossing to triplet surfaces. According to the preliminary result of *ab initio* calculations by Rokutan and Iwata [8], photoabsorption of OCS in the 200-250 nm region is ascribed to $^1\Sigma^-$(1^1A'')$\leftarrow$$^1\Sigma^+$ and $^1\Delta$ (2^1A' and 2^1A''). The $^1\Pi$ (3^1A') that is repulsive for S-C bond is not reached at 223 nm and it only participates in the dynamics via the conical intersection with 2^1A'. If that is the case, 2^1A'($^1\Delta$) is the only ^{1}A' state reached at 223 nm that provides positive b, and the observed two components with positive b are not assigned to two ^{1}A'$\leftarrow\leftarrow$^{1}A' transitions. Sivakumar *et al.* [1] have obtained negative b value for the CO fragments in low J levels and suggested that there exists overlapping electronic transition to the ^{1}A" Renner-Teller component of the $^1\Delta$ state. If smaller anisotropy of the fast component is attributed to the contribution of overlapping transition to ^{1}A" state, we have to assume that A' and A'' states give exactly the same $P(E_{\mathrm{T}})$ for the fast component. In this study, two different anisotropy parameters have been obtained for both of S(^{1}D$_2$) and S(^{3}P$_2$), but no negative anisotropy has

been obtained. Therefore, experimentally, this study does not provide an evidence for the contribution of the $^1A'' \leftarrow {}^1A'$ transition.

Further investigation on the difference between the two dissociation components will be described in the chapters 3 and 4.

References

[1] N. Sivakumar, G. E. Hall, P. L. Houston, J. W. Hepburn, and I. Burak, J. Chem. Phys. **88**, 3692 (1988).

[2] G. Nan, I. Burak, and P. L. Houston, Chem. Phys. Lett. **209**, 383 (1993).

[3] A. Stolow and Y. T. Lee, J. Chem. Phys. **98**, 2066 (1993).

[4] D. W. Chandler and P. L. Houston, J. Chem. Phys. **87**, 1445 (1987).

[5] B. J. Whitaker in "Research in Chemical Kinetics Volume I", edit. by R. G. Compton and G. Hancock, (Elsevier, 1993).

[6] K. Tonokura and T. Suzuki, Chem. Phys. Lett. **224**, 1 (1994).

[7] Y. Mo and T. Suzuki, J. Chem. Phys. **108**, 6780 (1998).

[8] M. Rokutan and S. Iwata, unpublished results.

[9] Y. Sato, Y. Matsumi, M. Kawasaki, K. Tsukiyama, and R. Bersohn, J. Phys. Chem. **99**, 16307 (1995).

Figures for Chapter 2

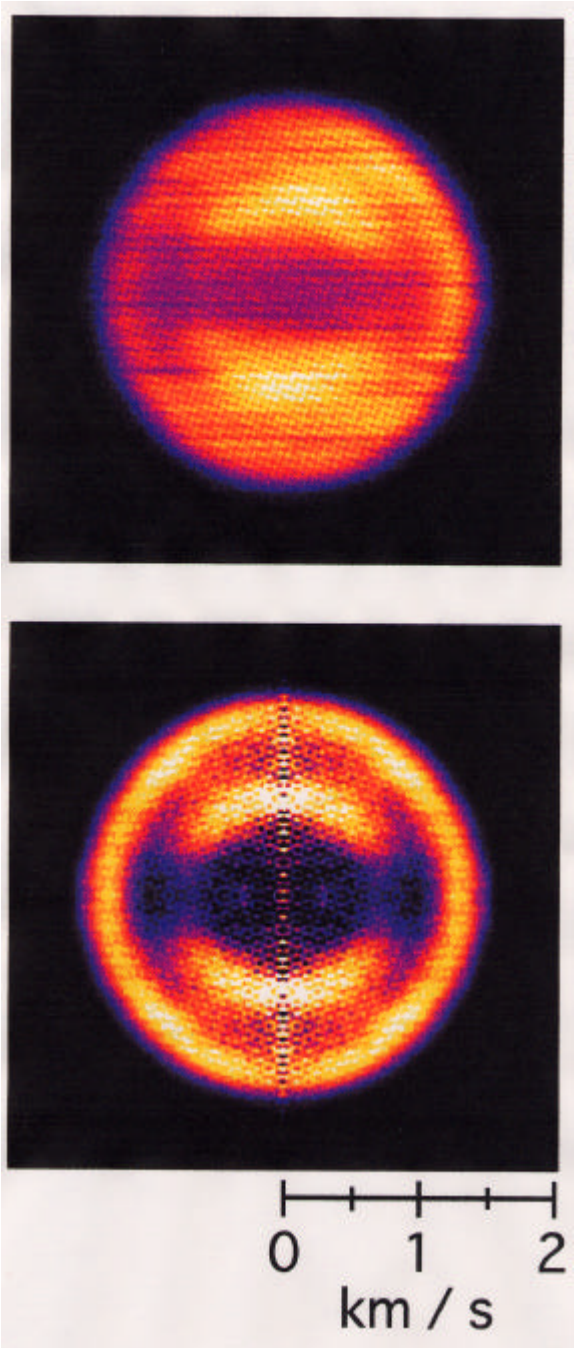

Fig. 2-1
(a) A raw (unsymmetrized) data of two dimensional ion image of $S(^1D_2)$ atoms produced by 223 nm photodissociation of OCS. The photolysis and probe laser polarization are aligned vertically in the figure. Sulfur atoms were ionized by (2+1) REMPI using the resonance of $^1F_3 \leftarrow\leftarrow {}^1D_2$ at 288.19 nm. Two velocity components are clearly seen in the figure. (b) An inverse Abel transform of the image shown in (a).

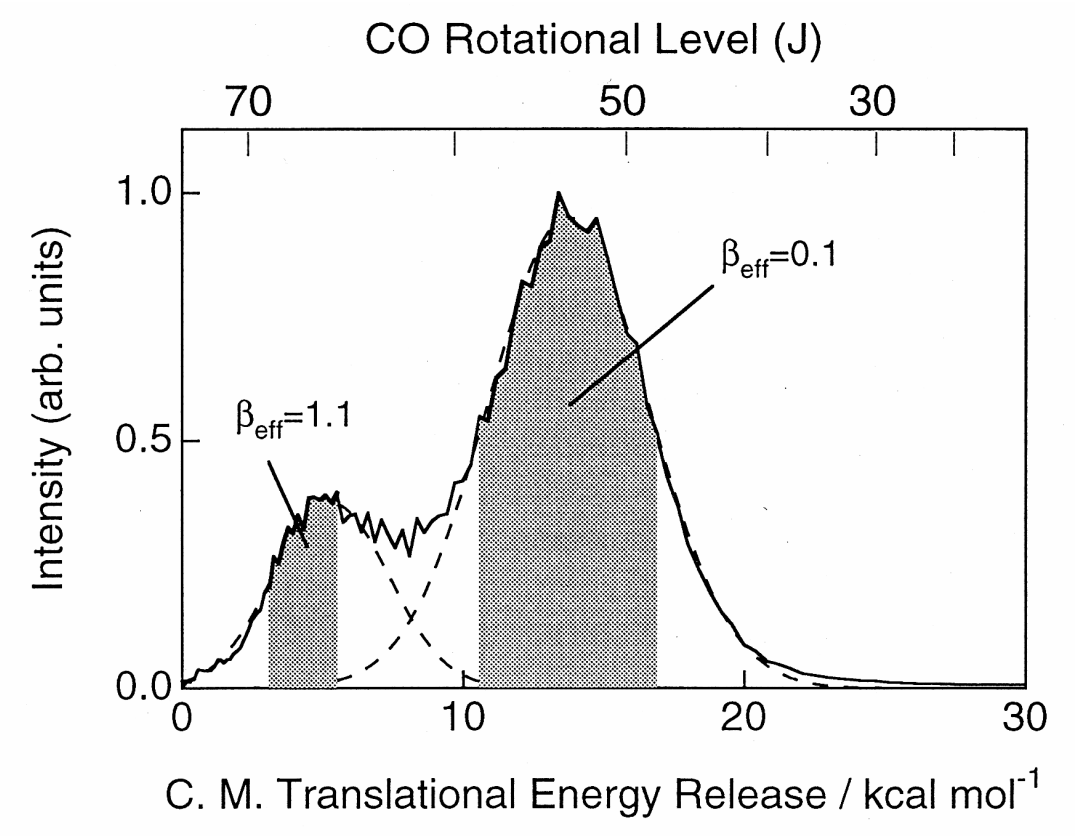

Fig. 2-2
The center-of-mass translational energy release in $S(^1D_2)$ channel calculated from the image shown in Fig. 1 (b). The observed distribution has been fitted by two Gaussian distributions with E_{peak} and ΔE of 5.3 / 4.1 and 13.8 / 5.7 kcal mol^{-1}. The effective anisotropy parameters were determined to be 1.1 and 0.1 for the energy ranges of 3.1 - 5.5 and 10.6 - 16.9 kcal mol^{-1} that are shown as shaded areas. The corresponding rotational levels of the counterpart fragment CO are indicated on the top axis.

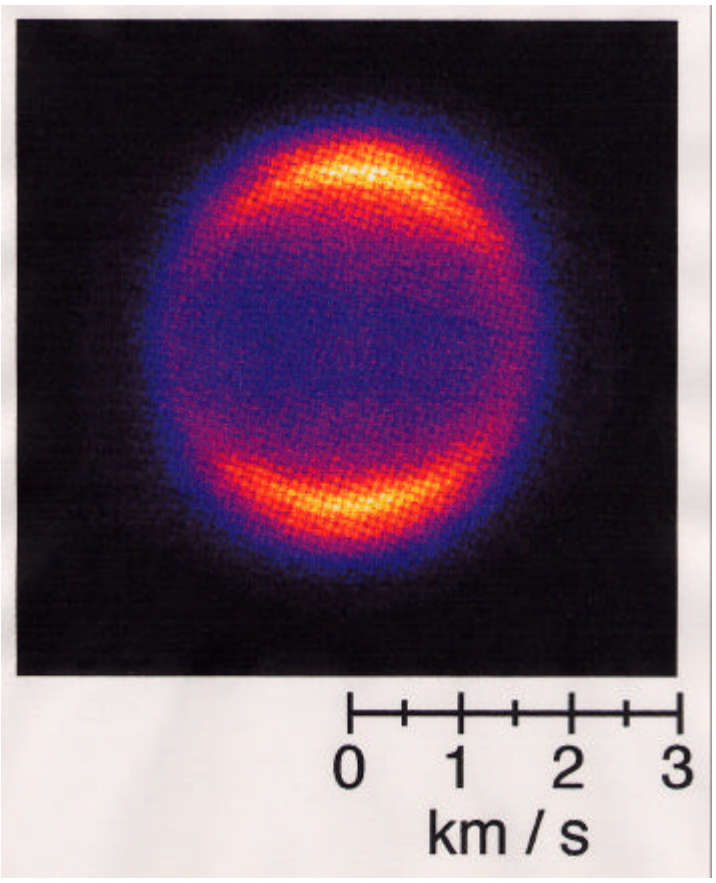

Fig. 2-3(a)
A raw (unsymmetrized) data of the two dimensional ion image of $S(^3P_2)$ atoms produced by 223 nm photodissociation of OCS. The photolysis and probe laser polarization are aligned vertically in the figure. Sulfur atoms were ionized by (2+1) REMPI using the resonance of $^3P_1$ and $^3P_2$ $\leftarrow\leftarrow$ $^3P_2$ at 308.20 nm.

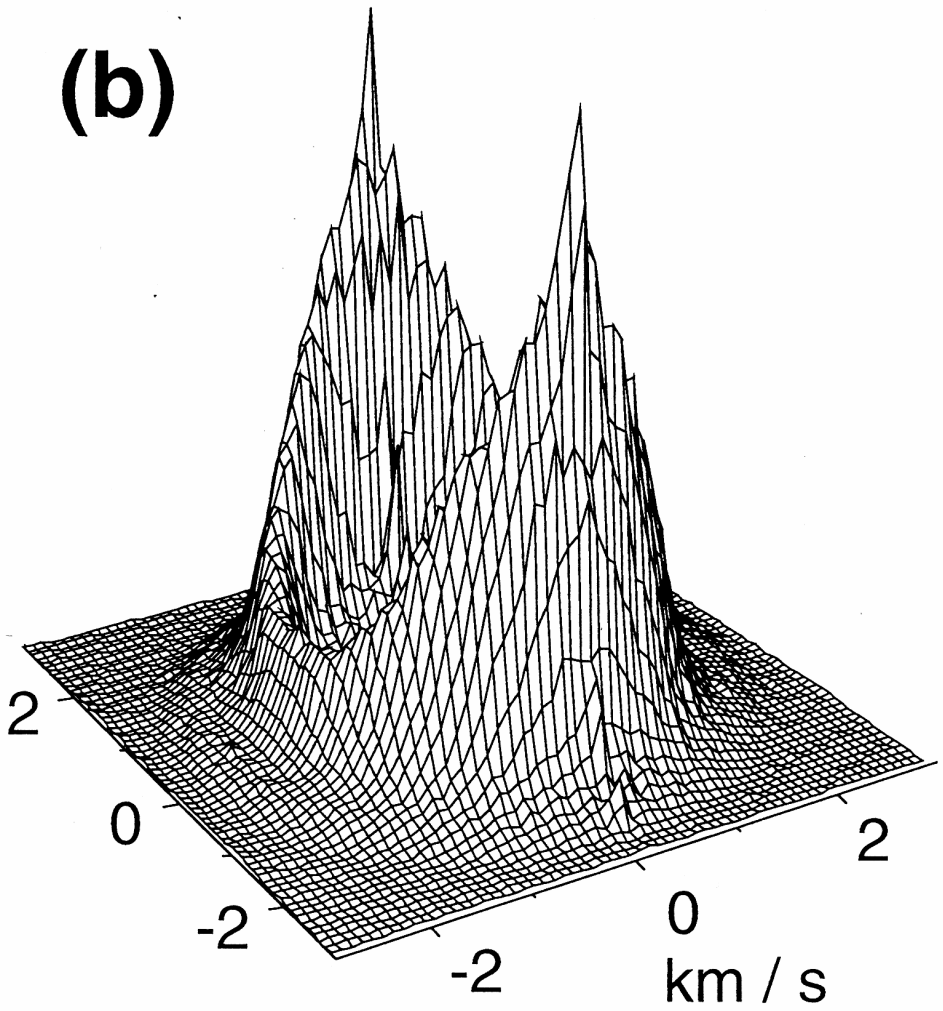

Fig. 2-3(b)
A raw (unsymmetrized) data of the two dimensional ion image of $S(^3P_2)$ atoms produced by 223 nm photodissociation of OCS. The photolysis and probe laser polarization are aligned vertically in the figure. Sulfur atoms were ionized by (2+1) REMPI using the resonance of $^3P_1$ and $^3P_2$ $\leftarrow\leftarrow$ $^3P_2$ at 308.20 nm.

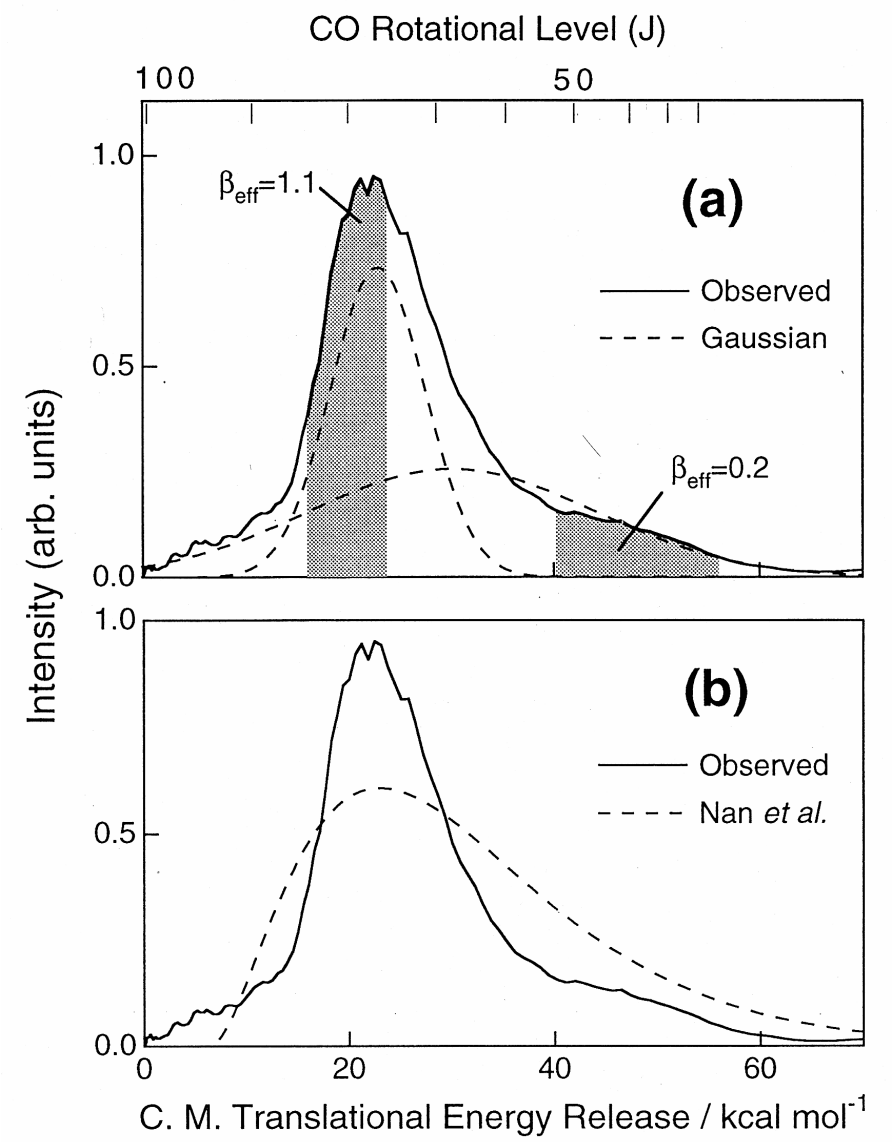

Fig. 2-4
(a) The center-of-mass translational energy release in $S(^3P_2)$ Channel. The observed distribution has been fitted by two Gaussian distributions with E_{peak} and ΔE of 22.3 / 9.0 and 29.4 / 27.4 kcal mol^{-1}. The effective anisotropy parameters were determined to be 1.1 and 0.2 for the energy ranges of 16.1 - 23.8 and 40.3 - 56.0 kcal mol^{-1} that are shown as shaded areas. The corresponding rotational levels of the counterpart fragment CO are indicated on the top axis. (b) The comparison of the observed distribution and the one assumed by Nan *et al.* [2] in their analysis.

Chapter 3

Simultaneous measurment of recoil velocity and alignment of $S(^1D_2)$ atoms in photodissociation of OCS [a]

[a] Published on *Physical Review Letters* **77**, 830-833 (1996)

3.1. Introduction

Scalar and vector quantities of reaction products provide detailed insights into the dynamics of atomic or molecular collisions and molecular photodissociation. In particular, knowledge of vector quantities and their correlation is essential for the elucidation of stereochemical properties. In recent years, much attention has been paid to the correlation between the angular momentum (***J***) and recoil velocity (***v***) in photofragments [1,2]. The importance of ***v***-***J*** correlation is that it is not lost by the formation of a long-lived collision complex, and that it serves as a versatile tool to probe the dynamics.

The ***v***-***J*** correlation for a molecular alignment is mainly created by the repulsive force and torque at the bond cleavage. Therefore, it reflects the topography of the potential energy surface (PES), but it is not sensitive to electronic symmetry. On the other hand, the ***v***-***J*** correlation in an atomic fragment is due to the electronic orbital alignment, so that it will reflect the electronic character of the PES. For example, in linear molecules the projection of electronic angular momentum onto the symmetry axis is a good quantum number. If the molecule dissociates along this axis, the projection of electronic angular momentum on the velocity axis (symmetry axis) is expected to be conserved during the dissociation.

Photodissociation often involves non-adiabatic transition(s) from an optically prepared state to some dark states. It is usually difficult to investigate the nature of these dark states. However, if electronic orbital alignment in atoms can provide information about the symmetry of these states, it will become an invaluable probe of dissociation dynamics.

Since the theoretical prediction made by Van Brunt and Zare in 1968 [3], the alignment of atoms produced by molecular photodissociation has been investigated [4-9].

These investigations were primarily concerned with overall alignment in the laboratory flame detected by polarized emission from atoms. Instead of observing emission, atomic fragments can be detected by resonance-enhanced multiphoton ionization (REMPI). REMPI allows us to examine not only the alignment from the polarization analysis, but also the velocity of atoms from ion imaging techniques [10] or time-of-flight measurements. Mu1tiphoton excitation is also more advantageous than a one-photon process for extracting higher order terms in angular momentum polarization. Recently, Wang *et al*. [9] have shown that a one-dimensional time-of-flight spectrum of C1($^2P_{3/2}$) produced by 355 nm photodissociation of $C1_2$ depends on the probe laser polarization. However, detailed information on the alignment has not been extracted [9]. In the present Letter, we describe a

two-dimensional ion imaging method and quantum-mechanical analysis used to determine the alignment and the recoil velocity of atomic fragments simultaneously. The method allows us to observe $S(^1D)$ atoms produced with two different velocity components clearly, to examine their alignment in the molecular frame, and to discuss the electronic symmetry of the asymptotic state.

3.2. Experimental

A supersonic molecular beam of OCS (10% in He) 1 mm in diameter was introduced parallel to the electric field vector of a time-of-flight mass spectrometer [10,11].

The molecular beam intersected with counterpropagated photolysis (223 nm) and probe laser beams at 79 mm downstream from the nozzle. Both of the laser beams were focused onto the molecular beam by axisymmetric lenses (f = 300 mm for photolysis and f = 250 mm for probe). The time delay between the photolysis and probe laser pulses was kept within 20 ns. Sulfur atoms were ionized by (2 + 1) REMPI using the resonance of $^1F_3 \leftarrow\leftarrow {}^1D_2$ at 288.19 nm, accelerated by electric fields, and projected onto a microchannel plate (effective diameter 38 mm) backed by a phosphor screen (P20). The transient image on the phosphor screen was monitored by a charge coupled device camera [756(H) X 581 (V) pixels], and the video signal was integrated for 125,000 – 127,000 laser shots. The background pressures in the beam source and the main chamber, with a molecular beam on, were 2×10^{-5} and 2×10^{-7} Torr. The photolysis beam was the second harmonic of the output of a XeCl-pumped dye laser, while the probe beam was the second harmonic of the output of a YAG-pumped dye laser. Both of the laser beams were linearly polarized. The laser intensities used were 0.2 mJ pulse^{-1} (photolysis) and 0.1 mJ pulse^{-1} (probe). A double Fresnel rhomb was used to rotate laser polarizations. The probe laser frequency was scanned over the entire Doppler-broadened absorption line during the integration of images. The spatial resolution of the images was limited by the ratio of the size of the beam-laser interaction region (<1 mm) to the size of an image (~20 mm in diameter). The effective beam-laser interaction width is estimated to be much smaller than the molecular beam width, since (2 + 1) REMPI is most efficient in the laser beam waist at the molecular beam center. Any precession of the angular momentum about external magnetic (the Earth) or electric (repeller) fields can be neglected for the time delay (<20 ns) between photolysis and probe.

3.3. Results and Discussion

The two-dimensional (2D) ion images of $S(^1D_2)$ produced by 223 nm photodissociation of OCS are shown in Figs. 3-1(a) – 3-1(d). Four sets of images were measured for polarization analysis. The effect of orbital alignment is most clearly seen by comparing Figs. 3-1(c) and 3-1(d) in which the photolysis laser polarization is set perpendicular to the imaging plane. The original photofragment density distribution is cylindrically symmetric around the polarization vector of the photolysis laser. If there is no alignment in atoms, the ion signal is proportional to the density of fragments, so that the ion image should be cylindrically symmetric around the center. The change of the image from Fig. 3-1(c) to (d) and also the symmetry breaking in Fig. 3-1(d) are due to orbital alignment in $S(^1D_2)$. Because the $^1F_3 \leftarrow\leftarrow {}^1D_2$ transition favors the probe laser polarization (e_{probe}) aligned parallel to J vector, signal intensity is reduced when e_{probe} is set perpendicular to $\boldsymbol{J}$. In Fig. 3-1(d), it is seen that the signal intensity is reduced along the direction of probe laser polarization.

This suggests $e_{\mathrm{probe}} \perp \boldsymbol{J}$ for the fragments moving parallel to e_{probe} ($e_{\mathrm{probe}} \parallel \boldsymbol{v}$) and, therefore, $\boldsymbol{J} \perp \boldsymbol{v}$ as a preferential alignment in the S atom. In the same way, the $\boldsymbol{J} \perp \boldsymbol{v}$ alignment in the S atom is seen by the intensity reduction at the center of Fig. 3-1(c). Alignment effects have also been observed in the images of $O(^1D_2)$ Produced by photodissociation of O_3 [12] and N_2O [13].

In Figs. 3-1(a) and 3-1(b), in which the photolysis laser polarization is parallel to the imaging plane, two velocity components are clearly seen [14]. One has fast speed and small angular anisotropy, while the other has slow speed and large anisotropy. In the following analysis, alignment is considered independently for the two velocity components.

In the case of diatomic molecular fragments produced by the photodissociation of triatomic molecules, a classical model of angular momentum and the assumption of complete $\boldsymbol{J} \perp \boldsymbol{v}$ correlation may be applied for the analysis of alignment [15]. For atoms, however, angular momentum ($\boldsymbol{J}$) must be treated quantum mechanically [16-20], since the magnitude of $\boldsymbol{J}$ is small. Neither is it possible to make an a priori assumption about the $\boldsymbol{v}$-$\boldsymbol{J}$ correlation. The correlation, which is implicit in the m distribution, must be extracted from the data.

The spatial distribution of photoions is determined by two factors,

$$\text{ion distribution} \propto I(\text{scat}) \times I(\text{det}) ,$$

where I(scat) is a differential cross section of photodissociation and I(det) is the ionization efficiency for photofragments. The differential cross section is expressed in space-fixed (SF) coordinates, with the Z axis defined along the photolysis laser polarization, by the following formula:

$$I(scat) = \frac{d^2 s}{dv d\Omega} = \frac{P_i(v)}{4p}[1 + b_i P_2(\cos q_t)] \quad \text{(for } i\text{th dissociation component)}, \quad (1)$$

where $P(v)$ is a speed distribution, and P is an anisotropy parameter. The polar angle of recoil velocity in this frame is expressed by (q_t, f_t). The remaining task for us is to evaluate I(det) for each scattering angle (q_t, f_t) With explicit treatment of the ***v***-***J*** correlation for S atoms.

The detection of reaction products by laser excitation is essentially the measurement of density. For a short pump-probe delay in photodissociation experiments, however, a density mode of detection is the same with a flux mode, since a laser pulse covers and detects all the velocity components equally. Hence, I(det) is independent of speed ***v*** but proportional to the optical transition intensity. The two-photon absorption intensity for a linearly polarized probe laser beam is expressed in the probe laser photon (PR) flame, where the Z axis is defined along the polarization vector, by the following formula:

$$I(\text{det}) \propto \sum_{k=0,2,4} P_k \, r_0^{(k)}(PR) \quad (2)$$

where

$$P_k = \sum_m (-1)^{J_i - m} \sqrt{2k+1} \begin{pmatrix} J_i & k & J_i \\ -m & 0 & m \end{pmatrix} \left| \sum_{n_e, J_e} \frac{\langle n_f J_f m | r \bullet \hat{e} | n_e J_e m \rangle \langle n_e J_e m | r \bullet \hat{e} | n_i J_i m \rangle}{E_{n_e} - E_{n_i} - hu + i(\Gamma_e / 2)} \right|^2$$

and $r_0^{(k)}(PR)$ the multipole moments the m population distribution. (:::) is 3j symbol, J_f, J_e, and J_i are the total angular momenta, n_f, n_e, and n_i denote all other quantum numbers for the fina1, virtual, and initial states, respectively. G_e is the homogeneous linewidth of the virtual state. m is the magnetic quantum number referenced to the photon frame. By neglecting the polarization effect for the ionization step in (2 + 1) REMPI, Eq.(2) is considered to be a detection efficiency of photofragments. Using the Wigner-Eckart theorem, P_k can be expressed as follows:

$$P_k = \sum_m (-1)^{J_i - m} \sqrt{2k+1} \begin{pmatrix} J_i & k & J_i \\ -m & 0 & m \end{pmatrix} \left| \sum_{Je} (-1)^{J_f + J_e} \begin{pmatrix} J_f & 1 & J_e \\ -m & 0 & m \end{pmatrix} \begin{pmatrix} J_e & 1 & J_i \\ -m & 0 & m \end{pmatrix} R(J_e) \right|^2 \quad (3)$$

$R(J_e)$ are defined by

$$R(J_e) = \sum_{n_e} \frac{\langle n_f J_f \| r^{(1)} \| n_e J_e \rangle \langle n_e J_e \| r^{(1)} \| n_i J_i \rangle}{E_{n_e} - E_{n_i} - hu + i(\Gamma_e / 2)}$$

where $\langle n_f J_f \| r^{(1)} \| n_e J_e \rangle$ and $\langle n_e J_e \| r^{(1)} \| n_i J_i \rangle$ are the reduced matrix elements of the transition dipole moment.

In Eq. (3), the evaluation of $R(J_e)$ seems necessary. However, Eq. (3) can be transformed into

$$P_k = \sum_{RT} \sum_{J_e J_e'} (-1)^{J_f + J_i} R(J_e) R^*(J_e')(2R+1)(2T+1)\sqrt{2k+1} \begin{Bmatrix} J_i & J_i & k \\ T & R & J_f \end{Bmatrix}$$

$$\begin{Bmatrix} J_i & J_f & R \\ 1 & 1 & J_e \end{Bmatrix} \begin{Bmatrix} J_i & J_f & T \\ 1 & 1 & J_e' \end{Bmatrix} \begin{pmatrix} 1 & 1 & T \\ 0 & 0 & 0 \end{pmatrix} \begin{pmatrix} 1 & 1 & R \\ 0 & 0 & 0 \end{pmatrix} \begin{pmatrix} T & R & k \\ 0 & 0 & 0 \end{pmatrix}$$

where {:::} are 6*j* symbols. From this equation it is readily recognized that the ratios P_0:P_2:P_4 are invariant to the relative values of $R(J_e)$ for $J_i \neq J_f$,. For the probing scheme we have used, it can be shown that the ratios are P_0:P_2:P_4 = 1 : 0.68 : -0.11. Therefore, for $J_i \neq J_f$, it is not necessary to evaluate R(Je). For $J_i = J_f$, the ratios must be calculated numerically.

The ***v-J*** correlation is naturally expressed in a velocity fixed (VF) frame where the Z axis is defined along the recoil velocity vector. In this frame, *m* is defined as so-called helicity (the projection of angular momentum onto the velocity). For simplification of the analysis, we have made two assumptions for angular momentum distribution in the VF flame: (1) the distribution is cylindrically symmetric around the velocity, and (2) the distribution is independent of scattering angle (q_t, f_t). With these assumptions, the multipole moments in the VF flame are expressed as follows:

$$r_0^{(k)}(VF) = \sum_m (-1)^{J_i - m} \sqrt{2k+1} \begin{pmatrix} J_i & k & J_i \\ -m & 0 & m \end{pmatrix} f_m$$

where f_m is a fractional population in each *m* state in the VF frame. The multipole moments in the VF frame can be transformed to those in the PR frame directly, VF $\rightarrow$ PR, or sequentially, VF $\rightarrow$ SF $\rightarrow$ PR. In the latter approach, the multipole moments in the SF frame can be multiplied with a differential cross section [Eq. (1)] for each scattering angle (q_t, f_t) and then transformed to the PR frame.

The experimental data were analyzed with a forward convolution method by considering two velocity components with different *m* distributions. We have assumed that there is no orientation of ***J*** in the VF coordinate, so that the angular momentum distribution is characterized by the ratio for |m| = 0:1:2. The calculated images are shown in Figs. 3-1(a') – 3-1(d') and the parameters used are tabulated in Table 3-1.

Although OCS is linear in the ground electronic state, it can be bent in excited states by Renner-Teller interactions. In fact, the major component in the 223 nm photoabsorption of OCS is assigned to the transition to the Renner-Teller A' component of a $^1\Delta$ state [21]. For the lower symmetry of the bent states (C_S point group), symmetry species can be classified as either A' or A" according to whether it is symmetric or antisymmetric for reflection by the molecular plane. The electronic state of the counterpart fragment CO X($^1\Sigma^+$) is classified as A'. Therefore, the overall symmetry of the asymptotic state is determined by the symmetry of the S($^1D_2$) atom. To discuss the symmetry of the S atom, another coordinate frame (MS, molecular symmetry) where the Z axis is defined perpendicular to the molecular plane is more useful. In the MS frame, $^1D_2$ states with $m = 0, \pm 2$ belong to A' symmetry, whereas those with $m = \pm 1$ belong to A''. The *m* distribution in the MS frame, obtained from the distribution in the VF frame, is shown in Table 3-2. The result indicates that 80% of the asymptotic states are in A' symmetry. Although the result suggests different degrees of alignment for the two dissociation components, the present experimental method using two-dimensional imaging and forward-convolution fitting does not allow us to be certain that the difference is significant.

Since the anisotropy parameter is 1.8, the photoabsorption process responsible for the slow component is almost pure A' – A'. The A'' component manifested by the population in $m = \pm 1$ state in the MS frame may be ascribed to Coriolis coupling in the dissociation process, however, further investigation is necessary. It is pointed out that the total angular momentum in the system is small since the rotational temperature of OCS in a supersonic molecular beam is expected to be very low.

This study has presented experimental and theoretical methods to determine the recoil velocity and alignment of atomic fragments simultaneously. A more rigorous analysis without the simplification we made and also a new experimental approach using 3D imaging [11] is expected to provide a further detailed picture of stereochemical dynamics.

References

[1] J. P. Simons, J. Phys. Chem. **91**, 5378 (1987).

[2] P. L. Houston, J. Phys. Chem. **91**, 5388 (1987).

[3] B. J. van Brunt and R. N. Zare, J. Chem. Phys. **48**, 4304 (1968).

[4] E. W. Rothe, U. Krause, and R. Düren, Chem. Phys. Lett. **72**, 100 (1980).

[5] J. Vigué, J. A. Beswick, and M. Broyer, J. Phys. **44**, 1225 (1983)

[6] A. G. Evseev, D. V. Kupriyanov, B. V. Picheyev, B. N. Sevastianov, and O. S. Vasyutinskii, Chem. Phys. **171**, 45 (1993).

[7] B. Ji, P. D. Kleiber, W. C. Stwalley, A. Yiannopoulou, A. M. Lyyra, and P. S. Julienne, J. Chem. Phys. **102**, 2440 (1995).

[8] H. Kato, Faraday Discuss. Chem. Soc. 82, 1, (1986)

[9] Y. Wang, H.-P. Loock, J. Cao, and C. X. W. Qian, J. Chem. Phys. **102**, 808 (1995).

[10] D. W. Chandler and P. L. Houston, J. Chem. Phys. **87**, 1445 (1987).

[11] K. Tonokura and T. Suzuki, Chem. Phys. Lett. **224**, 1 (1994).

[12] P. L. Houston, *private communication*; A. G. Suits, R. L. Miller, and P. L. Houston, *unpublished.*

[13] T. Suzuki, H. Katayanagi, Y. Mo, and K. Tonokura, Chem. Phys. Lett. **256**, 90 (1996).

[14] H. Katayanagi, Y. Mo, and T. Suzuki, Chem. Phys. Lett. **247**, 571 (1995).

[15] A. G. Suits, R. L. Miller, L. S. Bontuyan, and P. L. Houston, J. Chem. Soc. Faraday Trans. **89**, 1443 (1993).

[16] K. Blum, "Density Matrix Theory and Applications" (Plenum, 1981).

[17] R. N. Zare, "Angular Momentum" (Wiley, 1988).

[18] U. Fano and J.H. Macek, Rev. Mod. Phys. **45**, 553 (1973).

[19] D. A. Case, G. M. McClelland, and D. R. Herschbach, Mol. Phys. **35**, 541 (1978).

[20] A.C. Kummel, G. O. Sitz and R. N. Zare, J. Chem. Phys. **85**, 6874 (1986).

[21] M. Rokutan and S. Iwata, *private communication*.

Figures and tables for Chapter 3

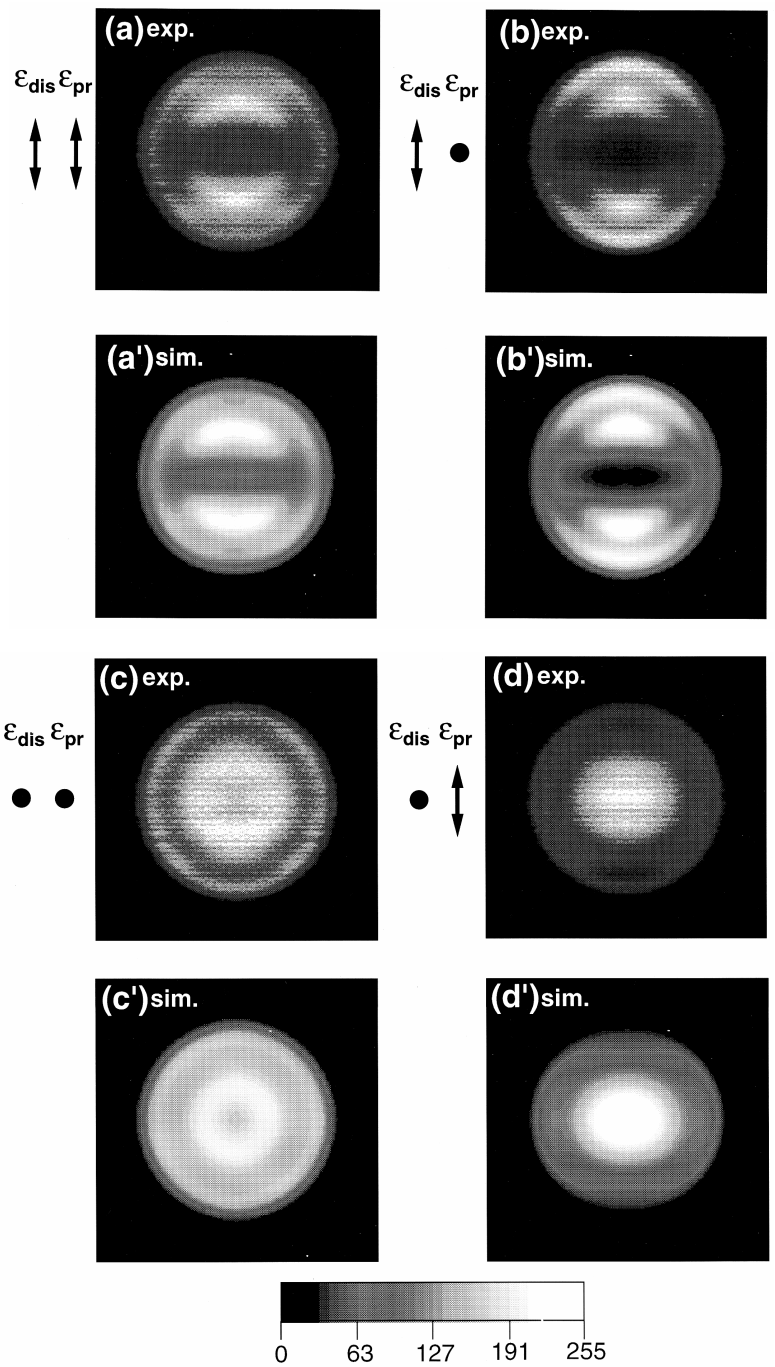

Fig. 3-1

2D ion images of $S(^1D_2)$ produced by 223 nm photodissociation of OCS. (a), (b), (c) and (d) are the experimental data, and (a'), (b'), (c') and (d') are the simulated images obtained by using the parameters in Table 1. The direction of the polarization vectors of the dissociation and probe laser beams are shown as e_{dis} and e_{pr}. The experimental data have been symmetrized for ease of comparison with the simulation.

Table 3-1. Parameters used for the simulation shown in Fig. 3-1.

Dissociation Component	Branching ratio	b	E_0 [a)]	s [a)]	f_m : m-distribution (VF) [b)] m=0	±1	±2
1	1.0	1.8	5.3	4.1	0.60	0.13	0.06
2	3.0	0.7	13.8	5.7	0.48	0.24	0.02

[a)] Energy units are in kcal / mol. The translational energy distributions were expressed by Gaussian functions $\frac{1}{s}\sqrt{\frac{p}{2}}\exp\left(-\frac{2(E-E_0)^2}{s^2}\right)$.

[b)] The distributions are normalized so that $\sum_{m=-2}^{2} f_m = 1$.

Table 3-2. The m-distribution in the MS (molecular symmetry) frame.

Dissociation Component	f_m : m-distribution (MS)[a)] m = 0	±1	±2
1	0.20	0.10	0.30
2	0.14	0.13	0.30

[a)] The distributions are normalized so that $\sum_{m=-2}^{2} f_m = 1$.

Chapter 4

Non-adiabatic Bending Dissociation in 16 Valence Electron System OCS [a]

[a] Published on *Journal of Chemical Physics* **109**, 5778-5794 (1998)

4.1. Introduction

Since a chemical reaction is described by nuclear motion on a potential energy surface (PES), the topography of the PES is the key to understanding photochemical processes. Although the PES's of polyatomic molecules exhibit increasing complexity due to multidimensionality and extensive surface crossings [1], elucidation of the PES topography and its relation to reaction dynamics is feasible in triatomic molecules [2]. This chapter presents novel non-adiabatic dissociation dynamics of a triatomic molecule, as revealed by experimental and computational studies.

OCS is one of the 16 valence electron systems such as CO_2, N_2O, and CS_2. The low lying excited electronic states of these molecules that arise from the promotion of an electron from the highest occupied molecular orbital (HOMO) to the lowest unoccupied molecular orbital (LUMO) are $^{1,3}\Sigma_u^-$, $^{1,3}\Delta_u$, and $^{1,3}\Sigma_u^+$ in symmetric molecules ($D_{\infty h}$), and $^1\Sigma^-$, $^1\Delta$, and $^1\Sigma^+$ in asymmetric molecules ($C_{\infty v}$) [3,4]. Dipole transitions from the ground state ($^1\Sigma^+$) to the excited states $^1\Sigma^-$ and $^1\Delta$ states are forbidden in the linear geometry due to the selection rule, $\Delta\Lambda = \pm 1$ and $+\not\leftrightarrow -$, while weakly allowed by bending deformation. In the bent geometry, the $^1\Delta_u$ state splits to $^1B_2$ and $^1A_2$ ($D_{\infty h} \rightarrow C_{2v}$) and $^1\Delta$ state to A' and A" ($C_{\infty v} \rightarrow C_s$) due to Renner-Teller interactions, where the transitions to $^1B_2$ (C_{2v}) and A' and A" (C_s) states are allowed. The transition to $^1A_2$ ($^1\Sigma_u^-$) is still forbidden in the bent geometry, while A"($^1\Sigma^-$) is allowed.

The first absorption band of OCS in the ultraviolet (UV) region is due to the transitions to $^1\Sigma^-$ and $^1\Delta$ states, for which three upper states, the A' and A" Renner-Teller components of $^1\Delta$ and A"($^1\Sigma^-$) are expected [3-8]. This band is rather broad, indicating that there is a fast dissociation process in the excited states. The dissociation dynamics was studied by Houston and coworkers by vacuum ultraviolet laser induced fluorescence (VUV-LIF) spectroscopy of the CO photofragment [9,10]. An intriguing result they observed was a bimodal rotational distribution of CO expressed by two overlapping Gaussian functions in 222 nm photodissociation [10,11]. The bimodality was initially attributed to the coexistence of singlet and triplet channels, $CO(^1\Sigma^+)+S(^1D_2)/CO(^1\Sigma^+)+S(^3P_J)$ [9]. However, it was reassigned later solely to the singlet channel [10], because the singlet/triplet branching ratio was only 0.95/0.05 at the absorption maximum at 222 nm [12], and the triplet channel could

not account for either of the two components. This assignment was confirmed in our preliminary report [13] by two-dimensional (2D) ion imaging of $S(^1D_2)$ atom in the 223 nm photodissociation of OCS, which revealed a bimodal speed distribution of $S(^1D_2)$ in an excellent agreement with the rotational distribution of CO [10]. 2D imaging of the $S(^3P_2)$ fragment has also shown that such a prominent bimodality does not occur in the triplet channel [13]. Sato *et al.* have observed the bimodal rotational distribution of CO in 217 and 230 nm photodissociation of OCS by (2+1) REMPI of CO [14]. Despite this experimental evidence for the bimodal distribution, however, there has been no convincing explanation for its origin. The present work was directed to the elucidation of the source of this bimodality.

Ab initio calculations on isovalent systems of CO_2 [15] and N_2O [16] in the 1980s have shown that the excited state surfaces are much complicated due to conical intersections and avoided crossings. Obviously, a computational approach is indispensable to untangle the dissociation dynamics of 16 valence electron systems. Thus, experimental and computational approaches were combined in the present work.

In the dissociation of symmetric triatomic molecules, the coupling between symmetric and antisymmetric stretching vibrations may complicate the dynamics [17,18]. This is avoided in asymmetric molecules, since the reaction coordinate, one of the stretching modes, can be uncoupled from the other. In UV photodissociation of OCS, the CO photofragment is not vibrationally excited [10]. Therefore, the CO stretching motion is considered to be a spectator in the dissociation [10]. This implies that a reduced-dimensional model neglecting C=O stretch vibration will sufficiently approximate the dissociation dynamics of OCS.

4.2. Experimental

4.2.1. Apparatus

A schematic diagram of our experimental apparatus is shown in Figure 4-1. A sample gas seeded in He or Ar was expanded from a pulsed valve (General Valve Series 9, 0.8 mm orifice diameter) with a stagnation pressure of about 1 atm and collimated by two skimmers both 0.5 mm in diameter. The molecular beam was introduced into a time-of-flight (TOF) mass spectrometer parallel to its electric field vector through the second skimmer embedded in the repeller plate. The molecular beam intersected perpendicularly with the counter-propagated pump and probe laser beams 79 mm downstream from the nozzle, where the beam diameter was 1 mm in the full width at half maximum (FWHM). When the pulsed

valve was operated, typical pressures in the beam source and in the main chamber were 2 x 10^{-5} Torr and ~2 x 10^{-7} Torr, respectively. The source chamber was evacuated by an oil diffusion pump (Edwards, Diffstack 250/2000), and the main chamber by a turbo molecular pump (Balzers, TMP500).

The pump beam was the second harmonic of the output of a Nd:YAG-pumped dye laser (Quanta-Ray GCR-230-25 and Lumonics HD-500). The second harmonic of the output of another dye laser (Quanta-Ray GCR-230-25 and Lumonics HD-500) was used as a probe beam. Both laser beams were linearly polarized and their polarization directions were varied independently by double Fresnel rhombs. State-selective ionization of S atoms was performed by (2+1) REMPI (resonance-enhanced multiphoton ionization) using the resonances of $^1F_3 \leftarrow\leftarrow {}^1D_2$ (288.188 nm), $^3P_2 \leftarrow\leftarrow {}^3P_0$ (310.949 nm), $^3P_2 \leftarrow\leftarrow {}^3P_1$ (310.096 nm), and $^3P_1 \leftarrow\leftarrow {}^3P_2$ (308.218 nm). The time delay between the pump and probe laser pulses was kept less than 20 ns. Both the pump and probe beams were focused with an axisymmetric lens (f = 250 or 300 mm). The pump laser energy was < 0.2 mJ $pulse^{-1}$ at 223 nm, 0.2 mJ $pulse^{-1}$ at 235 nm, and 0.1-1.0 mJ $pulse^{-1}$ at 248 nm.

The photoions produced were accelerated up to the kinetic energy of 5 keV and projected onto a dual microchannel plate backed by a phosphor screen (MCP, Hamamatsu, F2225-21PGFX, 36 mm in effective diameter). Although electric fields in the extraction and acceleration regions could be adjusted independently, the ion images were always measured with the same field strengths in the two regions to avoid image distortion due to the deflection of ions by disturbed electric field around the wire mesh. A high voltage pulse, 1600-1800 V in height and 200 ns in duration, was applied to the MCP to time-gate the $^{32}S^+$ ions by a home-made high voltage pulser using a transistor switch (Behlke, HTS-30). The transient image on the phosphor screen was captured by a video-rate (CCIR) interline charge-coupled device (CCD) camera (Sony, XC77-CE, 756 × 581 pixels) through a camera lens (Nikon, F = 1.2) and integrated by an image capture board with 16 bit on-board memory (Hamamatsu, IQV-50). Images were typically integrated for 125,000 - 127,000 laser shots. During the integration of images, the probe laser frequencies were scanned over the entire S absorption line broadened by the Doppler effect due to recoil velocity.

The timings between the pulsed molecular beam, pump and probe laser beams, and high voltage pulse for an MCP were controlled by a delay generator (Sanford Research Systems, DG535). The laser pulses were synchronized to the readout of a CCD camera (CCIR).

In order to obtain high brightness of the light spot on the phosphor screen, detected by an insensitive video-rate CCD camera, P20 was chosen as a phosphor material in favor of its emission wavelength (~540 nm) and high emission intensity. Since the emission lifetime of P20 is longer than 1 ms at an electron impact energy higher than 3 kV, a single mass selection was only achieved by switching the high voltage applied to the MCP.

The one-dimensional (1D) time-of-flight (TOF) spectra were measured by two methods. One was to monitor the AC component in phosphor voltage by setting the electron impact energy to the phosphor to be about 100V. The other was to monitor the emission from the phosphor with a photomultiplier tube with the electron impact energy to the phosphor of about 1 kV; at this voltage, the emission lifetime of P20 was less than 50 ns.

In the ion imaging experiment, ions are accelerated into the kilo-electron-volt range along the z flight axis, while the crucial kinetic energy for the x and y (field-free) directions are typically 1 eV or less. Therefore, it is important to avoid any distortion of electric field that would affect the velocity of ions in the x and y directions. In the present work, a uniform electric field was generated by a stack of stainless-steel guard rings (40 mm in diameter) spaced by ruby balls. Ion trajectory calculations showed that this arrangement is free from any field distortion that is detectable with the resolution of our apparatus. Although a Moire interference pattern has been observed with widely-spaced wire meshes (MN-17, 70 lines $inch^{-1}$, Buckbee-Mears), this was eliminated by replacing them to finer ones (MN-38, 333 lines $inch^{-1}$).

In general, a finer mesh reduces the transmission of ions, but it provides better spatial resolution in ion imaging. Bergmann *et al.* [19] have shown that the ions passing through a wire mesh are deflected according to the following formula

$$\Delta v_y = \frac{q\Delta E}{m v_z}[y - \frac{a}{2}]$$

where Dv_y is the change of velocity in y direction, q is the charge, DE is the difference of the field strength between the two sides of a mesh, m is a mass of an ion, v_z is the speed along the flight path, and a is the spacing of the wires in a mesh. The deviation in the arrival position in y direction on the detector is given by

$$\Delta v_y T_{tof} = \Delta v_y \frac{L}{v_z} = \frac{q\Delta E a}{2 m v_z}\frac{L}{v_z} = \frac{q\Delta E a L}{4 E_k}$$

where L is the flight length and E_k is the kinetic energy of an ion. When an ion is accelerated by a single electric field and is led into a field free region, the above formula is further reduced to

$$\Delta v_y T_{tof} = \frac{aL}{4l}$$

where l is the distance from the ion source to the end of the acceleration field. For L = 60 cm, l = 5 cm, and a = 76 μm, the deviation is calculated to be 0.23 mm. Note that this value is comparable with other factors that determine the resolution of an imaging detector. For instance, the size of a light spot on the phosphor is a couple of hundred microns in diameter, when the gain of an imaging detector is increased to compensate for the insensitivity of the video rate camera. The pixel numbers of a CCD chip also limit the resolution; the 400 × 400 pixels of a CCD camera in viewing the phosphor 40 mm in diameter provides a spatial resolution of 100 μm.

Because of the character of linear-bent transition, hot bands from the excited level of bending vibration may occur. Locker *et al.* have reported that the average absorption coefficient from (010) level is approximately twice larger than that from (000) [7]. Since the bending frequency is 520 cm^{-1} in the ground state, the population in (010) is about 11% of that of (000) at 273 K. Hot bands can be reduced by improving the vibrational cooling in a jet using Ar instead of He as a carrier gas. We have examined the vibrational cooling in the beam by measuring the intensity of the $2_0^1 V_1^4 K_1^2$ band with respect to the $2_0^1 V_0^4 K_0^1$ band in $\tilde{A} - \tilde{X}$ transition of acetylene [20-23] for the samples seeded in Ar (1.7 % in Ar, stagnation pressure 0.9 atm) and He (20 % in He, stagnation pressure 0.4 atm). The in-plane bending mode, named V, in the ground state of acetylene is 611.7 cm^{-1} that is similar to the bending frequency of OCS, 520 cm^{-1}. It was found that the relative intensity of the hot band decreased from 14% to 3.2% by changing the carrier gas from He to Ar. We have measured the ion images of $S(^1D_2)$ for OCS seeded 10 % in He and 3% in Ar, however, no difference was observed. Thus, hot bands, if any, are negligible in our experiment.

On the other hand, when $S(^3P_J)$ images were observed with a sample gas 10% in He or Ar, a significant amount of low energy S atoms were observed as shown in Figure 4-2. These slow $S(^3P_J)$ atoms were assigned to the product of $S(^1D_2)$ atoms quenched in photodissociation of OCS clusters. Since $S(^3P_J)$ is a minor product (about 5%) in UV photodissociation of OCS, its observation was sensitive to cluster formation. Thus, $S(^3P_J)$ data were obtained with the sample gas < 3% diluted in rare gases.

4.2.2. Image analysis

4.2.2.1. Inversion of a 2D image to a cylindrically symmetric 3D distribution

The image experimentally observed is a 2D projection of a 3D distribution of photofragment ions [24-26]. The original 3D distribution of neutral photofragments has cylindrical symmetry around the electric vector of a linearly-polarized pump laser beam. The symmetry is retained when the electric vector of linearly-polarized pump and probe laser beams are parallel to each other. In such a case, the section of the 3D ion distribution that corresponds to a differential cross section can be obtained from a single 2D projection data by an inverse Abel transform [24-27].

The transform inherently requires that the 2D projection is symmetric between the left- and right-hand sides of the symmetry axis, while an observed image often exhibits a slight asymmetry due to non-uniform detection sensitivity of the apparatus. This asymmetry was removed by symmetrization of observed images prior to the transform. Although symmetrization is often employed in ion imaging experiments, this procedure diminishes the apparent experimental noise. In order to allow close inspection of experimental uncertainty, we present unsymmetrized images rather than symmetrized ones. In our previous paper, we have evaluated the uncertainty that arises from symmetrization [28,29]. Two symmetric images were constructed from an original image by using either left or right halves, and an inverse Abel transform has been applied to these two. From the comparison of the two data, the uncertainty in the anisotropy parameter was determined to be $Db/b = 0.1 \sim 0.2$. The standard deviation in least squares fitting of each angular distribution is much smaller than $Db/b = 0.1 \sim 0.2$, and this value should be taken as the largest bound of an experimental error. The experimental uncertainty in the determination of the translational energy release, $P(E_T)$, was about 5 % for the entire energy range. Deblurring [30] was not performed for the observed images, since the point spread function (PSF) [31] is variable with experimental conditions [29]. No filtering has been performed on the original 2D data to removes noise prior to an inverse Abel transform.

4.2.2.2. Forward convolution analysis considering the alignment of $S(^1D_2)$ atom

An inverse Abel transform can reconstruct cylindrically symmetric 3D object from a single 2D projection data. However, the ion distribution does not necessarily retain the cylindrical symmetry of a neutral photofragment distribution, since the ion distribution reflects not only the scattering distribution of neutral fragments but also the scattering-angle-dependent ionization efficiency. The dependence of ionization efficiency upon the scattering angle arises from the electronic orbital alignment of $S(^1D_2)$ atom [32]. If the electron orbital of S atom is aligned in the molecular frame, the relative angle between the electronic orbital angular momentum and polarization vector of the probe laser beam varies as a function of scattering angle in the laboratory frame, which makes the ionization efficiency to be scattering-angle-dependent.

As described in a previous section, when the polarization of pump and probe lasers are aligned parallel to each other, an inverse Abel transform allows us to obtain the correlated speed-angular distribution of fragments. This is a convenient method for qualitative examination of the scattering distribution; however, it does not provide quantitative evaluation of the scattering distribution when the detection efficiency is scattering-angle dependent.

Orbital alignment is the correlation between an angular momentum $\boldsymbol{J}$ and a velocity $\boldsymbol{v}$, and it is phenomenologically the same as $\boldsymbol{v}$-$\boldsymbol{J}$ correlation in a diatomic fragment [33,34]. However, the $\boldsymbol{v}$-$\boldsymbol{J}$ correlation in the molecular fragment is created by mechanical torque imparted on the fragment upon bond cleavage, while an atomic fragment is purely electronic and is different in its origin. Furthermore, $\boldsymbol{v}$-$\boldsymbol{J}$ correlation in the diatomic fragment in the photodissociation of a triatomic molecule is trivial ($\boldsymbol{v}\perp\boldsymbol{J}$) for large J, since helicity is conserved during the process, while an a priori assumption cannot be made on the atomic orbital alignment.

In the case of $S(^1D_2)$, $\boldsymbol{J}$ equals to the orbital angular momentum $\boldsymbol{L}$, since the total electron spin $\boldsymbol{S}$ is zero. The dominant isotopes ^{32}S(natural abundance 95.02 %) and ^{34}S(4.21 %) lack nuclear spin [35], so there is no hyperfine depolarization. Since the typical pump-probe time delay is less than 20 ns, depolarization of $\boldsymbol{J}$ due to an external electromagnetic field prior to observation can also be neglected. The nascent angular momentum polarization distribution, therefore, can be measured.

The detection of reaction products by laser excitation is essentially a measurement of density. However, for a short *pump-probe* delay in photodissociation experiments, a density

mode of detection is the same as a flux mode, since the laser pulse covers and detects all the velocity components equally. Hence, the absorption intensity I is independent of speed $\boldsymbol{v}$ and proportional to the optical absorption intensity.

The optical absorption intensity I can be expressed by the following formula,

$$I \propto \sum_k P_k \sum_q r_q^{(k)}(SF) \boldsymbol{D}_{q0}^{(k)*}(f_p, q_p, c_p) \qquad (1)$$

where P_k denote the *geometrical factors* determined by the probing scheme (the type of transition and the number of photons absorbed), $r_q^{(k)}(SF)$, the multipole moments [36] of the probed atoms in the *space-fixed* (*SF*) frame that fully characterize the polarization of angular momentum, and $\boldsymbol{D}_{q0}^{(k)}(f_p, q_p, c_p)$, the rotation matrix that transforms the space-fixed frame to a probe laser photon frame (*PR*-frame) for Euler angles (f_p, q_p, c_p).[37] For linearly polarized light, the *probe-laser* photon frame is defined by its polarization direction as the z-axis and its propagation direction as the y-axis. Multipole moments reflect reaction dynamics, so these are called *dynamical factors*. Angular momentum polarization can also be expressed in terms of a density matrix; however, the multipole moment description is employed here for its clearer physical picture. Due to the cylindrical symmetry around the polarization vector of the linearly-polarized probe laser, only the multipole moment of component 0 (in other words the diagonal elements of density matrix) can be detected in the probe laser photon frame.

It is shown that the relative value of P_k is given by a simple formula, when the angular momenta of the initial and final states are different ($J_i \neq J_f$) [32,38]

$$P_k^{\circ} = P_k / P_0 = 5\sqrt{2k+1}\sqrt{2J_i+1}(-1)^{J_i+J_f} \begin{pmatrix} 2 & 2 & k \\ 2q & -2q & 0 \end{pmatrix} \begin{Bmatrix} J_i & J_i & k \\ 2 & 2 & J_f \end{Bmatrix} \qquad (2)$$

For the probing scheme employed for S(^{1}D$_2$), the ratios are $P_0 : P_2 : P_4$ = 1: 0.68 : -0.11 [32].

Since the photoexcitation of OCS is dominated by a parallel-type transition to the A' state, as will be seen later, its multipole moments may be approximated by the following formula [32, 39]

$$r_q^{(k)} = \frac{1}{4p}(1 + bP_2(\cos q_t)) r_0^{(k)}(VF) \boldsymbol{D}_{q0}^{(k)}(j_t, q_t, 0) \qquad (3)$$

where b is the anisotropy parameter and $r_0^{(k)}(VF)$ is the multipole moment in the velocity-fixed (VF) coordinate that is defined by the recoil velocity as the z-axis. The VF frame is regarded as the asymptotic form of Jacobi coordinate (r, R, q) for $R \rightarrow \infty$. The

magnetic quantum number described in this frame is so-called helicity. In Eq. (3), the first factor is the angular distribution of photofragments [40], and the second factor the polarization of angular momentum. In a cylindrically symmetric system, the projection of the angular momentum onto the symmetry axis is a good quantum number; hence there are no coherent terms in the angular momentum polarization described in the coordinate with the quantization axis (z-axis) along the symmetry axis [36]. For the same reason, when the multipole moment is described in the VF coordinate for the case where the transition dipole moment m is parallel to the recoil velocity $\boldsymbol{v}$, the terms of $q \neq 0$ will be considerably smaller than the $q = 0$ term. Therefore, these $q \neq 0$ terms are neglected in the present work. Then, $r_0^{(k)}(VF)$ is given by

$$r_0^{(k)}(VF) = \sum_m (-1)^{J-m} \sqrt{2k+1} \begin{pmatrix} J & k & J \\ -m & 0 & m \end{pmatrix} f_m \qquad (4)$$

where f_m is the fractional population in each m state in the VF coordinate. The last term in Eq. (3) is the rotation matrix for transforming VF to the space-fixed frame. The simulation was performed iteratively until we found the f_m distribution that reproduced the experimental data.

4.3. Theoretical Calculations

4.3.1. *Ab initio* molecular orbital configuration-interaction calculations

Complete active space self-consistent field (CASSCF) and multi-reference configuration interaction (MRCI) calculations were performed by using the DZP basis sets of Schafer *et al.* [41]. The symmetric species of the ground state is $^1\Sigma^+$; the molecular orbitals (MOs) and the electron configuration at the equilibrium geometry is as follows,

$(1\sigma)^2(2\sigma)^2(3\sigma)^2(4\sigma)^2(5\sigma)^2(1\pi)^4(6\sigma)^2(7\sigma)^2(8\sigma)^2(9\sigma)^2(2\pi)^4(3\pi)^4(4\pi)^0(10\sigma)^0(11\sigma)^0 \ldots (1^1\Sigma^+)$

where the character of each orbital at the equilibrium geometry can be described as,

9σ: CS σ bonding orbital, σ_{CS}, with a minor character of CO σ bonding orbital

2π: CO π bonding orbital, π_{CO}, with a minor character of SO π bonding orbital

3π: antibonding orbital constructed from 3*p* orbital on S and 2*p* orbital on O

4π: antibonding orbital constructed from CO π* and 3*p* orbital on S

10σ: CS σ* anti-bonding orbital, σ^*_{CS}, with a minor character of CO σ bonding orbital.

11σ: CO σ* anti-bonding orbital, σ^*_{CO}, with a minor character of CS σ* antibonding orbital

Four excited singlet states arise from $S(^1D) + CO(^1\Sigma^+)$ asymptote; these are $1^1\Pi$ and $1^1\Delta$ in the linear geometry. These states are split by bending deformation (Renner-Teller interactions). $1^1\Sigma^-$ and $2^1\Sigma^+$ states, correlated with $S(^3P) + CO(^3\Pi)$ and $S(^1S) + CO(^1\Sigma^+)$, are in the same energy region. In order to describe these low-lying states accurately, the active space orbitals were selected as follows;

$$[(9\sigma)(2\pi)(3\pi)(4\pi)(10\sigma)(11\sigma)]^{10}.$$

The CASSCF wave function spans all possible configurations generated by ten electrons in the nine active orbitals. The restricted close-shell SCF MOs were used in an initial state-averaged CASSCF calculation, and then the state-averaged CASSCF calculation for five A' and three A" states was performed to describe properly the excited states correlated with $S(^1D) + CO(^1\Sigma^+)$, $S(^1S) + CO(^1\Sigma^+)$ and $S(^3P) + CO(^3\Pi)$ asymptotes.

In the state-averaged CASSCF calculations, non-adiabatic coupling matrix elements between $1^1A'$ and $2^1A'$ in the C_s symmetry were analytically computed using the CP-MCSCF (Coupled-Perturbed MCSCF) solutions. The natural orbitals obtained from the CASSCF calculation were used in the final internally contracted MRCI calculations. The configuration state functions (CSFs) were generated by single and double excitations based on the reference configurations obtained by the CASSCF calculations. However, the total number of configurations, typically about 6,600,000, was too large to obtain the potential energies for various geometries. Therefore, about 300,000 reference configurations were selected in terms of the norms of the CSF coefficients. Transition dipole moments were evaluated from the CI wave functions. Potential energies and transition dipole moments calculated at 361 geometry were spline-interpolated to carry out time-dependent quantum dynamical calculations on the PES's.

All the *ab initio* calculations were performed using MOLPRO [42] on the IBM SP2 or NEC SX3.

4.3.2. Time-dependent quantum dynamical calculation

The wave packet calculations were performed based on the procedure of Offer and Balint-Kurti [43]. Jacobi coordinates (Figure 4-3) were employed to describe the relative positions of the three nuclei in the body fixed plane; R is the distance between the S atom and the center of mass of CO, r is the bond length of the CO molecule (fixed at r_{CO} = 1.13 Å in the present study), and q is the angle between the vectors **R** and **r**.

As discussed later, non-adiabatic transitions were taken into account to reproduce the experimental data. The procedure to include a non-adiabatic transition in wave packet calculations is outlined as follows. In the diabatic state representation, the two dimensional two-state problem is described by the following time-dependent Schrödinger equation ($\hbar$=1):

$$\boldsymbol{H}\boldsymbol{\Psi} = i\frac{\partial}{\partial t}\boldsymbol{\Psi} \tag{5}$$

where

$$\boldsymbol{H} = \begin{bmatrix} T+V_1 & V_{12} \\ V_{12} & T+V_2 \end{bmatrix} = \begin{bmatrix} T+V_1 & 0 \\ 0 & T+V_2 \end{bmatrix} + \begin{bmatrix} 0 & V_{12} \\ V_{12} & 0 \end{bmatrix} = \boldsymbol{H}_{diag} + \boldsymbol{H}_{off-diag} \tag{6}$$

and

$$\boldsymbol{\Psi} = \begin{bmatrix} y_1 \\ y_2 \end{bmatrix} \tag{7}$$

V_1 and V_2 are diabatic potentials, V_{12} is the coupling between the diabatic states y_1 and y_2, and T is the kinetic term. The off-diagonal Hamiltonian matrix $\boldsymbol{H}_{\text{off-diag}}$ is diagonalized by the unitary transformation, as follows

$$\boldsymbol{U}^{+}\boldsymbol{H}_{off-diag}\boldsymbol{U} = \boldsymbol{V}_{12} = \begin{bmatrix} -V_{12} & 0 \\ 0 & V_{12} \end{bmatrix} \tag{8}$$

The following procedure carries out the time propagation of the wave function:

$$\begin{aligned}
&\Psi(R,q;t=dt) = \exp(-i\boldsymbol{H}dt)\Psi(R,q;t=0) \\
&= \exp(-i\boldsymbol{H}_{diag}dt)\exp(-i\boldsymbol{H}_{off-diag}dt)\Psi(R,q;t=0) \\
&= \exp(-i\boldsymbol{H}_{off-diag}\frac{dt}{2})\exp(-i\boldsymbol{H}_{diag}dt)\exp(-i\boldsymbol{H}_{off-diag}\frac{dt}{2})\Psi(R,q;t=0) \\
&= \boldsymbol{U}\boldsymbol{U}^{+}\exp(-i\boldsymbol{H}_{off-diag}\frac{dt}{2})\boldsymbol{U}\boldsymbol{U}^{+}\exp(-i\boldsymbol{H}_{diag}dt)\boldsymbol{U}\boldsymbol{U}^{+}\exp(-i\boldsymbol{H}_{off-diag}\frac{dt}{2})\boldsymbol{U}\boldsymbol{U}^{+}\Psi(R,q;t=0) \\
&= \boldsymbol{U}\exp(-i\boldsymbol{V}_{12}\frac{dt}{2})\boldsymbol{U}^{+}\exp(-i\boldsymbol{H}_{diag}dt)\boldsymbol{U}\exp(-i\boldsymbol{V}_{12}\frac{dt}{2})\boldsymbol{U}^{+}\Psi(R,q;t=0)
\end{aligned} \tag{9}$$

where dt is a time-step that is sufficiently small to maintain unitarity. Complex Chebyshev polynomials were used in the approximation of the diagonal operator, exp(-$i\boldsymbol{H}_{diag}\,dt$)[44]. In operating the kinetic energy term on the wave function, the fast Fourier transform (FFT) between the position and momentum space was employed. When the coordinate space is finite, the wave packet reaches the boundary and appears from the other side in the FFT treatment. In order to avoid this problem, the following absorbing potential was introduced,

$$V_{damp} = -iCR^4 \tag{10}$$

where the coefficient C was determined by the procedure described by Vibok and Balint-Kurti [45].

An initial wave function $f_2(R, q; t=0)$ is determined by the product of the transition dipole moment function, $\vec{m}$, and the ground state wave function $f_1(R, q)$

$$f_2(R,q;t=0) = \vec{m} \cdot \hat{e} f_1(R,q) \tag{11}$$

where $\hat{e}$ is a unit vector in the direction of polarization of the pump laser beam in the space fixed frame, and $f_{1,2}$ are the adiabatic nuclear wave functions for the ground and excited states, respectively. Since the initial wave function is confined and located away from the avoided crossing region, the initial wave function in the diabatic representation, ψ_2, is assumed to be identical with that in the adiabatic representation, f_2,

$$y_2(R,q;t=0) \approx f_2(R,q;t=0) \tag{12}$$

The initial wave packet was then evolved with time on the PES's, to obtain the autocorrelation function $A(t)$,

$$A(t) = \int R^2 dR d(\cos q) y_2^{J'M'*}(R,q;t=0) y_2^{J'M'}(R,q:t) \tag{13}$$

The Fourier transform of the autocorrelation function provides the total photodissociation cross section, as follows

$$s^{total}(n) \sim n \int_{-\infty}^{\infty} dt \exp[i(E_{init} + hn)t] A(t) \tag{14}$$

In the asymptotic region defined at R = 4.0 Å, the outgoing wave functions were expanded by the rotational eigenfunctions, which provided the partial cross sections. According to the procedure of Balint-Kurti *et al.* [46], the energy dependence of the partial cross sections was estimated for individual rotational states of CO. The grid points sampled were 128 for q and 256 for R (1.8 $\leq R \leq$ 5.0). The time evolution was computed with the time step of dt= 10.47 a.u. up to t = 85786 a.u.

4.4. Results

4.4.1. Joint state distributions and overview of the reaction

Ultraviolet photodissociation of OCS has singlet and triplet dissociation channels,

$$\mathrm{OCS} \rightarrow \mathrm{CO}(^1\Sigma^+) + \mathrm{S}(^1\mathrm{D}_2) \qquad \Delta H = 98.3 \text{ kcal mol}^{-1} \qquad \text{(I)}$$

$$\rightarrow \mathrm{CO}(^1\Sigma^+) + \mathrm{S}(^3\mathrm{P}_0) \qquad \Delta H = 73.6 \text{ kcal mol}^{-1} \qquad \text{(IIa)}$$

$$\rightarrow \mathrm{CO}(^1\Sigma^+) + \mathrm{S}(^3\mathrm{P}_1) \qquad \Delta H = 73.0 \text{ kcal mol}^{-1} \qquad \text{(IIb)}$$

$$\rightarrow \mathrm{CO}(^1\Sigma^+) + \mathrm{S}(^3\mathrm{P}_2) \qquad \Delta H = 71.9 \text{ kcal mol}^{-1} \qquad \text{(IIc).}$$

Nan *et al.* have reported the yield of $S(^3P_J)$ to be only 0.05 [12]. It is certain that singlet channel (I) is dominant. Discrimination of the four exit channels is straightforward by state-selective detection of S atoms, and the internal energy distributions of the counterpart CO are determined by momentum and energy conservation laws. Therefore, the quantum state correlation between the CO and S fragments (also termed as 'joint probability' or 'joint state distribution') can be obtained easily.

Figure 4-4 shows 2D ion images of $S(^1D_2)$ and $S(^3P_J)$ atoms observed in 223 nm photodissociation of OCS. The result clearly indicates that the dissociation dynamics of singlet and triplet channels are different from each other. The singlet channel provides two speed components, fast and slow $S(^1D_2)$ atoms, with comparable intensity, while triplet channels are dominated by one speed component in all cases. Close inspection of the $S(^3P_J)$ images reveals noticeable difference among them; the difference in the translational energy release calculated from these images is seen in Figure 4-4. The data show that the peaks of the CO rotational distribution in each channel are, J = 76 in the $S(^3P_0)$ + CO channel, 71 and 79 in the $S(^3P_1)$+ CO channel, and 79 in the $S(^3P_2)$ + CO channel, respectively. The results show that the dissociation dynamics on the three triplet surfaces are different. In the present paper, we focus on the singlet channel.

4.4.2. Wavelength dependence of the singlet channel and qualitative analysis

Figure 4-5(a) shows an inverse Abel transform of the data shown in Figure 4-4, providing correlated speed-angular distribution of $S(^1D_2)$, $I(v,q)$. Although the two velocity components were visible in the original data, they can be seen more clearly in the transformed data. In the outer part of the image, fast S atoms with a rather isotropic angular distribution can be seen, while in the inner part, slow S atoms exhibit strong anisotropy. Two areas of

the image that correspond to the fast and slow components were extracted from the Figure 4-5(a), and their angular distributions were obtained by integrating the radial part,

$$P_1(q)\Big|_{v1}^{v2} = \int_{v1}^{v2} I(v,q)dv \qquad (15)$$

As seen in Figure 4-6, angular distributions were well fitted by the standard formula

$$P(q) = s\ /2p\{1 + bP_2(\cos q)\} \qquad (16)$$

where q is the angle between the electric vector of the pump laser and the recoil velocity, $P_2(x)$ is the second-order Legendre polynomial, and b is an anisotropy parameter [40]. For an instantaneous dissociation, b is given by $2P_2(\cos\ c)$, where c is the angle between the transition dipole moment (m) in the parent molecule and the recoil velocity ($\boldsymbol{v}$). Anisotropy parameters were determined to be 0.2 and 1.1 for the high and low translational energy components, respectively. These values are affected by the orbital alignment of $S(^1D_2)$ atoms, and the true anisotropy parameters will be found much higher in a later section.

Large positive anisotropy parameter observed for the slow $S(^1D_2)$ atoms indicates that this component is produced by dissociation from the A' excited state. In the case of dissociation from the A" state, the transition dipole moment is perpendicular to the molecular plane in the bent geometry of OCS, so that S atoms will be ejected perpendicular to the transition dipole moment, leading to a negative b value. Since there is only one possible A' electronic state, it is uniquely assigned to the A' Renner-Teller component of $^1\Delta$ state.

On the other hand, the almost isotropic distribution of the fast component suggests that it is the admixture of dissociation from both the A' and A" states. There are two possible A" states, the A" Renner-Teller component of the $^1\Delta$ state and the A"($^1\Sigma^-$) state. The A"($^1\Delta$) is located higher than the A'($^1\Delta$), while the A"($^1\Sigma^-$) is located near and possibly lower than the A'($^1\Delta$). In the inverse Abel transforms of the $S(^1D_2)$ images, shown Fig. 4-5, it is seen that the high-energy component changes from rather isotropic distribution to the anisotropic distribution predominantly perpendicular to the pump laser polarization in changing the photoexcitation wavelength from 223 to 248 nm. The result, therefore, indicates that the high-energy component is due to the admixture of dissociation from the A' and A" states, and that the contribution from the A" state is larger at the lower excitation energy. This means the A" state is located lower in energy. Thus, the upper state with A" symmetry is assigned to A"($^1\Sigma^-$) state.

Sivakumar *et al.* have performed VUV-LIF detection of CO in photodissociation of OCS at the excitation wavelengths of 222, 235, and 248 nm [10]. They observed a bimodal

rotational distribution of CO at 222 nm but not at other wavelengths, from which they suggested the assignment of the A" upper states to A"($^1\Delta$) rather than A"($^1\Sigma^-$) states [10]. From Fig. 4-5, however, it is seen that the bimodal speed distribution of S($^1D_2$) exists at 235 and 248 nm. The rotational distributions of the CO fragment, shown in Fig. 4-7, were estimated from the S($^1D_2$) fragment data using energy and momentum conservation laws. By comparing Fig. 4-7 with Fig. 4 in Ref. [10], we find an excellent agreement for one of the bimodal distributions of CO. The other peak in the bimodal distribution was unfortunately outside of the range which Sivakumar *et al.* have investigated for 235 and 248 nm excitation [10].

The advantage of measuring atomic fragments in the photodissociation of triatomic molecules is that the internal energy distribution of the counterpart diatomic molecule can be obtained without elaborate spectroscopic observation of the diatomic fragment. The disadvantage, however, is that the vibrational and rotational excitations in diatomic fragment cannot be differentiated. In the present case, however, it has been shown by VUV-LIF that the vibrational excitation of CO is negligible [10]. It is also noted that fast S atoms produced from A'($^1\Delta$) and A"($^1\Sigma^-$) states could be slightly different; as evidenced by *b* values that gradually change as a function of *J* within one peak of the bimodal rotational distribution of CO (see Table I in Ref [10]). This slight dependence of *b* on the recoil velocity of S($^1D_2$) has been neglected and one unique *b* value has been assigned to each component in the present work, which is only approximate.

4.4.3. Questions to be answered

As discussed above, the fast S($^1D_2$) atoms are produced both from A' and A" upper states with almost the same speed. This implies that the torque imparted on CO by these two states are almost equal. Walsh diagrams [5] predict that the HOMO(3π) splits to a' and a" and the LUMO (4π) into a' and a" orbitals by bending deformation of OCS. The orbitals in the plane of molecule are destabilized ($3\pi \rightarrow 12a'$) or stabilized ($4\pi \rightarrow 13a'$), while the a" orbitals are not affected, since these are perpendicular to the plane. Thus, the A'($^1\Delta$) and A"($^1\Sigma^-$) states are expected to have different potentials for the bending coordinate, while experimental data suggests that these are almost the same. *Why does dissociation from the A' and A" states produce almost the same speed of S atoms?*

Slow $S(^1D_2)$ atoms produced solely from A' state imply that there is an additional dissociation pathway for A'. *Why does only the A' state show a bimodal product state distribution?*

4.4.4. Evidence indicating the importance of bending motion

In elucidating the dissociation dynamics of OCS, it is clear that one has to take full account of the bending motion of the molecule. The important role of bending deformation is evidenced by several facts. First, the excited states have bent geometry, as predicted by Renner-Teller interactions in the $A'(^1\Delta)$ state. Furthermore, the transition dipole moments for $^1\Delta \leftarrow {}^1\Sigma^+$ and $^1\Sigma^- \leftarrow {}^1\Sigma^+$ are zero in the linear, so that Franck-Condon regions are located in the bent portions of the upper state PES's.

Second, the rotational excitation of CO fragment is only explained by the transformation of bending energy into the rotation of CO. If one tries to explain rotational excitation of CO by a simple impulsive model, unrealistically large impact parameters must be assumed. This clearly demonstrates the inapplicability of an impulsive model to photodissociation of OCS. By using a Jacobi coordinate shown in Figure 4-3, the torque imparted on the diatomic molecule is expressed by

$$F_q = -\frac{\partial V}{\partial J} \qquad (17).$$

which is also expressed by bond lengths and an bending angle (R_{CO}, R_{CS}, c) as

$$F_J = -\frac{\partial V}{\partial R_{CS}}\frac{\partial R_{CS}}{\partial J} - \frac{\partial V}{\partial c}\frac{\partial c}{\partial J} \qquad (18).$$

An impulsive model takes into account the first term but neglects the second, corresponding to the transformation of bending force into the rotation of diatomic molecule [2]. In the photodissociation of OCS, the second term is important.

4.4.5. Potential energy surfaces and transition dipole moment functions

Table 4-1 tabulates the experimental data and the theoretical results for the equilibrium geometry and the dissociation energy in the ground electronic state [47-48]. In Table 4-2 are listed the C-S stretch and bending frequencies [49]. It has been experimentally established that the CO product is not vibrationally excited in the photodissociation of OCS [10], so that CO stretch is a spectator in the reaction. Furthermore, the r_{CO} distance (r_{CO} = 1.155386 Å) of OCS in the electronic ground state is similar to that of an isolated CO molecule (r_{CO} =

1.1283 Å). Therefore, the r_{CO} distance was fixed at r_{CO} = 1.13 Å in our *ab initio* calculations.

Figure 4-8 shows the potential energy curves as a function of R in the linear geometry with r_{CO} =1.13 Å. (In all of the figures of the PESs, the energy is indicated with respect to the minimum of the ground electronic state.) Our theoretical value for D_e was 4.16 eV, while the thermochemical data is 4.26 $\pm$ 0.1 eV. In the dissociation limit defined at R = 4.0 Å, the energy difference between the S(^{1}S) and S(^{1}D) states was 1.83 eV, while the experimental value is 1.60 eV [47]. Likewise, the energy difference between CO($^1\Sigma^+$)+S(^{1}S) and CO($^3\Pi$)+S(^{3}P) asymptotes is calculated to be 4.75 eV, while the experimental value is 4.89 eV. As shown later, the maximum of calculated absorption spectrum is about 0.4 eV higher than the experimental data. These values indicate the error limits in our *ab initio* calculations, although the essential features of the dynamics are reasonably well reproduced as shown below.

There are three electronic states, $1^1\Sigma^+$, $1^1\Pi$, and $1^1\Delta$, correlated with the CO($^1\Sigma^+$) + S(^{1}D) asymptote in the $C_{\infty v}$ symmetry. $1^1\Sigma^+$ is the ground electronic state. $1^1\Delta$ is a bound state and has a minimum at around R = 2.4 Å; however, it has a curve crossing with a repulsive $1^1\Pi$ state at around 2.8 Å. The $^1\Sigma^-$ state correlated with CO($^3\Pi$) + S(^{3}P) asymptote exists in the same energy region for $R\in$ [1.8, 2.8] (Å), and it also undergoes a curve crossing with the $1^1\Pi$ state. These crossings are avoided in the bent geometry due to Neumann-Wigner's non-crossing rule, forming conical intersections. Thus, the bending distortion on both A' ($^1\Delta$) and A"($^1\Sigma^-$) surfaces leads to prompt adiabatic dissociation into CO($^1\Sigma^+$) + S($^1D_2$) via A'($^1\Pi$) and A"($^1\Pi$) .

Figures 4-9(a) and (b) show the potential energy curves and the orbital correlation diagram against q with R = 2.2 Å and r_{CO} = 1.13 Å. Figure 4-9(b) is similar to the Walsh diagram [5] but is plotted against q in Jacobi coordinates with ten core orbitals omitted. It is seen that the potential energy curves are strongly angle-dependent. The Renner-Teller pairs of $1^1\Delta$ splits to 2^1A' and 2^1A" states, and of $1^1\Pi$ to 3^1A' and 3^1A" states. The $1^1\Delta$ state is characterized by two single excitations of (3πx) $\rightarrow$(4πx) and (3πy) $\rightarrow$(4πy) in the linear geometry; in the bent geometry the 2^1A' state is single excitation of (12a') $\rightarrow$ (13a'), while the 2^1A" state is of (12a') $\rightarrow$ (4a") (see Fig. 4-9(b)). As shown in Fig. 4-9(b), the 13a' MO is stabilized more than the 4a" MO by bending, since the electron density of the $2p_C$ AO of π^*_{CO} spreads among $3p_S$, $2p_C$, and $2p_O$ AO's by bending, inducing a strong bonding between

the SC and CO centers. Therefore, the $2^1A'(^1\Delta)$ is more stable than the $2^1A''(^1\Delta)$. In Fig. 4-9(a) is also seen that the topography of $1^1A''$ state ($1^1\Sigma^-$) state is quite similar to $2^1A'(^1\Delta)$ state. This is because $1^1\Sigma^-$ state arises from a single excitation of (3a") $\rightarrow$ (13a') where 3a" MO has almost the same energy with 12a' MO.

The transition dipole moment functions (TDMF's), obtained for $1^1A''$ –$1^1A'$ and $2^1A'$ – $1^1A'$ transitions, are shown in Figure 4-10, as a function of q for r_{CO} = 1.13 Å and R = 2.2 Å. Both the dipole moments for $1^1\Sigma^-$ - $1^1\Sigma^+$ and $1^1\Delta$ - $1^1\Sigma^+$ are zero in the linear geometry, and the Franck-Condon regions on the upper states are located in the bent geometry. The TDMF's oscillate with θ, since the characters of the CI, i.e. the coefficients of CSF's, strongly vary with θ.

Figure 4-11 shows the two dimensional PES's at r_{CO} = 1.13 Å. As seen in Fig. 4-9 (a), the minimum in the ground electronic state is at R = 2.2 Å and q = 0.0°. Figures 4-11 (b) and (c) show the $1^1A''$ and $2^1A'$ have local minima at around R = 2.3 Å and q = 45.0° and the conical intersections with the $^1\Pi$ state around R = 2.5 Å and q = 0.0°. The topography of these PES's are surprisingly similar, reflecting that the HOMO orbitals of 12a' and 3a" have similar characters. As seen in Fig. 4-9 (b), the 12a' and 3a" orbitals change to $3p_x$(S) and $3p_y$(S) for $q > 80°$ without changing their energies. This indicates that the 12a' and 3a" MOs have mainly the character of S atomic orbitals. Rabalais *et al.* have pointed out that in 16 valence electron systems, the HOMO-LUMO transition is characterized by charge transfer from the end atom to the central atom [3]. The fact that the absorption wavelength changes from VUV in CO_2 to UV in OCS has been qualitatively explained by the difference of electronegativity of O in CO_2 and S in OCS atoms. This is accordance with the degenerate electronic structures of $2^1A'$ and $1^1A''$ arising from the localized character of the HOMO on the S atom in OCS.

4.4.6. Wave packet calculations on the single PES

In order to examine dissociation dynamics on the $2^1A'$ and $1^1A''$ states, the wave packet dynamics have been calculated for the total angular momentum of J' = 1. The product state distributions thus calculated for the two transitions were quite similar, which is not surprising, recalling the similarity of the two PES's. Figure 4-12 shows the rotational distributions of CO due to $2^1A' \leftarrow 1^1A'$ and $1^1A'' \leftarrow 1^1A'$ transitions computed by integrating the partial cross sections $\sigma_j(E)$ over the excitation energy. It is seen that the speed distributions of $S(^1D_2)$

atom (or the rotational distributions of CO) were singly peaked in both cases, reflecting the rotational Franck-Condon principle. The result clearly indicates that the dynamics leading to a bimodal distribution is missing in the single potential energy surface of 2^1A'. The missing feature is ascribed to non-adiabatic transition from 2^1A' to 1^1A' states, as these two states approach around $q = 60°$. In order to prove this hypothesis, we have performed wave packet calculations including non-adiabatic transition.

4.4.7 Non-adiabatic coupling matrix elements and non-adiabatic wave packet calculations

In the present work we have taken into account only the first derivative of electronic wavefunctions with respect to the nuclear coordinates to simplify the problem [50-54], although the method to include the elements up to the second derivative has been discussed in Refs. [56] and [57].

In order to solve the two dimensional two-state problems in the diabatic representation (see Eq. (8)), we have determined the diabatic potentials, V_1 and V_2, and the non-adiabatic coupling element, V_{12}, given by,

$$\begin{cases} V_1 = E_1 \cos^2 a + E_2 \sin^2 a \\ V_2 = E_1 \sin^2 a + E_2 \cos^2 a \\ V_{12} = (E_2 - E_1) \cos a \sin a \end{cases} \tag{19}$$

where E_1 and E_2 are the adiabatic potentials of the 1^1A' and 2^1A' states, and α is the mixing angle which is a function of the internal coordinates. The mixing angle is related to the non-adiabatic coupling matrix element (NACME) in the adiabatic representation, as follows;

$$-\frac{\P a}{\P Q} + \left\langle f_1 \left| \frac{\partial}{\partial Q} \right| f_2 \right\rangle \approx 0 \tag{20}$$

where Q is the internal coordinate, and f_1 (1^1A') and f_2 (2^1A') are the eigenfunctions of the electronic Hamiltonian. In the one-dimensional two-state problem, a is estimated by a simple integration of the above equation with respect to Q.

In the present work, the NACMEs between 1^1A'(f_1) and 2^1A' (f_2) were calculated by using CP-MCSCF solutions. We have seen in Figure 4-9(a) that the 2^1A' and 1^1A' surfaces experience an avoided crossing by the bending deformation. This is clearly explained by the orbital correlation diagram against q [see Figure 4-9(b) and the section 4.10]. To make the calculations tractable, we employed a simplified model where the mixing angle a depends

only on the bending coordinate q. The adiabatic potential energy surfaces obtained at the MRCI level were used to calculate V_1, V_2, and V_{12}. As shown in Fig. 4-13 the diabatic curves cross each other around the peak position of the NACME. In Fig. 4-11 (d), the seam of crossing is indicated on the two-dimensional diabatic potential surface of 1^1A' state.

Figure 4-14(a) shows the initial wave packet on 2^1A' and Figs 4-14(b) and 4-14(c) show the snapshots of wave packet motion on the V_2 and V_1 diabatic surfaces. Since the Franck-Condon region is on the steep slope for the bending coordinate, the wave packet propagates toward larger q after photoexcitation. In Fig. 4-14(b), it is seen that after 25 fs the wave packet splits into two, one big packet going outward and a small fraction trapped around the local minimum at R = 2.3 Å and q = 45.0°. At 50 fs later, the outgoing packet is centered at around R = 3.3 Å and q = 135°, whereas the trapped part is reflected back to q = 10, causing a recurrence. As seen in Fig. 4-14(c), a fraction of the wave packet already appears on the lower diabatic surface at 25 fs with more at 50 fs.

The rotational distributions of CO calculated by including non-adiabatic transition are shown in Fig. 4-12 (a). The calculation including the non-adiabatic transition shows a subsidiary peak corresponding to the slow S atom, in qualitative agreement with our experimental data. Since the excitation energy has been calculated to be higher than the experimental values, the rotational distributions appear to be higher in J than the experimental results. The wavelength dependence of the rotational distribution of CO is shown in Fig. 4-15. The excitation energies of (a) E = 44370, (b) 46570, and (c) 48770cm^{-1} correspond to the excitation wavelengths of l = 248, 235, and 223 nm employed in our experiment. (Due to the shift of the calculated absorption spectrum versus experimental data, the peak position (48770 cm^{-1}) of the calculated spectrum was regarded to be corresponding to 223 nm photoexcitation, and the other two energies were chosen in such a way that the energy differences from 48770 cm^{-1} reproduce ΔE(223 - 248 nm) = 4520 and ΔE(223 - 235 nm) = 2290 cm^{-1}.) The contributions from A' and A" upper states are indicated in each figure.

The experimental investigation revealed four features in the rotational distributions; (i) the bimodal distribution shifts together to higher J for increasing the excitation energy, (ii) the A' and A" states contribute to the main peak, while the subsidiary peak only arises from the A' state, and (iii) the contribution of the A'← A' transition increases for increasing the excitation energy, and (iv) the subsidiary peak becomes stronger for shorter wavelength, accordingly. The features (i) and (ii) were reproduced qualitatively in our calculations including the

non-adiabatic transition between $1^1A'$ and $2^1A'$. The main peak of J shifts from 51, 62, and to 70 for increasing an excitation energy from 44370, 46570, and to 48770 cm^{-1}. The CO rotational distribution peaked at J = 70 in dissociation at E = 48770 cm^{-1} is compared with J = 55 observed experimentally, which corresponds to an error of $\Delta E = B_e\{70(70+1) - 55(55+1)\}$ = 3648 cm^{-1}, where B_e is the rotational constant of CO. The discrepancy of 3700 cm^{-1} between theoretical and experimental results is systematically seen in all of the calculations shown in Fig. 4-15, which arises from inaccuracy of our *ab initio* calculations.

The feature (iii) mentioned above was not reproduced well by our calculations, since the contribution of the $2^1A'$ - $1^1A'$ transition was underestimated than the experiment. Refinement of the PES's is necessary to improve the agreement with experimental data.

4.4.8. Analysis including the alignment of $S(^1D_2)$ and the evaluation of non-adiabatic transition efficiency

The 2D ion images of $S(^1D_2)$ in 223 nm photodissociation of OCS measured with four sets of pump-probe polarization are shown in Fig. 4-16 (a), (b), (c), and (d). Both the pump and probe laser beams were linearly polarized in all cases. In comparing figures (a) and (b), and also (c) and (d), it is seen that the image varies with the change of the probe laser polarization, indicating that there is electronic orbital alignment in $S(^1D_2)$ fragment. The effect of orbital alignment is most clearly seen by comparing Fig. 4-16(c) and (d) in which the photolysis laser polarization is set perpendicular to the imaging plane. The original photofragment density distribution is cylindrically symmetric around the polarization vector of the photolysis laser beam. Therefore, if there is no alignment in the atoms, the ion image should be cylindrically symmetric around the center. The change of the image from (c) to (d) and also the symmetry breaking in (d) are due to orbital alignment in $S(^1D_2)$. Because the $^1F_3 \leftarrow\leftarrow {}^1D_2$ transition favors the probe laser polarization (e_{probe}) aligned parallel to the $\boldsymbol{J}$ vector, signal intensity is reduced when e_{probe} is set perpendicular to $\boldsymbol{J}$. In Fig. 4-16 (d), it is seen that the signal intensity is reduced along the direction of probe laser polarization. This suggests $e_{\mathrm{probe}} \perp \boldsymbol{J}$ for the fragments moving parallel to e_{probe} ($e_{\mathrm{probe}} \parallel \boldsymbol{v}$) and, therefore, $\boldsymbol{J} \perp \boldsymbol{v}$ as a preferential alignment in S atom. In the same way, the $\boldsymbol{J} \perp \boldsymbol{v}$ alignment in S atom is seen by the intensity reduction at the center of Fig. 4-16 (c).

The experimental data were analyzed by a forward-convolution method by considering two velocity components with different m distributions in the VF frame. We assumed J

distribution is cylindrically symmetric around v vector, and expressed the angular momentum polarization by the ratios of the population in $|m| = 0 : 1 : 2$. The simulated images are shown in Fig. 4-16(a'), (b'), (c') and (d') and the parameters are tabulated in Table III.

It is noted that the analysis made here is rigorous only for the case of $m \parallel \boldsymbol{v}$. The dissociation from the A" component requires a more general formula without the assumption of cylindrical symmetry of $\boldsymbol{J}$ around $\boldsymbol{v}$. It is also pointed out that for the scattering angle $q \sim 45$ degree, coherent excitation of A' and A" can occur, which has not been considered in the present analysis. Since excellent agreement between the experimental data and simulation has been obtained without considering these subtleties, further detailed analysis considering these two possibilities will require more detailed experimental data. Complete determination of density matrix including coherent terms can be determined using other polarization combinations of pump and probe laser beams. The anisotropy parameters, 1.8 and 0.7, obtained by the present analysis are in excellent agreement with those reported by Sivakumar *et al.*, 1.8 [10], and Sato *et al.*, 1.7 and 0.6 [14], which suggests that the approximations made in the present analysis are reasonable.

The anisotropy parameters obtained from an inverse Abel transform without considering alignment of $S(^1D_2)$ atoms were 1.1 and 0.2. The large difference between the two sets of values, (1.1 and 0.2) and (1.8 and 0.7), clearly indicates that the alignment must be considered in quantitative analysis. From the anisotropy parameter of 0.7, the ratio of A' and A" components in the fast fragment is calculated to be 1 : 0.33. With this ratio and the branching ratio of fast and slow components, fast/slow = 3.0/1.0, the ratio of the fast and slow fragments arising from the $A'(^1\Delta)$ state is calculated to be 1 : 0.44. This implies that the yield of non-adiabatic dissociation from the A' state in 223 nm photodissociation is 0.35 ± 0.02. This surprisingly high value clearly shows the importance of non-adiabatic bending dynamics in UV photodissociation of OCS.

4.4.9. Absorption spectrum and Feshbach resonance

In Fig. 4-17(a) shows the calculated photodissociation cross-section for the $2^1A' \leftarrow 1^1A'$ and $1^1A'' \leftarrow 1^1A'$ transitions and Fig.4-17(b) the sum of the two transitions, where the $J''=0$, (0,0,0) state was used as an initial state. Since the dissociation yield is unity, Fig. 4-17 can be regarded as corresponding absorption spectra. The center of our spectrum is shifted to shorter wavelength by 18 nm with respect to the experimental spectrum. As seen in Fig.

4-17 (b), our theoretical spectra show sharp structures on top of the Gaussian-shaped continuum.

The prominent structures seen in Fig. 4-17 (a) exhibit an energy spacing of 250 cm^{-1}. In order to understand the origin of these resonance peaks, the wavefunctions y_1^e and y_2^e in the upper and lower diabatic surfaces were obtained by the spectral method [58] for the strong peaks in the spectrum at E = 47476, 49012, and 50281 cm^{-1} as indicated in Fig. 4-17 (a). The wavefunctions y_2^e shown in Fig. 4-18 (d), (e), and (f) exhibit the nodal structure for C-S stretching in the Franck-Condon region, which is regarded as Feshbach resonance. The wavefunctions on the 1^1A" surface show similar features. As seen in Fig. 4-18 (a), (b), and (c), the resonance states that exhibit a sharp spectrum do not have a large fraction of wave packet on the lower diabatic surface. The non-adiabatic transition that reduces recurrence to the Franck-Condon region is reflected by the broad background feature in the calculated spectrum.

The experimental spectrum reported so far exhibited a broad Gaussian-shaped continuum centered at around 223 nm with weak vibrational progressions [3, 6-8]. The sharp structure predicted by the analysis presented above has never been observed. Although it is possible that the recurrence predicted by theory is exaggerated by reduced dimensionality in our model or inaccuracy of PES's, it is noted that the reported absorption spectra have been measured for temperatures > 195 K, which may diminish any structure in the absorption spectrum by the thermal distribution of OCS. Therefore, in order to examine the structure predicted by wave packet calculations, we have measured an action spectrum of OCS in a molecular beam. The probe laser frequency was fixed to the center of resonance line of $S(^1D_2)$ atom, and the yield of $S(^1D_2)$ was measured as a function of pump laser frequency. It is expected that this method preferentially monitors electronic transition to the 2^1A' state, since dissociation from A" state provides S atoms that show large Doppler shift. The action spectra, shown in Figure 4-19, do not exhibit the sharp structure predicted from the calculations. The results show that the recurrence obtained by 2D wave packet calculation is being exaggerated.

The discrepancy indicates the limitation of our reduced dimensional model or inaccuracy of the PES. Further investigation using 3D calculations will be necessary to reproduce the experimental data.

4.4.10. Implications to other Renner-Teller systems

Analysis of one electron orbital energies from the Walsh diagram predicts that, when a triatomic molecules with 16 valence electrons is bent, one of the HOMOs (degenerate π orbital in the linear geometry) that lies in the plane is destabilized, while the other HOMO perpendicular to the plane is largely unaffected. The destabilization of HOMO for bending deformation makes the ground state molecule to be linear. Likewise, one of the LUMOs (π^* orbital) in the plane is stabilized by bending the molecule, while the other LUMO is almost unchanged. Thus, by promoting an electron from HOMO to LUMO, molecule is bent, which serves as a simple explanation to the Renner-Teller interaction that unfolds the degeneracy of the excited state. The bent state corresponds to the promotion of an electron from π(a') to π^*(a') orbital in an asymmetric molecule, so that it becomes A' symmetry, belonging to the same symmetry species with that of the ground state. Therefore, avoided crossings between the A' upper state and the ground state in the bent geometry are considered to be inherent in asymmetric triatomic molecules with 16 valence electrons.

In this sense N_2O, that is isovalent with OCS, may exhibit similar behavior. In fact, *ab initio* calculations reported by Hopper clearly indicated that the excited A'($^1\Delta$) state is stabilized by bending deformation and approaches the ground electronic state [16]. However, experimental studies of photodissociation of N_2O by REMPI spectroscopy of N_2 [59], Doppler spectroscopy of O($^1D_2$) [60] and 2D ion imaging of O($^1D_2$) [61] have not clearly revealed the non-adiabatic dissociation pathway. This interesting difference between OCS and N_2O will be elucidated in future work.

4.5. Conclusion

We have described experimental and theoretical studies on the ultraviolet photodissociation of OCS. Photoexcitation occurs onto A' Renner-Teller component of A'($^1\Delta$) state and A"($^1\Sigma^-$) state. Due to the conical intersection of these states with A'($^1\Pi$), excited molecules undergo rapid C-S bond rupture. The A' and A" surfaces have similar topography, so that dissociation on these two surfaces provide almost the same product state distribution; bending forces on the upper states induce strong rotational excitation of CO.

In addition to the dissociation on the upper surface, the A'($^1\Delta$) state has avoided crossings with the ground state in the bending coordinate, which induces dissociation due to

non-adiabatic transition. The non-adiabatic transition yield is estimated experimentally to be 0.35±0.02 in 223 nm photodissociation. The non-adiabatic transition creates the wave packet on the plateau of the ground state surface that is almost in the same energy with the asymptote, which transforms bending energy gained on the upper surface more efficiently into the product rotation, resulting in higher rotational state distributions of CO and smaller velocities of S atom.

The absorption spectrum consists of a broad featureless part and weak structure on top of it. The weak structure is assigned to Feshbach resonance arising from temporarily trapped trajectories in C-S stretching coordinate in the Franck-Condon region. Contribution of the broad absorption is expected to be larger for A' state, since the recurrence of the wave packet to the Franck-Condon region is diminished by non-adiabatic transition to the ground state. However, the structure predicted by calculations was not reproduced by the action spectroscopy of ultracold OCS in a molecular beam. The result indicates that the recurrence of wave packet to the Franck-Condon region is exaggerated in our 2D model calculations.

Close contact or avoided crossing between $A'(^1\Delta)$ and the ground state is inherent in 16 valence electron systems as predicted by Walsh diagrams. However, non-adiabatic transitions in photodissociation are not always visible as pointed out for N_2O. Further systematic study will elucidate the generality (or specificity) of non-adiabatic dissociation dynamics in these systems.

References

[1] J. Michl and V. Bonacic-Koutechy, “Electronic aspects of organic photochemistry” (Wiley Interscience, 1990).

[2] R. Schinke, “Photodissociation Dynamics” (Cambridge University Press, 1993).

[3] J. W. Rabalais, J. M. McDonald, V. Scherr, and S. P. McGlynn, Chem. Rev. **71**, 73 (1971).

[4] R. S. Mulliken, Can. J. Chem. **36**, 10 (1958); Rev. Mod. Phys. **14**, 204 (1942); J. Chem. Phys. **3**, 720 (1935); J. Chem. Phys. **46**, 497 (1949); **46**, 675 (1949); Phys. Rev. **41**, 751 (1932); **43**, 279 (1933); **60**, 512 (1941); Chem. Rev. **41**, 219 (1947).

[5] A. D. Walsh, J. Chem. Soc. 2266 (1953).

[6] W. H. Breckenridge and H. Taube, J. Chem. Phys. **52**, 1713 (1970).

[7] J. R. Locker, J. B. Burkholder, E. J. Bair, H. A. Webster, J. Phys. Chem. **87**, 1864 (1983).

[8] J. A. Joens and E. J. Bair, J. Phys. Chem. **88**, 6009 (1984).

[9] N. Sivakumar, I. Burak, W.-Y. Cheung, P. L. Houston, and J. W. Hepburn, J. Phys. Chem. **89**, 3609 (1985).

[10] N. Sivakumar, G. E. Hall, P. L. Houston, J. W. Hepburn, and I. Burak, J. Chem. Phys. **88**, 3692 (1988).

[11] R. Schinke, J. Phys. Chem. **90**, 1742 (1986).

[12] G. Nan, I. Burak, and P. L. Houston, Chem. Phys. Lett. **209**, 383 (1993).

[13] H. Katayanagi, Y. Mo, and T. Suzuki, Chem. Phys. Lett. **247**, 571 (1995).

[14] Y. Sato, Y. Matsumi, M. Kawasaki, K. Tsukiyama, and R. Bersohn, J. Phys. Chem. **99**, 16307 (1995).

[15] P. J. Knowles, P. Rosmus, and H.-J. Werner, Chem. Phys. Lett. **146**, 230 (1988).

[16] D. G. Hopper, J. Chem. Phys. **80**, 4290 (1984).

[17] R. T. Pack, J. Chem. Phys. **65**, 4765 (1976).

[18] E. J. Heller, J. Chem. Phys. **68**, 3891 (1978).

[19] T. Bergmann, T. P. Martin, and H. Schaber, Rev. Sci. Instrum. **60**, 347 (1989).

[20] C. K. Ingold and G. W. King, J. Chem. Soc. 2702 (1953).

[21] K. K. Innes, J. Chem. Phys. **22**, 863 (1954).

[22] J. K. G. Watson, M. Herman, J. C. Van Craen, and R. Colin, J. Mol. Spectrosc. **95**, 101 (1982).

[23] J. C. Van Craen, M. Herman, R. Colin, J. K. G. Watson, J. Mol. Spectrosc. **111**, 185 (1985); **119**, 137 (1986).

[24] D. W. Chandler and P. L. Houston, J. Chem. Phys. **87**, 1445 (1987).

[25] B. J. Whitaker, in "Research in Chemical Kinetics Volume I", edited by R. G. Compton and G. Hancock (Elsevier, 1993).

[26] A. J. R. Heck and D. W. Chandler, Annu. Rev. Phys. Chem. **46**, 335 (1995).

[27] R. N. Bracewell, "The Fourier Transform and Its Applications" (McGraw-Hill, 1986).

[28] T. Suzuki, K. Tonokura, L. S. Bontuyan, and N. Hashimoto, J. Phys. Chem. **98**, 13447 (1994).

[29] K. Tonokura, L. B. Daniels, T. Suzuki, and K. Yamashita, J. Phys. Chem. A **101**, 7754 (1997).

[30] R. N. Strickland and D. W. Chandler, Appl. Opt. **30**, 1811 (1991).

[31] A. K. Jain, "Fundamentals of digital image processing" (Prentice Hall, 1989).

[32] Y. Mo, H. Katayanagi, M. C. Heaven, and T. Suzuki, Phys. Rev. Lett. **77**, 830 (1996).

[33] J. P. Simons, J. Phys. Chem. **91**, 5378 (1987).

[34] P. L. Houston, J. Phys. Chem. **91**, 5388 (1987).

[35] Handbook of Chemistry and Physics 74th edition (CRC Press, 1993).

[36] K. Blum, "Density Matrix Theory and Applications (second edition)" (Plenum, 1996).

[37] R. N. Zare, "Angular Momentum" (Wiley-Interscience, 1988).

[38] Y. Mo and T. Suzuki, J. Chem. Phys. submitted.

[39] Y. Mo and T. Suzuki, J. Chem. Phys. in press.

[40] R. N. Zare, Mol. Photochem. **4**, 1 (1972).

[41] A. Schafer, H. Horn, R. Ahlrichs, J. Chem. Phys. **97**, 2571 (1992), and references therein.

[42] MOLPRO is a package of *ab initio* programs written by H.-J. Werner and P. J. Knowles with contributions from J. Almlöf, R. D. Amos, M. J. O. Deegan, S. T. Elbert, C. Hampel, W. Meyer, K. Peterson, R. Pitzer, A. J. Stone, and P. R. Tayor.

[43] A. R. Offer and G. G. Balint-Kurti, J. Chem. Phys. **101**, 10416 (1994).

[44] H. Tal-Ezer and R. Kosloff, J. Chem. Phys. **81**, 3967 (1984).

[45] A. Vibok and G. G. Balint-Kurti, J. Phys. Chem. **96**, 8712 (1992).

[46] G. G. Balint-Kurti, R. N. Dixon, and C. C. Marson, J. Chem. Soc. Faraday Trans. II **86**, 1741 (1990).

[47] A. A. Radzig and B. M. Smirnov, "Reference data on atoms, molecules and ions Vol. 31" (Springer, 1985).

[48] W. L. Weise, M. W. Smith, and B. M. Miles, NSRDS-NBS (U.S.) **22**, 134 (1969).

[49] Y. Morino and T. Nakagawa, J. Mol. Spectrosc. **26**, 496 (1968).

[50] M. Bear, Mol. Phys. **40**, 1012 (1980).

[51] P. Halvick and D. G. Truhlar, J. Chem. Phys. **96**, 2895 (1992).

[52] H. J. Werner and W. Meyer, J. Chem. Phys. **74**, 5802 (1981).

[53] A. J. Dobbyn and P. J. Buenker and S. D. Peyerimhoff, Mol. Phys. **91**, 1107 (1997).

[54] D R. Yarkony, J. Chem. Phys. **92**, 2457 (1990).

[55] S. Han, H. Hettema and D. R. Yarkony, J. Chem. Phys. **102**, 1955 (1995).

[56] M. Peric, R. J. Buenker and S. D. Peyerimhoff, Mol. Phys. **71**, 673 (1990).

[57] B.H. Lengsfield and D. R. Yarkony, in "Advance in Chemical Physics Vol. 82", edited by M.Bear and C.-Y. Ng (Wiley, 1992; Part 2, p.1)

[58] M. D. Feit, J. A. Fleck, and A. Steiger, J. Comput. Phys. **47**, 412 (1982).

[59] T. F. Hanisco and A. C. Kummel, J. Phys. Chem. **97**, 7242 (1993).

[60] L. L. Springsteen, S. Satyapal, Y. Matsumi, L. M. Dobeck, and P. L. Houston, J. Phys. Chem. **97**, 7239 (1993).

[61] T. Suzuki, H. Katayanagi, Y. Mo, and K. Tonokura, Chem. Phys. Lett. **256**, 90 (1996).

Figures and tables for Chapter 4

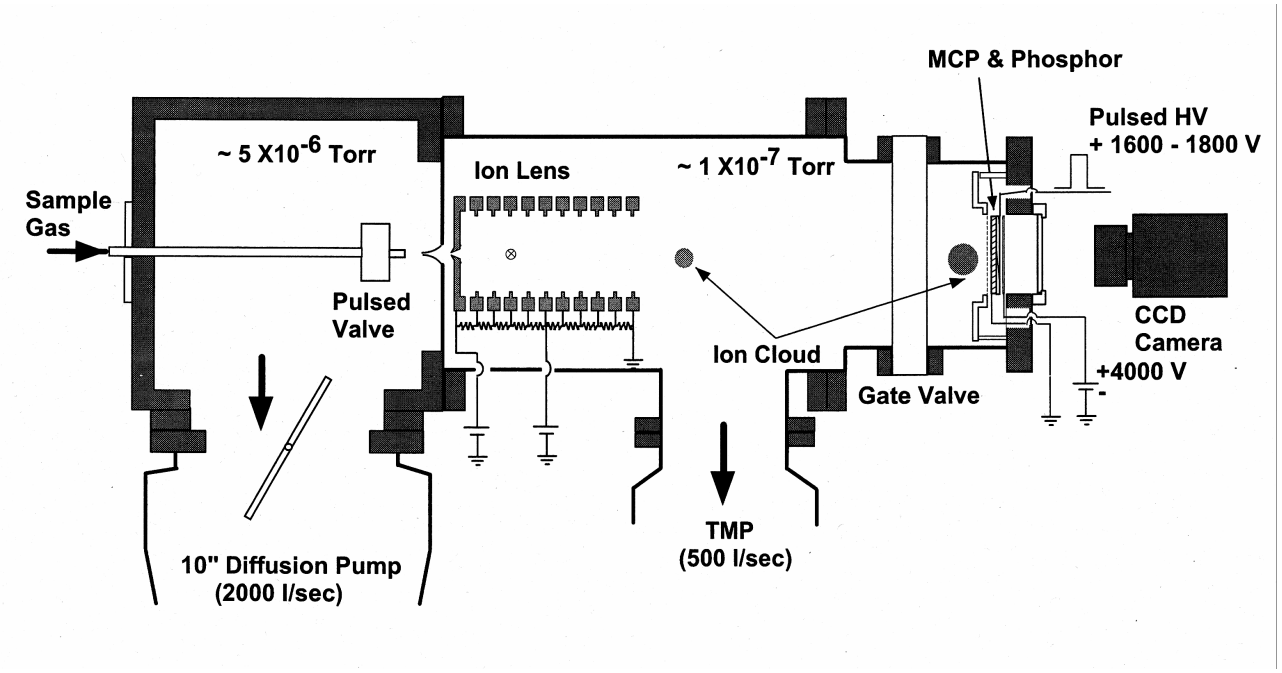

Fig. 4-1
Schematic view of the experimental apparatus.

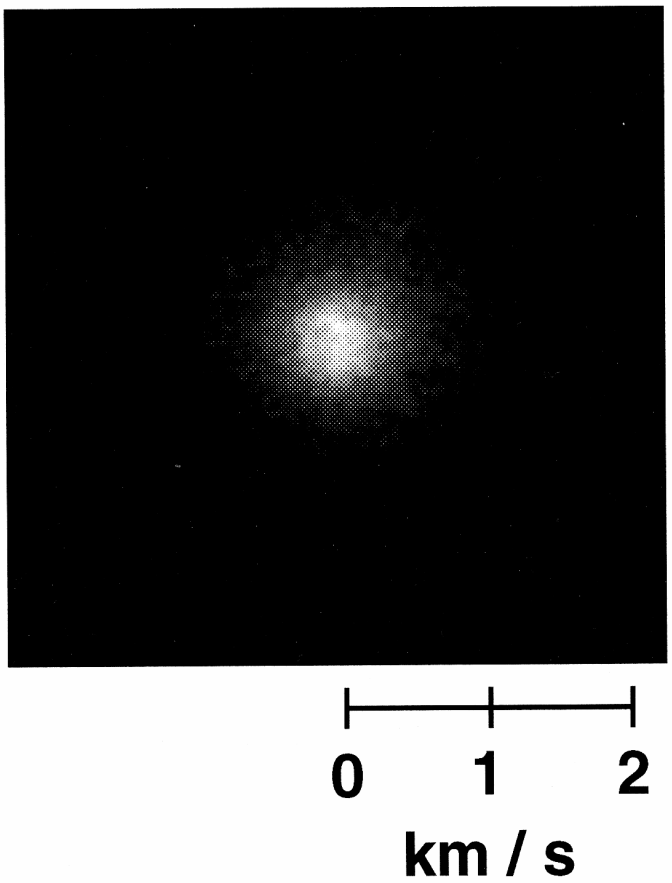

Fig. 4-2
The 2D image of $S(^3P_2)$ produced by 223 nm photodissociation of OCS. A high sample pressure 10% in Ar and a stagnation pressure 3 atm produced OCS clusters which result in a low speed isotropic distribution of S atoms.

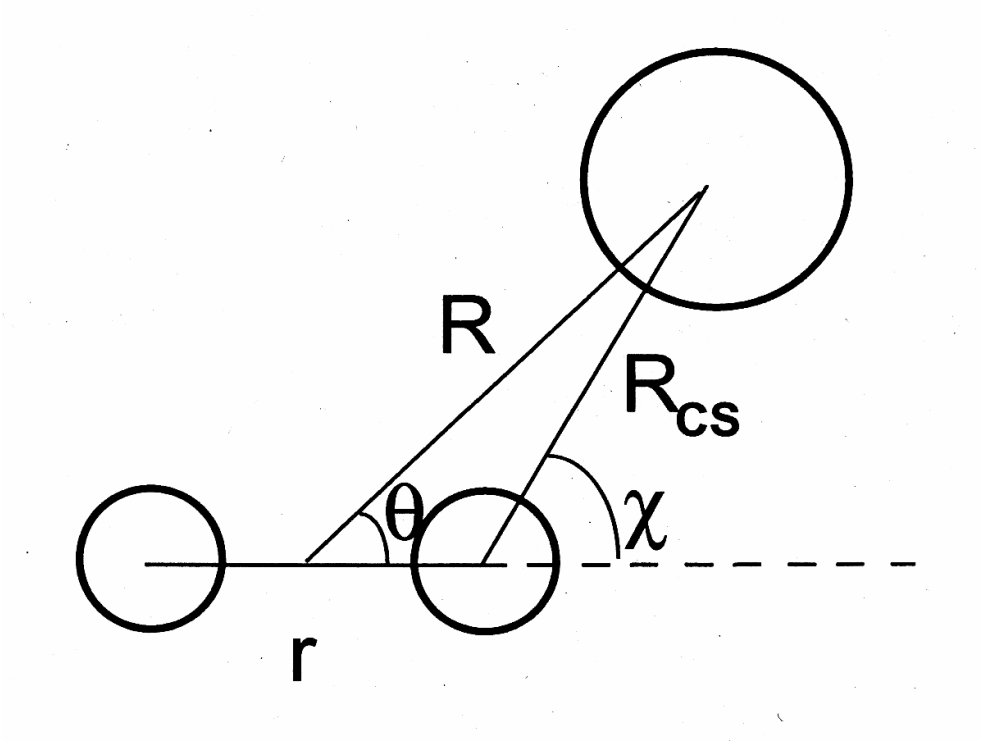

Fig. 4-3
Jacobi coordinates and bond length-bond angle coordinates.

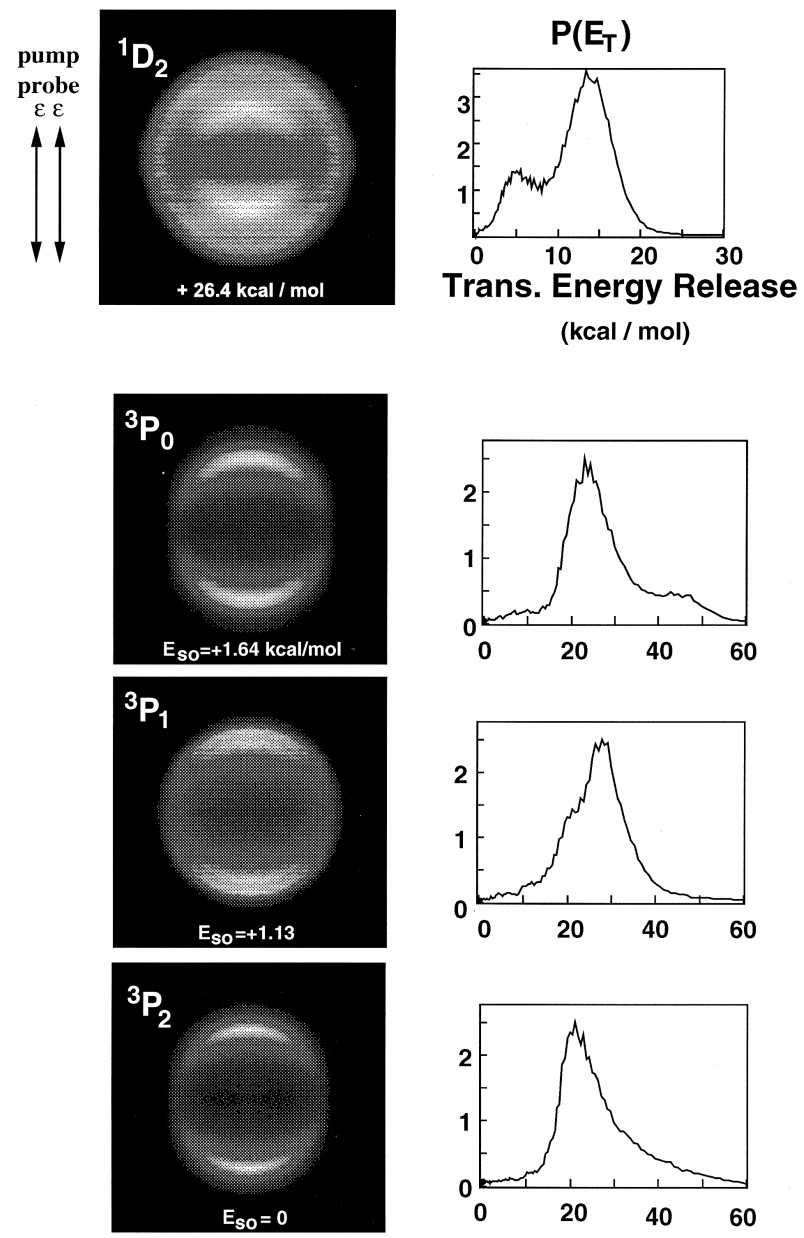

Fig. 4-4
The 2D images of S($^1D_2$) and S(^3P_J; J = 0, 1, 2) produced by 223 nm photodissociation of OCS and the center of mass translational energy release calculated from the images. Both the pump and probe laser polarization are aligned vertical in these figures. The S($^1D_2$) distribution consists of two velocity components (isotropic and anisotropic), while the S(^3P_J) distributions are predominantly anisotropic. Note the different S(^3P_J) distributions reflecting the different rotational excitation of CO.

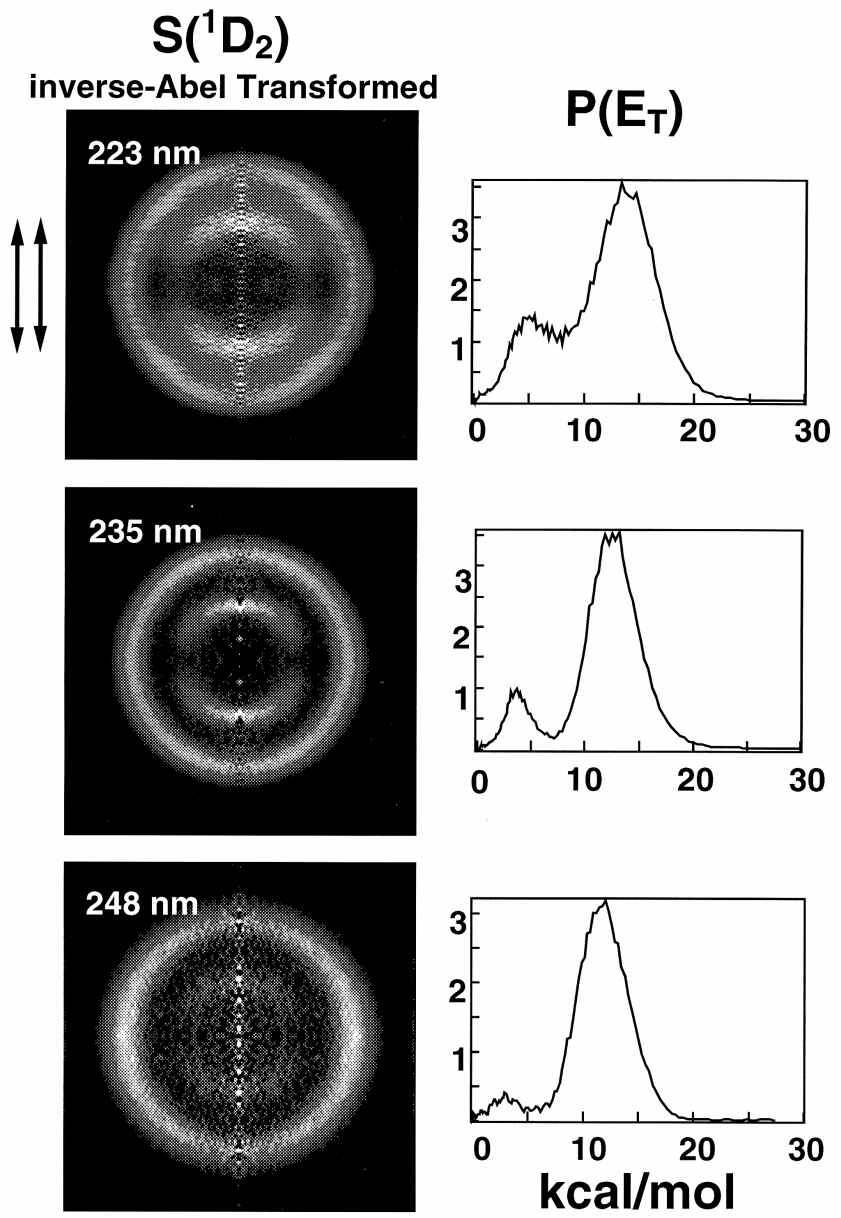

Fig. 4-5
Inverse Abel transforms of $S(^1D_2)$ images observed for photodissociation at 223, 235, and 248 nm and the center of mass translational energy release calculated from the images. Both pump and probe laser polarizations are aligned vertical in these figures. It is seen that the fast component gradually changes from an isotropic (223 nm) to an anisotropic distribution (248 nm).

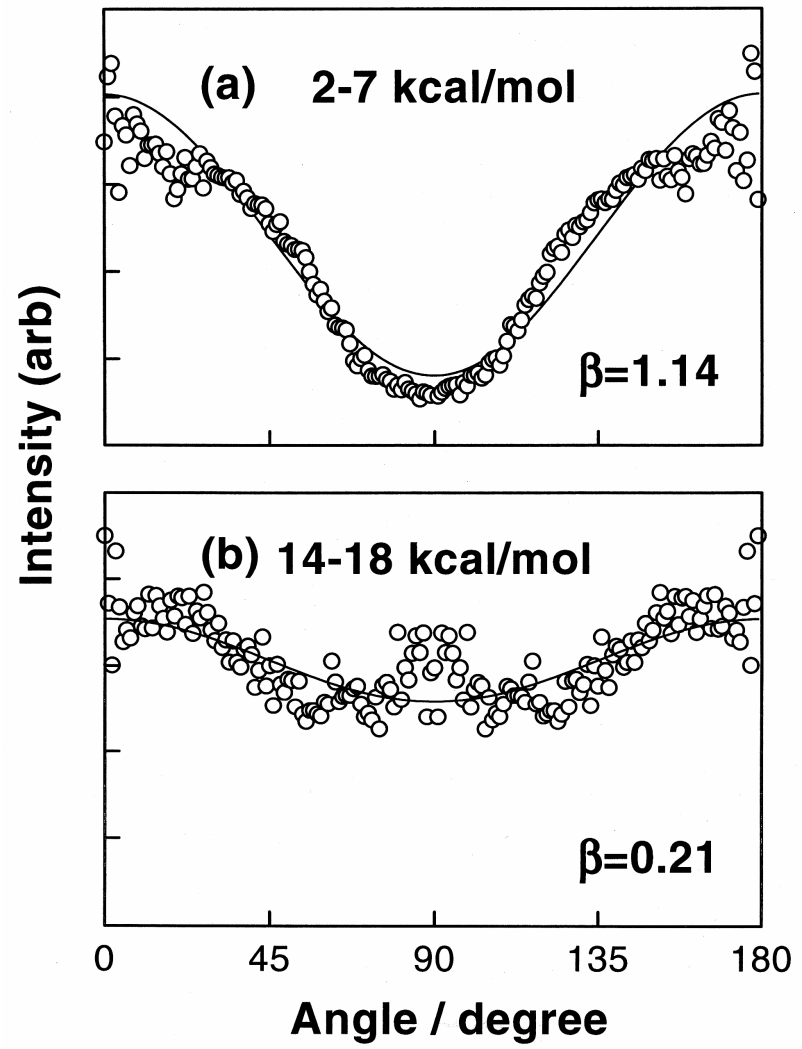

Fig. 4-6
Angular distributions of high and low speed components of $S(^1D_2)$ produced in 223 nm photodissociation and the least square fits of the standard formula $I(q) \propto 1+bP_2(\cos q)$ to the data.

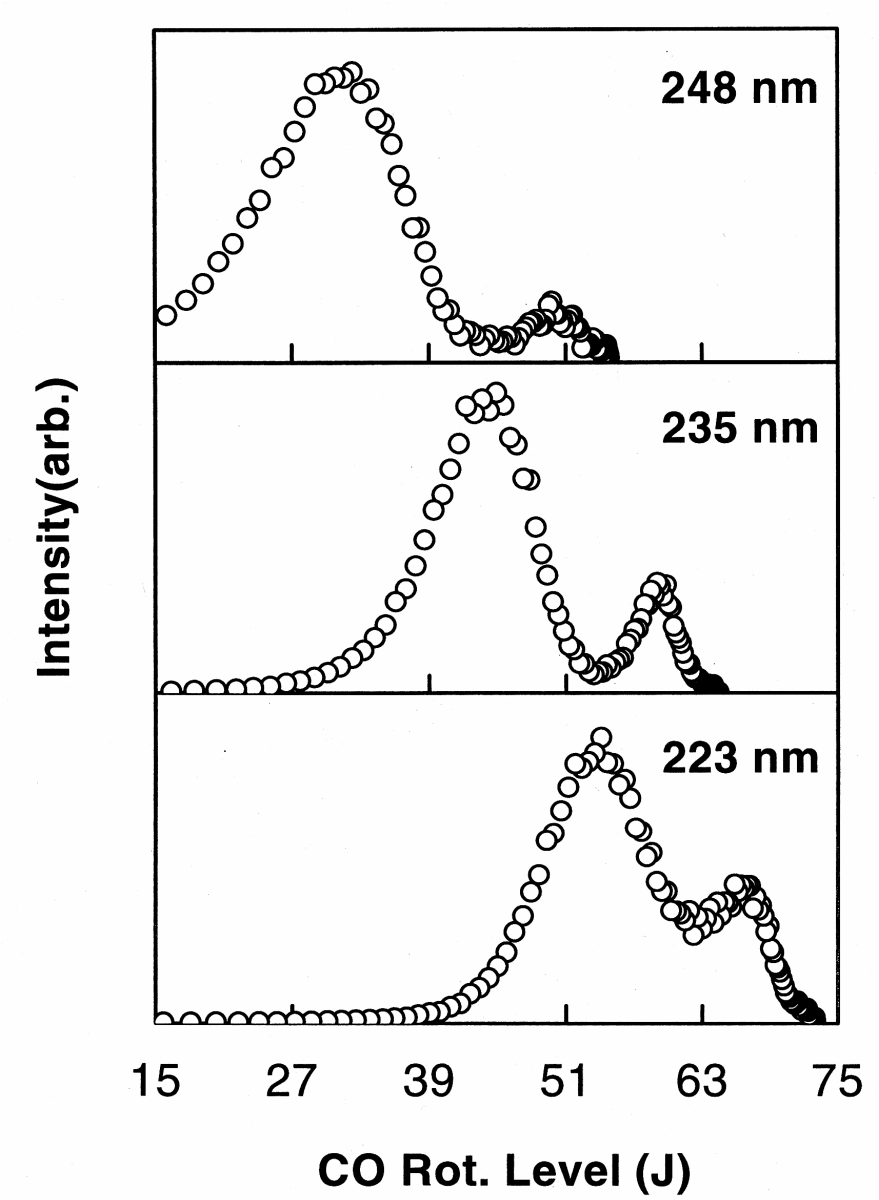

Fig. 4-7
Rotational distributions of CO calculated from the center of mass translational energy release shown in figure 5. These plots have the same scale with the former report by Sivakumar *et al.* using vacuum ultraviolet laser induced fluorescence detection of CO for comparison.

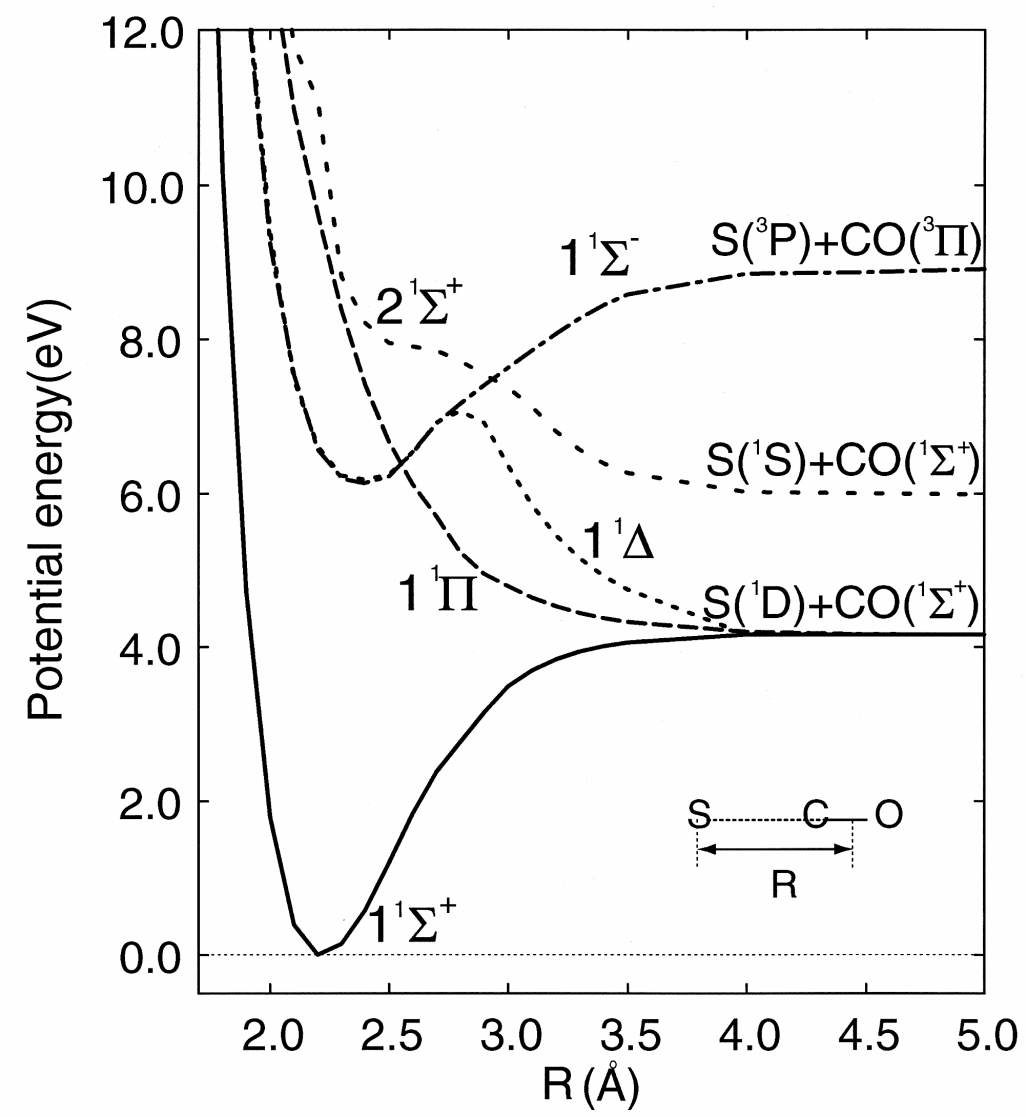

Fig. 4-8
Potential energy curves as a function of R in the linear geometry with r_{CO} fixed to 1.13 Å.

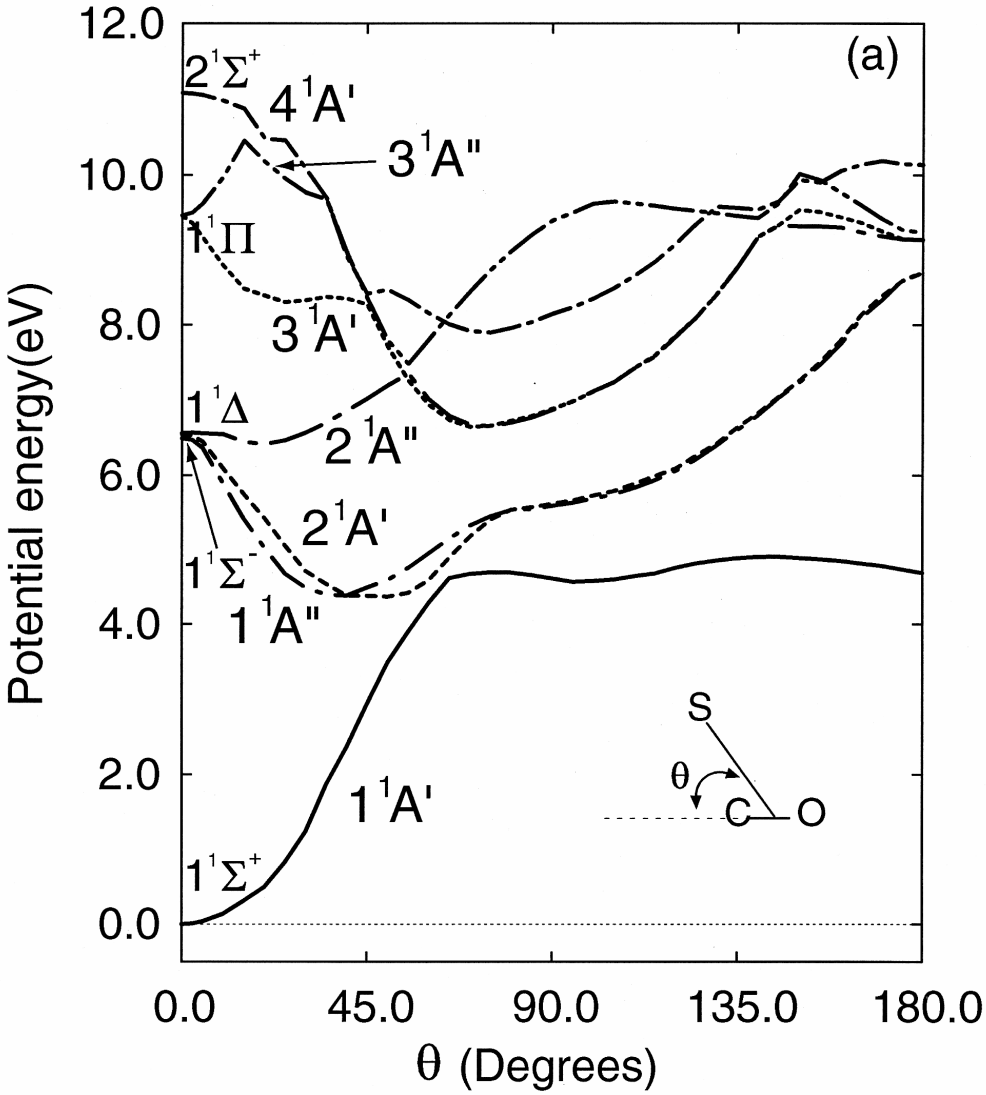

Fig. 4-9(a)
Potential energy curves plotted against q for R = 2.2 Å and r_{CO} = 1.13 Å.

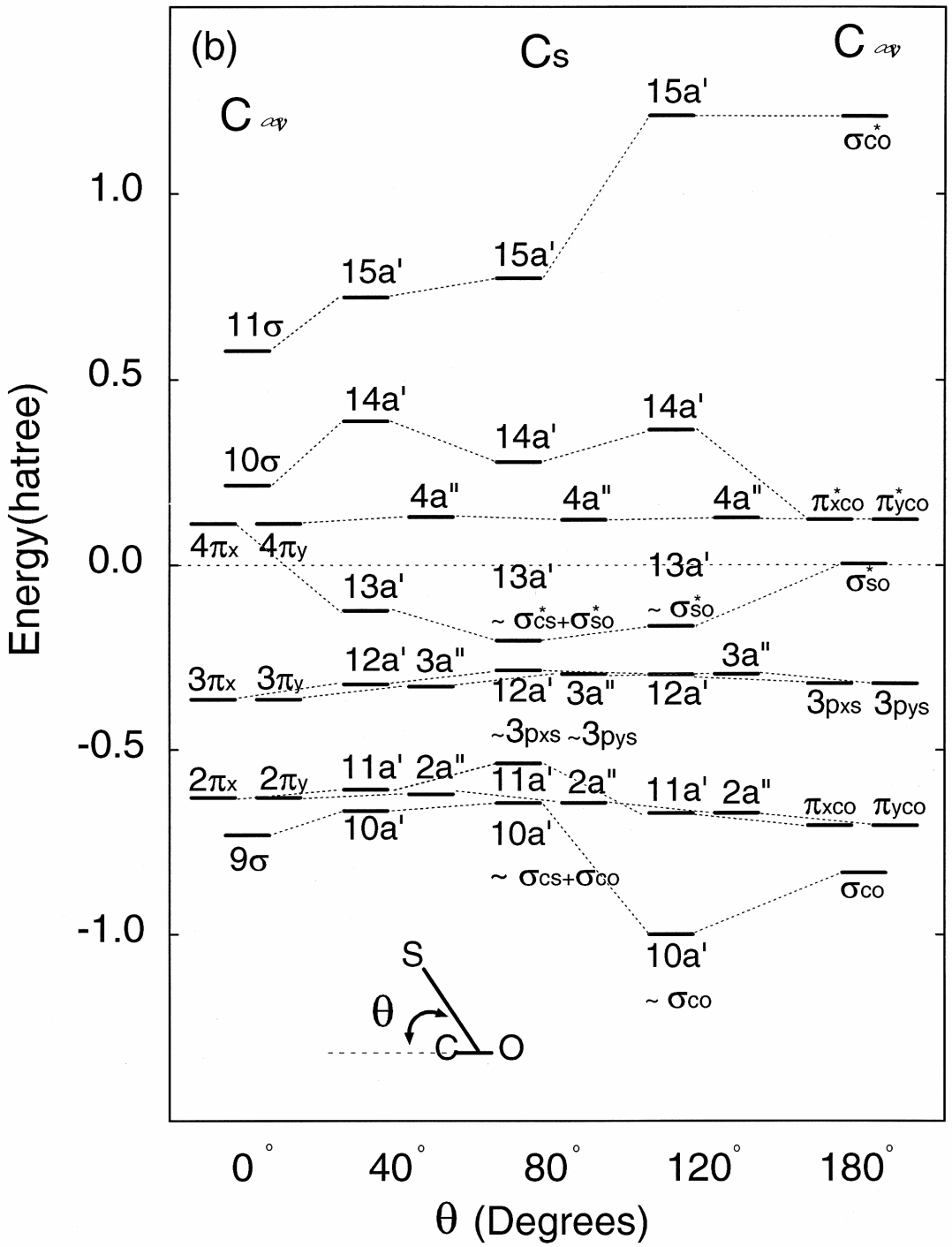

Fig. 4-9(b)
Orbital energies plotted against q for R = 2.2 Å and r_{CO} = 1.13 Å.

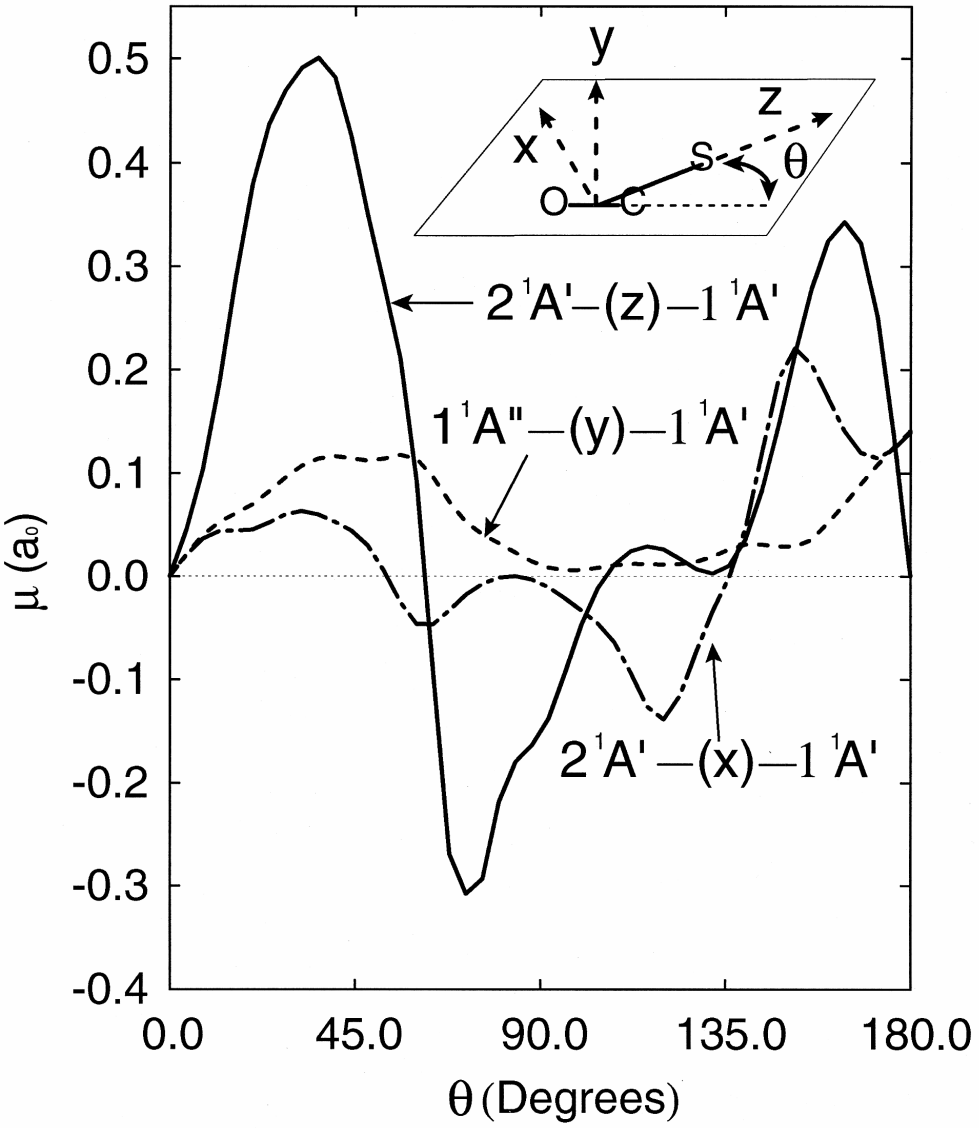

Fig. 4-10
Transition dipole moment for 1^1A" –1^1A' and 2^1A' – 1^1A' plotted as a function of q for r_{CO} = 1.13 Å and R = 2.2 Å. In our body fixed coordinate, the z-axis is fixed along R, and molecular plane is defined as xz plane, so that 1^1A" – 1^1A' transition dipole is along y axis, while the 2^1A' – 1^1A' transition along x and z axes.

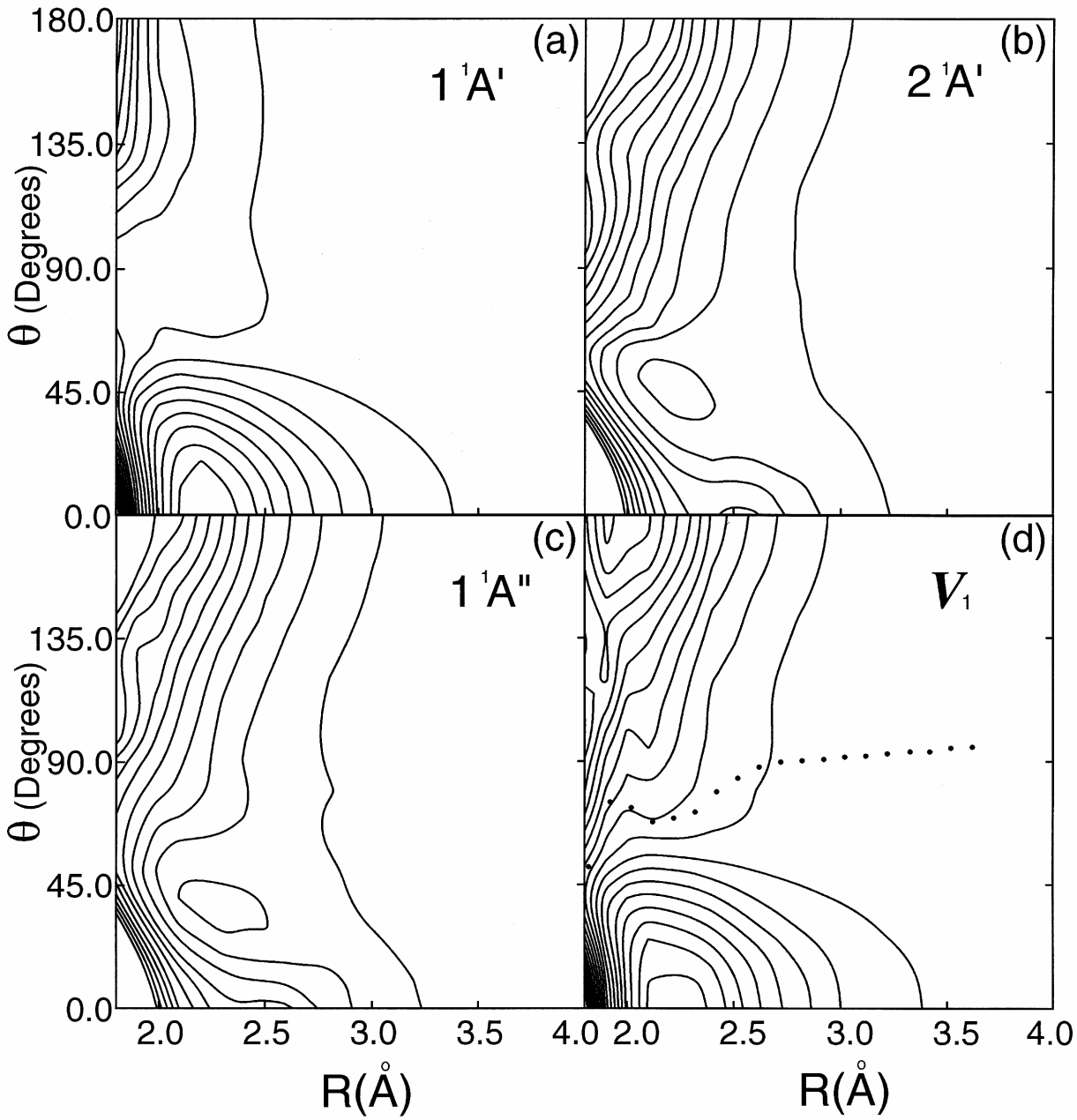

Fig. 4-11
Two dimensional PES's of OCS at r_{CO} = 1.13 Å. (a) 1^1A', (b) 2^1A', (c) 1^1A", and (d) V_1 lower diabatic surface constructed from (a) and (b).

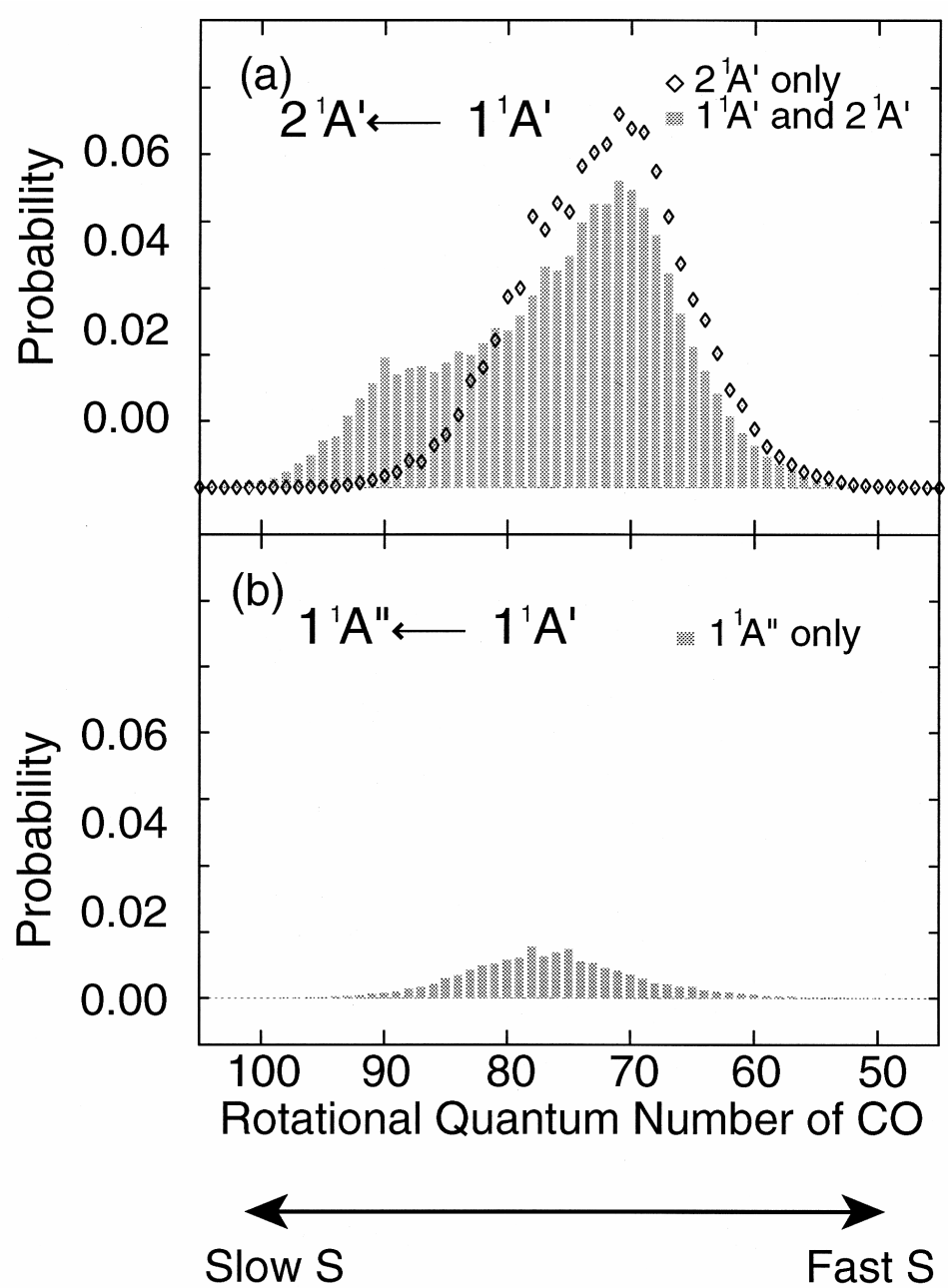

Fig. 4-12

(a) Rotational distribution of CO predicted by the calculations with and without the non-adiabatic coupling between 1^1A' and 2^1A'. The open square represents the result for the single 2^1A' surface, while filled box the result including non-adiabatic coupling between 2^1A' and 1^1A'. Higher *J* number of CO corresponds to slow speed of S, while low *J* corresponds to high speed of S. (b) Dissociation no the single 1^1A" surface.

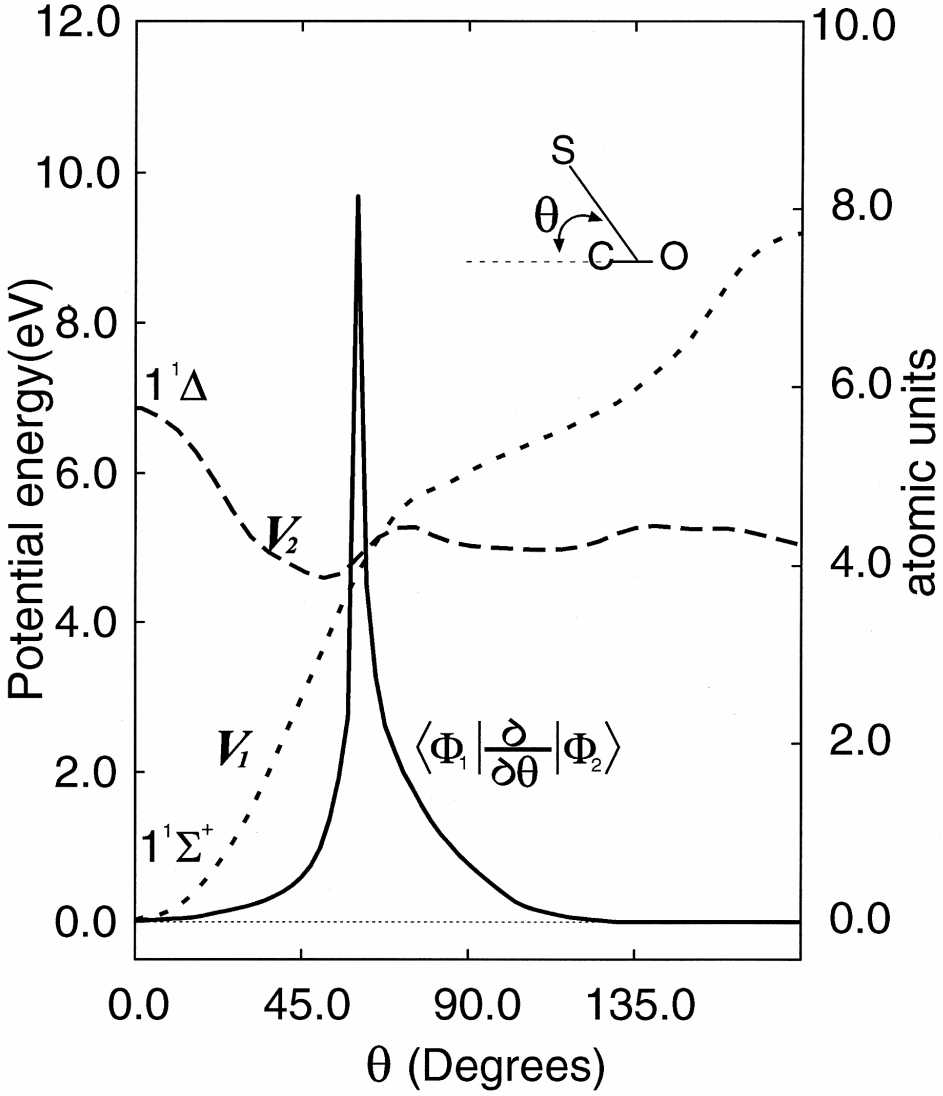

Fig. 4-13

Diabatic curves V_1 and V_2 obtained from $2^1A'$ and $1^1A'$ states using $\left\langle f_1 \left| \frac{\partial}{\partial q} \right| f_2 \right\rangle$

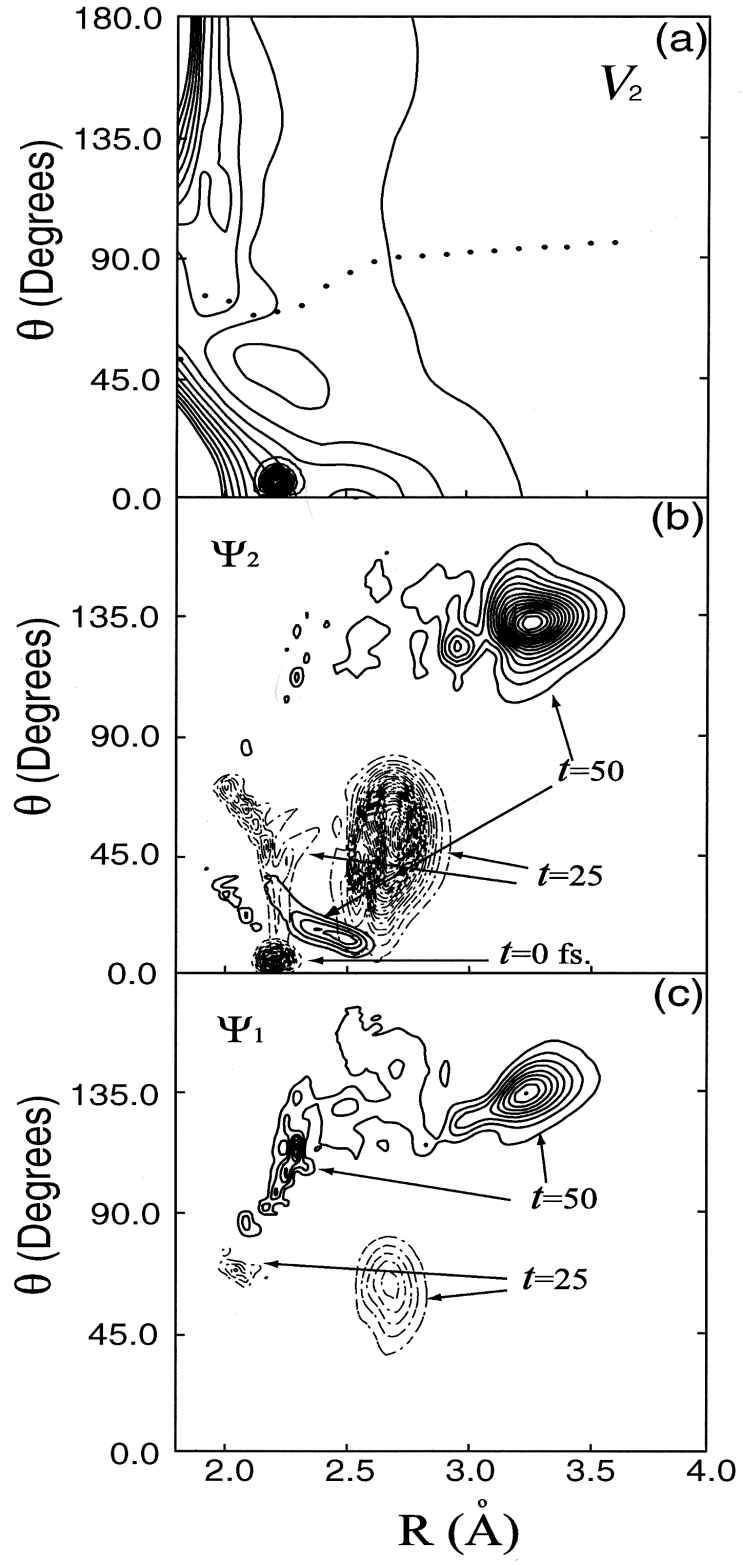

Fig. 4-14
Snapshots of wave packets; (a) initial wave packet at the Franck-Condon state, (b) wave packet at t=25 and 50 fs on the upper diabatic surface, and (c) wave packet on the lower diabatic surface.

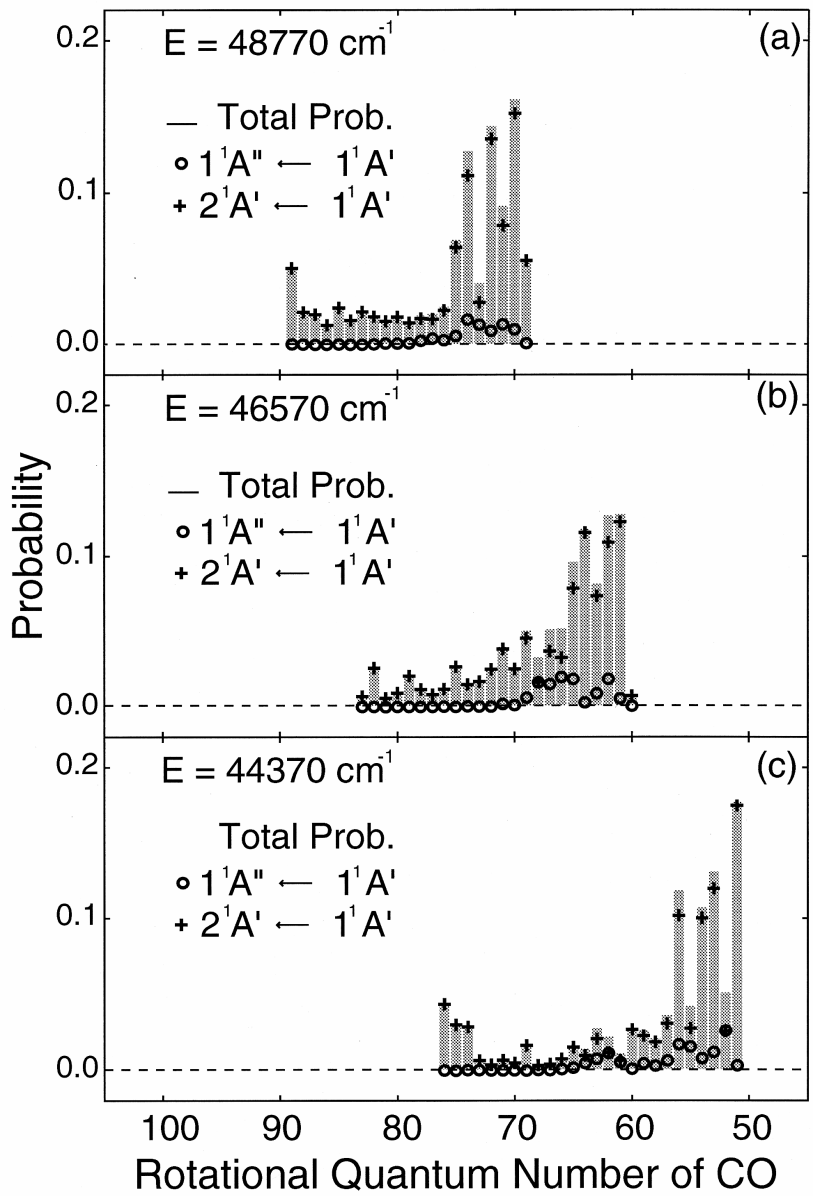

Fig. 4-15
The wavelength dependence of the rotational distribution of CO calculated for the excitation energies of (a) E = 44370, (b) 46570, and (c) 48770cm^{-1} corresponding effectively to the excitation wavelengths of l = 248, 235, and 223 nm employed in our experiment.

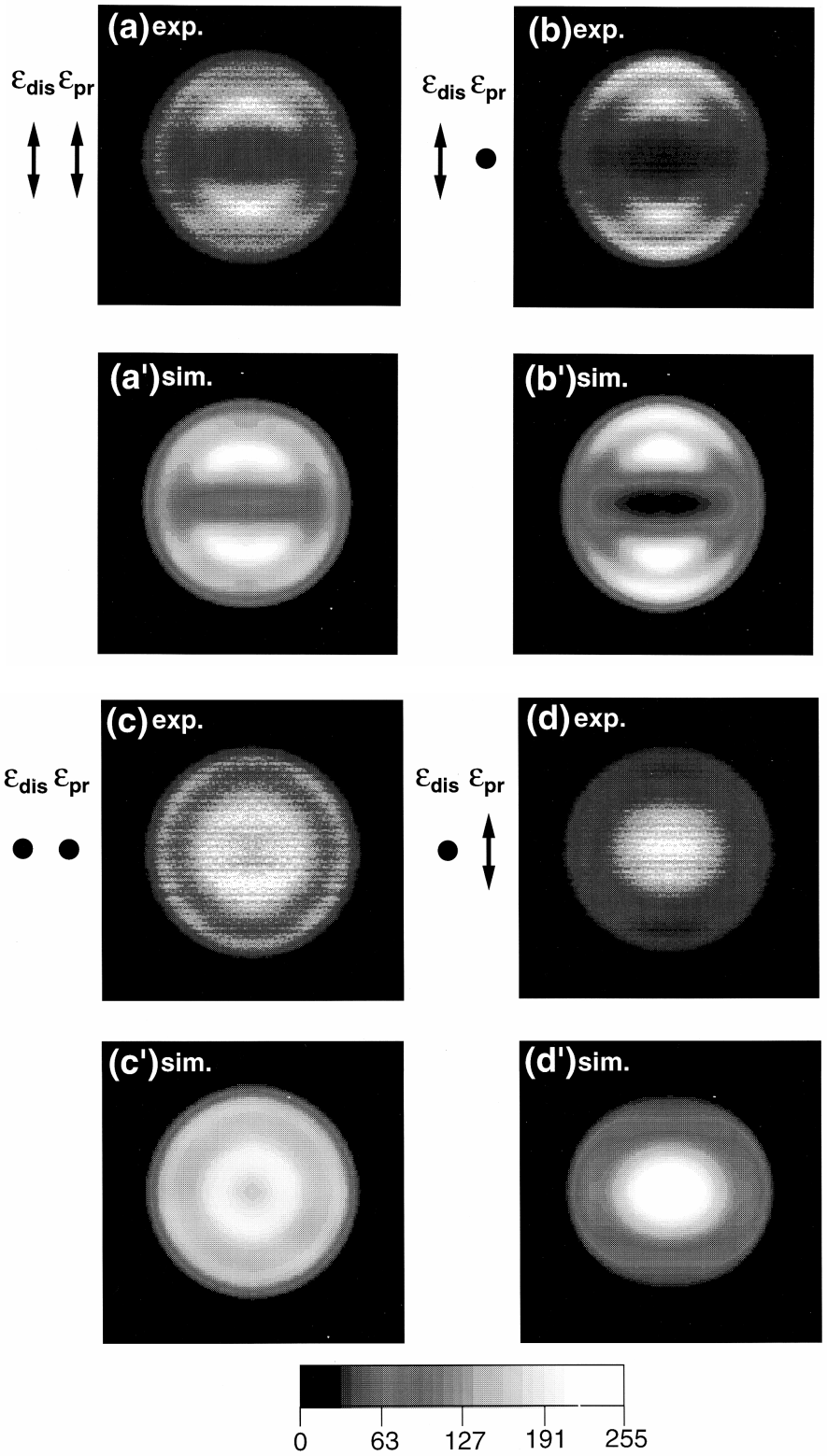

Fig. 4-16
2D ion images of $S(^1D_2)$ produced by 223 nm photodissociation of OCS. (a), (b), (c), (d) are the experimental data, and (a'), (b'), (c'), and (d') are the simulated images obtained by using the parameters in Table 3. The direction of the polarization vectors of the dissociation and probe laser beams are shown as e_{dis} and e_{pr}. The experimental data have been symmetrized for ease of comparison with the simulation.

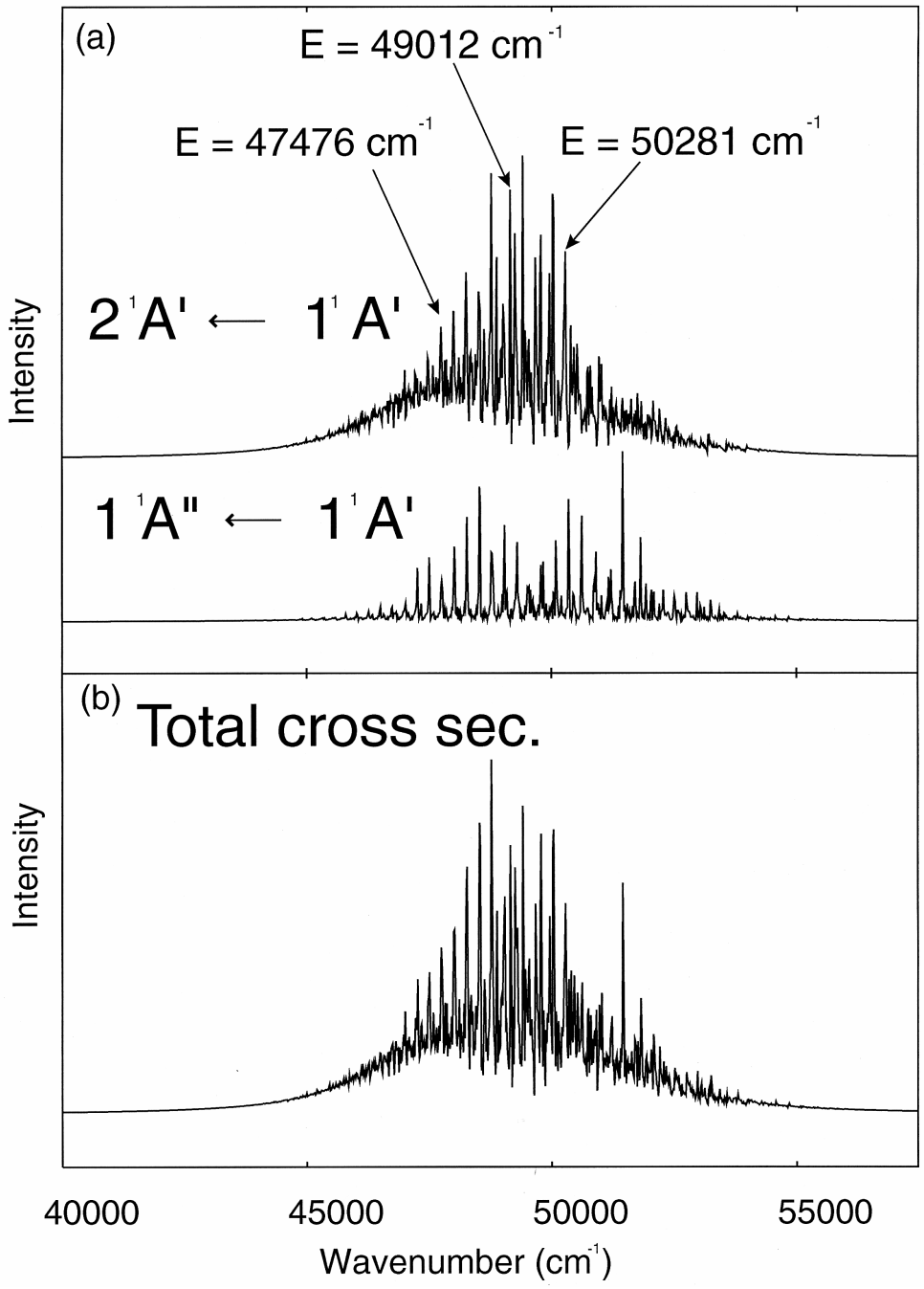

Fig. 4-17

(a) The calculated photodissociation cross-section for $2^1A' \leftarrow 1^1A'$ and $1^1A'' \leftarrow 1^1A'$ transitions and (b) the sum of the two transitions. $J''=0$, (0,0,0) state was assumed as an initial state.

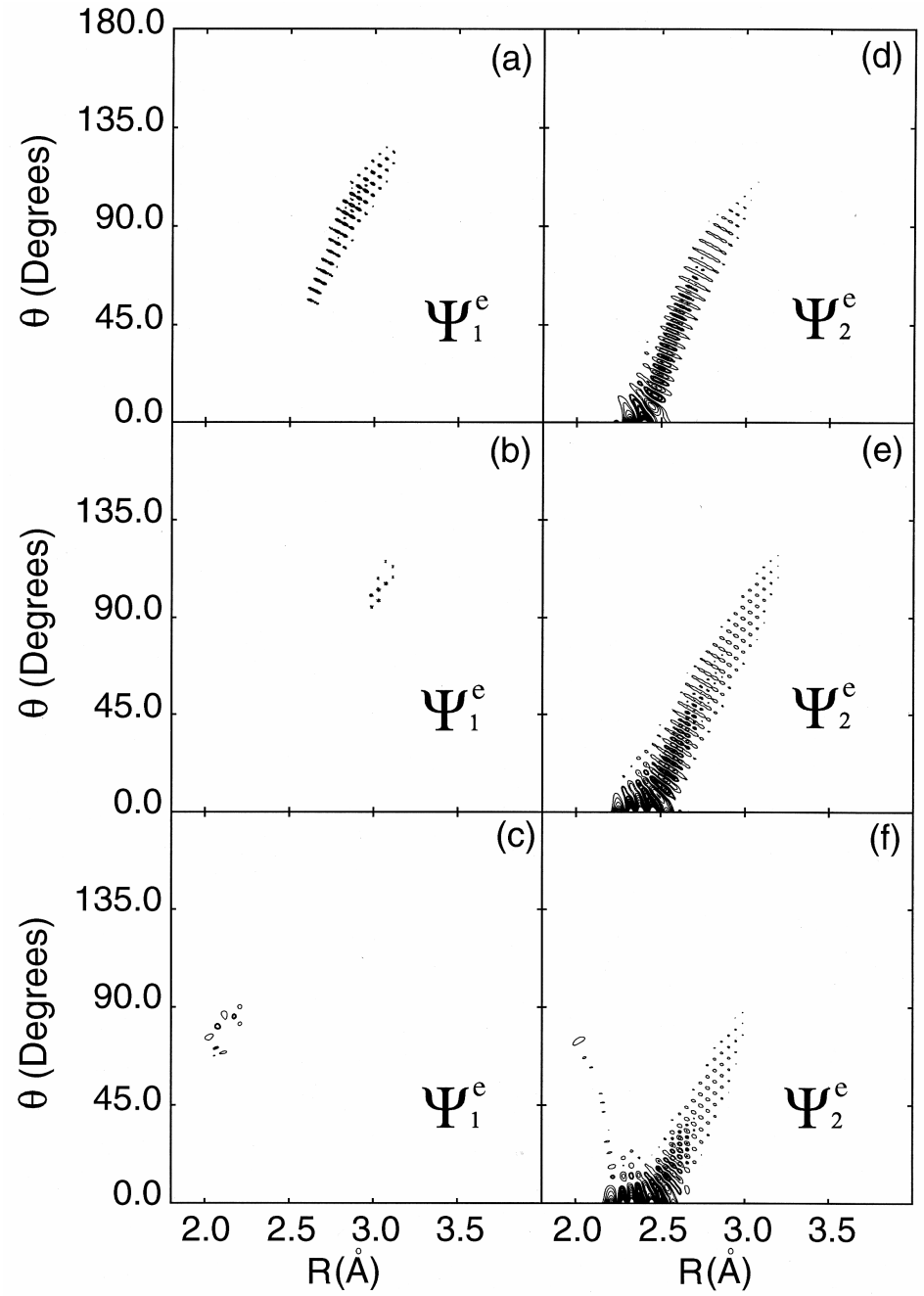

Fig. 4-18

The wavefunctions y_1^e and y_2^e in the lower and upper diabatic surfaces obtained by the spectral method [58] for the strong peaks in the spectrum at E = 47476, 49012, and 50281 cm^{-1} as indicated in Fig. 17 (a). The wavefunctions y_2^e shown in (d), (e), and (f) exhibit the nodal structure for G-S stretching in the Frank-Condon region, which is regarded as Feshbach resonance. As seen in (a), (b), and (c), the resonance states that exhibit a sharp spectrum do not have a large fraction of wavefunction on the lower diabatic surface.

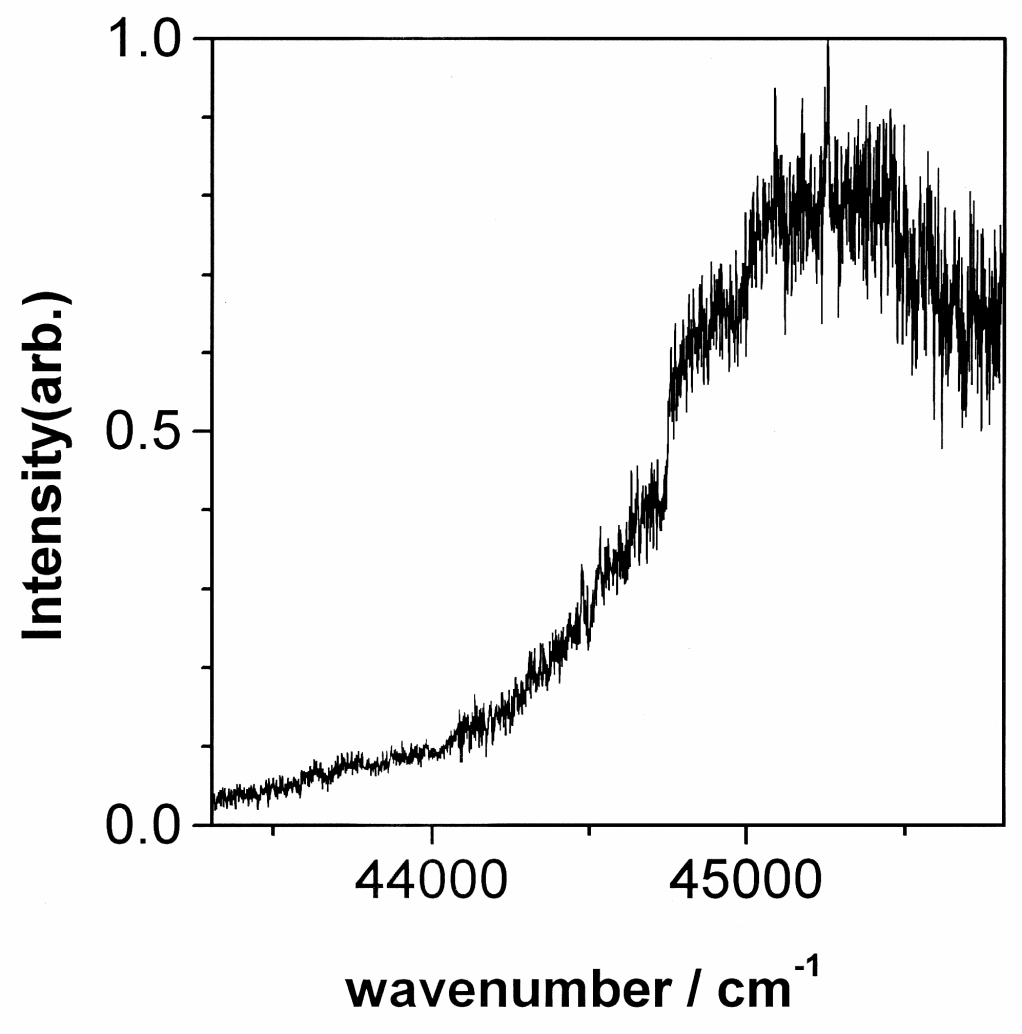

Fig. 4-19
$S(^1D_2)$ action spectrum of jet-cooled OCS. The spectrum corresponds to an absorption spectrum, since the dissociation yield is unity. The probe laser frequency was fixed at the center of Doppler-broadened absorption line of $S(^1D_2)$ and pump laser frequency was scanned. The sharp structure predicted by calculation (Fig. 17) is not seen. The broad structure reproducible is indicated by vertical lines.

Table 4-1. Spectroscopic constants

	This Work	Exp.
R_{CS}(Å)	1.55	1.562021[a]
r_{CO}(Å)	1.13	1.155386[a]
θ_e(∠OCS, deg.)	180.0	180.0[a]
D_e(eV)	4.16	
D_0(eV)		4.26[b]

a) Reference [47]

b) Reference [48]

Table 4-2. Vibrational frequencies in the ground electronic state (cm^{-1})

Vibrational level	This work	Exp.[a]
$(1,0^0,0)$	948	858.95
$(0,2^0,0)$	1045	1047.1
$(0,0^0,1)$		2062.2

Reference [49]

Table 4-3. Parameters used for the simulation of Fig. 4-16

Speed component	Branching Ratio	b	E_0[a)]	s[α)]	m_J distribution		
					0	±1	±2
Slow	1.0	1.8	5.3	4.1	0.60	0.14	0.06
Fast	3.0	0.7	13.8	5.7	0.48	0.24	0.02

a) Energy units are kcal mol^{-1}. The translational energy distributions were expressed by Gaussian functions,

$$\frac{1}{s}\sqrt{\frac{2}{p}}\exp\left\{-2\frac{(E-E_0)^2}{s^2}\right\}.$$

Chapter 5

Non-adiabatic bending dissociation of OCS: The effect of bending excitation on the transition probability [a]

[a] Published on *Chemical Physics Letters* **360**, 104-110 (2002)

5.1. Introduction

Carbonyl sulfide has a broad photoabsorption spectrum in the 200-250 nm region [1] corresponding to electronic transitions to the dissociative $2^1A'$ and $1^1A''$ states. Upon photoexcitation, OCS decomposes into CO (X $^1\Sigma^+$) with $S(^1D_2)$ or $S(^3P_J)$ in the ratio 95:5 [2-4], where vibrational excitation in $CO(^1\Sigma^+)$ is negligibly small [5]. In our previous work, we measured the translational energy and angular distributions of $S(^1D_2)$ fragments for the excitation wavelengths of 223–248 nm and observed bimodal distributions of $S(^1D_2)$ [6], i.e. bimodal rotational distributions of $CO(^1\Sigma^+)$ [2,3,7]. From consideration of the Walsh diagram, the bimodal distribution was speculated to be due to the adiabatic and non-adiabatic dissociation processes, where the latter is induced by a bending motion in the $2^1A'$ state. This speculation was supported by wave packet calculations on ab initio potential energy surfaces [6]. The probability of the non-adiabatic transition from the $2^1A'$ to the ground ($1^1A'$) state was as large as 0.35 [6]. The non-adiabatic transition from $1^1A''$ to $1^1A'$ is symmetry forbidden.

In view of the important role of a bending motion in photodissociation of OCS, the present work examines the effect of bending excitation on the non-adiabatic transition probability in OCS. We use thermally excited OCS molecules in the molecular beam as a sample. The presence of vibrationally excited molecules in the beam has been reported by Sugita *et al.* [8]. We apply a high-resolution ion-imaging technique to explore rotational distributions of CO in photodissociation starting from the (000) and (010) state of OCS.

5.2. Experimental

The ion imaging apparatus used in the present work was similar to the one reported earlier [6]. A sample gas 2% seeded in Ne, instead of Ar in our previous work [6], was expanded from a Piezo electric driven pulsed nozzle [9] with a stagnation pressure of 1 atm relative to the vacuum, and it was collimated by a 0.8 mm diameter skimmer 19 mm downstream from the nozzle. The molecular beam was introduced into a main chamber and crossed with a laser beam in the stacked electrodes operated in a velocity mapping condition [10]. In our previous work, we found that photodissociation of OCS clusters produces $S(^3P_J)$

atoms with low translational energies. Therefore, we have ascertained that there is no $S(^3P_J)$ signal with low translational energy and that OCS clusters were not present in the beam [6].

Linearly polarized laser light (100 μJ/pulse) obtained by doubling the output of a nanosecond Nd:YAG-pumped dye laser was focused onto the molecular beam with a convex lens (f=250 mm). The focused UV light intersected the molecular beam at 79 mm downstream from the nozzle. The laser wavelength was tuned through the $B(^1\Sigma^+)$? ? $X(^1\Sigma^+)$ two-photon transition of CO around 230 nm. Since this wavelength is accidentally at the center of the first absorption band of OCS (200-250 nm) [1], a single UV laser pulse could serve for both photodissociation of OCS and ionization of CO.

The CO^+ ions produced by (2+1) resonance enhanced multiphoton ionization (REMPI) [8] were accelerated up to the kinetic energy of 2 keV and projected onto a dual microchannel plate (MCP) backed by a phosphor screen. A high voltage pulse 300 ns in duration was applied to the MCP to time gate the CO^+ ions. The transient image on the phosphor screen was captured by a thermoelectrically-cooled charge-coupled-device (CCD) camera and accumulated on the CCD chip for 45000 laser shots.

While $CO(B^1\Sigma^+)$ is weakly predissociative for $j \geqq 38$ [11], Rottke and Zacharias reported that the rate of predissociation is j-independent [12]. The two-photon transition intensity in the Q-branch is given by

$$I = (2j+1)\left(1 + \frac{9j(j+1)}{45(2j-1)(2j+3)}\frac{m_S^2}{m_I^2}\right) \qquad (1)$$

where m_S and m_I are transition dipole factors. [13]. However, since the upper limit for the actual value of m_S^2/m_I^2 is 1/17 [14], the line strength is well approximated by $(2j+1)$ within an error of 0.3 % in the j=39-69 range. From these considerations, the population of CO in each j state was obtained by dividing the observed line intensity by $(2j+1)$ as discussed by Sato *et al.*[7].

For observing photofragment image of CO in each rotational j state, the laser wavelength was scanned around a single rotational line of CO to cover the entire Doppler width. The observed images of CO^+ were two-dimensional (2D) projections of three-dimensional (3D) neutral CO product scattering distributions. Since the CO spatial distributions were cylindrically symmetric around the electric vector of the laser beam, the sections of the 3D distributions were computed by inverse Abel transformations.

The speed resolution was $\Delta v/v$= 5% at 1.3 km/s. The photolysis photon energy slightly varied for different rotational state of CO due to the nature of one-color experiment. However, this variation (50 cm^{-1}) was safely negligible in comparison with the photon energy about 43500 cm^{-1}.

5.3. Results and discussion

5.3.1. Non-adiabatic transition probability

In our previous paper, three photodissociation processes were identified for the $CO(^1\Sigma^+)$ + $S(^1D_2)$ channel: these were the adiabatic dissociations from the (I) $2^1A'$ and (II) $1^1A''$ states and (III) the non-adiabatic dissociation from the $2^1A'$ state. In the following, we use the non-adiabatic transition probability defined by

$$F_{NA} = \frac{F_{III}}{F_I + F_{III}} \qquad (2)$$

This value was calculated by the following procedure. First of all, the process (III) produces CO in high *j* states which are well separated from the low *j* CO component produced by (I) and (II). Thus, F_{III} was obtained from the product state distribution itself. The F_I and F_{II} were obtained by analyzing scattering distributions of CO in low *j* states.

5.3.2. CO rotational distributions measured for different initial states of OCS

Figure 5-1(a) shows a (2+1) REMPI spectrum of nascent CO produced by 230 nm photodissociation of OCS in the molecular beam carried by Ne. From this spectrum, the rotational distribution shown in Fig. 5-1(b) was extracted. The CO fragments are highly rotationally excited and the distribution exhibits two maxima at *j*=49 and 62. The obtained rotational distribution was consistent with previous observations of CO by Sivakumar *et al.* [3] and Sato *et al.* [7] and also of the counterpart S atoms in our previous work [15]. Since the observed distribution was an admixture of the contributions from different initial states of OCS, these contributions were separated in the next step.

In this photodissociation process, CO is exclusively produced in the X $^1\Sigma^+$ state and its vibrational excitation is negligible [5]. Sulfur atoms are produced both in the $^1D_2$ and the ^3P_J states, however, the former has a dominant branching ratio of 0.95 [4]. Thus, the following energy conservation law applies,

$$hn + E_{int} - D_0 = E_{SO}(S) + E_{trans} + Bj\,(j + 1) \qquad (3)$$

where hn is the photon energy (43497 cm^{-1} at 229.9 nm), E_{int} is the internal energy of a parent molecule, D_0 is the dissociation energy (25164 cm^{-1}) [16], $E_{SO}(S)$ is the spin-orbit energy (9239 cm^{-1}) of S($^1D_2$) with respect to the ground state S($^3P_2$), E_{trans} is the center-of-mass translational energy release, B is the rotational constant (1.9313 cm^{-1}) of CO(X $^1\Sigma^+$), and j is the molecular rotational quantum number of CO. The higher order rotational constants are neglected because of their small contribution, 1% at j=60, on the rotational energy [5,17]. The translational energy of CO molecule produced in a particular rotational state has a one-to-one correspondence with E_{int} as follows:

$$E_{trans}(\text{cm}^{-1}) = 9094 - E_{int} - 1.9313\,j\,(j + 1) \qquad (4)$$

Figures 5-2 (a), (b), and (c) show the Abel-transformed ion images and the translational energy distributions determined for j = 64, 65, and 69, respectively. In Fig. 5- 2(a), the separation of the two peaks is 1.5 kcal/mol that corresponds to the bending energy (n_2: 524 cm^{-1}) in the ground state, so the higher energy peak was assigned to photodissociation starting from the (010) level. Likewise, Fig. 5-2(b) shows dissociation starting from the (000), (010) and (020) levels. A single peak in Fig. 5-2(c) was assigned to photodissociation from (010) from the equation (4); this state cannot be populated by photodissociation from the (000) level.

From the observed ion images for rotational states of j=51–68, we obtained the (v_2=0):(v_2=1):(v_2=2) ratios, P_v, for each j state as summarized in Table 1. The CO rotational state distributions in photodissociation from the different initial states of OCS were calculated by multiplying the population in each rotational state, I_j, with the ratio, P_v, for each (0v0) initial state of OCS in Table 5-1:

$$I_{j,\,v=0,1,2} = I_{j,\,\text{total}} \cdot P_v \qquad (5)$$

The results for v_2=0 and 1 are shown in Fig. 5-3.

Unfortunately, this approach could be undertaken only down to j=51: although ion images were observed for j < 51, the speed resolution was insufficient to resolve multiple peaks. Thus, we have extrapolated the above procedure to low j states by the least-squares fitting. It has been known already that the rotational energy distribution of CO can be well

approximated by two Gaussian functions. Therefore, the individual rotational energy distributions for photodissociation from the (000) and (010) initial states, albeit available only for the limited region of $51 < j < 68$, were analyzed by the least-squares fitting of the two Gaussian functions. The sum of these functions obtained individually for the (000) and (010) levels reproduced the observed overall CO rotational distribution (Fig. 5-3).

When the bimodal distributions were expressed by Gaussian functions, the crossing points of the two Gaussians were found at j=58 for (000) and j=59 for (010) initial states. From this fact, we termed the product CO of $j \leqq 58$ as a "low j component", while $j > 58$ as a "high j component". The low j component is mainly produced by adiabatic pathways (I) and (II), while the high j component by non-adiabatic pathway (III) as reported in our previous work [15].

5.3.3. Effect of bending excitation on non-adiabatic transition probability

Figure 5-4(a) shows an inverse Abel transform of the image of CO (j=52), where the inner ring (dissociation from (000)) exhibits almost isotropic angular distribution, while the outer ring (010) reveals a more pronounced angular anisotropy. The difference in angular anisotropy is more clearly seen in Fig. 5-4(b). The anisotropy parameters in dissociation from the (000) and (010) levels are summarized in Fig. 5-5. The values for j=51-60 are in excellent agreement with the results reported by Sato *et al.* [7]. All the CO and $S(^1D_2)$ results provided b=1.8 at j=60, which proves that this component is due to photodissociation from the 2A' state. On the other hand, the anisotropy parameters observed for the low j component were different for (000) and (010): at the lowest j=51 in Fig. 5-5, $b_{v=0}$=0.27 and $b_{v=1}$=0.66 were observed for the (000) and (010) initial states, respectively. This implies that the pathways (I) and (II) contribute with different ratios in photodissociation from the (000) and (010) levels. More quantitatively, the intensity ratio between the in-plane and out-of-plane transitions, i.e. (2A'? 1A') / (1A"? 1A'), contributing to the low j component can be related to the anisotropy parameters as follows,

$$b_v = b_{A'} X + b_{A''} (1 - X) \qquad (6)$$

where $b_{A'}$ and $b_{A''}$ are the anisotropy parameters expected for individual transitions. We determined $b_{A'}$=1.8 experimentally, while $b_{A''}$ is –1 due to geometrical constraint. X is the contribution of the transition 2A'? 1A'. For the (000) initial state, the above equation

provides $X_{v=0}$ = 0.45(4). Likewise, $X_{v=1}$ is 0.59(4) for (010). The parentheses in X values show 1s errors for the last digits calculated from the repeated experiments. Sudden decrease of anisotropy parameters in a range j >61 is explained by tangential velocity effect[18].

From these results, the non-adiabatic transition probabilities, F_{NA}, in photodissociation starting from the (000) and (010) levels were estimated to be 0.34(6) and 0.21(5), respectively. The previous estimation from the S($^1D_2$) image was also 0.35 [6], supporting the present analysis. The result suggests that the value for (010) is slightly smaller than that for (000). Theoretical analysis is now in progress to examine the effect of bending excitation on the non-adiabatic transition probability in photodissociation of OCS.

The contribution of photoexcitation to the 2^1A' state is 56 % for the initial state of (000) while 65 % for (010), indicating that the bending excitation of OCS enhanced the transition probability to the 2^1A' state. Since the 1^1A" and 2^1A' potential energy surfaces have quite similar topographies, the Franck-Condon factors in transitions from the ground state to these states are similar to each other. Hence the enhanced contribution of the photoexcitation to the 2^1A' state is ascribed to the vibrational coordinate dependence of the transition dipole moment functions. Indeed, the transition dipole moment to 2^1A' increases more steeply than the moment to 1^1A" for OCS bending [6].

5.3.4. Photoabsorption strength from (010) level

The ratio between the yields of photodissociaiton from the (000) and (010) states was (010)/(000)=0.59. If we assume Boltzmann distribution for vibrational temperature of 300 K, the relative population in the (010) state is calculated to be as small as (010)/(000) = 0.08. Since 300 K is an upper bound for the vibrational temperature, it is concluded that the transition from (010) is more than seven times stronger than the transition from (000). This is understood from the fact that the transitions originally forbidden from the ground state ($^1\Sigma^+$) to the $^1\Delta$ and $^1\Sigma^-$ states (2^1A' and 1^1A" in C_s symmetry) in the linear geometry are induced by bending distortion. On the other hand, Locker *et al.* measured the molar absorption coefficient for OCS vapor and concluded that the coefficient from (010) was 2.5 times larger than that from (000) at 230 nm [19]. Our result indicates that the absorption coefficients of hot bands from bending excited states of OCS are significantly larger than this previous estimation[19].

References

[1] J.W. Rabalais, J.M. McDonald, V. Scherr, S.P. McGlynn, Chem. Rev. **71**, 73 (1971).

[2] N. Sivakumar, I. Burak, W.Y. Cheung, P.L. Houston, J.W. Hepburn, J. Phys. Chem. **89**, 3609 (1985).

[3] N. Sivakumar, G.E. Hall, P.L. Houston, J.W. Hepburn, I. Burak, J. Chem. Phys. **88**, 3692 (1988).

[4] G. Nan, I. Burak, P.L. Houston, Chem. Phys. Lett. **209**, 383 (1993).

[5] A.M. Rijs, E.H.G. Backus, C.A. de Lange, M.H.M. Janssen, N.P.C. Westwood, K. Wang, V. McCoy, J. Chem. Phys. **116**, 2776 (2002).

[6] T. Suzuki, H. Katayanagi, S. Nanbu, M. Aoyagi, J. Chem. Phys. **109**, 5778 (1998).

[7] Y. Sato, Y. Matsumi, M. Kawasaki, K. Tsukiyama, R. Bersohn, J. Phys. Chem. **99**, 16307 (1995).

[8] A. Sugita, M. Mashino, M. Kawasaki, Y. Matsumi, R. Bersohn, G. Trott-Kriegeskorte, K.H. Gericke, J. Chem. Phys. **112**, 7095 (2000).

[9] D. Proch, T. Trickl, Rev. Sci. Instrum. **60**, 713 (1989).

[10] D.H. Parker, A.T.J.B. Eppink, J. Chem. Phys. **107**, 2357 (1997).

[11] G.W. Loge, J.J. Tiee, F.B. Wampler, J. Chem. Phys. **79**, 196 (1983).

[12] H. Rottke, H. Zacharias, Opt. Commun. **55**, 87 (1985).

[13] R.G. Bray, R.M. Hochstrasser, Mol. Phys. **31**, 1199 (1976).

[14] P.J.H. Tjossem, K.C. Smyth, J. Chem. Phys. **91**, 2041 (1989).

[15] H. Katayanagi, Y. Mo, T. Suzuki, Chem. Phys. Lett. **247**, 571 (1995).

[16] W.L. Weise, M.W. Smith, B.M. Miles, NSRDS-NBS **22**, 134 (1969).

[17] G. Guelachvili, D. Devilleneuve, R. Farrenq, W. Urban, J. Verges, J. Mol. Spectrosc. **98**, 64 (1983).

[18] A.V. Demyanenko, V. Dribinski, H. Reisler, H. Meyer, C.X.W. Qian, J. Chem. Phys. **111**, 7383 (1999).

[19] J.R. Locker, J.B. Burkholder, E.J. Bair, H.A. Webster, J. Phys. Chem. **87**, 1864 (1983).

Figures and tables for Chapter 5

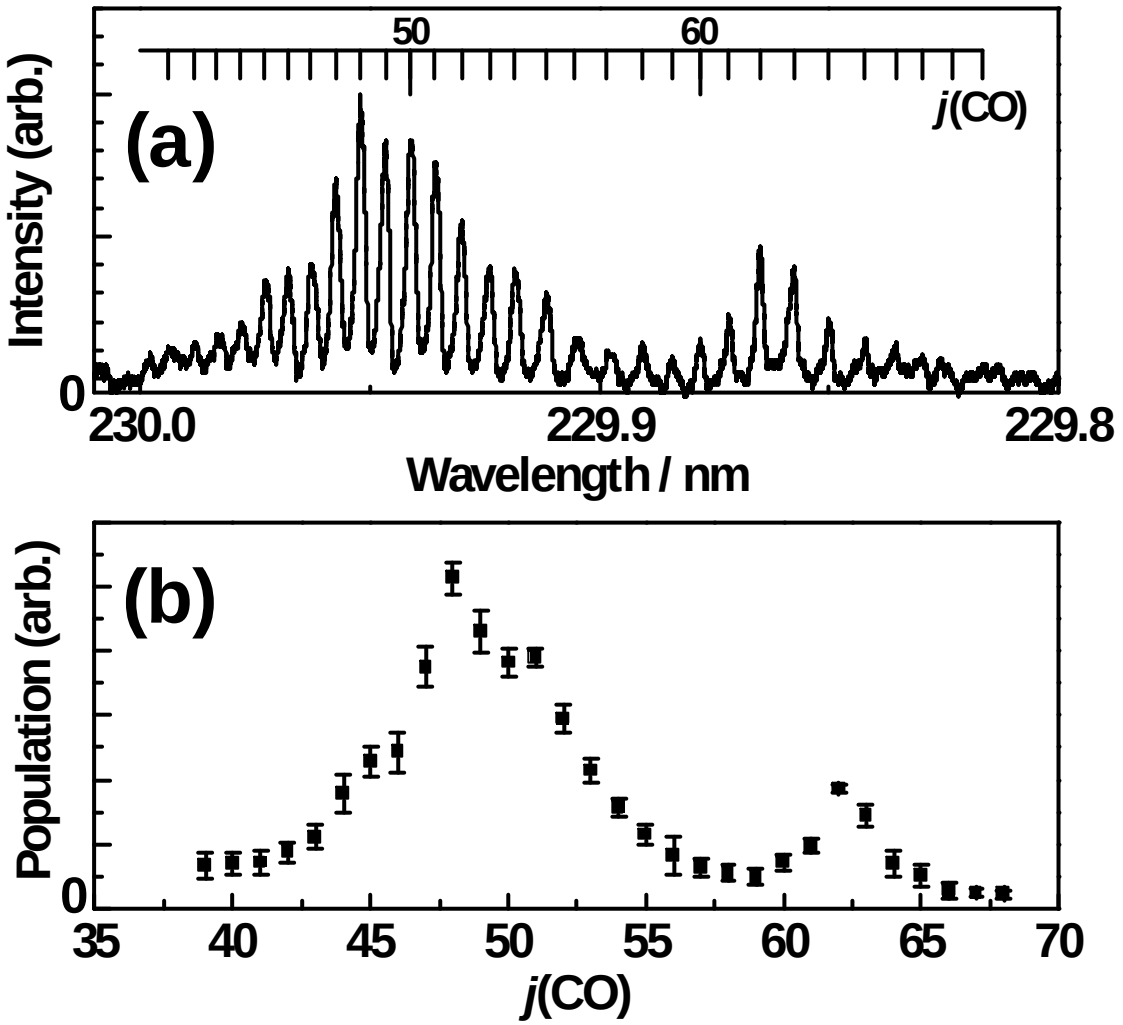

Fig. 5-1.
(a) Typical (2+1) REMPI spectrum of CO via CO(B $^1\Sigma^+$) produced by the 230 nm photodissociation of OCS. The rotational assignment is shown in the spectrum. (b) Rotational distribution of CO obtained by averaging five REMPI spectra. Error bars indicate standard deviations.

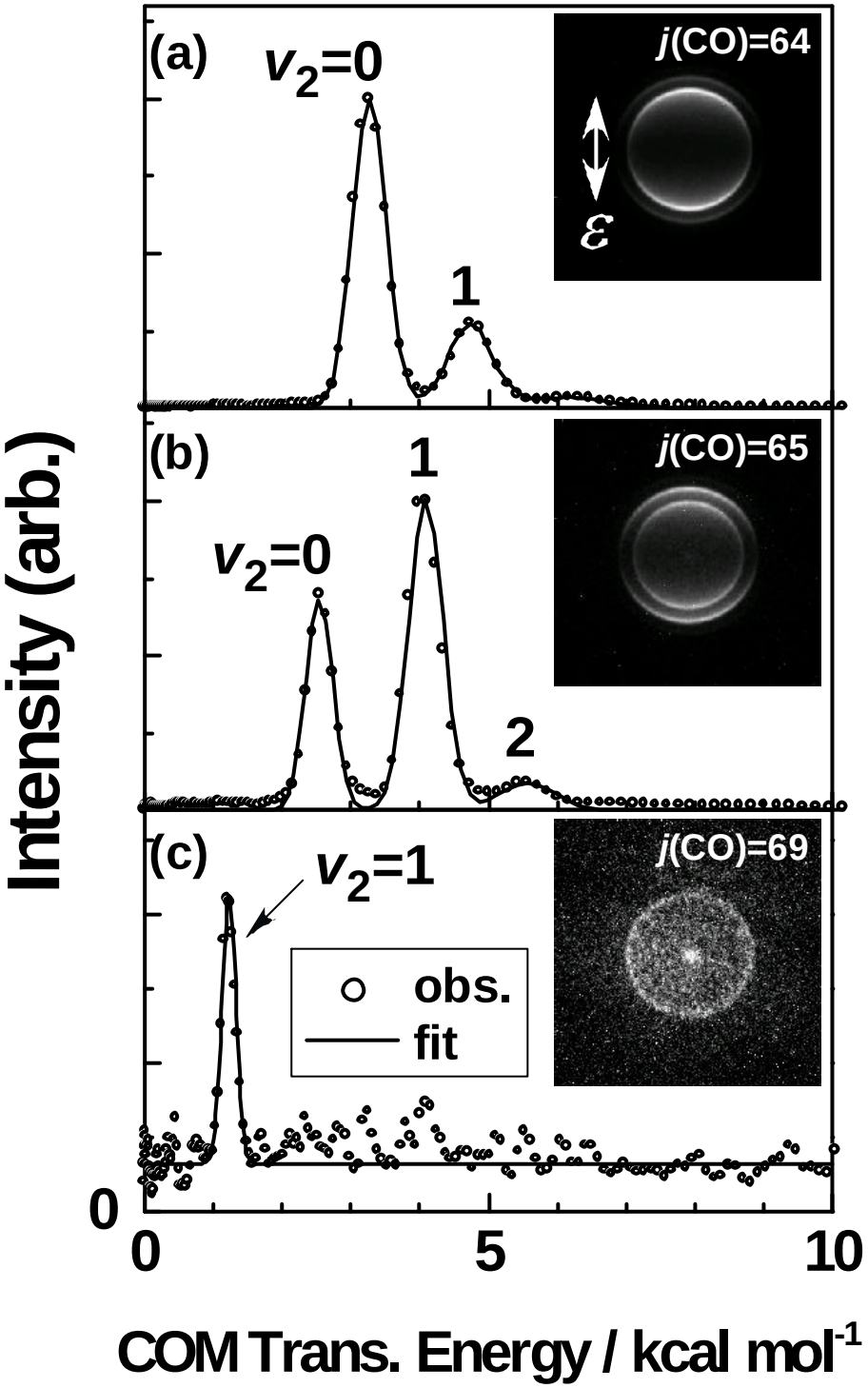

Fig. 5-2.
Ion images and center-of-mass translational energy distributions observed for (a) j=64, (b) j=65 and (c) j=69. The laser polarization (e) is shown by an arrow. The observed distributions were well reproduced by linear combinations of Gaussians shown as solid lines in each panel. The assignments of the initial state ($0v_20$) are shown in the figure.

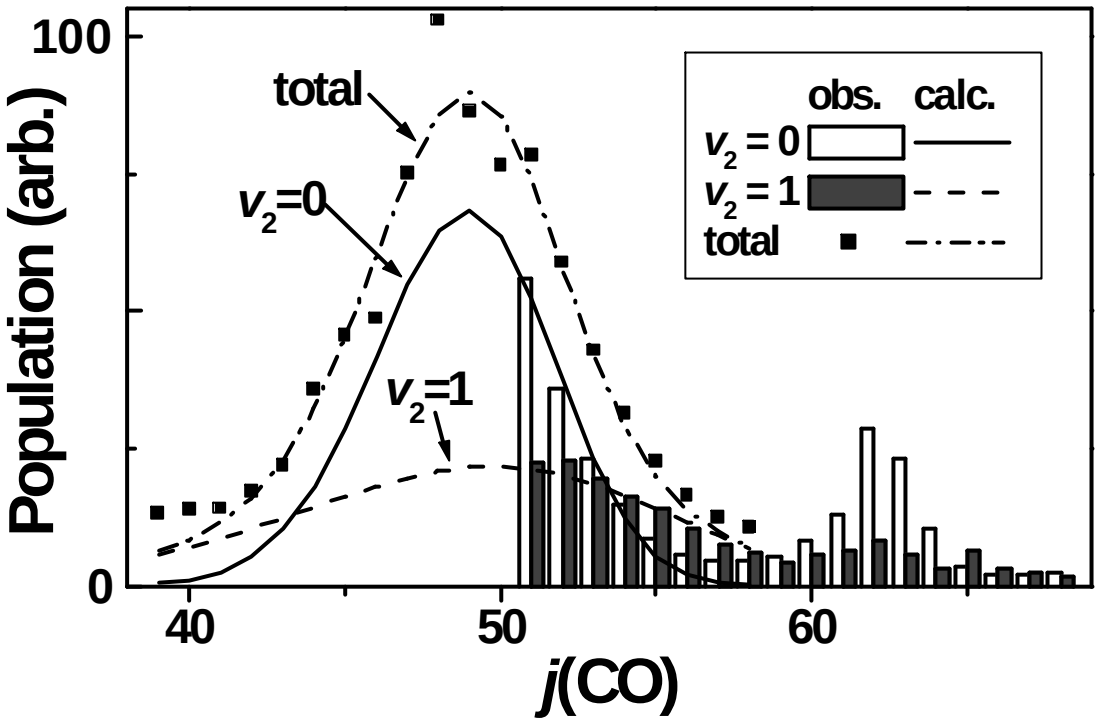

Fig. 5-3.
Rotational distribution of CO in photodissociation from the (000) and (010) states of OCS. The v_2=2 contribution was neglected, and the populations were normalized as $I_{total} = I_{v=0} + I_{v=1}$. The solid and broken lines show Gaussian distributions obtained by the least-squares fitting to the low j components in dissociation from (000) and (010), respectively. Dash dot curve, the sum of those (000) and (010) Gaussian distributions, represents the overall CO distribution quite well.

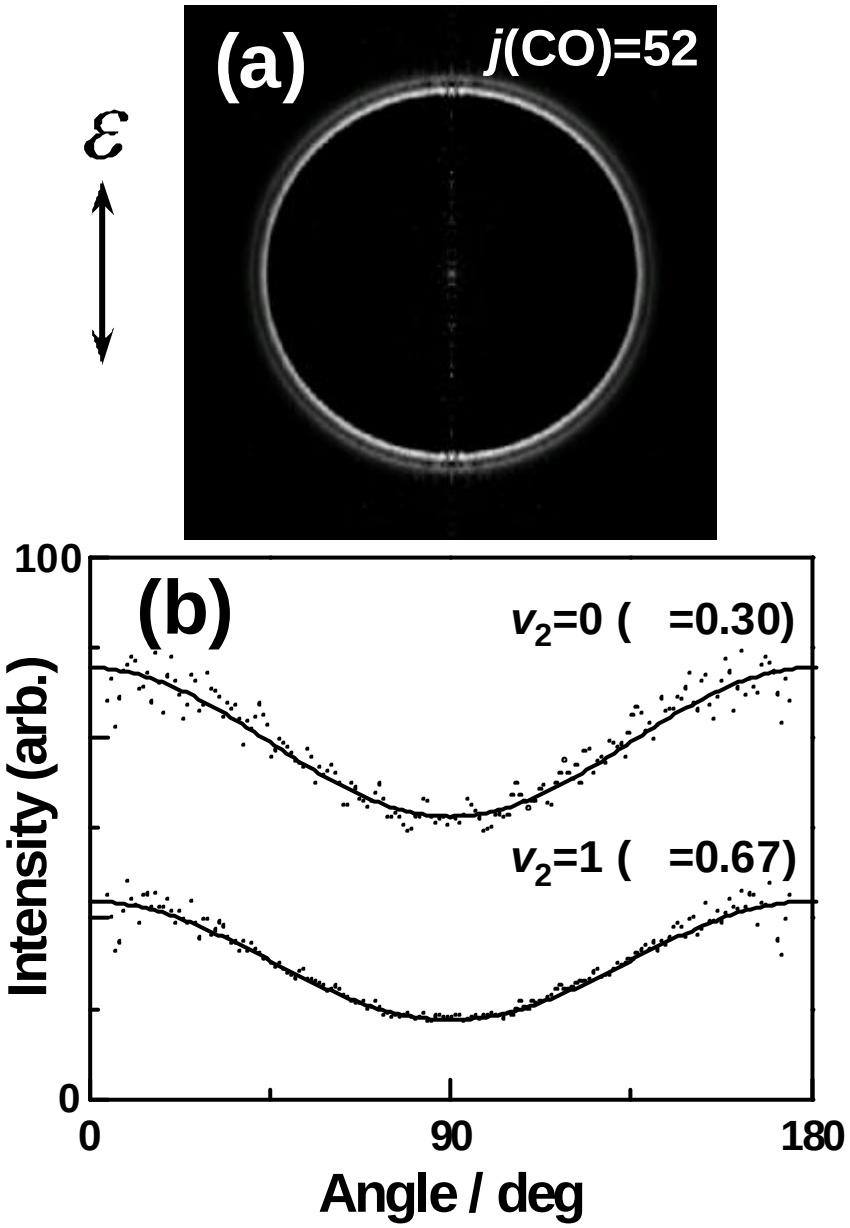

Fig. 5-4.
(a) Inverse Abel transform of the CO^+ image for j(CO)=52. The laser polarization (e) is vertical in the figure. Inner ring corresponds to photodissociation from (000) and outer ring from (010). (b) Angular distributions obtained for (000) and (010). Solid curves represent the least-squares fittings of the equation $1 + bP_2$ (cos$q$) where $P_2(x)$ is the second order Legendre polynomial.

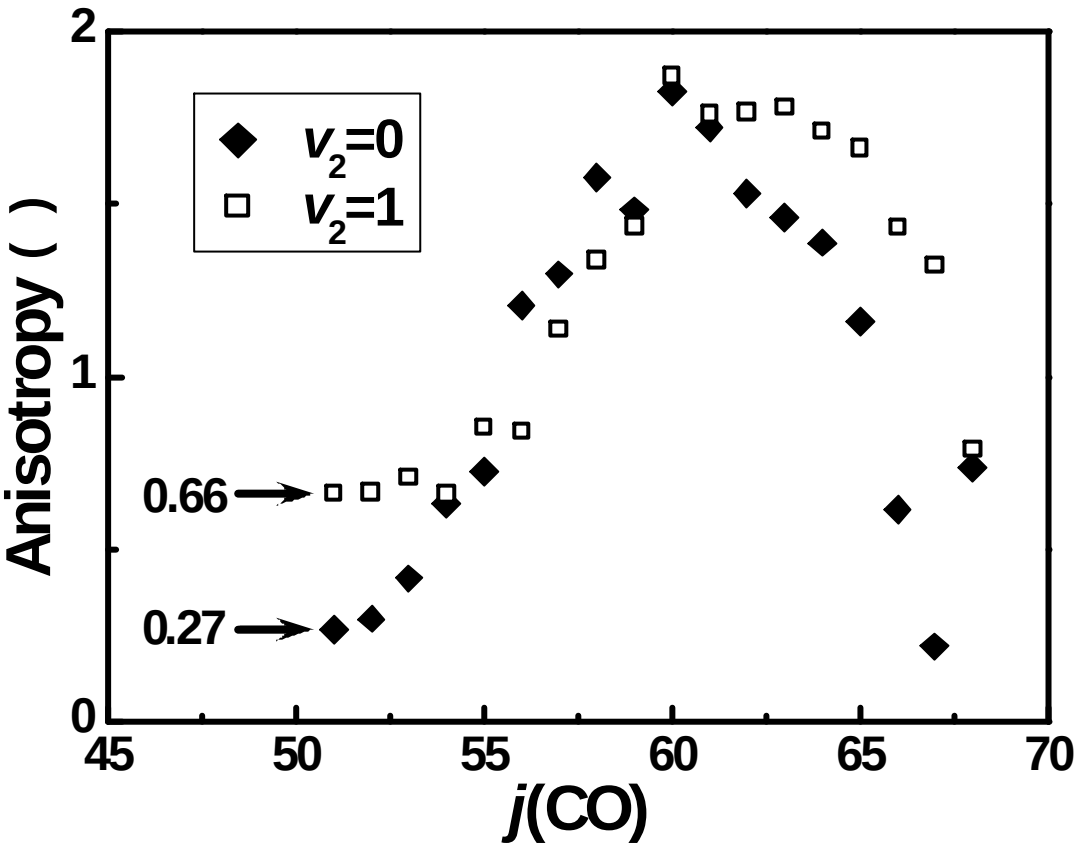

Fig. 5-5.
Anisotropy parameters (b) determined for each j state in photodissociation from (010) and (000). From repeated experiments for j=51, 64, and 68, the errors in each b value were estimated to be smaller than $\pm$0.1.

Table 5-1

Overall rotational distribution of CO (I_{total}), relative contributions from different initial states of OCS for each j state (P_v %), and rotational distribution (I_v) determined for each initial state ($0v_20$) of OCS

j	Population [a]	Contribution from each initial state P_v%			Population I_v		
	I_{total}	$P_{v=0}$	$P_{v=1}$	$P_{v=2}$	$I_{v=0}$	$I_{v=1}$	$I_{v=2}$
51	1.00(4) [b]	68	28	4	68	28	4
52	0.75(6)	58	38	4	44	28	3
53	0.55(5)	54	46	0	30	25	0
54	0.40(3)	43	48	9	17	19	3
55	0.29(4)	38	62	0	11	18	0
56	0.21(7)	32	57	11	7	12	2
57	0.16(4)	33	53	14	5	8	2
58	0.14(3)	39	48	13	5	7	2
59	0.12(3)	48	37	15	6	5	4
60	0.18(3)	51	35	14	9	69	3
61	0.25(3)	60	30	10	15	77	3
62	0.48(2)	73	21	6	35	10	3
63	0.37(4)	80	20	0	30	7	0
64	0.18(5)	73	23	4	13	41	1
65	0.13(5)	32	60	8	4	8	1
66	0.07(3)	35	54	11	2	4	1
67	0.06(2)	40	42	18	3	3	1
68	0.06(2)	45	36	19	3	2	1

[a] Numbers in parentheses show standard deviations of the last one digit for each j calculated from five repeated experiments.

[b] I_{total} was normalized as the intensity of j=51 to be unity.

Table 5-2

Contributions of each channel in dissociation from different initial state of OCS [a]

OCS Initial state	Total	Reaction pathways (I)A'	(II)A"	(III)non-adiabatic	Non-adiabatic transition probability
(000)	0.63(4)	0.23(2)	0.28(3)	0.12(2)	0.34(6)
(010)	0.37(3)	0.19(2)	0.13(2)	0.05(1)	0.21(5)

[a] Numbers in parentheses show standard deviations of the last one digit.

Chapter 6

One- and two color photoelectron imaging of the CO molecule via the B $^1S^+$ state [a]

[a] Submitted to *Journal of Chemical Physics*

6.1. Introduction

The importance of the CO molecule in atmospheric chemistry and combustion processes is beyond question [1]. In the earth's atmosphere the molecule is formed by the oxidation of methane in the troposphere. The reaction of CO with OH radicals is very fast and produces the greenhouse gas CO_2 [2]. In addition, CO is abundant in the planetary atmospheres of Mars and Venus, and is an important constituent of comets. The molecule is extremely well studied with a plethora of spectroscopic techniques and theoretical methods, and many of its excited valence and Rydberg electronic states and ionic states are well-characterized [3].

In the present work, the CO molecule is studied *via* a two-step ionization process using the $B^1\Sigma^+$ 3sσ (6σ) Rydberg state as a stepping-stone, while employing imaging methods of the photoelectrons generated in the ionization process. Both one-color nanosecond and two-color femtosecond experiments are performed. The intermediate $B^1\Sigma^+$ state located at 86916.18 cm^{-1} (~ 10.78 eV) represents the lowest member of a Rydberg series converging upon the $X^2\Sigma^+$ ionic ground state of CO^+, and its properties are well-characterized [4]. Accurate vibrational and rotational constants of the $B^1\Sigma^+$ state were derived in [4], based on the observation of rotational levels *N'* = 0-63 (R branch) and *N'* = 0-33 (P branch). Further improved spectroscopic rotational parameters have been obtained for N' up to 87 in a more recent resonantly-enhanced multiphoton ionization photoelectron spectroscopy (REMPI-PES) study [5]. Of course, the $X^1\Sigma^+$ ground electronic state is known in even greater detail [3].

The low-lying ionic states of CO^+ are also well known. In addition to He(I) and threshold photoelectron spectroscopic work with relatively low resolution [6-10], high-resolution laser based pulsed-field ionization photoelectron spectroscopy (PFI-PES) studies were reported by employing resonantly enhanced multiphoton [11-13], two-color [14], and VUV [15-16] excitation schemes. These PFI-PE studies have produced values for the ionization energies (IEs) comparable to that obtained from Rydberg series analysis [17]. In a recent high-resolution synchrotron-based PFI-PE study, vibrational levels associated with the $X^2\Sigma^+$ ground ionic state were determined in great detail [18]. The IEs of the $X^2\Sigma^+$ ground ionic state (14.01363 ± 0.00004 eV [17]) and the $A^2\Pi$ excited ionic state (16.536 eV [16]) are relevant to the present study.

From these studies on the intermediate $B^1\Sigma^+$ Rydberg state of CO and the $X^2\Sigma^+$ ionic ground state of CO^+, it is known that these possess potential energy curves with very similar

positions of their minima (r_e = 1.1197 Å for $B^1\Sigma^+$ [4] and r_e = 1.1151 Å for $X^2\Sigma^+$ [3]). Also, the shapes of both curves are virtually identical as evidenced by the small difference in vibrational spacings of CO ($B^1\Sigma^+$) and $CO^+(X^2\Sigma^+)$. The one-photon ionization step from the intermediate $B^1\Sigma^+$ Rydberg state to the $X^2\Sigma^+$ ionic ground state of CO^+ is expected to be highly Franck-Condon diagonal, implying a strong $\Delta v = 0$ propensity.

However, in a previous REMPI-PES study of CO *via* the $B^1\Sigma^+$ Rydberg state Sha *et al.* [19] observed surprising deviations from Franck-Condon behavior in the photoionization process, with final ionic state vibrational branching up to Δv=4. A Rydberg–valence interaction of the $B^1\Sigma^+$ Rydberg state, which could cause the non-Franck-Condon transitions in the photoelectron spectra, does not seem to be operational: for the B state, neither indications for predissociation nor perturbations arising from neighboring electronic states have been observed [20]. Sha *et al.* [19] reported a connection between the non-Franck-Condon behavior and the observed angular distribution of the photoelectrons, but the essence of the mechanism responsible for the non-Franck-Condon behavior in the photoionization step remained in the dark.

In a recent (2+1) REMPI-PES study, where rotationally 'hot' CO was generated in the photofragmentation of OCS and subsequently studied, similar deviations from the expected Δv=0 Franck-Condon behavior were observed. The intensities of the $\Delta v \neq 0$ transitions varied strongly within the energy region studied and were explained by the excitation of autoionizing 'superexcited' Rydberg states. These 'superexcited' states are states of the neutral species, located above the lowest ionization threshold. Rijs *et al.* have speculated that they belong to Rydberg series converging upon the $A^2\Pi$ excited ionic state whose members autoionize into the $X^2\Sigma^+$ continua [5].

While in conventional photoelectron spectroscopy employing He(I) radiation of 21.22 eV the observation of 'superexcited' states remained a rarity, in REMPI-PES accessing such states is the rule rather than the exception [21-24]. In He(I) UV-PES, the excitation takes place above the ionization energies of the large majority of the valence orbitals. Moreover, the excitation energy is far below the energy required to ionize inner shell orbitals, leading to a low density of accessible Rydberg states of the neutral leading up to these limits. For this reason conventional UV-PES studies have provided little information on 'superexcited' states. The situation is very different in REMPI-PES, where with a limited number of visible or UV photons an energy region below the ionization energies of several of the valence orbitals is

excited. In this energy range the possibility of accessing metastable states of the neutral, located above lower ionization thresholds and subsequently decaying *via* processes of autoionization and dissociation, appears to be a common occurrence. The present study is another illustration of this general phenomenon.

6.2. Experimental

A sample gas seeded in He was expanded from a pulsed valve with an orifice 0.5 mm in diameter at a stagnation pressure of 1 atm relative to the vacuum. The pressure in the source chamber was kept at $2x10^{-5}$ Torr by means of a 1500 L/sec turbomolecular pump. The supersonic free jet was skimmed in the source chamber by an electroformed nickel skimmer with an aperture 2 mm in diameter and collimated by a second skimmer with a 1 mm aperture in a buffer chamber. The molecular beam was finally introduced into the main chamber equipped with an electron imaging apparatus, and crossed perpendicularly with an ionization laser beam 400 mm downstream from the nozzle. The buffer chamber, evacuated by a 200 L/sec turbomolecular pump, serves to prevent effusion of a gas from the source into the main chamber, thus eliminating background noise upon multiphoton ionization. When the pulsed valve was operated, the typical pressure in the main chamber was ca. 10^{-8} Torr as maintained by a 500 L/sec turbomolecular pump. All turbomolecular pumps were backed by a 37 m^3/h oil-free scroll pump.

The excitation and ionization laser beam was the second harmonic of the output of a Nd:YAG-pumped dye laser. State-selective ionization of CO molecules was performed by one-color (2+1) REMPI *via* the v' = 0 and 1 levels of the $B^1\Sigma^+$ state at 230.106 nm (v'= 0 ← v''=0) and 224.713 nm (v'=1 ← v''=0). The laser beam was focused with a quartz lens (f=500 mm). The typical laser power was 30 μJ/pulse at 230 nm and 70 μJ/pulse at 225 nm. The laser polarization was aligned parallel to the face of an imaging detector.

A two-color pump-probe experiment was also performed with a femtosecond laser system [25,26]. The output of a diode-pumped Ti:Sapphire laser was amplified by a Nd:YLF pumped regenerative amplifier to generate a 1 kHz pulse train centered at 802 nm. This light was split into two equal intensity beams to pump two commercial optical parametric amplifiers (OPAs) to generate tunable UV light. The pump pulse at 230 nm was generated by sum-frequency generation in a BBO crystal, using the fundamental light from the regenerative amplifier and the UV light at 322.5 nm from the OPA. Tunable probe pulses were provided by

the output of another OPA, with its wavelength range between 240 and 375 nm. The cross correlation between the pump and probe beams was *ca.* 200 fs. The pump and probe pulses were focused by quartz lenses with focal lengths of 450 mm (pump) and 500 mm (probe), respectively. The typical pulse energies were less than 1 μJ/pulse for both pump and probe pulses.

Photoelectrons produced by the ionization laser were accelerated up to a kinetic energy of ~ 2 keV in an electric field parallel to the molecular beam and projected onto a position-sensitive imaging detector. The electric field formed an immersion lens that focuses the electrons spatially such that the image only reflects the electron momentum parallel to the detector face. The field-free region (40 cm) was shielded with a μ-metal tube to avoid an external magnetic field that might otherwise deflect the electron trajectories. The imaging detector consisted of a dual microchannel plate backed by a phosphor screen (77 mm in effective diameter), and an intensified video-rate charge-coupled device (ICCD) camera (572 x 768 pixels). The photoelectron image on the phosphor screen is captured by the camera and integrated for 45,000 laser shots. The observed electron images were transformed back to the 3D photoelectron scattering distributions by inverse Abel transformation.

The electron optics provided an immersion lens effect, and its magnification factor was calibrated using the ionization energy of CO^+ ($X^2\Sigma^+$, v^+=0) ← CO ($X^1\Sigma^+$, v"=0), 14.01363 eV [17]. The speed resolution Δv was limited by the resolution of our imaging system, so the energy resolution ΔE=mvΔv degraded proportional to v or $\sqrt{E}$. The kinetic energy resolution ΔE in the present work was about 140 meV at 2.15 eV and 30 meV at 0.09 eV.

We have performed identical measurements for different sample gas mixtures of neat CO and 5% and 1% CO diluted in He. All of these yielded the same results, suggesting that the effect of the CO dimer, if any, is negligible in our experiments. All the results discussed in the present paper are for the 1% sample gas.

6.3. Analysis

The observed photoelectron images are two-dimensional (2D) projections of three-dimensional (3D) scattering distributions. The original 3D distributions were reconstructed from the 2D projections by inverse Abel transforms, using the fact that the electron distributions are cylindrically symmetric around the electric vector of the linearly

polarized light when pump and probe laser polarization are aligned parallel to each other. The transform inherently requires that the 2D projection is symmetric between the left- and right-hand sides of the symmetry axis, while observed images exhibited slight asymmetry due to non-uniform detection sensitivity of the apparatus. Therefore, observed images were symmetrized prior to the transform. As we discussed previously, it is quite important to evaluate possible errors arising from asymmetry of images [27,28]. As a standard procedure to examine these errors, we have taken the four quadrants of a photoelectron image and analyzed them independently. For example, four raw images obtained for the $v'= 0 \leftarrow v''=0$ transition were converted to sixteen symmetrized images.

The images were carefully examined for different experimental conditions such as different voltages for the acceleration electrodes, different voltages for the phosphor screen, and different focusing of the camera lens. The analysis was also performed assuming slightly different aspect ratios and different positions of the image center. Thus, we ascertained that the possible error is mainly from the asymmetry of photoelectron images.

The photoelectron angular distributions (PADs) reflect the detailed photoionization dynamics. The PAD is a measure of the flux of outgoing photoelectrons, $I(\theta)$, as a function of the angle θ between the laser polarization direction and the direction of the electron k-vector. Its general form in (2+1) and (2+1') REMPI is given by [29,30]:

$$I(\theta) \sim 1 + \beta_2 P_2(\cos\theta) + \beta_4 P_4(\cos\theta) + \beta_6 P_6(\cos\theta). \qquad (1)$$

In this expression, $P_n(\cos\theta)$ are the Legendre polynomials of degree n, and β_n are the weighting coefficients. From sixteen images in one data set, the standard deviations 1σ for the fitting parameters β_n were determined.

6.4. Results

6.4.1. One-color (2+1) REMPI

Figure 6-1 shows the raw photoelectron images observed by (2+1) REMPI of the CO molecule *via* (a) the v'=0 and (b) the v'=1 levels in the $B^1\Sigma^+$ state. These two images exhibit drastic differences, *i.e.* the image observed *via* v'=0 consists of a number of sharp rings, while only a single intense ring is seen in the image *via* v'=1. These rings correspond to final vibrational states of the CO cation upon ionization. Further smaller splittings due to rotational structure are beyond our instrumental resolution.

The photoelectron kinetic energy distributions were obtained by integrating the angular part of the 3D photoelectron scattering distributions reconstructed by inverse Abel transforms. The result for the v'=0 case is shown in Fig. 6-2(a). An intense peak was observed at 2.15 eV and was assigned to the v^+=0 ← v'=0 transition. In addition to this Δv=0 transition, seven weaker peaks with spacings of ~0.25 eV were observed between 0 and 2 eV. These were assigned to the v^+=1-8 ← v'=0 transitions. The intensity of the transition to v^+=8 shows a sudden increase. The photoelectron kinetic energies and their assignments are listed in Table I. The vibrational branching ratios estimated from the peak areas are compared in Fig. 6-2(b) with those reported by Sha *et al*. [19]. They have determined the branching ratios up to v^+=4 using a time-of-flight (TOF) photoelectron spectrometer. Note that a TOF spectrometer has a limited electron acceptance angle, hence the vibrational branching ratios were determined after considering photoelectron angular distributions for each vibrational channel separately. This procedure is notoriously difficult for the particular case of CO, since the angular distributions vary significantly with the final vibrational states as described later. Considering such difficulties, overall agreement between the two independent measurements is remarkably good. It is also noted that the enhanced intensity for the v^+=8 is observed for the first time in the present work. This observation gives important clues about the mechanisms underlying the ionization dynamics, as discussed below.

The photoelectron angular distributions (PADs) for each ionization channel v^+=0-8 ← v'=0 were extracted from the inverse Abel-transformed image and plotted in Fig. 6-3. The PAD for v^+=0 is simple, whereas other PADs for v^+?0 are complicated and strongly state-dependent. The solid lines are the least-squares fits of the function expanded up to the 6th order Legendre polynomial. The obtained β_n values for each PAD are listed in Table I.

Similarly, Fig. 6-4 and 6-5 show the energy and angular distributions of photoelectrons upon ionization *via* v'=1. As was already clear from the raw image, this channel is dominated by the Δv=0 transition at 2.28 eV. A tiny peak due to the v^+=0 ← v'=1 transition is seen in Fig. 6-4. This channel exhibits a clearly different angular distribution from that of the Δv=0 channel as shown in Fig. 6-5.

6.4.2. Two-color (2+1') REMPI

The $B^1\Sigma^+$ state of CO is a Rydberg state for which the Δv=0 propensity rule is expected to hold upon ionization. Therefore, the anomalous vibrational activity upon ionization in the

v^+=0-8 ← v'=0 transition suggests the presence of a resonance with a superexcited state embedded in the ionization continuum.

In order to examine whether such resonances occur at other wavelengths, we have performed two-color (2+1') REMPI-PES experiments. We employed a femtosecond laser system as a light source. The results reported here were measured at zero time delay between the pump and probe laser pulses. The photoelectron kinetic energy distributions obtained for eight different probe (ionization) wavelengths are presented in Fig. 6-6. In all these cases, the pump wavelength was in resonance with the v'=0 level in the $B^1\Sigma^+$ state. Each photoelectron kinetic energy distribution showed only a single peak corresponding to the Δv=0 transition, except the one for the 230 nm probe (one-color experiment with a femtosecond laser), indicating that ionization at wavelengths longer than 230 nm is essentially diagonal. The results confirm that the observed off-diagonal ionization occurs in a particular ionization wavelength range. Ideally, one should vary the ionization wavelength continuously to explore the energy width of the resonant state or states. However, such extensive measurements are yet to be performed.

6.5. Discussion

6.5.1. Angular anisotropy

The absolute values of the anisotropy parameters are different from those reported by Sha *et al.* [19]. However, the overall agreement between the two experiments is reasonably good. Since the $B^1\Sigma^+$ state of CO is the 3sσ Rydberg state, the outgoing photoelectron wave on one-photon ionization is expected to be predominantly of *p*-character. Then, the anisotropy parameter β_2 is expected to be close to its limiting value 2. The observed β_2 parameters of 1.42 and 1.59 for the Δv=0 ionization channel *via* v'=0 and 1, respectively, are noticeably lower than the limiting value, indicating that such an atomic picture of ionization does not apply for this molecular Rydberg state. From our two-color experiments, we also found that the β_2 parameter varies with ionization wavelength, but is always considerably smaller than 2, indicating that the relatively small β value is a general feature in ionization from the B state. Rijs *et al.* [5] have reported that the 3sσ orbital of the B state possesses 74% *s*, 24% *p* and 2% *d* character. They calculated electric dipole matrix elements for ionization with an excess energy of 2.15 eV and obtained considerable *s* and *d* partial wave components in the outgoing

photoelectron waves. The observed β value considerably smaller than 2 is qualitatively consistent with their calculations [5]. The small difference between the β_2 parameters 1.42 and 1.59 for ionizations $v^+=0 \leftarrow v'=0$ and $v^+=1 \leftarrow v'=1$ is larger than our experimental uncertainty. However, its origin is unclear.

The angular anisotropies in the off-diagonal channels were quite small, but they were measurable. Interestingly, the $v^+=6$ channel *via* the B(v'=0) state shows a small negative β_2 parameter, indicating that electrons are ejected perpendicular to the electric vector of the laser light. This clearly indicates that the reduction of the anisotropy parameter is not due to molecular rotation prior to ionization: molecular rotation reduces the alignment of photoexcited molecule and consequently the anisotropy of photoelectron angular distribution; however, it would not reverse the sign of the β value. Large fluctuations in the angular anisotropy parameters for different ionization channels indicate that the partial wave composition of photoelectrons varies strongly for different vibrational channels.

6.5.2. Vibrational branching

The non-Franck-Condon intensity distribution upon ionization from the $B^1\Sigma^+$ state to the $X^2\Sigma^+$ ground state are clearly due to autoionization from superexcited states. When autoionization is induced by electronic or rotational perturbations, the vibrational part of the transition matrix element is proportional to

$$\left|\langle f|m\rangle\right|^2 \qquad \text{(electronic and rotational)} \qquad (2)$$

whereas when autoionization is induced by vibrational perturbations it is proportional to

$$\left|\left\langle f\left|\frac{\partial}{\partial R}\right|m\right\rangle\right|^2 \qquad \text{(vibrational).} \qquad (3)$$

The labels m and f represent the vibrational quantum numbers in the superexcited state and in the cation. A vibrationally excited Rydberg state with a $X^2\Sigma^+$ ion core does not explain a long progression, because of the propensity rule of Δv=-1 in vibrational autoionization.

A striking feature of the observed vibrational intensity distribution in (2+1) REMPI *via* the v'=0 level is that the $v^+=8$ peak is particularly intense. It is highly likely that this peak is produced by vibrational autoionization from a Rydberg state with a $X^2\Sigma^+$ ion core ($v^+ = 9$). However, direct one-photon excitation from the B state to these highly vibrationally excited Rydberg states is almost completely forbidden, due to pseudo orthogonality of the vibrational

wavefunctions associated with $B^1\Sigma^+$ and $X^2\Sigma^+$. In addition, if such Rydberg states with an $X^2\Sigma^+$ ion core are produced by direct excitation from the $B^1\Sigma^+$ state, it should occur at various excitation wavelengths. However, non-Franck-Condon behavior seems to occur in a restricted wavelength range only. These facts suggest that the Rydberg states with an $X^2\Sigma^+$ ion core (v^+ = 9) are produced indirectly by electronic dephasing from another superexcited state reached by a one-photon transition from the B state. Similarly, strong and very narrow peaks at near-zero electron kinetic energies have been observed in experiments on NO [31] and N_2O [32].

Another reason that we need to invoke a superexcited state other than a Rydberg state with a $X^2\Sigma^+$ ion core is that vibrational autoionization only explains an enhanced peak at v^+=8, but not a long progression from v^+=1-7. A long progression must originate from a superexcited state with a significantly different geometry from that of the $X^2\Sigma^+$ state.

When only a one-photon induced one-electron excitation process is considered, the superexcited state is speculated to be the 3s member of a Rydberg series converging to the $A^2\Pi$ state of CO^+. However, if this is the case, the vibrational quantum number must be very high. The vibronic energy of Rydberg states converging to the $A^2\Pi$ state is generally described by

$$E = T_A - R_\infty / (n - \delta)^2 + \omega_0 v - \omega_0\chi_0 v^2 \qquad (4)$$

In this expression, T_A is the ionization energy to the $A^2\Pi$ state, R_∞ is the Rydberg constant, n is the principal quantum number, δ is the quantum defect, and ω_0 and $\omega_0\chi_0$ are the harmonic and anharmonic vibrational constants. By substituting spectroscopic values into this expression, the vibronic energies of the Rydberg states converging to the $A^2\Pi$ ionic state can be estimated. Since the electronic origin of the 3s Rydberg state with a $A^2\Pi$ ion core is located below the lowest ionization energy (IE), the vibrationally excited level of the 3s(π^{-1}) state nearest to the three-photon energy is the v=18 state. The Franck-Condon factor of the transition from the v'=0 level in the $B^1\Sigma^+$ state to this v=18 state is extremely small.

As alternative possibilities, one-photon induced two-electron excitation to a repulsive neutral state or other members of Rydberg series converging to the $A^2\Pi$ ion core should also be considered. Although such transitions will have very small cross sections by one-photon absorption, configuration interactions will allow them to some degree. Excitation to a Rydberg state with an $A^2\Pi$ ion core followed by autoionization into the $X^2\Sigma^+$ ionic continuum is not likely to produce an observed intensity distribution: our Franck-Condon calculations

predicted the vibrational progression extending up to v^+=8. However, they do not show a gradually declining intensity distribution from v^+=1 towards higher quantum numbers, but instead show intensities, that oscillate appreciably with vibrational quantum number v^+. On the other hand, excitation to a neutral dissociative state with a steep repulsive curve above the lowest ionization threshold is known to be capable of producing long vibrational progressions over a wide energy range [33]. From the observed vibrational intensity distribution, it seems therefore likely that such a dissociative neutral state is providing the long vibrational progression.

6.5.3. Possible superexcited state(s)

It is noted that photoexcitation to a repulsive potential normally provides a photoabsorption spectrum over a rather broad range of excitation energies. This seems to contradict the fact that when the ionization wavelength is detuned, both the irregular behavior of the angular anisotropies and the unexpected vibrational branching ratios disappear. Although the range of ionization wavelengths we have examined at this point is rather limited, the results suggest that this effect is local in energy. Rijs *et al.* [5] have observed one-color (2+1) REMPI-PES of rotationally excited CO molecules produced in the photodissociation of OCS, and they found that the non-Franck-Condon vibrational progression persisted up to the N'=36 level, but no longer existed at N'=48. Let us examine this observation from the viewpoint of energetics. The energy gap for the B-X transition of CO is T+(B'-B")N"(N"+1) for a Q branch. T is the vibronic term value of the $B^1\Sigma^+$ state. This energy gap equals the two-photon energy. Likewise, the energy gap for the transition from the B state to a superexcited state is T*-T+(B*-B')N"(N"+1) for a Q branch. T* is the vibronic term value of a superexcited state. Note that the ionization step is a one-photon process, so the three-photon energy continuously moves away from the resonance condition for increasing values of N". The detuning of the three-photon energy from the superexcited state is calculated as

$$\mathrm{D}\boldsymbol{E}(\boldsymbol{N}) - \mathrm{D}\boldsymbol{E}(\mathbf{0}) = \frac{\boldsymbol{N}''(\boldsymbol{N}''+\mathbf{1})}{\mathbf{2}}\left(\mathbf{2}\boldsymbol{B}^* - \mathbf{3}\boldsymbol{B}' + \boldsymbol{B}''\right) \qquad (5)$$

for a Q branch transition. This quantity depends on the unknown value of B*. If we take the proposal by Rijs *et al.*, B* is ~ 1.58 cm^{-1} for a Rydberg state with $A^2\Pi$ ion core, the above quantity is -507 cm^{-1} for N"=36. This indicates that the intrinsic line width of the superexcited Rydberg state(s) with the $A^2\Pi$ ion core is at least 510 cm^{-1}. This shows that if the superexcited state(s) are reached by a direct three-photon absorption process from the ground state, the

lifetime is quite short. The line width associated with a direct excitation to a purely repulsive and therefore very short-lived state is expected to be even larger. The fact that the resonance disappears at N'=48 seems to contradict the latter picture.

It appears that in addition to superexcited state(s) reached by three-photon transitions from the ground electronic state a dissociative state, either accessed through direct photoexcitation or through coupling with a superexcited state that carries oscillator strength from the neutral B state, should play a key role. As to the former, it is likely that one or more superexcited Rydberg states with $A^2\Pi$ ion core are likely candidates. The energy levels of the Rydberg series converging to the $A^2\Pi$ state of the CO cation, which have been reported by Ogawa *et al*. [34], are summarized in Fig. 6-7. Leyh *et al*. have provided more detailed assignments of these states [35]. Due to the selection rules for one-photon optical transitions, the overall symmetry of the superexcited states must be either $^1\Sigma^+$ or $^1\Pi$. Therefore, if the ion core is $A^2\Pi$, the Rydberg electron must have a projection of its orbital angular momentum on to the molecular axis of = 2. Rijs *et al.* [5] have speculated that the resonance states encountered in the one-color (2+1) REMPI-PES *via* the B state are the 5'd' δ (v=1) and '5s+4d' σ (v=3) members. These resonance states correspond to the m=5 and m=4 states, respectively, in Fig. 6-7. Starting from the $B^1\Sigma^+$ state, it would require a one-photon two-electron process to make the simultaneous transitions from ground to excited state core ($A^2\Pi \leftarrow X^2\Sigma^+$) and for the Rydberg electron (nsσ, ndσ, or nd$\delta \leftarrow$3sσ). Perhaps the small amount of *p*-character of the 3sσ molecular orbital could play a role here.

With the limited information available, it is difficult to unambiguously elucidate the complex ionization mechanism. Clearly, the observed intense v^+=0 peak is predominantly due to the direct ionization process into the $X^2\Sigma^+$ continua. In order to explain the observed long vibrational progression, it is conceivable that initial photoexcitation leads to a neutral bound state, most likely a Rydberg state with an $A^2\Pi$ ion core that is strongly coupled to a neutral dissociative state. In the course of the dissociation process, autoionization through electronic coupling produces the v^+=0-8 levels of $X^2\Sigma^+$. In addition to this process of electronic autoionization, electronic coupling with this dissociative state also produces approximately iso-energetic vibrationally excited (v'~9) superexcited Rydberg states with an $X^2\Sigma^+$ ion core. These states subsequently undergo vibrational autoionization. This process, with Δv = -1 propensity, produces an enhanced ionization peak at v^+=8. We note that the observation of the

enhanced v^+=9 peak in our experiment *via* $B^1\Sigma^+$ (v'=1) (see Fig. 6-4) is qualitatively in line with the present picture.

Presumably, the channels leading to v^+=1-8 have multiple indirect ionization pathways that can interfere with each other in a complex fashion. This would cause large variations in the angular distributions of photoelectrons as a function of vibrational quantum number v^+. A further investigation of this process would require studies on the isotopomers of CO and observation of neutral photofragments.

6.6. Conclusions

Photoelectron imaging methods were employed in (2+1) and (2+1') REMPI-PES studies of the CO molecule *via* the intermediate $B^1\Sigma^+$ (v'=0, 1) state to the $X^2\Sigma^+$ (v^+) ionic ground state. For one-color (2+1) REMPI-PES *via* $B^1\Sigma^+$ (v'=0), large deviations from the expected Franck-Condon Δv=0 propensity rule were observed in the photoelectron spectrum which showed v^+=0-8 ← v'=0 transitions. A puzzling feature of these experiments was the unusually strong intensity for the v^+=8 ← v'=0 transition. The PADs exhibited strong state-dependence: the PAD for the transition to v^+=0 was simple and anisotropic, whereas those for transitions to v^+=1-8 were complicated and nearly isotropic. For (2+1) REMPI-PES *via* $B^1\Sigma^+$ (v'=1), on the other hand, the Δv=0 transition dominated the photoelectron spectrum. Two-color (2+1') REMPI-PES experiments were also performed, and revealed that only Δv=0 transitions were observed for all probe wavelengths. These observations suggest a competition between direct ionization into the $X^2\Sigma^+$ (v^+) continua, and accidental resonance with and subsequent autoionization from a superexcited Rydberg state with $A^2\Pi$ ionic core. The results are consistent with a picture in which a dissociative state is invoked to couple Rydberg states with $A^2\Pi$ ionic core to Rydberg states with $X^2\Sigma^+$ ion core. Finally, an important feature of the present study is that photoelectron imaging experiments appear to be very suitable for extracting information about superexcited states through their wavelength dependence and state-dependent PADs.

References

[1] T.E. Graedel, P.J. Crutzen, "Atmospheric Change: An Earth System Perspective" (Freeman, 1993).

[2] R.P. Wayne, "Chemistry of Atmospheres" (Oxford University Press, 1993).

[3] K.P. Huber and G. Herzberg, "Molecular Spectra and Molecular Structure, Vol. IV. Constants of Diatomic Molecules" (Van Nostrand-Reinhold, 1979).

[4] M. Eidelsberg, J.-Y. Roncin, A. Le Floch, F. Launay, C. Letzelter, and J. Rostas, J. Mol. Spectrosc. **121**, 309 (1987).

[5] A.M. Rijs, E.H.G. Backus, C.A. de Lange, M.H.M. Janssen, N.P.C. Westwood, Kwanghsi Wang, and V. McKoy, J. Chem. Phys. **116,** 2776 (2002).

[6] J.L. Gardner and J.A.R. Samson, J. Chem. Phys. **60**, 3711 (1973).

[7] J.L. Gardner and J.A.R. Samson, J. Electron Spectrosc. Relat. Phenom. **13**, 7 (1978).

[8] B. Wannberg, D. Nordfors, K.L. Tan, L. Karlsson, and L. Mattson, J. Electron Spectrosc. Relat. Phenom. **47**, 147 (1988).

[9] K. Norwood, J.-H. Guo, G. Luo, and C.Y. Ng, Chem. Phys. **129**, 109 (1989).

[10] K. Norwood, J.-H. Guo, G. Luo, and C.Y. Ng, Chem. Phys. **90**, 6026 (1989).

[11] S.T. Pratt, E.D. Poliakoff, P.M. Dehmer, and J.L. Dehmer, J. Chem. Phys. **78**, 65 (1983).

[12] S.T. Pratt, P.M. Dehmer, and J.L. Dehmer, J. Chem. Phys. **79**, 3234 (1983).

[13] M.A. Hines, H.A. Michelsen, and R.N. Zare, J. Chem. Phys. **93**, 8557 (1990).

[14] S.R. Mackenzie, E.J. Halse, E. Gordon, D. Rolland, and T.P. Softley, Chem. Phys. **209**, 127 (1996).

[15] W. Kong, D. Rodgers, J.W. Hepburn, Kwanghsi Wang, and V. McKoy, J. Chem. Phys. **99**, 3159 (1993).

[16] W. Kong and J.W. Hepburn, J. Phys. Chem. **99**, 1637 (1995).

[17] A. Mellinger, C.R. Vidal, and Ch. Jungen, J. Chem. Phys. **104**, 8913 (1996).

[18] M. Evans and C.Y. Ng, J. Chem. Phys. **111**, 8879 (1999).

[19] G. Sha, D. Proch, Ch. Rose, and K.L. Kompa, J. Chem. Phys. **99**, 4334 (1993).

[20] S.G. Tilford and J.T. Vanderslice, J. Mol. Spectrosc. **26**, 419 (1968).

[21] C.A. de Lange, J. Chem. Soc., Faraday Trans. **94**, 3409 (1998).

[22] C.A. de Lange, in: “The Role of Rydberg States in Spectroscopy and Reactivity”, edited by C. Sandorfy (Kluwer Academic Publishers, 1999; p. 457).

[23] C.A. de Lange, Int. Rev. Phys. Chem. **20**, 1 (2001).

[24] C.A. de Lange, Adv. Chem. Phys. **117**, 1 (2001).

[25] M. Tsubouchi, B. Whitaker, L. Wang, H. Kohguchi, and T. Suzuki, Phys. Rev. Lett. **86**, 4500 (2001).

[26] J. K. Song, M. Tsubouchi, and T. Suzuki, J. Chem. Phys. **115**, 8810 (2001).

[27] K. Tonokura, L. B. Daniels, T. Suzuki, and K. Yamashita, J. Phys. Chem. A **101**, 7754 (1997).

[28] T. Suzuki, H. Katayanagi, S. Nanbu, and M. Aoyagi, J. Chem. Phys. **109**, 5778 (1998).

[29] C. N. Yang, Phys. Rev. **74**, 764 (1948).

[30] T. Suzuki and B. J. Whitaker, Int. Rev. Phys. Chem. **20**, 313 (2001).

[31] J. Kimman, P. Kruit, and M.J. van der Wiel, Chem. Phys. Lett. **88**, 576 (1982).

[32] P. M. Guyon, T. Baer, and I. Nenner, J. Chem. Phys. **78**, 3665 (1983).

[33] W. Kong and J.W. Hepburn, Can. J. Phys. **72**, 1284 (1994)

[34] M. Ogawa and S. Ogawa, J. Mol. Spectrosc. **41**, 393 (1972).

[35] B. Leyh, J. Delwiche, M.-J. Hubin-Franskin, and I. Nenner, Chem. Phys. **115**, 243 (1987).

Figures and tables for Chapter 6

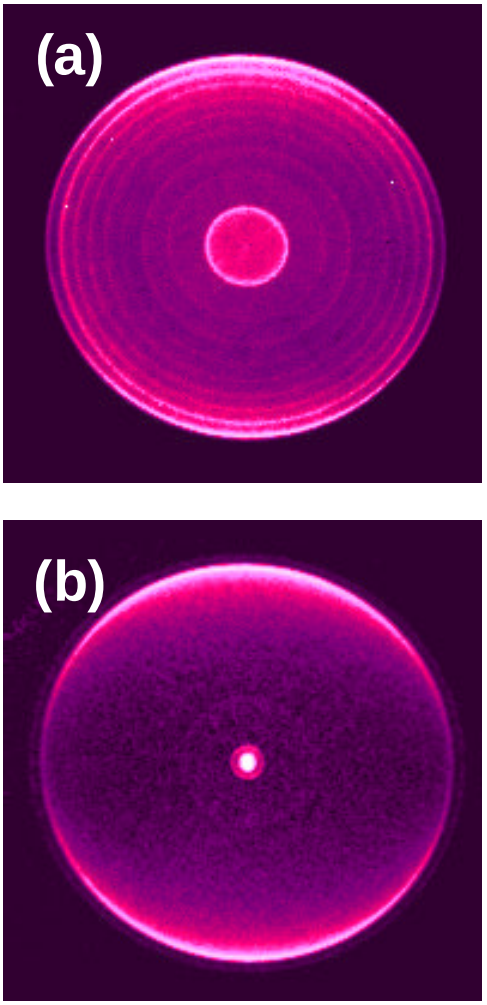

Fig. 6-1
The 2D photoelectron images observed by one-color (2+1) REMPI of CO *via* (a) the *v*'=0 and (b) the *v*'=1 levels in the B^1S^+ state. The ionization laser polarization is aligned vertically in the figure. The ionization laser wavelengths are tuned to 230.106 nm for the *v*'= 0 ← *v*"=0 transition and to 224.713 nm for the *v*'= 1 ← *v*"=0 transition, respectively.

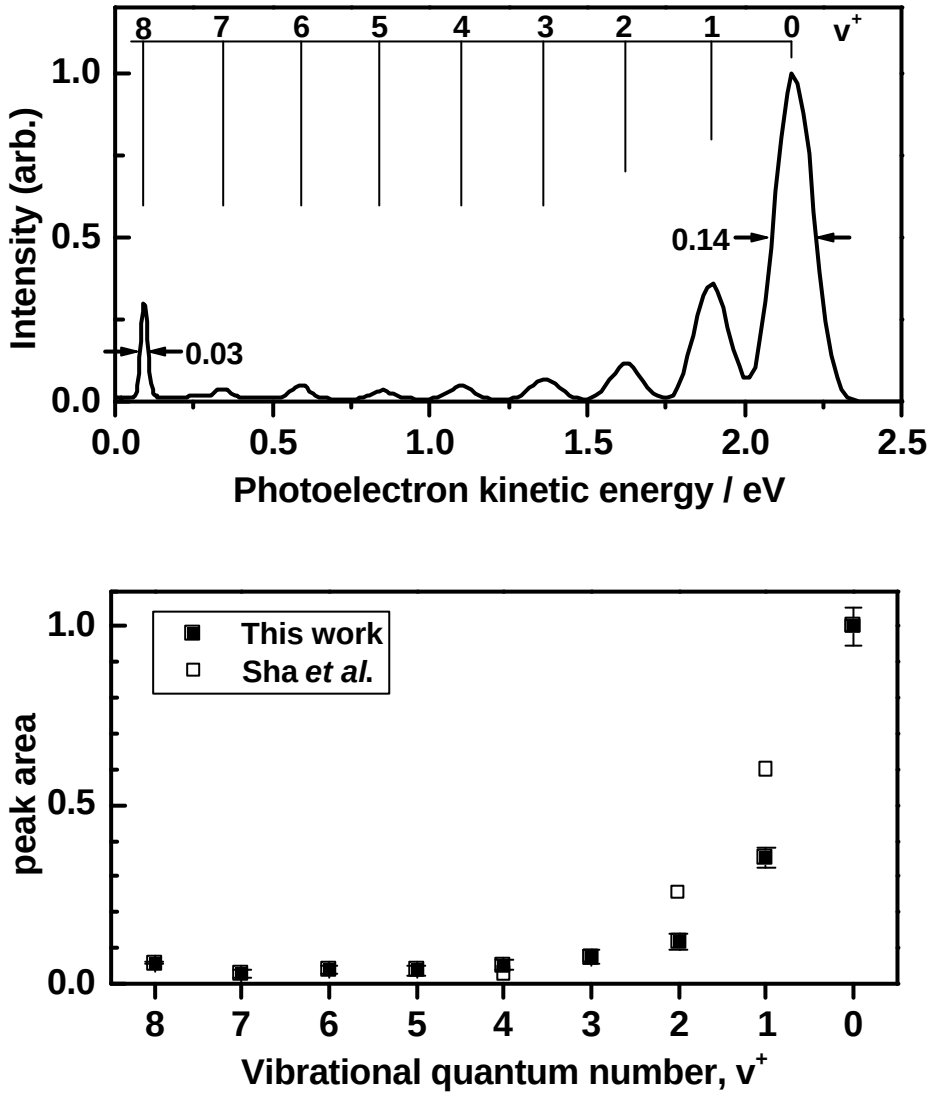

Fig. 6-2
(a) The photoelectron kinetic energy distributions in (2+1) REMPI of CO *via* the $B^1\Sigma^+$ (v'=0) state, obtained by integrating the angular part of the 2D section. (b) The vibrational branching ratios estimated from the areas of each peak. For comparison the results reported by Sha *et al*. [19] are shown as open squares.

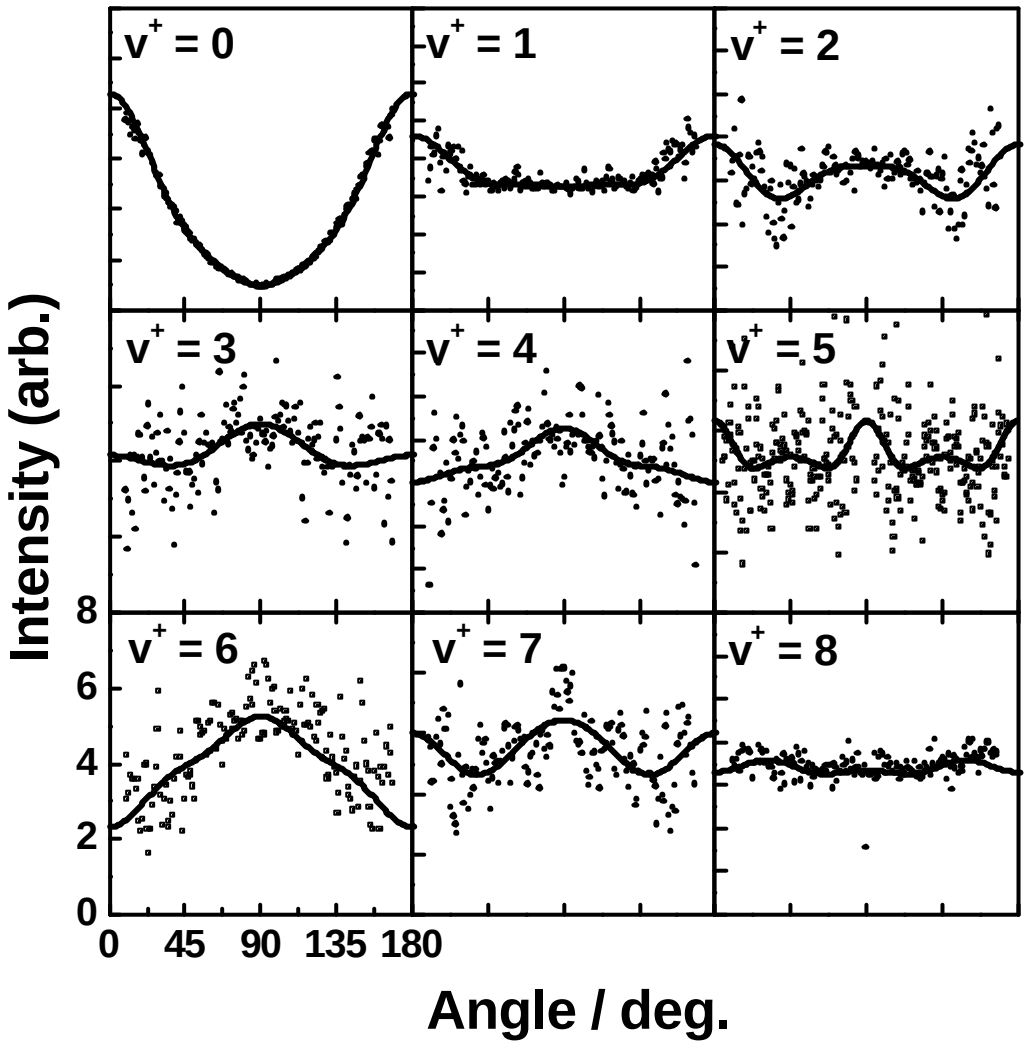

Fig. 6-3
The photoelectron angular distributions (PADs) for each v^+ channel upon ionization from the $B^1\Sigma^+(v'=0)$ state, which were extracted from the inverse Abel-transformed images. The solid lines are the least-square fits of the experimental angular distributions to an expression which includes Legendre polynomials up to 6th order.

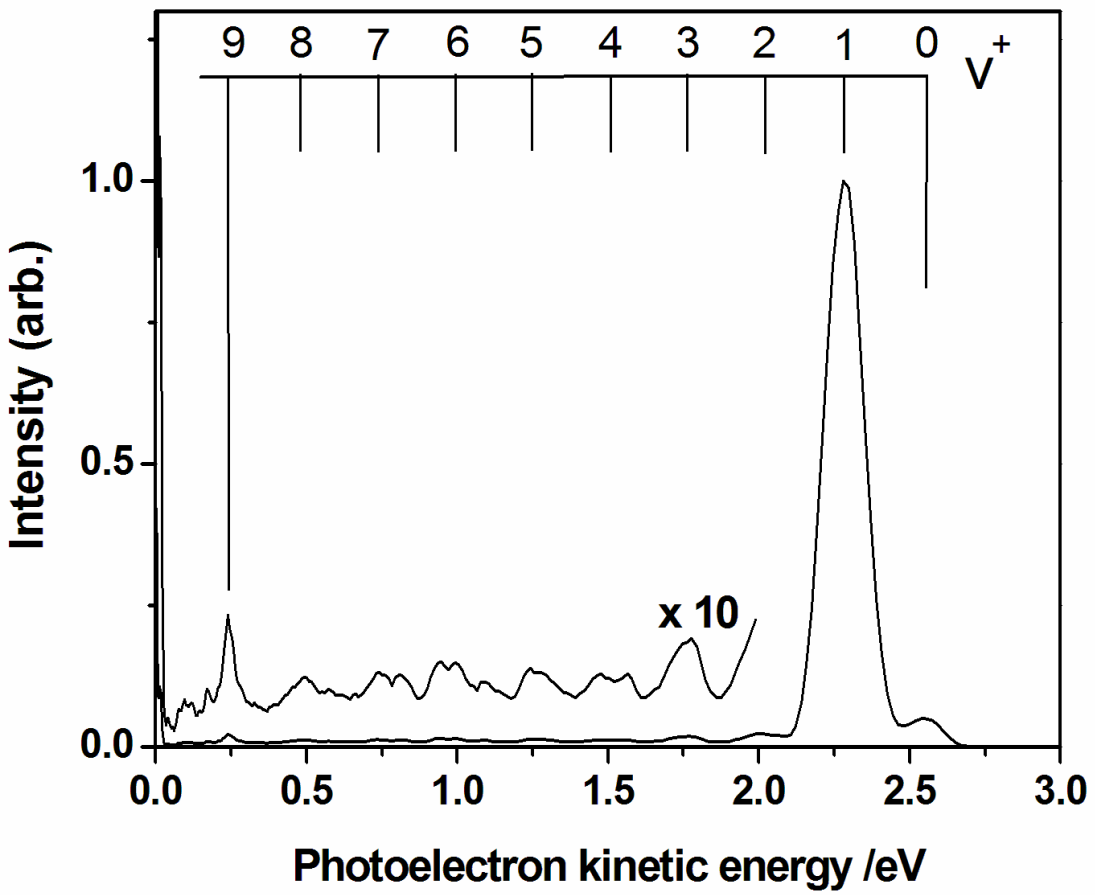

Fig. 6-4
The photoelectron kinetic energy distributions in one-color (2+1) REMPI of CO *via* the $B^1\Sigma^+$ (v'=1) state. The spectra obtained from repeated experiments in the low-energy region are ten times magnified and overlaid in the figure. These confirm a significant peak at 0.25 eV, whose position corresponds to v^+=9.

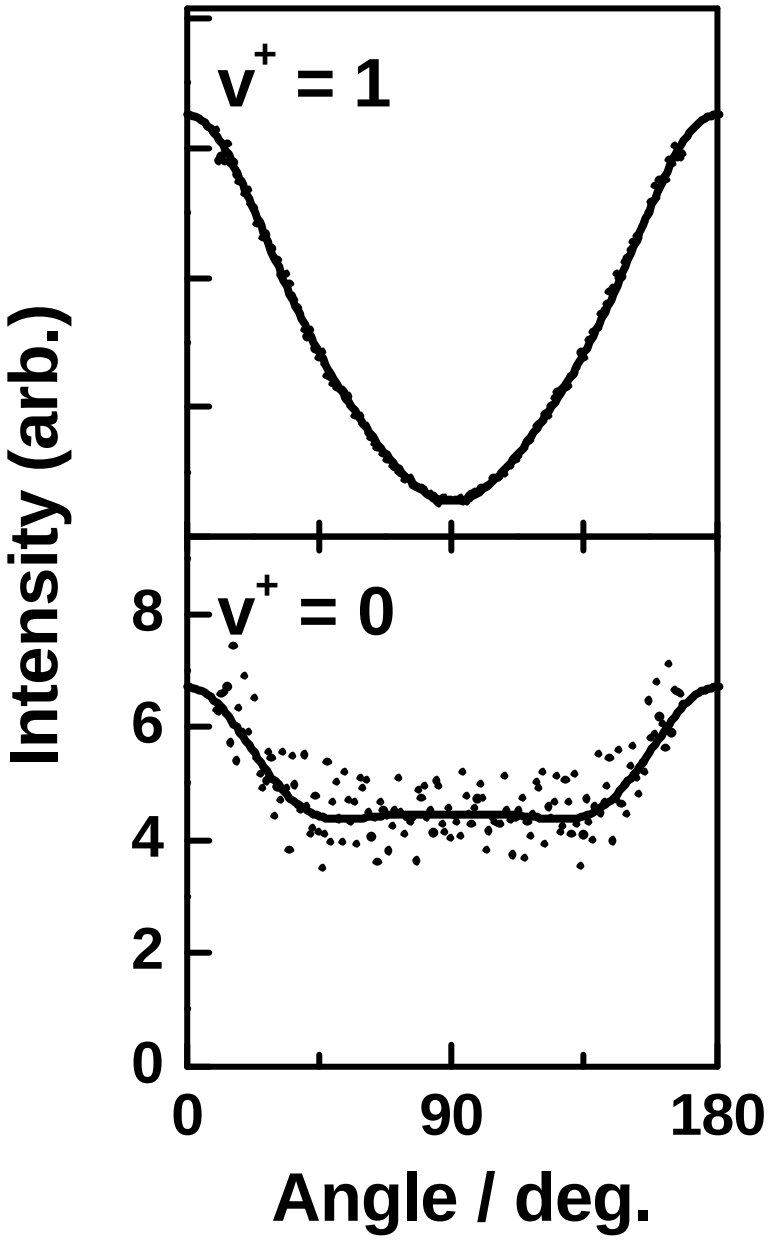

Fig. 6-5
The photoelectron angular distributions (PADs) for v^+=1 and 0 channels upon ionization *via* the $B^1\Sigma^+$ (v'=1) state. The solid lines represent the least-square fits of the experimental angular distributions to an expression which includes Legendre polynomials up to 6th order.

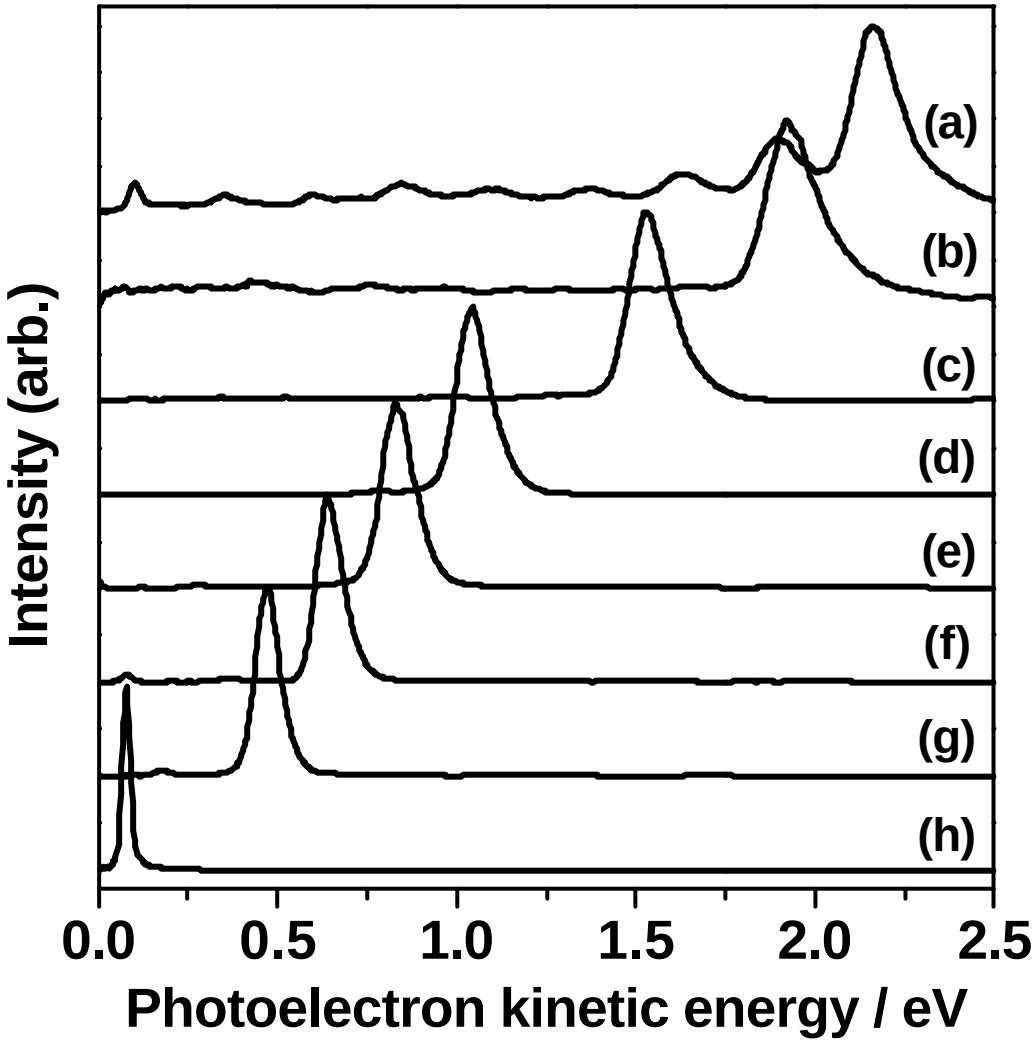

Fig. 6-6
Photoelectron kinetic energy distributions extracted from the two-color femtosecond (2+1') photoelectron images measured using a 230 nm pump pulse which is two-photon resonant with the origin band of the B ← X transition of CO, and employing a (a) 230 nm; (b) 240 nm; (c) 260 nm; (d) 290 nm; (e) 305 nm; (f) 320 nm; (g) 335 nm; and (h) 375 nm probe pulse. The pump-probe time delays are 0 ps in all the measurements. In each spectrum, the highest photoelectron energy corresponds to ionization to the lowest vibrational level of the CO^+ X $^2\Sigma^+$ state.

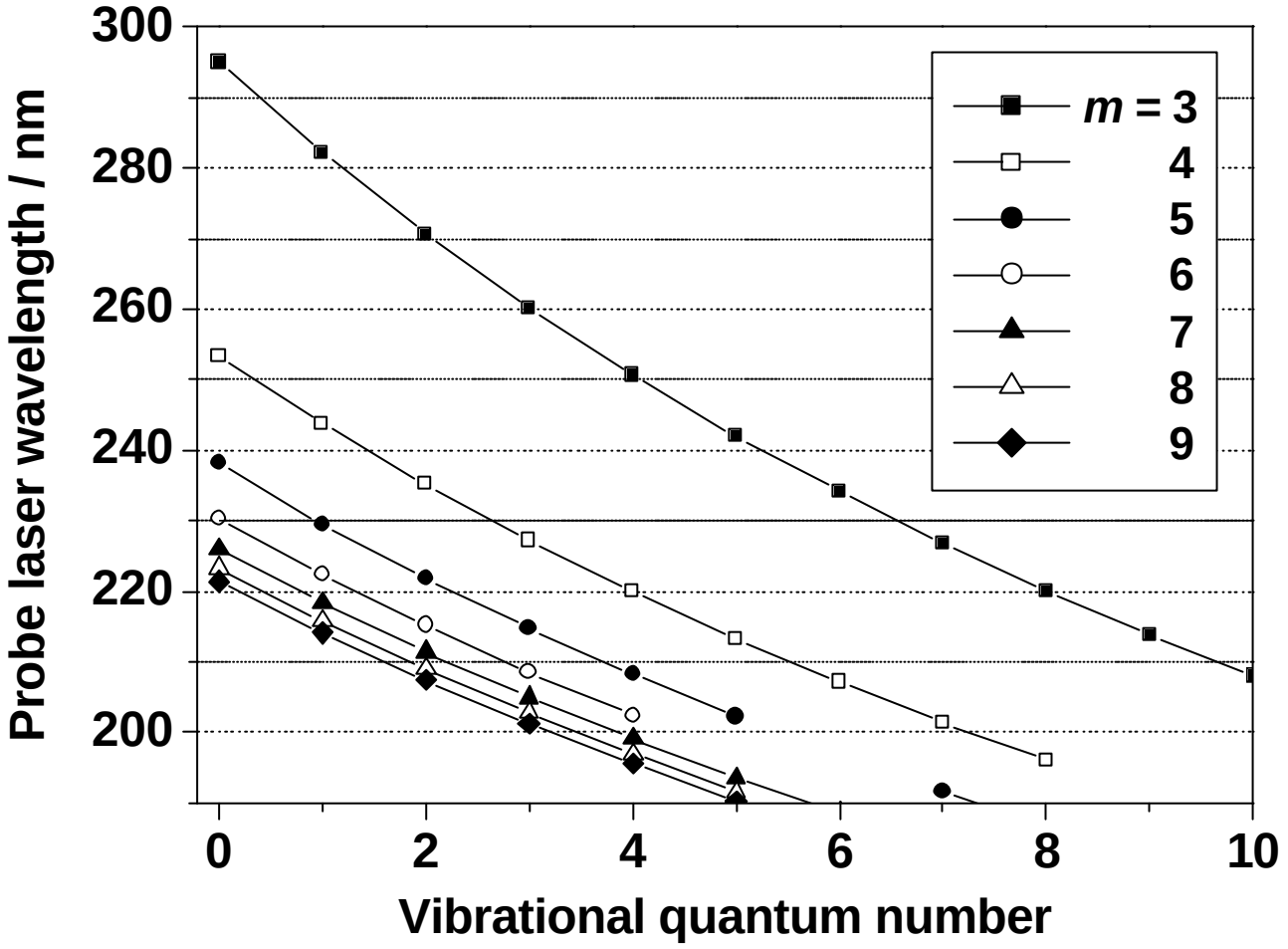

Fig. 6-7
Energy levels of various vibronic Rydberg states converging to the $A^2\Pi$ state of the CO cation. All data are taken from [34], in which the absorption spectrum of CO in the vacuum ultraviolet region, 69 – 88 nm, has been measured. Each energy level is plotted in order to correspond to the probe laser wavelength used in this work. Symbol *m* indicates the (*m*-1)*s* Rydberg state or the *md* Rydberg state.

Table 6-1

Photoelectron kinetic energies E, vibrational branching ratios R_v, and Legendre weighting coefficients of photoelectron angular distributions b_n of one-color (2+1) REMPI-PES of the CO molecule *via* $B^1\Sigma^+$ (v'=0 and 1).

v_i	Δv	E / eV	R_v	b_2	b_4	b_6
v'=0	0	2.150	1.000	1.42(20)	0.24(19)	0.03(14)
	1	1.891(8)	0.354(27)	0.30(28)	0.01(11)	0.03(12)
	2	1.622(7)	0.118(22)	0.06(20)	0.11(11)	0.13(09)
	3	1.361(5)	0.075(19)	-0.04(15)	0.04(20)	-0.01(13)
	4	1.097(5)	0.052(14)	-0.09(19)	0.06(13)	-0.01(13)
	5	0.845(6)	0.037(13)	0.15(17)	0.10(15)	0.08(26)
	6	0.590(8)	0.036(11)	-0.15(22)	0.15(21)	0.10(19)
	7	0.339(8)	0.028(09)	-0.12(22)	0.18(32)	-0.00(10)
	8	0.091(3)	0.057(04)	0.06(05)	0.04(09)	-0.01(05)
v'=1	-1	2.546(5)	0.040(09)	0.25(12)	0.27(12)	0.08(09)
	0	2.283(1)	1.000	1.59(03)	0.23(03)	0.17(03)

[a] Estimated standard deviations are indicated in parentheses.

Chapter 7

State correlations in the unimolecular dissociation of ketene [a]

[a] Published on *Journal of Physical Chemistry A* **104**, 10247-10258 (2000)

7.1. Introduction

The singlet dissociation channel of ketene has become a prototype for the study of barrierless unimolecular decomposition [1,2]. Continuous absorption in the near-ultraviolet, followed by rapid nonradiative conversion from the excited singlet to the ground state, makes it possible to prepare isolated molecules with a laser-selected energy at a well-defined time. This fortunate photophysics has permitted energy-dependent decomposition rates and product distributions to be measured for this particular reaction more conveniently than for most groundstate reactions. The extensive experimental investigations have encouraged similarly extensive theoretical work on this particular reaction, now one of the most completely characterized unimolecular reactions known. New experiments interrogating the correlated product state distribution, including the present work, build on this foundation, addressing old questions in new ways.

Following dipole-forbidden optical excitation from the $^1A_1$ ground state (S_0) to the $^1A_2$ excited state (S_1), ketene undergoes a radiationless transition to S_0, followed either by dissociation to CH_2 (a $^1A_1$) + CO (X $^1\Sigma^+$) or by intersystem crossing to the triplet and dissociation over a barrier to CH_2 (X $^3B_1$) + CO (X $^1\Sigma^+$). Recent ab initio calculations confirm this general picture of the nonadiabatic interactions and state couplings [3]. Rate constants for the singlet channel have been measured over a wide range of excess energies from threshold to 2500 cm^{-1} via both photofragment excitation (PHOFEX) spectroscopy near threshold [4,5] and picosecond spectroscopy of CH_2 at higher energies [6]. The rates near threshold are very well described by phase space theory (PST) [7,8]. At higher energies, the dissociation rate increases less rapidly than the PST prediction. The observed rates can be accounted for with a tightening transition state using variational RRKM theory [9.11]. At an energy 2500 cm^{-1} above the singlet threshold, PST overestimates the dissociation rate by about a factor of 10. Product state distributions of both CO [12-14] and CH_2 [15,16] have been measured using laser-induced fluorescence (LIF) as a function of excess energy. Early measurements of CO product rotational distributions [12,13] were in good agreement with PST at energies up to 2500 cm^{-1}, although the superposition of coincident singlet and triplet CH_2 channels led to some uncertainty in the interpretation. Subsequent measurements of CO (v = 1), where the triplet CH_2 contribution is negligible, showed subtle deviations from the PST rotational distributions, increasing at higher energy [14]. The singlet CH_2 state rotational distributions follow PST near threshold, but become much colder than the PST predictions at higher excess

energies [15,16]. The yields of vibrationa11y excited fragments, both CO (v = 1) [17] and the first bending excitation of CH_2 (n_1,n_2,n_3) = (0,1,0) are found to exceed PST predictions, an effect attributed to vibrational adiabaticity in the conserved modes and predicted by the separate statistical ensembles (SSE) model, [18] as well as variational RRKM, if the populations of the conserved modes at the transition state are assumed to be the same as those in the final products [9].

The global product distributions can be considered orthogonal projections of a two-dimensional coincident state distribution, as illustrated in Figure 1. The triangular region in the upper right square shows the correlated energy states of the singlet channel, with the diagonal boundary representing the available energy limit at 308 nm. Each black symbol represents a rotational state of CO (v = 0) with a coincident rotational level of CH_2 (0,0,0). An overlapping green set of symbols represents the possible states of the (0,1,0) bending excitation of CH_2 with its possible coincident CO states. A red cluster of symbols in the lower right of the triangle shows the possible pairs of states including CO (v = 1). At this energy, 35 rotational states of CO (v = 0) and 10 rotational states of CO (v = 1) combine with about 80 CH_2 (0,1,0) states and about 220 CH_2 (0,0,0) states to produce almost 6000 accessible coincident pair channels, each depicted by a symbol on this plot. This plot could be expanded to include the triplet CH_2 channel by adding the term value of singlet CH_2 (a) to the CH_2 internal energy scale shown on the vertical axis and moving the origin down to the zero point of the triplet CH_2 (X) state. It is evident that any CO state that can be produced in the singlet channel could, in principle, also be produced in coincidence with triplet CH_2.

The distribution of probability within this triangle provides a more revealing test of the fragmentation process than its projections onto the single-particle axes [19,20]. Phase space theory assigns the weight of each energetically accessible coincident channel to be proportional to the number of ways the two fragment angular momenta can couple with an orbital angular momentum, consistent with the total angular momentum of the parent molecule. (For the fragmentation of a low angular momentum parent molecule, the additional energetic constraint due to the centrifugal barrier is practically negligible.) The usual product state distributions are projections of the density of this two-dimensional grid onto the CO energy axis or the CH_2 energy axis, as shown in the plots below and to the side for a PST weighting of coincident states. Green symbols to the left and red symbols below respectively show the rotational populations of CH_2 (0,1,0) and CO (v = l). CO states with internal energies less than about 1000 cm^{-1} may have contributions from two vibrational channels of

coincident singlet CH_2. The green points in the CO distribution illustrate the partial contribution made by CO with vibrationally excited CH_2 partners to the total CO (v = 0) population, shown in black. Similarly, the red points in the CH_2 distribution indicate the partial contribution of CH_2 with vibrationally excited CO partners to the total CH_2 (0,0,0) population, shown in black. The 3 : 1 ratio of ortho : para nuclear spin modifications of the CH_2 fragments is suppressed for graphical simplicity in Figure 1 , in which only the ortho (nuclear spin = l) modifications of CH_2 states are plotted. One of the most striking deficiencies of PST for ketene dissociation at increasing energies is the strong deviation of experimental CH_2 state distributions from the PST prediction, whereas the CO distribution remains approximately statistical. The observed CH_2 rotational distributions were found to resemble Boltzmann distributions, [15,16] with an increasing effective temperature at higher available energies, approximately 700 K for CH_2 (0,0,0) at the 2333 cm^{-1} available energy of 308-nm excitation. The far left panel of Figure 1 illustrates the experimentally determined, Boltzmann-like distributions observed.

State-resolved velocity measurements such as Doppler spectroscopy, time-of-flight methods, or ion imaging provide ways of viewing slices rather than projections of the correlated state distributions [19]. Metastable CO time-of-flight methods have been developed and applied to the 308-nm dissociation of ketene by Wodtke and co-workers [21,22]. These experiments provide vertical slices through the correlated state distribution shown in Figure 1 at spectroscopically selected CO states. The present chapter reports the results of Doppler spectroscopy on the singlet CH_2 products, which relate to horizontal slices through the same correlated state distribution produced in the 308-nm dissociation of jet-cooled ketene. Although a complete set of correlated data for either fragment is, in principle, sufficient for reconstructing the full matrix of correlated states, the task is not trivial, and the new orthogonal view is advantageous for identifying qualitative agreements and quantitative differences with previous results. The way in which the dissociation distributes probability among the accessible channels, and in particular the shape of the deviations from the most random PST distribution, gives some insight into energy flow in the dissociating molecule beyond the transition state and the statistical nature of the transition state.

7.2. Experimental

Ketene was synthesized by the pyrolysis of acetic anhydride flowing past a hot filament. Unreacted acetic anhydride and water were removed from the flow in a dry-ice-cooled trap, and the ketene was collected in a liquid-nitrogen-cooled trap downstream. A 10% mixture of ketene in helium was expanded through a pulsed slit jet into a stainless steel chamber. The slit was 115 mm long and 50 μm wide, with a seal actuated by three synchronously driven solenoid-type pulsed valves (General Valve). The construction of the valve was based on the design of Hu *et al.* [23], similar to that described later by Liu *et al.* [24]. The chamber was mounted directly on a 400 ft^3 min^{-1} Roots blower / rotary pump combination. This provided sufficient pumping capacity to reduce the background pressure between valve firings to $\leqq 5$ mTorr at 10 Hz, ensuring that the expansion was supersonic in the region probed. The gas pulses had a duration of about 400 μs. The total gas consumption was about 500 std cm^3 min^{-1} at a backing pressure of 650 mbar. We estimate rotational and translational temperatures of 15-20 K in the ketene expansion, on the basis of Doppler spectroscopy of CH_2, as described below.

The CH_2CO was photolyzed by unpolarized 308-nm light from a XeCl excimer laser (Lambda Physik Compex102) propagated along the slit axis about 2 cm downstream from the slit. The singlet CH_2 product was probed at wavelengths near 800 nm using frequency-modulated (FM) transient absorption. Many aspects of the apparatus and method have been described previously [25,26]; only brief additional details are provided here. Continuous light from an Ar^+-pumped Ti:sapphire ring laser (Coherent 899-29) with a bandwidth of <1 MHz was electrooptically modulated, producing sidebands at ± 200 MHz from the carrier frequency. The modulated probe beam was then copropagated with the photolysis light along the slit expansion. The probe beam was reflected back through the slit jet sample at a small angle, providing a second absorption path through the same approximate region, and focused onto a photodiode detector. The 200-MHz beat signal arising from the differential absorption or retardation of the sidebands was filtered, amplified, and mixed with the 200-MHz reference signal in an I&Q demodulator. The resulting transient signals were low-pass filtered (70 MHz), averaged in a digital oscilloscope (LeCroy 9310A), and transferred to a computer for storage. Transient waveforms from 30 photolysis shots were averaged at each 100 MHz step of the probe laser frequency. The archived data can be

considered either as laser-frequency-indexed series of transient waveforms or as time-indexed series of FM spectra, acquired in-phase (I) and in quadrature (Q). The I&Q signals are different linear combinations of absorption and dispersion line shapes; a knowledge of the absolute reference phase angle is required to isolate the FM absorption and dispersion components. The phase calibration and correction were achieved using translationally thermalized, Gaussian FM lines in the manner previously described [25]. Relaxed CH_2 lines formed from the photolysis of ketene in the expansion region of the supersonic jet gave an upper bound to the translational temperature of the beam of 20 K. The spectroscopy of $^1CH_2$ in the b^1B_1 - a^1A_1 transition is complex, with significant perturbations leading to unpredictable line strengths, rendering assignment of the very large number of observable lines difficult, particularly those with large values of J or K_a. The data presented here were recorded on a selection of previously assigned transitions [27,28], covering a range of low-J_{KaKc} states in the vibrational ground state of CH_2.

A separate glass cell was used in an experiment to measure the translational anisotropy of CH_2 photofragments from thermal ketene samples, in a manner previously described [26]. The cell contained two parallel, 1 in. by 3 in., flat, high-reflectivity mirrors. The vertically polarized probe beam was reflected in a horizontal plane 20 times between these mirrors on its way to the photodiode receiver. The photolysis beam was polarized using a Brewster stack of 10 fused silica plates, passed through a photoelastic modulator (Hinds Instruments PEM 90), and propagated between the multipass mirrors. The timing of the photolysis laser was synchronized with the stress cycle of the PEM and controlled by the data acquisition computer to enable the acquisition of FM Doppler profiles with the linear photolysis polarization alternately parallel or perpendicular to the propagation direction of the probe beam. A slowly moving thermal sample of neat ketene at 30 mTorr was used for these measurements.

7.3. Results

7.3.1. Selection of rotational lines

Transient FM spectra of CH_2 photofragments were acquired for a selection of rotational states, mostly using transitions in the b $^1B_1$ (0,8,0) $\leftarrow$ a $^1A_1$ (0,0,0) band. Table 7-1 lists the transitions used and the rotational energies of the detected CH_2 states. The highest-energy

accessible coincident quantum states of CO (v = 0 and v = 1) are also tabulated, assuming the ketene parent molecule to have no internal energy and using the average vacuum wavenumber of the XeCl excimer emission doublet, 32 449 cm^{-1}. This gives 2333 cm^{-1} of available energy for singlet CH_2 and CO from the zero point of ketene. Vibrationally excited CO can only be produced in coincidence with singlet CH_2 states with a rotational energy less than 190 cm^{-1}. Only spectra for rotational states of the ground vibrational state of CH_2 were recorded, as we were unfortunately unable to identify usable lines originating from the first excited bending state (0,1,0) of CH_2 in the spectral region of our Ti:sapphire laser [27,28]. The highest-energy rotational state of CH_2 for which we could detect usable nascent Doppler spectra was the 6_{52} state. Only a small number of transitions originating from higher-energy rotational states have been assigned. A very weak signal was detected from the 7_{52} state (with 787 cm^{-1} of rotational energy) at 12 264.03 cm^{-1}. Either the population of this state or the line strength of this transition is substantially weaker than for those of lower-energy states.

Linear interpolation of effective CH_2 rotational temperatures reported by Garcia-Moreno et al. [15] gives a temperature of about 700$\pm$100 K for 308-nm excitation. With this distribution, 57$\pm$6% of the CH_2 (0,0,0) population would have a rotational energy in the energy region included in our sample. This incomplete coverage limits our ability to construct the entire correlated state distribution from our measurements, but not as severely as if the CH_2 product state distributions were well described by the much hotter PST distributions.

Figure 7-2 shows representative FM Doppler profiles across the range of states probed. These spectra were selected from the transient data with a time gate 50-100 ns following the photolysis and phase corrected to remove small contributions of dispersion [25]. Multiple scans of each transition were taken and were found to be consistent from day to day. The spectra of the weaker lines shown are averages of several scans to improve the signal-to-noise ratio. Some partially overlapping lines were included in the analysis. As long as the separation of line centers exceeds the maximum Doppler shift by more than twice the modulation frequency, then at least half of each antisymmetric line can be observed without interference from the neighboring line. It is immediately evident that only the lowest rotational states of CH_2 show "spikes" near the line center that are associated with the coincident CO (v = 1) channel. Less striking inflections in the direct absorption line shapes were reported earlier [27] and similarly interpreted as a probe of the vibrational branching ratio of CO (v = 1):(v = 0) in coincidence with selected CH_2 states. With the cooling of the parent internal energy in

the slit jet and the signal improvements associated with the use of frequency modulation, the present Doppler measurements permit a more careful analysis than was previously possible.

7.3.2. Controls and characterization of Doppler profiles

The shape of a Doppler profile of a photofragment probed by LIF or absorption spectroscopy is the subject of an extensive literature [29-32]. Special considerations for FM Doppler spectroscopy have been addressed in refs [25] and [26] and in a review article [33]. In general, the Doppler profile will depend on the speed distribution of the detected fragment, its angular distribution, and its rotational polarization. The speed distribution is directly related to the internal energy distribution of the undetected cofragment. Each correlated state channel can display a velocity anisotropy due to a correlation between m, the transition dipole moment of the parent molecule at the time of absorption, and the final fragment velocity, $\boldsymbol{v}$. The rotational polarization is the anisotropy of the fragment angular momentum, $\boldsymbol{j}$, which may be correlated with $\boldsymbol{v}$ and/or m. Several control experiments indicate that both velocity anisotropy and rotational polarization have a negligible effect on the observed Doppler profiles of the detected CH_2 fragments.

7.3.2.1. Velocity anisotropy

A sensitive test for velocity anisotropy is to compare Doppler profiles measured with the probe laser propagating parallel and perpendicular to the pump laser polarization vector. The parallel geometry is unfortunately inaccessible in our slit jet with collinear pump and probe laser beams. Accordingly, we have used a low-pressure thermal sample of ketene in a multipass cell and switched the polarization of the photolysis laser using a photoelastic modulator to acquire FM Doppler profiles in these two geometries, as described in a previous study [26]. The blended pair of lines 4_{04} - 4_{14} and 5_{05} - 5_{15} is compared in Figure 3 for the two photolysis polarizations. There is no systematic difference with the polarization geometry that can be attributed to a nonvanishing anisotropy. A value of the anisotropy parameter, b, as large as ± 0.1 would result in a clearly visible difference above the noise level shown.

The comparison of signals acquired from photolysis of a thermal sample of ketene should be used with some caution when the dissociation of a jet-cooled sample is considered. Rotation of the excited ketene prior to dissociation can reduce the fragment anisotropy relative to the value that would have been observed in a prompt dissociation [32,34]. The

dissociation time scale observed in jet-cooled ketene excited to an energy 2500 cm^{-1} above the singlet threshold was about 100 ps; effusive samples were found to dissociate only about 20% faster [6]. This dissociation is more than 10 times slower than a typical rotational period for ketene at 20 K and about 50 times slower than a typical rotation at room temperature. Additional depolarization mechanisms may be related to the vibronically induced nature of the $^1A_1$ to $^1A_2$ (A") transition and a distribution of geometry changes following excitation. In any case, the velocity anisotropy is evidently very small, and we proceed in the analysis of the CH_2 Doppler spectra as if the fragmentation were strictly isotropic.

7.3.2.2. Rotational polarization

In the limit of isotropic fragment velocities, the only rotational polarization that can be observed is the ***v-j*** correlation, parameterized by the bipolar moment $b^0_0(22)$ [29]. This correlation has been observed for the CO fragment by Morgan *et a1*. [22] but is not expected to be strong for CH_2, because the magnitude of its angular momentum is smaller than the average angular momentum of its CO cofragment [35-36]. We can confirm that the ***v-j*** correlation of the detected CH_2 states is small by comparing Doppler line shapes for different rotational branch transitions probing the same rotational state. Profiles acquired on the 4_{31} - 3_{21} and 3_{31} - 3_{21} transitions are shown in Figure 7-4, and do not differ by an amount in excess of the experimental noise. Thus, there does not appear to be a measurable ***v-j*** correlation in this CH_2 fragment, typical of the those that we interrogate in this work.

7.3.2.3. Nuclear spin effects

Conservation of nuclear spin in the dissociation produces ortho and para modifications ($K_a + K_c$ = odd and even, respectively) of the CH_2 fragments in the same 3 : 1 ratio as in the parent ketene molecule [37]. For this reason, most of the states we chose to measure were the more-populated ortho states. One comparison of spectra measured on the 3_{30} - 2_{20} and 3_{31} - 2_{21} transitions showed identical Doppler line shapes within the experimental noise, suggesting no significant variation with the nuclear spin modifications between these states differing in energy by about 1 cm^{-1}. Although the 9 cm^{-1} difference in minimum internal energies of the ortho and para parent molecules is not evident in these spectra, we include the energetic consequences of nuclear spin conservation in the thermal averaging described in sections 7.3.3.1 and 7.3.3.2 below.

7.3.2.4. Jet cooling conditions

One final additional set of measurements was performed to assess the effective cooling in the slit jet. The photolysis laser beam was displaced toward the nozzle in order to dissociate ketene in the dense collision zone of the slit jet, while translationally cooled CH_2 was probed in a region 2 cm downstream. Reaction and quenching through collisions occur rapidly enough that it was difficult to calibrate relative populations of the different rotational states of singlet CH_2, but the line shapes were relaxed to Gaussian forms with a width characteristic of 15-20 K by the time the fragments reached the probe volume. Other measurements under comparable conditions in this apparatus, using CHBr fragments from the photodissociation of $CHBr_3$, yielded temperatures of 20$\pm$5 K for both rotational distributions and translational temperatures [38]. Ketene has several low-frequency vibrational modes that could contribute disproportionately to threshold dissociation channels. We believe that the jet expansion conditions provide good vibrational cooling on the basis of the abrupt disappearance of the spike in the Doppler spectra as the energy of the CH_2 increases above the maximum energy for which CO (v = 1) can be formed. A nearby pair of nascent rotational lines probing the 4_{14} and 5_{15} states of CH_2 is illustrated in Figure 7-5(b). The 4_{14} state is nominally 20 cm^{-1} below the maximum for coincident CO (v = 1), and the 5_{15} state is 58 cm^{-1} above the cutoff, neglecting parent energy. No trace of CO (v = 1) is evident in the Doppler spectrum of the higher-energy CH_2 state, suggesting that the parent energy selection is good and, in particular, that hot bands are not a significant concern. The shape and width of the sharp feature in the center of the FM spectrum of the 4_{14} state in Figure 7-5b are primarily determined by the parent speed distribution of ketene in the slit jet. An assumed parent temperature as low as 10 K or as high as 30 K leads to significantly worse fits to this part of the spectrum than that obtained with a best-fit temperature of 20 K. In analyzing the nascent CH_2 Doppler profiles, therefore, we assume a 20-K distribution of parent internal energies and use a convolution of trial center-of-mass speed distributions with a 20-K Gaussian parent velocity to compare to our laboratory frame Doppler measurements.

7.3.3. Correlated state distributions

With the simplifications of negligible velocity anisotropy and rotational polarization, the Doppler profile of a state-selected CH_2 fragment is easily computed from a trial distribution of coincident CO states. Energy conservation in the center-of-mass (COM) frame gives the

translational energy in terms of the photon energy, the bond dissociation energy for the singlet channel, and the internal energies of parent and fragments.

$$E_T = hn + E_{int}(CH_2CO) - D_0(CH_2 - CO) - E_{int}(CH_2) - E_{int}(CO) \quad (1)$$

For a selected internal energy state of CH_2, each accessible coincident CO state produces a characteristic translational energy, broadened only by the distribution of parent internal energy and the bandwidth of the photolysis laser. The CH_2 fragment's COM velocity distribution, $f(v)$, is thus a sum of narrowly peaked speeds, one for each coincident CO state. Assuming an isotropic velocity distribution, normalized according to

$$1 = 4p \int_0^\infty f(v) v^2 \, \mathrm{d}v \quad (2)$$

the corresponding Doppler-broadened absorption spectrum is given by [39]

$$D(w) = \int_{|w|}^\infty \frac{f(v) v^2}{2v} \, \mathrm{d}v \quad (3)$$

Here, w is the velocity-equivalent Doppler shifts, the fractional detuning from the line center times the speed of light. In the laboratory fume, the Doppler profile is broadened by a one-dimensional Gaussian convolution with the parallel component of the parent molecules' thermal velocity distribution, giving a broadened spectrum we denote as $D'(w)$. Finally, for FM detection, one measures a finite difference spectrum. Each point in the FM spectrum is related to the difference in absorption at the optical frequencies of the sidebands, shifted by integer multiples of d (in velocity units) away from the main laser frequency.

$$\mathrm{FM}(w) \propto D^1(w-d) - D^1(w+d) + \frac{J_1 J_2 + J_2 J_3}{J_0 J_1 + J_1 J_2}\left[D^1(w-2d) - D^1(w+2d)\right] \quad (4)$$

Small corrections are included for higher-order sidebands [40], the first term of which is shown, where J_n is the nth-order Bessel function of argument M, the modulation index used in the frequency modulation [33], typically 0.9 in our experiments.

7.3.3.1. Trial Doppler fits to PST

To illustrate this procedure, we take the parameter-free PST distribution of CO in coincidence with CH_2 in a quantum state high enough in energy to permit only CO (v = 0) and compute the corresponding FM Doppler spectrum. Figure 7-6 shows the PST state distribution and the resulting FM Doppler spectra for the 5_{14} state of CH_2, compared to experiment. The least-constrained version of PST has an impact parameter limited only by angular momentum conservation, that is, the centrifugal barrier is neglected. The PST CO rotational and vibrational distributions coincident with each particular CH_2 state probed were calculated, including a sum over a Boltzmann-weighted rotational distribution of ketene, using a prolate symmetric top approximation and a rotational temperature of 20 K and including conservation of nuclear spin. The dashed curves in Figure 7-6(a),(b) show the results of this calculation. Including the centrifugal barrier in the form of a maximum impact parameter, b_{max} = 4 Å [41], results in a reduction of the last few otherwise open channels, as shown with the solid lines of Figure 7-6(a) and (b). The PST distribution of coincident CO states from a cold ketene parent is characterized by a linear increase with j(CO) until j(CO) = $j(CH_2)$, with a constant probability at higher j(CO) until the energy limit is reached. The centrifugal barrier produces a more gradual falloff in the last few accessible CO states, and the finite temperature of the ketene sample (with its nonzero values of total angular momentum) softens the abrupt change of slope at j(CO) = $j(CH_2)$. The PST simulations of FM Doppler spectra are conspicuously sensitive to the small population of the minimum translational energy channels, but the qualitative discrepancy between experiment and PST is also strong in regions of the spectrum away from the line center. It is worth emphasizing that this mostly flat rotational distribution of PST, not reproduced in our measurements, is also a strict prediction of several generalized statistical models, including SSE [18], CPST [14], and an early generalization of variational RRKM for treating product distributions [9]. Identifying the specific deviations from the PST reference case is in the spirit of the adiabatic and nonadiabatic treatment of exit channel effects on capture rates of Nikitin and Troe [42]. We discuss the nature of these deficiencies below, but now describe a method of finding coincident rotational distributions that do agree with the observed spectra.

7.3.3.2. Rotational state distributions from forward convolution

The failure of PST to predict the observed line shapes leads us to extract the rotational state distributions from the observed spectra. We have explored several approaches to this. For the rotational states of CH_2 with only CO (v = 0) in coincidence, we construct a set of basis functions in the space of FM Doppler spectra, one for each energetically allowed rotational state of CO, including the broadening due to parent internal energy and the transformation from COM to lab frame. A linear combination of these functions is sought that best matches the observed spectra. The normal equations are highly singular, as the low rotational states of CO produce very similar contributions. Singular-value decomposition (SVD) [43] with retention of the most significant components of the fit provides a first-order, unbiased estimate of the coincident CO rotational distribution. Figure 7-7(a) shows the SVD fit to the same data previously shown in Figure 7-6. The coincident state distribution produced from the first six terms of the SVD fit is shown with symbols in Figure 7-7(b). The inclusion of four or fewer terms leaves systematic errors in the fit to the spectrum; the inclusion of eight or more terms produces oscillations in the derived state distribution.

An alternative means of deriving the coincident state distribution underlying the measured Doppler spectrum is to adjust a small number of parameters in a flexible, but plausible, functional form for $P(j_{\mathrm{CO}})$. We tried several such functions, the first inspired by the functional form of prior distributions in polyatomic dissociations

$$P(j_{\mathrm{CO}}) = f_r(j_{\mathrm{CO}})^a [1 - f_r(j_{\mathrm{CO}})]^b \tag{5}$$

where

$$f_r(j_{\mathrm{CO}}) = \frac{E_{\mathrm{rot}}(j_{\mathrm{CO}})}{E_{hn} - D_0^0(\mathrm{CH_2CO}) - E_{\mathrm{CH_2}}} \tag{6}$$

and a and b are parameters to be optimized. This functional form is not quite flexible enough to fit the form of the PST distribution, and systematic differences were found in many cases between our best fits and the measurements using this two-parameter function. We found that adding an additional adjustable constant term to all accessible rotational states provided a three-parameter form that could represent the PST distribution, as well as all of our

experimental spectra, for the v = 0 component of the coincident CO distribution. The result of this three-parameter fit is compared to the SVD fit in Figure 7-7. The simulated Doppler spectrum is indistinguishable from the SVD fit, and the corresponding state distribution is shown by the solid line in Figure 7-7(b).

A third functional form was implemented, with two adjustable exponential factors combined with the form of eq 5 to give additional flexibility to the shape of the low- and high-energy regions of $P(j_{CO})$. The results of this four-parameter fit are also shown in Figure 7-7. Not surprisingly, the optimum fit to the spectrum is again indistinguishable. The best coincident state distribution is shown in Figure 7-7(b) with the dashed line. The qualitative similarity of the six-term SVD solution and the three-parameter and four-parameter fits gives a feel for the required features and uncertainties of the correlated state distribution that can be derived from the FM Doppler spectrum.

For those CH_2 states with the possibility of being formed in coincidence with CO (v = 1), we used the three-parameter representation of the coincident CO (v = 0) state distribution and an additional parameter for the (v = 1):(v = 0) branching ratio. The low translational energy of CH_2 formed in coincidence with CO (v = 1), along with the close energy spacing of the low-j_{CO} energy levels leads to high sensitivity to the magnitude, but low sensitivity to the shape, of the CO (v = 1) contribution to the CH_2 Doppler profiles. Therefore, we have chosen to use the PST shape for the CO (v = l) contribution. The available energy is only 190 cm^{-1} above the v = 1 threshold, an energy such that the CO (v = 1) rotational distributions should still be well described by a loose, vibrationally adiabatic transition state [13,14] and a distribution of CO states adequately represented by PST.

An example of a two-component fit is shown in Figure 7-8 for the 4_{14} state of CH_2. The shape of the coincident CO rotational distribution for the v = 0 component is very similar to that derived from higher-energy CH_2 states. The amplitude of the v = 1 component, shown by the dashed line, reflects a total population of 0.07 relative to the normalized v = 0 population. Without including prior information in the fits, the contribution of slow CH_2 with coincident CO (v = 1) is not easily distinguished from the contribution of slow CH_2 formed in coincidence with the last one or two energetically accessible rotational states of CO (v = 0). Our chosen analysis method rejects, by construction, what we consider unlikely rotational distributions of CO (v = 0), with local maxima in the one or two highest accessible rotational states, even though such distributions could be found that fit the data as well as our preferred analysis.

7.3.3.3. Vibrational branching ratios

The vibrational branching ratios derived from the fitting routine for the various states probed are listed in Table 7-1. The global CO (v = 1):(v = 0) vibrational branching ratio at this energy has been measured [17] to be 0.022±0.004. This is inconsistent with PST, which predicts a much lower branching ratio of 0.006, but is consistent with the SSE and variational RRKM predictions. Our experimental state-specific branching ratios can be combined to yield a global branching ratio for comparison to the LIF experiments in the following fashion. The CO vibrational branching ratio for unobserved CH_2 states with energies below 200 cm^{-1} was interpolated using the ratios in Table 7-1, assuming that the v = 1 fraction depends only on the energy of the CH_2 state. The global rotational distribution of singlet CH_2 can be empirically described by temperatures for the (0,0,0) and (0,1,0) vibrational levels of 700 K±150 K [15] and 315 K±100 K [16], respectively, with a vibrational branching ratio of 1:0.24. The global CO vibrational branching ratio can thus be formed by a sum over the relevant levels using the CH_2 Boltzmann populations and the interpolated coincident state branching ratios. The result is a global CO (v = 1):(v = 0) branching ratio of 0.015±0.005, consistent with that measured by CO LIF.

The state-specific CO branching ratios are remarkably close to the PST values. The SSE model predicts PST-like rotational distributions within each vibrational channel, but with a roughly 3-fold difference in vibrational branching ratio. For each coincident state, SSE thus predicts a vibrational branching ratio three times larger than PST, clearly inconsistent with the experimental result. The rotationally resolved vibrational branching ratios should not, however, be considered a naturally useful diagnostic of the unimolecular dynamics. Because each different vibrational product channel can be considered as an independent process, it is more useful to characterize the relative branching among all the vibrational channels, summed over rotation, and the joint rotational distribution within each vibrational channel, as these evidently represent approximately uncoupled steps of the reaction. The fortuitous correctness of the PST state-specific vibrational branching ratios results from an underestimate of the total CO (v = 1) population and a conceptually unrelated, but similarly large, underestimate of the fraction of the CH_2 states produced in the CO (v = 0) channel with an energy low enough to have CO (v = 1) as a possible partner. Similarly, the SSE values of the rotationally resolved vibrational branching ratios are incorrect because of an inappropriate rotational weighting of

the correct total vibrational branching ratios. Nevertheless, the observed state-resolved branching ratios serve as primary information in the interpretation of experimental data. For example, in analyzing the rotational distribution of CH_2 (0,0,0) measured by LIF, one could use the branching ratios of Table 7-1 to decompose the global distribution into components due to the CO (v = 0) channel and a smaller component with a colder rotational distribution due to the CO (v = 1) channel.

7.4. Discussion

7.4.1. Phase space theory and product state distributions

One practical reason for studying unimolecular reactions at this level of detail is to explore the limits of confidence for approximate theories of reaction rates. Predictive calculations for the rates of barrierless unimolecular reactions are an important requisite for combustion modeling, for example. Product distributions are, however, only indirectly related to rate theories [44]. The evolution of a molecule from the transition state to separated fragments is an additional dynamical step under the influence of the inter fragment potential at different ranges, depending on the energy and the specific choice of transition state. Only in the PST limit, where the transition state is defined at the centrifugal barrier and the anisotropy of the long-range interfragment potential is ignored, does the statistical distribution at the transition state correspond directly to the final state distribution. For other types of transition states, additional assumptions are required concerning conserved, mixed, or dynamically controlled degrees of freedom beyond the transition state [44,45]. The issues of adiabaticity and the fate of transitional modes in the exit channel are central questions of current investigation [20,46 - 48].

Phase space theory can occasionally provide a good description of product state distributions, while overestimating the rates. This can happen if the intrafragment interaction is strong enough to randomize the state distribution after passage through an inner transition state. Such effects are clearly seen in NO_2, for example [48,49], illustrating that the inference of a loose transition state on the basis of only a statistical product state distribution is risky.

For ketene, the situation is reversed: PST is known to provide a poor quantitative description of both rates and product distributions at the energies of the present experiments. The questions to ask, then are how much are the final state distributions influenced by exit channel interactions and how much do they reflect properties of the transition states?

Correlated state distributions are useful experimental data in addressing these kinds of questions [19,20].

Referring back to the triangular plot of correlated states in Figure 7-1, the distortion from PST of the correlated rotational distribution of the CO (v = 0) + CH_2 (0,0,0) channel can be characterized as a shifting of probability down and to the right. The similarity of the observed total CO (v = 0) rotational distribution to PST is evidently due to a coincidental compensation of the underestimate by PST of the contribution to the low rotational levels of CO produced along with CH_2 (0,1,0), and an overestimate of the low-j(CO) portion of the vibrationless channel. This same change in shape at higher available energies --- a tendency for the rotational distributions to approach a Gaussian form, with reduced population at low rotational levels --- has been observed in the global CO (v = 1) populations at energies more than 1000 cm^{-1} above the CO (v = 1) threshold [14].

7.4.2. Constrained phase space theory

The singlet CH_2 state distributions deviate increasingly from PST at higher excess energies, whereas the deviations of the CO rotational state distributions from PST remain minor. These observations led to the reasonable conjecture that the more widely spaced CH_2 rotational levels may uncouple from the transitional modes sooner along the dissociation path than the CO levels, which remain strongly coupled with the transitional modes. An empirically constrained PST (CPST) was thus proposed [14], in which the experimental state distribution of CH_2 is used as a weighting function. The CO rotational distribution formed in coincidence with each CH_2 state is computed with PST, but the weight of each CH_2 state is constrained to match the measured CH_2 distribution. This CPST model was found to describe the initial deviations from PST of the total CO (v = 1) rotational distribution at energies between 350 and 1000 cm^{-1} above the threshold for forming CO (v = 1). At still higher energies, adjustable models provided somewhat better fits.

The measurement of CH_2 Doppler profiles provides a direct test of the assumptions of CPST. A single CH_2 state is spectroscopically selected, and the constraints on the CH_2 population can only affect the scaling and not the shape of coincident CO rotational distribution, which is assumed to follow PST. We observe large, qualitative differences between our Doppler spectra and the PST coincident state distributions. At the 2333 cm^{-1} available energy of our experiments, we note that the CO (v = 0) + CH_2 (0,0,0) channel is clearly not described by a single constraint on the CH_2 distribution, just as Wade *et a1*. [14]

rejected CPST for the CO (v = 1) channel at energies more than 1000 cm^{-1} above threshold. We hope to be able to extend the present measurements to some transitions at longer wavelengths probing the (0,1,0) bending state of CH_2, to test CPST at lower energies, where it has been formed to provide better agreement with global CO populations.

7.4.3. Separate statistical ensembles

The SSE model [18] provides a simple prediction of vibrational branching ratios, equivalent to the vibrational prior [50], combined with a PST prediction of the correlated rotational distribution for each separate vibrational channel. The difference between SSE and PST consists of a rescaling of the relative populations of each coincident vibrational channel without modification of the shape of its correlated rotational distribution. Both rotational and vibrational parts of the model work well for NCNO dissociation [18]. Applied to ketene dissociation, the vibrational branching ratios are well described over a wide range of energy [13,16]. The asymmetrical rotational partitioning between CO and CH_2 at energies more than a few hundred wavenumbers above threshold requires explanation beyond PST and SSE. The improved treatment of vibrations in SSE does not address the rotational problem in ketene dissociation.

7.4.4. Restricted phase space theory

Most closely related to our current experiments are the state-resolved CO time-of-flight (TOF) measurements of Morgan *et a1*. [22] These experiments probe the distribution of CH_2 internal energies coincident with specific CO states, that is, vertical sections through the triangular plot of Figure 7-1, compared with our CH_2 Doppler measurements, which give horizontal sections. The TOF data for selected CO states were first reduced by forward convolution methods to a COM translational energy distribution and an energy-dependent value of the ***v-j*** correlation. PST calculations of the translational energy distributions were found deficient, and additional restrictions to PST were proposed to account for their observations. Restricted PST (RPST) calculates the PST distribution of singlet CH_2 states coincident with a specific CO state subject to the additional constraints of a maximum and a minimum impact parameter, b_{max} and b_{min}, respectively, intended to represent structural information about the transition states leading to specific product channels. These two parameters permit the selective rejection of higher and lower angular momentum states of CH_2. To represent the data, different b_{min} and b_{max} values were selected for each j_{CO}, and for those CO states with coincident CH_2 (0,1,0), a second pair of parameters was used to describe

this channel. The parameters selected to match the TOF data were, furthermore, found to produce reasonable agreement with global state distributions.

The angular momentum conservation in PST already explicitly imposes upper and lower bounds on the impact parameters, generally much more restrictive than the upper bound related to a centrifugal barrier. It is instructive to compare the b_{max} and b_{min} parameters used in RPST to describe the correlated state distribution with the bounds implied by angular momentum conservation alone. For graphical simplicity, we replace the diatom plus asymmetric top (CO + CH_2) with a model system of diatom plus spherical top. This simplification provides a unique and monotonic relation between the top energy and angular momentum, avoiding the actual, but immaterial, irregularities of level spacing and *K*-dependent energies. We choose the diatomic rotational constant to be that of CO and the spherical top rotational constant to be 12 cm^{-1}, preserving the coarse-grained density of rotational levels for CH_2. With this model, we use PST to compute the distribution of *l*, the orbital angular momentum, for each coincident rotational channel of a single vibrational channel. The available energy is set to 2000 cm^{-1}, and the total angular momentum is set to 3 to represent a typical value in a cold ketene sample. The results can be plotted as the PST probability of orbital angular momentum for a selected CO state as a function of $j(CH_2)$. Figure 7-9 shows contour plots of these orbital angular momentum distributions for j(CO) = 5, 15, and 25. The projection of this *l* distribution onto the $j(CH_2)$ axis gives the PST coincident state distribution for the selected CO state. The increasing probability of higher *j* states of CH_2 is due to the wider range of allowed orbital angular momenta, as well as the $2j + 1$ degeneracy that corresponds to the increasing number of K_a K_c states for each *j* in the spherical top limit.

Fixed values of the impact parameter are represented by curves of l_{max} as a faction of $j(CH_2)$ in these plots, proportional to the increasing relative velocity for lower-energy states of CH_2. A value of 4 Å for b_{max} produces the blue upper bounds on *l* shown in Figure 7-9. This value represents a typical centrifugal barrier [41], and it can be seen to reject only a small fraction of the phase space at the highest few accessible channels. The much smaller values of b_{max} and b_{min} used to characterize CH_2 (0,0,0) by RPST are represented as red curved upper and lower bounds, respectively, on *l* in the same plots. Only those *l* states in the slice between the red upper and lower bounds are included in the RPST, giving strong leverage over the shape of the permitted CH_2 distributions. The main features of this figure apply to "real" CH_2 as well as its spherical analogue, although the upper and lower bounds on *l* cannot be drawn as a single, sharp line when $j(CH_2)$ does not uniquely determine the energy.

We can compare the coincident CO distributions derived from the our Doppler experiments with the RPST parametrization based on the metastable CO TOF experiments. To do so requires an interpolation of the b_{min} and b_{max} parameters for all CO (v = 0) states, followed by a RPST calculation of the full correlated rotational distribution for the CO (v = 0) + CH_2 (0,0,0) channel. When transformed to the FM Doppler spectrum for selected CH_2 (0,0,0) states, many of these simulations appear to agree with our experiments even less well than does pure PST. There can be several reasons for this disagreement. The TOF and Doppler experiments are subject to very different transformations from raw data to state distributions, and different features of the state distributions are more tightly constrained in the two experiments. Irregularities introduced in the interpolation of the j(CO) dependence of the very sensitive RPST parameters influence the Doppler simulations and not the TOF fits. Some features of the TOF data are not well represented by the RPST parametrization, particularly the time offset in the initial arrival time for the low internal energy CO states, as if the lowest internal energy coincident CH_2 states were missing. Finally, some additional speed-dependent sensitivity corrections due to Doppler selection in the metastable tagging experiments were not included in the original analysis [51].

Figure 7-10 compares a selection of CO rotational distributions in coincidence with selected CH_2 (0,0,0) states for PST with a 4-Å centrifugal barrier, RPST using parameters interpolated from the values of Morgan *et a1*. [22] and the empirical distributions derived from our Doppler measurements. Compared to the normalization of PST, RPST shows a state-dependent reduction in probability produced by the additional restrictions on the impact parameter. The total state count of RPST is reduced to about 27% of the PST value, with some coincident channels reduced more than others, as was schematically shown in Figure 7-9. The lowest-energy CH_2 states are sharply restricted in RPST for all but the highest rotational states of CO, giving a sharp spike at high j(CO) for the 1_{10} state of CH_2. Such a distribution would have an unmistakable Doppler signature, which is not observed. Only the shapes and not the absolute magnitudes of the correlated state distributions derived from the Doppler spectra are determined from our measurements. To plot the experimental Doppler curves in Figure 10 on the same scale as the PST and RPST results requires a normalization procedure that uses the experimental rate [6] and global product distributions [15.16] relative to PST. The area under the "observed" correlated state distributions will be smaller than the area under the reference PST distribution by a factor of 8, accounting for the observed reduction in the experimental dissociation rate compared to PST at this excess energy [17], times a state-dependent

correction factor to account for the fraction of the actual CH_2 population formed in each specific state compared to the PST value. Combined errors in interpolated rates and product distributions used in this normalization may lead to scaling errors as large as 50% for the red curves in Figure 7-10 relative to the fixed normalization of PST. The *shapes* of the red curves are more accurately determined from the independent Doppler analysis.

In comparisons of our experiments with RPST, an asymmetry of the formulation is evident. One might just as well consider adjusting upper and lower bounds on the impact parameter for each CH_2 state, rather than for each CO state, thereby providing an equally flexible parametrization. It remains unclear to us whether restrictions on impact parameters provide a useful description of the dynamics of energy flow in the exit channel of a barrierless reaction.

7.4.5. Directly dissociative reverse reactions

The deviations from PST of the correlated rotational state distribution of the vibrational channel with an available energy of 2333 cm^{-1} can be summarized as an overall deficiency of high-energy CH_2 states and a deficiency of those channels with low energy in both CH_2 and CO fragments. The global state distributions from the Moore group, the CO TOF measurements from the Wodtke group, and our CH_2 Doppler profiles are all consistent with these qualitative features. Possible interpretations of the colder CH_2 distributions have been discussed before, [14,15,47] but the suppression of the correlated low-energy pairs is a new observation in the correlated state measurements. These low internal energy correlated rotational states are exactly the ones that are described best by PST at lower energies, when they are the only open channels, yet they fail to contribute according to their statistical weights at higher total energy.

Product interactions in the exit channel, beyond a tightened transition state, can be invoked to describe these effects. A tendency to follow rotationally adiabatic paths would, however, result in a relative excess of the low internal energy channels, contrary to our observations. Some specific dynamic effects of the anisotropic long-range potential may be responsible for the asymmetry of the rotational partitioning, although we are unaware of simple arguments consistent with the observations. Exit-channel dynamical calculations, in the spirit of those proposed by Hamilton and Brumer [45], would probably be instructive. In this approach, the time-reversed association reaction is considered using classical trajectories. Initial conditions are sampled uniformly in the phase space of the asymptotic fragments at

fixed *E* and *J*, and approach trajectories are computed under the influence of the interfragment potential. PST rates and product distributions would be exact if all trajectories that were not reflected by the centrifugal barrier reached the deep well of the complex and stuck long enough to randomize the reaction coordinate energy into other modes. Two classes of failed association trajectories can be identified. The first class of trajectories can be characterized by direct repulsion from orientational barriers at larger fragment separation, for example, a turning point in the C-C distance occurring at a C-O-C configuration. The fraction of such medium-range repulsive encounters on a potential with a barrierless minimum-energy path will be closely related to the energy-dependent deviation from PST rates and product distributions, if this is the dominant type of failed association [42,45,46]. To account for the correlated state distributions in this way, one would need to find that high rotational states of CH_2 selectively rebound from CO and that high rotational states of CO selectively associate with low rotational states of CH_2. Theoretical work is required to test this idea.

A second class of failed association trajectories samples the deep well but redissociates after a single vibrational period of the reaction coordinate. This outcome reflects a deviation from the statistical requirement that energy randomization be rapid compared to the reaction. If this direct redissociation is ever significant, it should first be detected for those fragment pairs with a maximum in relative velocity. These are indeed the fragment states that appear to be under-represented in the correlated state distribution at 2333 cm^{-1}. Those fragments that reach an inner turning point and immediately dissociate originate from a part of product phase space that will not be formed in the time-forward dissociation reaction, even though it is permitted by angular momentum and energy conservation. This effect is a failure of the statistical equilibrium assumption and has nothing to do with energy-dependent transition states. It remains an open question as to whether a significant number of such directly dissociative reverse reactions occur between CH_2 and CO at energies as low as 2000 cm^{-1}. Trajectory calculations to test such ideas are in progress [52]. The success of a purely statistical variational RRKM calculation [11] to produce quantitative agreement with experimental rates from threshold up to 6000 cm^{-1} gives some assurance that nonstatistical effects can be neglected. The distinctive correlated state distributions would then need to be explained in terms of specific exit channel interactions.

7.5. Conclusions

High-resolution absorption spectroscopy of singlet CH_2 produced in the 308-nm photodissociation of jet-cooled ketene has provided a view of the state distribution of CO produced in coincidence with selected CH_2 states. The results can be compared to "orthogonal" measurements of state-resolved TOF on the CO fragments [22]. There is a qualitative agreement that, for the product channel producing both CO and CH_2 in their vibrational ground states, the correlated rotational channels with low internal energy in each fragment are suppressed relative to PST predictions, as are the high-energy CH_2 states. The results provide a distinctive test for statistical and dynamically corrected statistical theories of unimolecular reaction.

References

[1] W. H. Green, C. B.Moore, W. F. Polik, Annu. Rev. Phys. Chem. **43**, 591 (1992).

[2] C. B. Moore, Faraday Disc. **102**, 1 (1995).

[3] Q. Cui, K. Morokuma, J. Chem. Phys. **107**, 4951 (1997).

[4] I.-C. Chen, W. H. Green, C. B. Moore, J. Chem. Phys. **89**, 314 (1988).

[5] W. H. Green, A. J. Mahoney, Q.-K. Zheng, C. B. Moore, J. Chem. Phys. **94**, 1961 (1991).

[6] E. D. Potter, M. Gruebele, L. R. Khundkar, A. H. Zewail, Chem. Phys. Lett. **164**, 463 (1989).

[7] P. Pechukas, J. C. Light, J. Chem. Phys. **42**, 3281 (1965).

[8] C. E. Klots, J. Chem. Phys. **75**, 1526 (1971).

[9] S. J. Klippenstein, R. A. Marcus, J. Chem. Phys. **91**, 2280 (1989).

[10] S. J. Klippenstein, R. A. Marcus, J. Chem. Phys. **93**, 2418 (1990).

[11] S. J. Klippenstein, A. L. L. East, W. D. Allen, J. Chem. Phys. **105**, 118 (1996).

[12] D. J. Nesbitt, H. Petek; M. F. Foltz, S. V. Filseth, D. J. Bamford, C. B. Moore, J. Chem. Phys. **83**, 223 (1985).

[13] S. K. Kim, Y. S. Choi, C. D. Pibel, Q.-Z. Zheng, Moore, C. B. J. Chem. Phys. **94**, 1954 (1991).

[14] E. A. Wade, H. Clauberg, S. K. Kim, A. Mellinger, C. B. Moore, J. Phys. Chem. A **101**, 732 (1997).

[15] I. Garci´a-Moreno, E. R. Lovejoy, C. B. Moore, J. Chem. Phys. **100**, 8890 (1994).

[16] I. Garci´a-Moreno, E. R. Lovejoy, C. B. Moore, J. Chem. Phys. **100**, 8902 (1994).

[17] E. A. Wade, A. Mellinger, M. A. Hall, C. B. Moore, J. Phys. Chem. A **101**, 6568 (1997).

[18] C. Wittig, I. Nadler, H. Reisler, M. Noble, J. Catanzarite, G. Radhakrishnan, J. Chem. Phys. **83**, 5581 (1985).

[19] C. G. Morgan, M. Drabbels, A. M. Wodtke, Adv. Photochem. **23**, 279 (1997).

[20] L. Oudejans, R. E. Miller, W. L. Hase, Faraday Discuss. **102**, 323 (1995).

[21] M. Drabbels, C. G. Morgan, D. S. McGuire, A. M. Wodtke, J. Chem. Phys. **102**, 611 (1995).

[22] C. G. Morgan, M. Drabbels, A. M. Wodtke, J. Chem. Phys. **104**, 7460 (1996).

[23] T. Hu, E. L. Chappel, S. W. Sharpe, J. Chem. Phys. **98**, 6162 (1993).

[24] K. Liu, R. S. Fellers, M. R. Viant, R. P. McLaughlin, M. G. Brown, R. J. Saykally, Rev. Sci. Instrum. **67**, 410 (1996).

[25] S. W. North, X. S. Zheng, R. Fei, G. E. Hall, J. Chem. Phys. **104**, 2129 (1996).

[26] M. L. Costen, S. W. North, Hall, G. E. J. Chem. Phys. **111**, 6735 (1999).

[27] B.-C. Chang, M. Wu, G. E. Hall, T. J. Sears, J. Chem. Phys. **101**, 9236 (1994).

[28] A. J. Marr, T. J. Sears, B.-C. Chang, J. Chem. Phys. **109**, 3431 (1998).

[29] R. N. Dixon, J. Chem. Phys. **85**, 1866 (1986).

[30] G. E. Hall, P. L. Houston, Annu. Rev. Phys. Chem. **40**, 375 (1989).

[31] M. Brouard, S. Duxon, P. A. Enriquez, J. P. Simons, J. Chem. Soc., Faraday Trans. **89**, 1427 (1993).

[32] R. J. Gordon, G. E. Hall, Adv. Chem. Phys. **96**, 1 (1996).

[33] G. E. Hall, S. W. North, Annu. Rev. Phys. Chem. **51**, 243 (2000).

[34] S. Yang, R. Bersohn, J. Chem. Phys. **61**, 4400 (1974).

[35] S. J. Klippenstein, J. I. Cline, J. Chem. Phys. **103**, 5451 (1995).

[36] S. W. North, G. E. Hall, J. Chem. Phys. **104**, 1864 (1996).

[37] I.-C. Chen, W. H. Green, C. B. Moore, J. Chem. Phys. **89**, 314 (1988).

[38] B.-C. Chang, M. L. Costen, A. J. Marr, G. Ritchie, G. E. Hall, T. J. Sears, J. Mol. Spectrosc. **202**, 131 (2000).

[39] J. L. Kinsey, J. Chem. Phys. **66**, 2560 (1977).

[40] J. M. Supplee, E. A. Whittaker, W. Lenth, Appl. Opt. **33**, 6294 (1994).

[41] J. Yu, S. J. Klippenstein, J. Chem. Phys. **95**, 9882 (1991).

[42] E. E. Nikitin, J. Troe, Ber. Bunsen-Ges. Phys. Chem. **101**, 445 (1997).

[43] W. H. Press, B. P. Flannery, S. A. Teukolsky, W. T. Vettering, "Numerical Recipies" (Cambridge University Press, 1986).

[44] T. Baer, W. L. Hase, "Unimolecular Reaction Dynamics: Theory and Experiments" (Oxford University Press, 1996; Chapter 9).

[45] I. Hamilton, P. Brumer, J. Chem. Phys. **82**, 595 (1985).

[46] J. Troe, Ber. Bunsen-Ges. Phys. Chem. **101**, 438 (1996).

[47] S. C. Smith, Faraday Discuss. **102**, 17 (1995).

[48] S. A. Reid, H. Reisler, J. Phys. Chem. **100**, 474 (1996).

[49] S. A. Reid, A. Sanov, H. Reisler, Faraday Discuss. **102**, 129 (1995).

[50] R. D. Levine, R. B. Bernstein, "Molecular Reaction Dynamics and Chemical Reactivity" (Oxford University Press, 1987; p 274).

[51] C. G. Morgan, A. M. Wodtke, University of California at Santa Barbara, Santa Barbara, CA. Private communication, 1996.

[52] K. Forsythe, S. Klippenstein, S. Gray, Argonne National Labora-tory, Argonne, IL. Private communication, 2000.

Figures and tables for Chapter 7

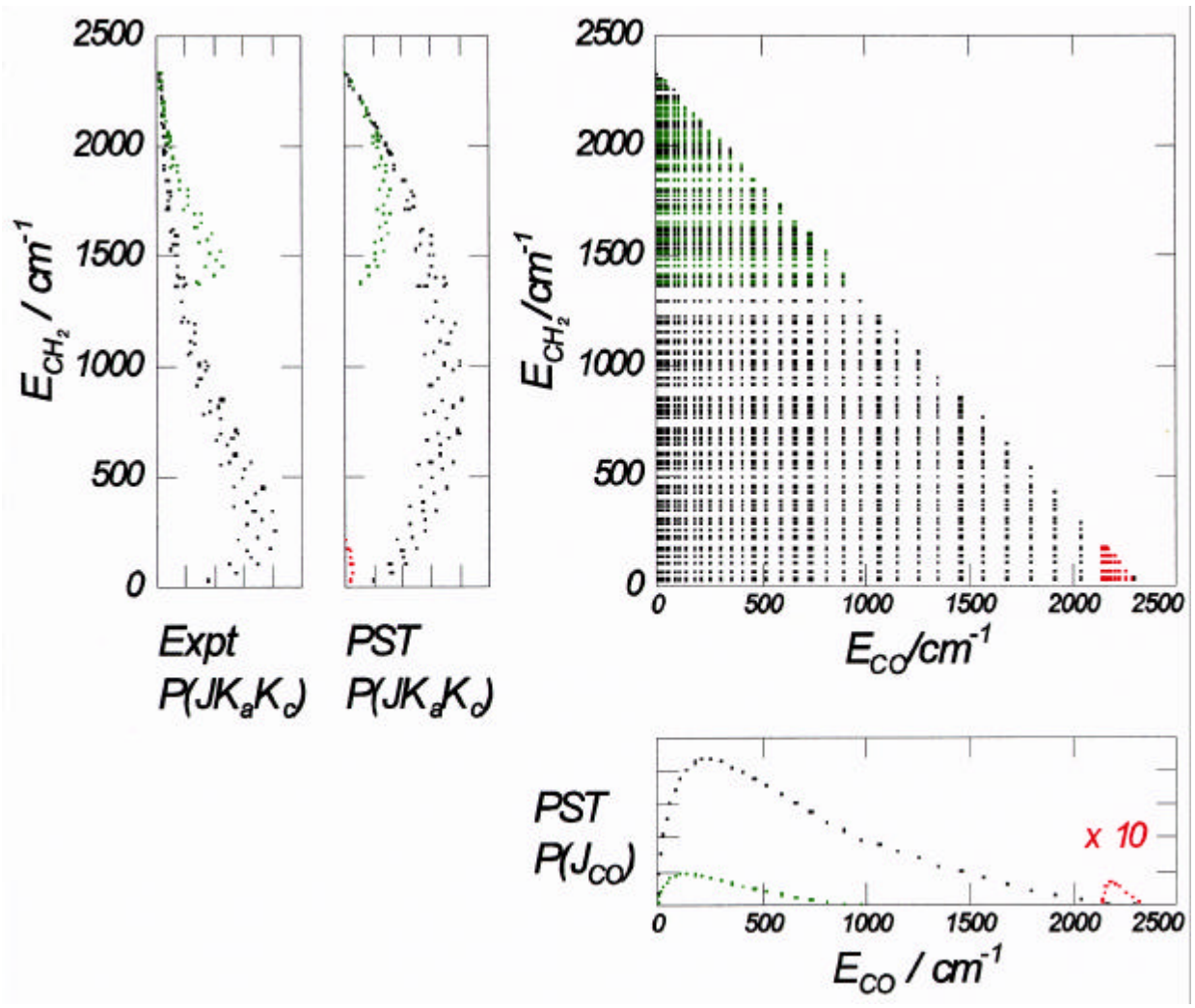

Fig. 7-1
Correlated final states of ketene dissociation. Three vibrational channels are color-coded. Black, CO (v = 0) + CH_2 (0,0,0); green, CO (v = 0) + CH_2 (0,1,0); and red, CO (v = 1) + CH_2 (0,0,0). Global state distributions are projections of probability from the triangle onto the CO and CH_2 energy axes. Black and green measurements on CH_2 can be made of (0,0,0) and (0,1,0) total populations; low-energy CH_2 states can have a partial contribution from the red channel. Black and red measurements of CO can be made of (v = 0) and (v = 1) total populations; low-energy CO states have a partial contribution from the green channel. PST state distributions are illustrated for CO and CH_2. The experimental CH_2 distributions more closely resemble Boltzmann distributions than the PST distribution, whereas the CO distribution is not greatly different from PST.

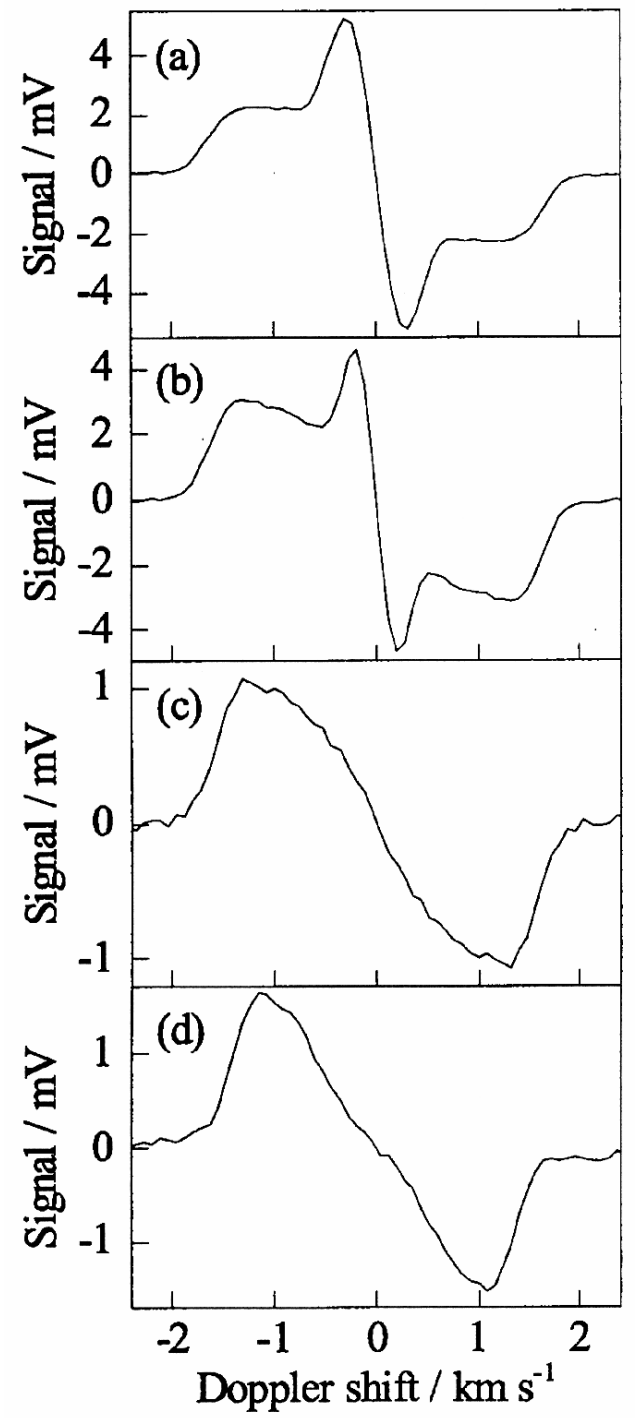

Fig. 7-2

Nascent FM Doppler spectra of selected rotational states of singlet CH_2. The J_{KaKc} quantum numbers and rotational energies of the detected CH_2 states are (a) 2_{12}, 60 cm^{-1}; (b) 4_{14} , 170 cm^{-1}; (c) 5_{15}, 248 cm^{-1}; and (d) 6_{52}, 655 cm^{-1}. The detuning of the laser frequency is expressed in this and subsequent figures as an equivalent Doppler shift in velocity units.

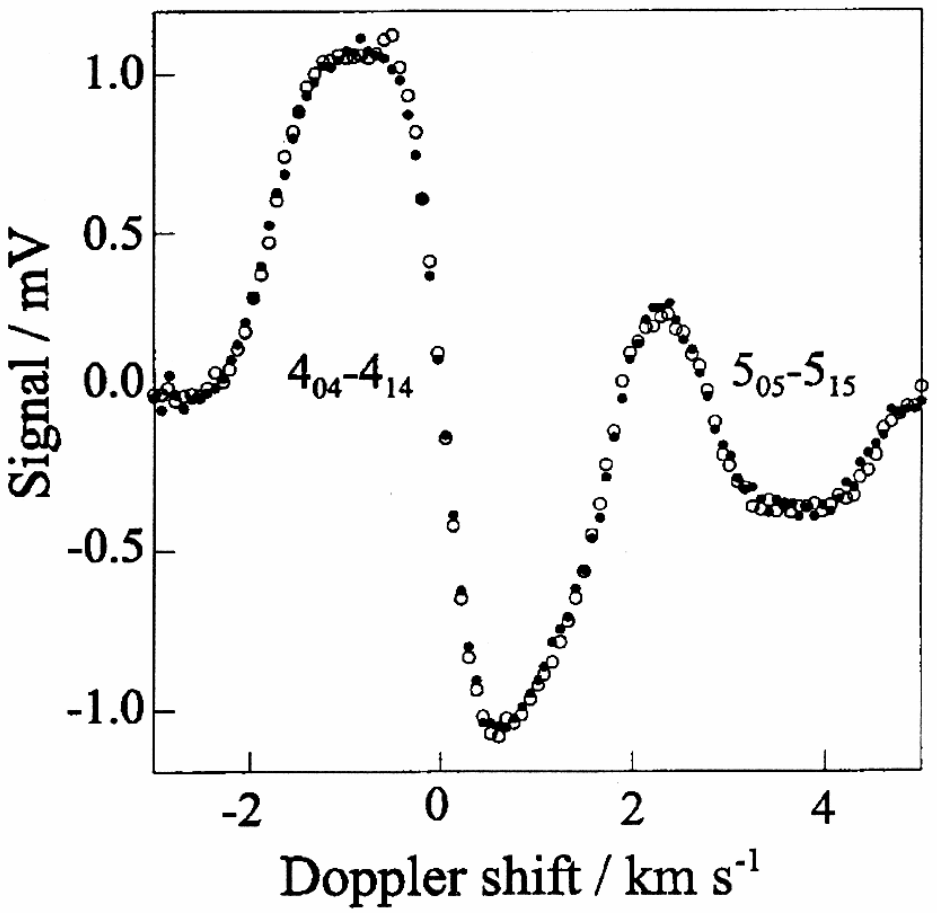

Fig. 7-3
Test for velocity anisotropy of CH_2 figments from room temperature dissociation of ketene at 308 nm. Interleaved measurements are shown for two pump-probe geometries, switching the linear polarization direction of the photolysis laser. ●, photolysis laser polarization parallel to probe propagation direction; ○, photolysis laser polarization parallel to probe polarization direction.

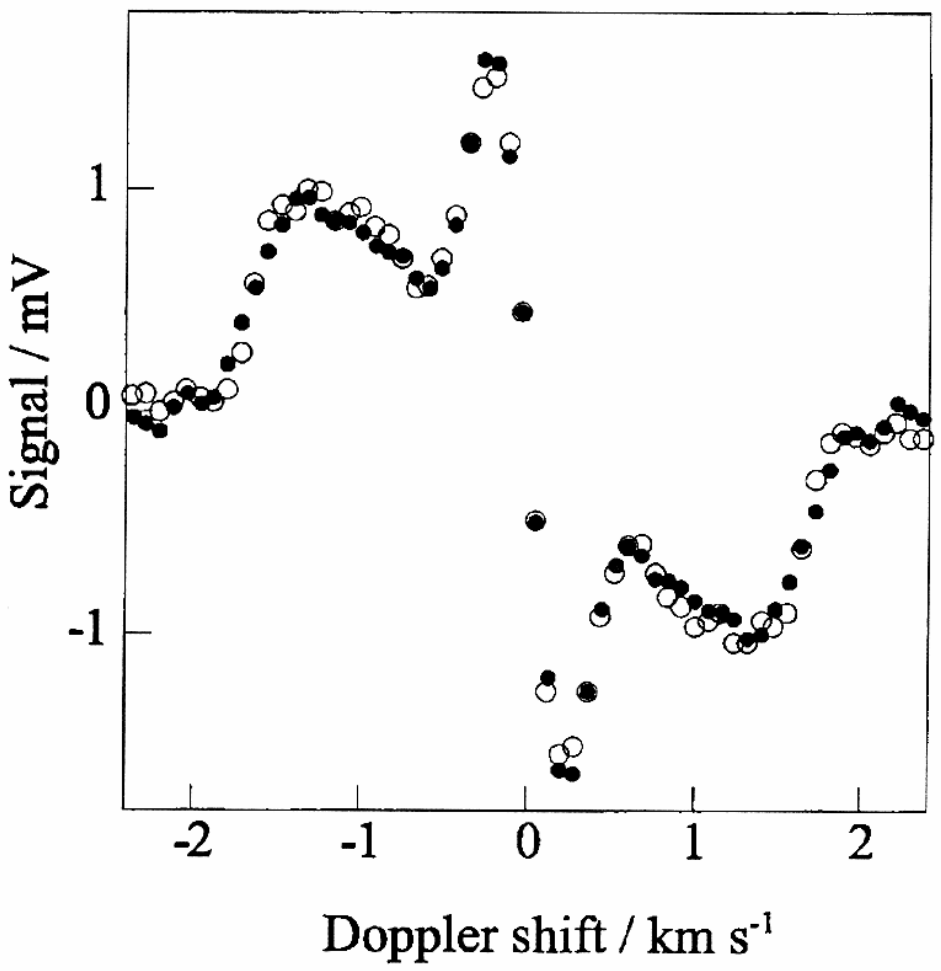

Fig. 7-4
Test for rotational polarization of CH_2 figments. Comparison of R- and Q-branch transitions 4_{31}-3_{21} (●) and 3_{31}-3_{21} (○). The signal from the weaker Q-branch transition has been scaled up by a factor of 3.2 to compare the shapes, which are indistinguishable.

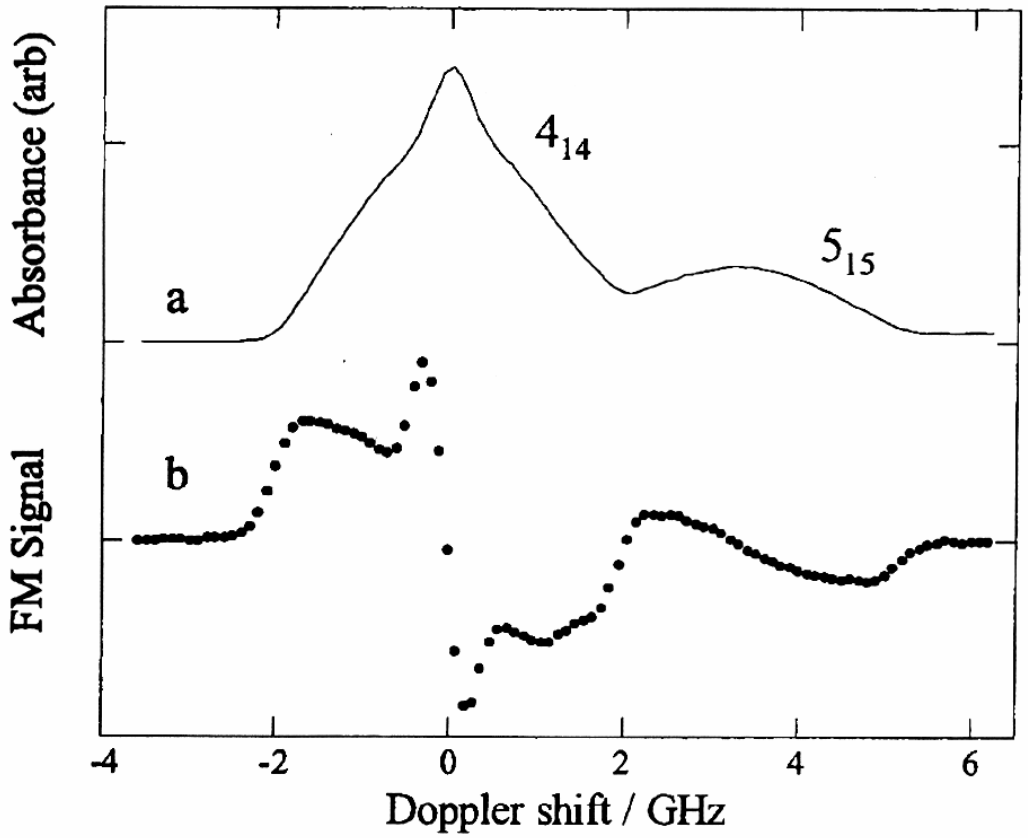

Fig.7- 5
Adjacent rotational lines of CH_2 display a slow component attributed to CO (v = 1) produced in coincidence with CH_2 in the 4_{14} but not the 5_{15} rotational state, 78 cm^{-1} higher in energy. (a) FM spectrum transformed to absorption and (b) raw FM spectrum.

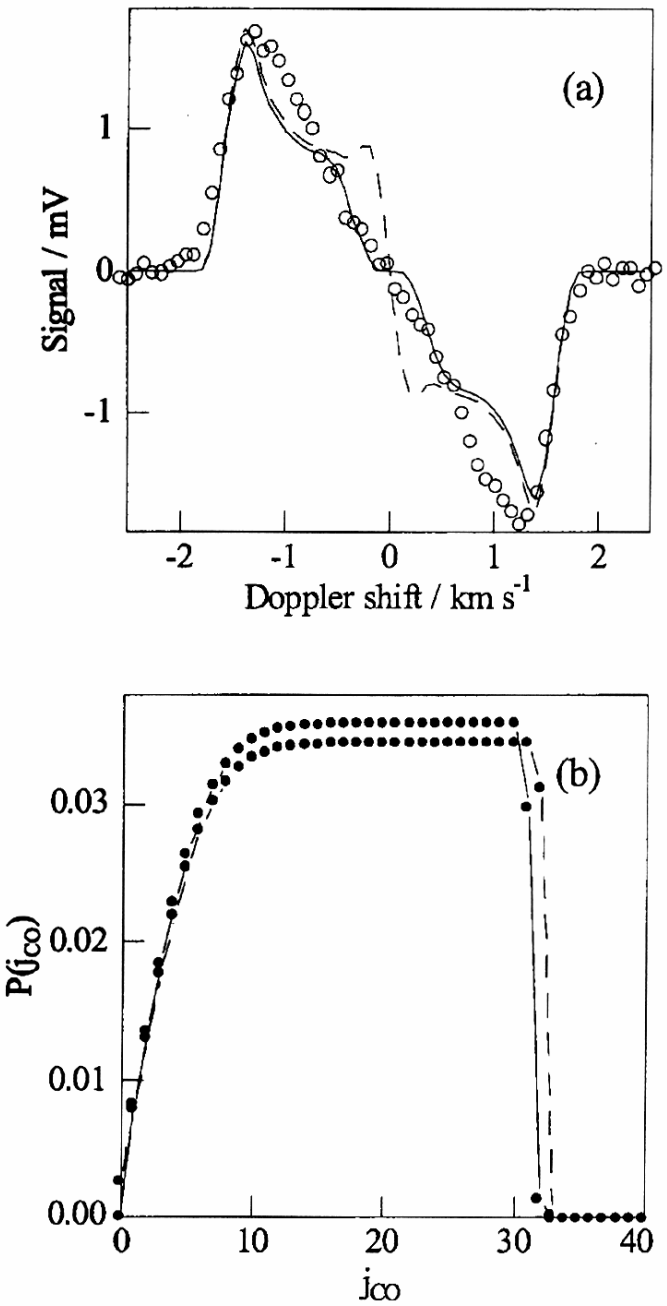

Fig. 7-6

FM Doppler spectra for CH_2 rotational state 5_{14}. (a) Comparison of observed (symbols) and simulations, scaled to a common maximum. Solid line is PST calculation with a 4-Å b_{max}. Dashed line is PST calculation with $b_{max} = \infty$. (b) PST distribution of CO (v = 0) rotational states in coincidence with the 5_{14} level of CH_2 from a 20 K sample of ketene excited at 308 nm, leading to the simulations in panel (a). The dashed line neglects the centrifugal barrier; the solid line shows the effect of a 4-Å maximum impact parameter.

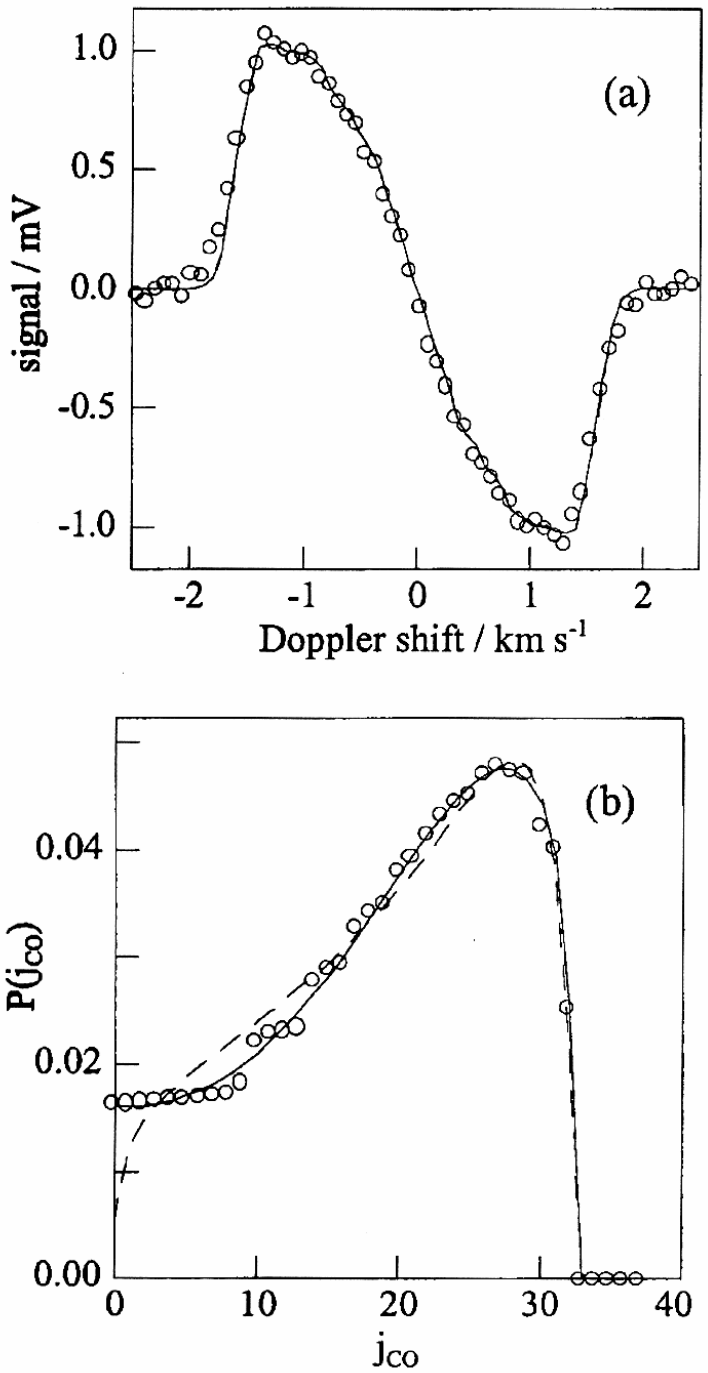

Fig.7- 7

Three least-squares fits to a CH_2 5_{15} FM Doppler profile. (a) Data (symbols) and fits (indistinguishable solid lines). (b) Coincident distribution of j_{CO} derived by three different least-Squares methods. Symbols are from a six-term SVD solution to the under determined 32 linear equations; the solid line is a fit to a three-parameter function; the dashed line is a fit to a four-parameter function.

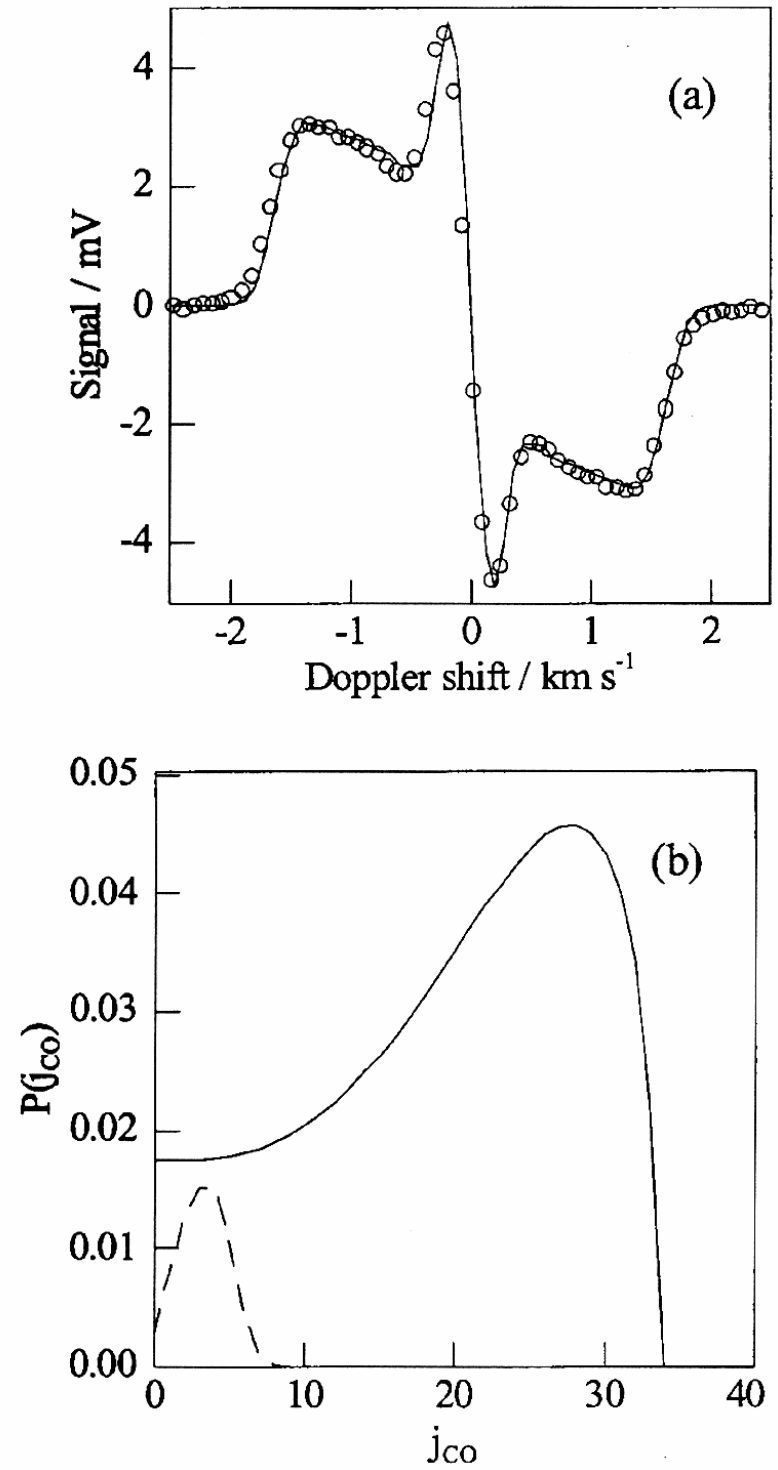

Fig. 7-8

Sample fit to FM Doppler profile for CH_2 4_{14} state. (a) Data (symbols) and fit (line). (b) Coincident rotation distribution for CO (v = 0) component, solid line; coincident distribution for CO (v = 1) component, dashed line. This fit gives 0.07 for the vibrational branching ratio of CO produced in coincidence with this CH_2 state, the ratio of areas under the dashed and solid curves.

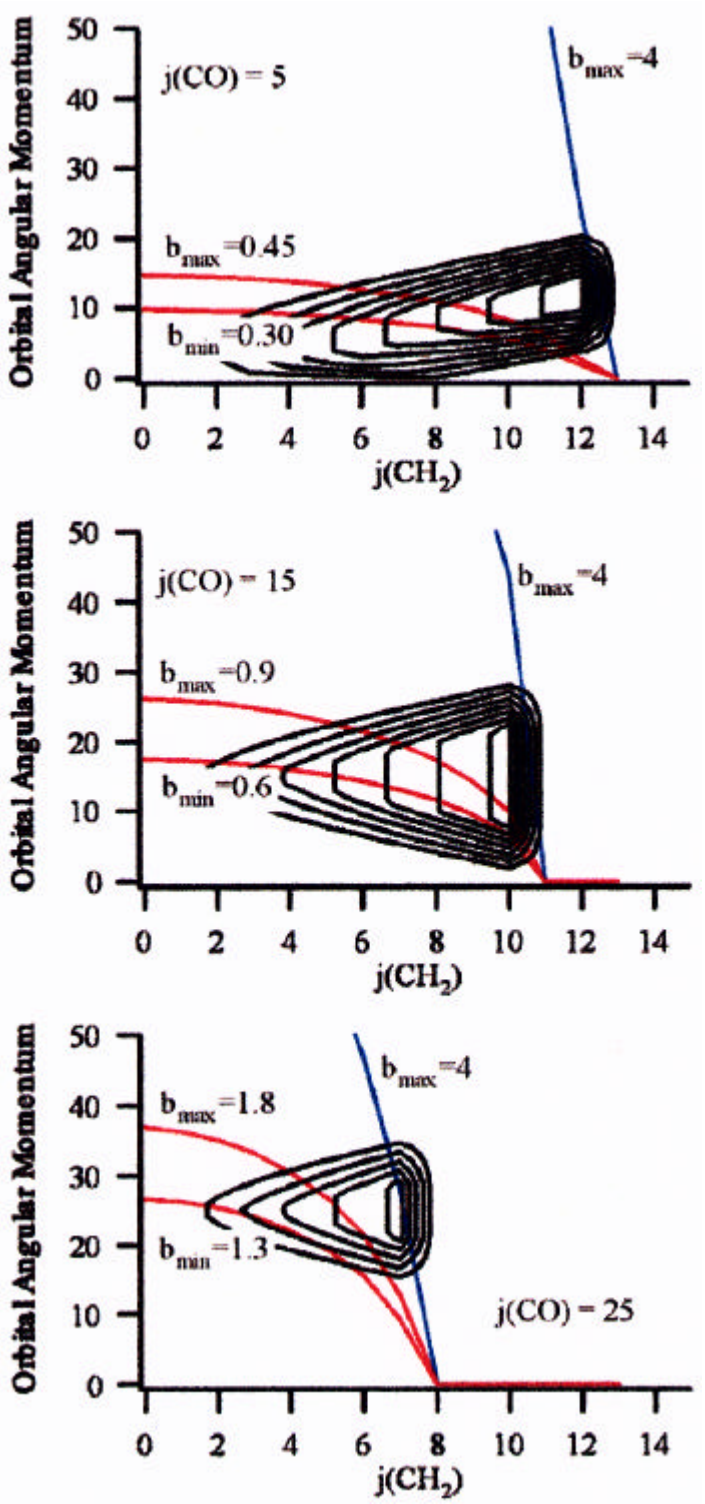

Fig.7- 9

Orbital angular momentum distributions for coincident channels in a diatom plus spherical top model of PST and RPST. Upper and lower bounds on the impact parameter (in Å) correspond to the indicated bounds on *l*.

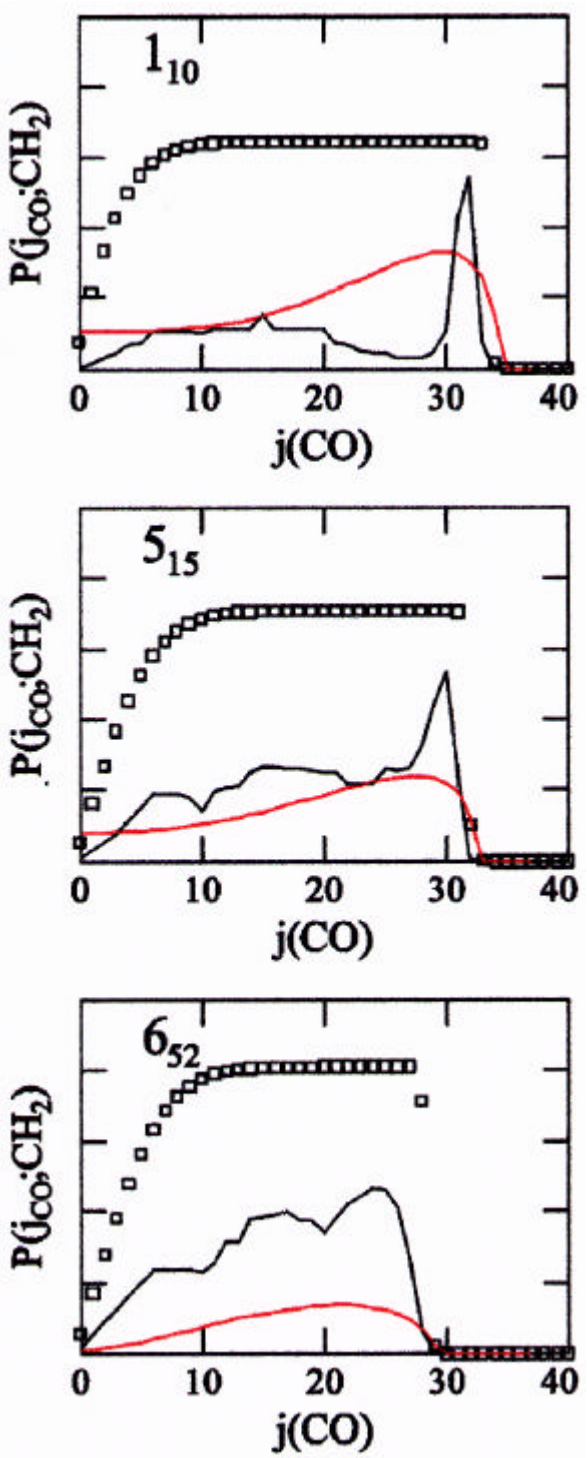

Fig. 7-10
Comparison of CO rotational distributions coincident with selected CH_2 (0,0,0) rotationa1 states: J_{KaKc} = 1_{10}, 5_{15}, and 6_{52}. The open squares are correlated distributions computed with PST. The solid black lines are computed with RPST using interpolated b_{min} and b_{max} parameters from ref 22. The red lines are the experimental distributions derived from the Doppler profiles. Their shapes have been determined from analysis of the Doppler spectra; normalization relative to PST has been estimated from experimental rates and global product distributions.

Table 7-1. CH_2 transition used in the b $^1B_1$ (0,8,0)←a $^1A_1$ (0,0,0)

transition	frequency (cm^{-1})	energy (cm^{-1})	j_{max} CO $v = 0^b$	j_{max} CO $v = 1^b$	$(v = 1):(v = 0)^c$
$2_{02}-1_{10}$	12 234.82	31.3	34	8	0.23 ± 0.04
$2_{02}-2_{12}$	12 206.550	59.6	33	7	0.16 ± 0.04
$3_{31}-2_{21}$	12 224.50	98.5	33	6	0.18 ± 0.03
$3_{30}-2_{20}$	12 223.25	99.6	33	6	0.17 ± 0.06
2_{02} - 3_{12}	12 134.13	132.0	33	5	0.16 ± 0.03
$3_{31}-3_{21}$	12 164.49[a]	158.5	33	4	0.09 ± 0.04
$4_{31}-3_{21}$	12 230.21[a]	158.5	33	4	0.09 ± 0.04
$4_{04}-4_{14}$	12 204.09	170.4	33	3	0.06 ± 0.02
$5_{05}-5_{15}$	12 204.19	247.9	32	closed	0.0
$4_{04}-5_{14}$	12 070.10	304.4	31	closed	0.0
$6_{06}-6_{16}$	12 206.546	339.7	31	closed	0.0
$5_{42}-6_{52}$	12 294.95	655.2	29	closed	0.0

[a] These transitions are from a different vibrational band, terminating in a state of mixed b (0,11,0) and a (0,9,0) character. [b] Highest rotational level of CO energetically allowed from 308-nm excitation of ketene in its lowest nuclear-spin-conserving state. [c] Experimental ratio of CO vibrational states produced in coincidence with each CH_2 rotational state.

Chapter 8

C-Br Bond Rupture in 193 nm Photodissociation of Vinyl Bromide [a]

[a] Published on *Chemical Physics* **231**, 345-353 (1998)

8.1. Introduction

The C=C torsion in ethylene upon $\pi^*\leftarrow\pi$ electronic excitation is a classic example for an essential role of molecular deformation in photochemical process. The $^1(\pi,\pi^*)$ state has a potential minimum at a perpendicular geometry of the two CH_2 groups, where the crossing of $^1(\pi,\pi^*)$ and the ground state surfaces induces efficient internal conversion leading to *cis-trans* photoisomerization [1,2]. Under collision-free conditions, vibrationally-excited ethylene thus produced in the ground state ultimately undergoes atomic or molecular hydrogen elimination [3-5].

Halogen substitution of ethylene provides an interesting variation to the photochemical dynamics of ethylene, since it introduces $^1(\pi(X),\sigma^*(C\text{-}X))$ and $^1(n(X),\sigma^*(C\text{-}X))$ repulsive surfaces in the vicinity of the $^1(\pi,\pi^*)$ state. The surface crossing between the $^1(\pi,\pi^*)$ and $^1(\pi$ or $n,\sigma^*)$ states is expected to induce rapid C-X bond rupture. On the other hand, branching to the ground state leads to H, X, H_2 and HX elimination [6-23].

In our previous works [13,18], photodissociation of vinyl chloride (VCl) and dichloroethylenes (DCEs) has been investigated by two-dimensional (2D) ion imaging method [24-26]. The electronic relaxation processes from the $^1(\pi,\pi^*)$ state? have been discussed in terms of the speed and angular distributions of Cl atoms, since both relaxation to the repulsive and ground states produce Cl atoms. Fine structure branching of Cl ($^2P_{3/2}$ and $^2P_{1/2}$) was also employed as a probe of adiabaticity in the dissociation process. It was found that the dissociation from the ground state yields both of Cl($^2P_{3/2}$) and Cl*($^2P_{1/2}$), despite that the ground state is adiabatically correlated with the Cl asymptote [8,11,14,15,18]. The result indicated an efficient non-adiabatic transition from the ground state to the upper state surface leading to Cl* is induced even with a small kinetic energy for C-Cl stretching coordinate. This manifests the role of molecular vibration that induces a non-adiabatic transition between multidimensional potential energy surfaces of polyatomic molecules.

In this chapter, 193 nm photodissociation of vinyl bromide (VBr) is discussed. It is of particular interest to examine fine-structure branching of Br(^2P_J), since the spin-orbit splitting in the asymptotes is increased by a factor of four from 2.5 kcal mol^{-1} in Cl to 10.5 kcal mol^{-1} in Br.

8.2. Experimental

A supersonic beam 1 mm in diameter, generated by a pulsed valve (General Valve series 9, or a piezoelectric valve [27]) and two skimmers 0.5 mm in diameter, was introduced into a time-of-flight (TOF) mass spectrometer in the direction parallel to the electric field vector. The source and main chambers were evacuated by a diffusion pump (Edwards Diffstack 250/2000, 2000 l s^{-1}) and a turbo molecular pump (Mitsubishi PT500, 500 l s^{-1}), respectively. For Br($^2P_{3/2}$) measurement, a sample gas of VBr 1 % seeded in He was expanded with a stagnation pressure of 0.6 - 1.0 atm. More concentrated sample (5%) and higher stagnation pressure (1.8 atm) were used for Br($^2P_{1/2}$) measurements in order to compensate for the low signal level.

There was no noticeable change of the images for different concentration of the sample (1 - 10 %), stagnation pressure (0.5 - 2 atm), and nozzle temperature (293 - 393 K), indicating that there is no contribution of clusters to the observed signal. When the pulsed valve was operated, the vacuum pressures were $(3 - 6) \times 10^{-6}$ Torr in the beam source and $(1 - 5) \times 10^{-7}$ Torr in the main chamber, respectively. The sample purchased from Aldrich (purity 98%) was used without further purification.

At 79 mm downstream from the nozzle, the molecular beam intersected with the pump and probe laser beams which were counter-propagated perpendicular to the molecular beam. The output of an ArF laser (Lambda Physik Compex 101F) was polarized using ten quartz plates held at Brewster angle and was used as a pump beam. A probe beam was the second harmonic of the output of a YAG-pumped dye laser (Spectra Physics GCR230 + Lumonics HD500) generated in a BBO(b-BaB_2O_4) crystal. The wavelength of the dye laser was calibrated with a Fizeau wavelength meter (New Focus 7711). The time delay between the photolysis and probe laser pulses was kept within 20 ns with a delay generator (Stanford Research Systems DG535). Br($^2P_{3/2}$) and Br*($^2P_{1/2}$) atoms were ionized by (2+1) REMPI using the resonances of $^4D_{3/2} \leftarrow\leftarrow {}^2P_{3/2}$ (260.63 nm) and $^2S_{1/2} \leftarrow\leftarrow {}^2P_{1/2}$ (262.55 nm). The probe laser beam was focused by an axisymmetric lens (f = 250 mm), while the photolysis beam was unfocused. The pump laser intensities used were < 5 mJ cm^{-2} $pulse^{-1}$ (193 nm), while the probe laser intensities were 20 - 200 μJ $pulse^{-1}$.

The ions produced by REMPI were accelerated up to the kinetic energy of 4.5 keV and projected onto an imaging ion detector (Photek OFD40/2) which consists of a pair of

microchannel plates (40 mmϕ Chevron) and a phosphor screen (P20) attached to one end of the fiber-optic bundle mounted through a vacuum flange. Standard 1D TOF spectra of ions were measured by applying constant voltages on the microchannel plates (- 850 V for the first plate and + 850 V for the second) and monitoring an AC component of the phosphor voltage. Ion images were measured by applying a pulsed high voltage (Directed Energy, GRX-1.5K-E) to the first microchannel plate (MCP). The TOF of Br^+ was about 6.7 - 7.3 μs depending on the acceleration voltage (~ 4.5 kV). The two isotopes of ^{79}Br (natural abundance 50.69%) and ^{81}Br (49.31%) were well-resolved in the 1D TOF spectra, while these isotopes were not separated in 2D imaging because of long HV pulse duration (200 - 500 ns) applied to the MCP. The secondary electrons ejected from the MCP were projected onto a phosphor screen (P20) kept at 3.5 - 4.5 kV, and the transient image that appears at the end of fiber-optic bundle located outside of the vacuum chamber was captured by a thermoelectrically-cooled CCD camera (Princeton Instruments CCD-512SF, 512 × 512 pixels). The images were typically integrated for 50,000 laser shots. While integrating the images, the probe laser wavelength was scanned for a number of times over the entire Doppler-broadened absorption line. The apparatus was operated at 25 Hz.

For the acceleration of ions, both of the electrodes using electroformed meshes and so-called velocity mapping setup without meshes [28] have been employed. Although the latter provides two-dimensional spatial focusing of ions, the former used with a small field gradient and fine wire meshes (Backbee-Mears, 333 lines $inch^{-1}$) yielded good spatial resolution [18]. Essentially the same result was obtained with both setups, except that the shadow of meshes was eliminated in velocity mapping. In both cases, a series of stainless steel rings were used for the electrodes to avoid the penetration of ground potential that distorts the field.

The fine structure branching ratio of Br in photodissociation of VBr was determined by comparing the Br and Br* signals with those in 193 nm photodissociation of HBr, for which the branching ratio of [Br*]/[Br] = 0.14/0.86 has been established [29,30]. Molecular beams of HBr were generated by expanding sample gases of HBr (3 % to 17 % seeded in He) with a stagnation pressure of 1 - 2 atm relative to the vacuum from a pulsed nozzle at a room temperature. In order to ascertain that the measurement of the branching ratio is not affected by any orbital alignment of Br, the signal intensities of Br atoms were measured for different polarization combinations, $e_d \parallel e_p$ and $e_d \perp e_p$, where e_d and e_p are the polarization vectors of the pump and probe laser beams. The signal ratio of [Br*]/[Br] was found to be invariant to

the probe laser polarization within an experimental error. The branching ratio [Br*]/[Br] in 193 nm photodissociation of VBr was determined to be 0.06 ± 0.03.

The observed ion images are the 2D projection of the 3D distributions of photofragments. The 2D data were inverted to the flux velocity contour maps by inverse Abel transforms [24-26]. After performing basic image processing on a workstation (Sun SP/LX) [31], an inverse Abel transform was performed on a personal computer (Pentium-120MHz). Due to the property of an inverse Abel transform, the central columns of the transformed data are affected by the noise in an original image, which reduces the accuracy of an analysis for very low translational energy region. Therefore, in order to ascertain the analysis of the low energy region, a forward convolution analysis (iterative fitting) based on Monte-Carlo simulation was employed. We found good agreement between the two approaches.

8.3. Results and Analysis

8.3.1. Speed and angular distributions of Br (^2P_J) atoms

The raw images of Br($^2P_{3/2}$) and Br*($^2P_{1/2}$) are shown in Fig. 8-1a and Fig. 8-2a, respectively. Polarization of the pump and probe lasers are in the vertical direction in the figures. The signal level of Br* was low, so that background noise produced solely by the probe laser beam (shown in Fig. 8-2(b)) was subtracted from Fig. 8-2a to obtain the two-color signal of Br* (shown in Fig. 8-2(c)). On the other hand, background noise was negligible for the Br signal. As seen in Figs. 8-1(a) and 8-2(c), both of the Br and Br* distributions are dominated by high translational energy components with strong angular anisotropy, although slow components are also visible in the inner parts of the images. Fig. 8-1(b) and 8-2(d) are the inverse Abel transforms of the images shown in Figs 8-1(a) and8-2(c), respectively.

It is noted that, if electronic orbitals of Br fragments are aligned, the detection efficiency of Br atoms varies as a function of the angle between the recoil velocity and probe laser polarization. In such a case, photofragment ion distribution will differ from the distribution of neutral fragments, and more complicated analysis is required to extract the original distribution of neutral fragments from the data [32-34]. In the present case, however, the ion images of Br exhibited no dependence on the probe laser polarization, indicating that the electronic orbital of Br is not aligned. Although electronic orbital alignment is diminished by hyperfine coupling in halogen atoms, it is possible to observe residual alignment, if any

[34]. The present result is consistent with photodissociation of VCl and DCEs in which no alignment has been observed for Cl (^2P_J) [14,15,18].

Figure 8-3 shows the angular distributions of (a) Br and (b) Br* corresponding to the center-of-mass (C.M.) translational energy release of 30 - 40 kcal mol^{-1}. Solid lines are the least square fits to the experimental data with a standard functional form of

$$I(q) = s \ / 4p[1 + bP_2(\cos q)]$$

where q is the angle between the polarization of the pump laser and the recoil velocity vector, $P_2(x)$ is the second-order Legendre polynomial, and b is an anisotropy parameter [35]. Anisotropy parameters were determined to be b = 1.3 for Br and b = 1.2 for Br* which are much larger than the value b = 0.45 ± 0.02 (fine-structure unresolved) reported by Wodtke *et al.* using PTS [19].

The speed distribution of Br, $P(v)$, was obtained by integrating the flux velocity contour map (an inverse Abel transform of the image observed) for the angular part. Then, $P(v)$ was converted to the C.M. translational energy release, $P(E_T)$, by assuming energy and momentum conservation in the two-body dissociation into C_2H_3 and Br (Fig. 8-4).

8.3.2. Examination of secondary photodissociation of the molecular product HBr

HX molecular elimination is a major exit channel in photodissociation of vinyl halides; classical trajectory calculations and transition state theory using a global ground state potential of VBr predict that the yield of HBr is an order of magnitude larger than that of Br [20-22]. Therefore, secondary photodissociation of HBr needs to be examined,

$$C_2H_3Br + hn_{pump} \rightarrow C_2H_2 + HBr$$

$$HBr + hn_{pump} \text{ or } hn_{probe} \rightarrow H + Br.$$

If Br atoms are produced by this process, they are expected to appear with small translational energies, since HBr fragments are slow [19] and the mass ratio Br/H is as large as 80.

For molar extinction coefficient 500 l mol^{-1} cm^{-1} of HBr at 193 nm [36], photodissociation of HBr (v = 0) by a pump laser pulse (< 5 mJ cm^{-2} pulse^{-1}) is negligible (< 1 %). We have confirmed that $P(E_T)$ of Br and Br* did not change by reducing the pump laser fluence to be less than 300 μJ cm^{-2} pulse^{-1}.

On the other hand, the secondary photodissociation by a probe laser pulse needs to be more carefully examined. Although, the absorption cross section of HBr(v = 0) at the probe

laser wavelength of 260 nm is quite small, vibrationally excited HBr has larger photoabsorption cross sections; the absorption cross section of HBr (v = 1) at 258.9 nm has been estimated to be $(5.5 \pm 1.1) \times 10^{-20}$ cm^2 which is 34 ± 7 times larger than that of HBr (v = 0) at the same wavelength [37]. The absorption cross section is expected to be even higher for higher vibrational levels ($v \geq 2$).

By taking into account the secondary photodissociation, the yield of Br^+ with low translational energy will be expressed by the following formula

$$[Br^+] \propto I_{probe}^{n}\{[Br] + s_{abs} I_{probe}[HBr]\}.$$

In reducing the laser power, the translational energy distribution is expected to converge to a certain form, when [Br] >> $s_{abs}I_{probe}$[HBr]. In Fig. 8-5 shown are $P(E_T)$ measured with different probe laser intensities. As seen in the figure, the distribution measured at the lowest intensity of 50 μJ pulse^{-1} is considered to be converged.

8.4. Discussion

8.4.1. High translational energy component of Br

The excitation wavelength of 193 nm is in the middle of strong (ε~10,000) π*←π band of VBr [39]. Therefore, VBr is photoexcited to the $^1(\pi,\pi^*)$ state. Although the $^1(\pi,\pi^*)$ state is bound for C-Br stretching coordinate, the anisotropic distribution of Br(^2P_J) indicates that C-Br bond rupture occurs within a rotational period. Such a prompt C-Br rupture, with high translational energy release, is attributed to the dissociation induced by the surface crossing between $^1(\pi,\pi^*)$ and ^{1}(n or π,σ*) states.

For an instantaneous dissociation, b is given by $2P_2(\cos c)$, where c is the angle between the transition dipole moment and the recoil direction. If we use b =1.2 and axial recoil approximation with the ground state geometry, the direction of the transition dipole moment is calculated to be 31.1 ± 3° from the C-Br axis, or 26.4 ± 3° from the C=C bond (see Fig. 8-6(b)). The axial recoil from the ground state planar geometry is rationalized for VBr by two reasons. One is that the repulsive surfaces are expected to be planar, since electronic excitations are localized at the C-Br bond. The other reason is that, even if VBr is twisted, the C=C twist is essentially the rotation of CH_2 group with respect to CHBr, since the moment

of inertia of CHBr group is 140 times larger than that of CH_2. Therefore, C-Br bond direction is not affected by the C=C twist.

Ab initio calculation performed by Yamashita at the level of cc-pVTZ/ECP28MWB[2s3p]/CASSCF predicts that the angle between the transition dipole moment of the $\pi^*\leftarrow\pi$ transition and C-Br bond is 27.4 ° [39]. The agreement between our data and the calculation indicates that the dissociation is extremely fast (*b* is not reduced by molecular rotation of VBr).

The peak of $P(E_T)$ is quite similar for the Br and Br* channels, despite that Br* is energetically higher than Br by 10.5 kcal mol^{-1}, indicating that Br* is not produced by non-adiabatic transition in the asymptotic region. The peak of $P(E_T)$ for Br channel is wider than that for Br* and cannot be fitted to a single Gaussian function. This suggests that the Br formation is due to more than two repulsive surfaces.

8.4.2. Low translational energy component of Br

There are several possible dissociation channels leading to low energy Br. These are C-Br bond rupture via internal conversion (IC) to the ground state,

$$C_2H_3Br\ (\pi,\pi^*) \rightarrow C_2H_3Br^{**}\ (\tilde{X}) \rightarrow C_2H_3 + Br(^2P_J) \qquad (a)$$

the formation of an excited of vinyl radical,

$$C_2H_3Br\ (\pi,\pi^*) \rightarrow C_2H_3(\tilde{A}) + Br(^2P_J) \qquad (b)$$

and

$$C_2H_3Br\ (\pi,\pi^*) \rightarrow C_2H_3Br^{**}\ (\tilde{X}) \rightarrow C_2H_2\ Br + H \rightarrow C_2H_2 + H + Br. \qquad (c)$$

Relevant exit channels and thermochemical values are shown in Table 1 [20-22,40-42].

As for channel (b), the adiabatic $\tilde{A}-\tilde{X}$ electronic excitation energy of C_2H_3 has not been experimentally determined; Hunziker *et al.* reported an absorption spectrum that is compatible with the $\tilde{A}-\tilde{X}$ transition of vinyl radical, however, the (0,0) band has not been established [43]. Mebel *et al.* have performed *ab initio* calculations on vinyl radical and provided the $\tilde{A}-\tilde{X}$ vertical excitation energy of 3.23 eV and the adiabatic excitation energy of 2.37 eV [41]. If we employ the C-Br bond energy of 79.2 kcal mol^{-1} obtained by G2 theory with effective core potential [44], the available energy for channel (b) is estimated to be less than 14.2 kcal mol^{-1} ($Br(^2P_{3/2})$ channel). From the energetic viewpoint, this channel cannot be ruled out. However, it is noted that the $^1(\pi,\pi^*)$ PES has a large gradient along the

C=C twisting which presumably directs the system to the crossing point with ^{1}(n or π,σ^*) and the ground states. Therefore, this reaction seems unfavorable from the dynamic viewpoint.

In Fig. 8-4, it is seen that the $P(E_T)$s of Br and Br* channels are different in the lowest energy region; the $P(E_T)$ of Br* decreases monotonically as E_T approaches to 0 kcal mol^{-1}, while that of Br channel is slightly enhanced in the same region. Similar enhancement of $P(E_T)$ in the low energy region has been observed in 193 nm photodissociation of DCEs, which was ascribed to adiabatic secondary dissociation leading to Cl atoms. Therefore, the enhancement of Br distribution at low energy is assigned to secondary C-Br bond rupture of C_2H_2Br radical. An exit barrier is not expected for the dissociation from HCCHBr into C_2H_2 + Br, since the kinetic rate constant for the addition of Br to acetylene at high pressure limit shows a negative temperature dependence [44]. Accordingly, the Br distribution at low energy was peaked at ~ 0 kcal mol^{-1} in Fig. 8-4.

If the Br atom is ejected from α-bromovinyl radical, translational energy release could be peaked away from 0 kcal mol^{-1}, since H atom needs to migrate from β position. However, low energy Br distribution is peaked around 0 kcal/mol, indicating that this is not the case. Therefore, our result does not support preferential ejection of α-hydrogen. On the similar reaction of 193 nm photodissociation of VCl, Riehl and Morokuma have estimated the stability of α-, *cis* -β, and *trans* β-chlorovinyl radicals (Fig. 8-6b) by *ab initio* calculations and found that α-chlorovinyl radical is the most stable; C-H_α bond energy calculated was 105.7 kcal mol^{-1} and C-$H_{\beta,trans}$ was 109.1 kcal mol^{-1} [23]. Interestingly, however, Huang *et al.* observed that β hydrogen is ejected more than α hydrogen in photodissociation of VCl and α-D VCl, although *cis* and *trans*-H atoms have not been discriminated [9-11]. This was in accord with the work by Laursen *et al.* on photoinitiated reaction of $CH_2CCl \rightarrow CHClCH$ in rare gas matrices, where no reverse reaction of $CHClCH \rightarrow CH_2CCl$ was observed [45], and β-chlorovinyl radical was suggested to be more stable than α-chlorovinyl radical.

We suggest that low energy Br and Br* atoms are mainly produced by channel (a). It is noted that the ground state of VBr is correlated adiabatically to the asymptote of CH_2CH + Br, so that the system must undergo non-adiabatic transition to produce Br*. One dimensional non-adiabatic transition theory predicts that the event with small velocity leads to adiabatic process, as shown by Massey adiabaticity parameter,

$$x = \frac{R}{v}\frac{\Delta E}{\hbar}$$

where R is the length of the interaction region of the potential curves, ΔE is the energy separation of the interacting states, and v is the relative speed of separation. However, non-adiabatic transition to the upper surface leading to $^2P_{1/2}$ is induced by molecular vibration other than C-X stretching [18].

In Fig. 8-4 the variation of anisotropy parameter as a function of a translational energy is also shown. The error bars indicate the confidence range of 95%. It is seen that the anisotropy persists down to low energy region in Br* channel. From the forward convolution on Br* distribution, the anisotropy of the low energy channel was estimated to be $b \cong 0.6$. The reduction of anisotropy in Br channel as the translational energy approaches to 0 is ascribed to the contribution of isotropic distribution due to the channel (c-1).

The lifetime of metastable state can be estimated from the anisotropy parameter. Using the ground state rotational constants of VBr, A = 54265.29, B = 4162.537, and C = 3862.453 MHz; k = -0.988) [46] and assuming T_{rot} = 20K, the reduction of anisotropy is calculated as a function of time, as shown in Fig. 8-7. If we assume the anisotropy parameter of 1.3 for an instantaneous dissociation and 0.6 (obtained from Br* data) for the dissociation from a metastable ground state, the lifetime of the ground state is estimated to be 2.2 ps. By considering an experimental uncertainty about the b values,. the lifetime is most likely to be 1-5 ps. Classical trajectory calculations performed by Abrash *et al.* predict that the lifetime of VBr in the ground state is 2 ps at an internal energy of 5.0 eV (corresponds to the photodissociation wavelength of 248 nm) and 470 fs at 6.44 eV (193 nm) [21]. Our value of 2.2 ps is within factor of 5 from the theoretical prediction. The lifetime of metastable VBr is presumably determined by the rate of HBr elimination [20-22]. Since VBr is activated by electronic relaxation from the excited state, the initial direction of the trajectory on the ground state surface is much biased. Therefore, deviation from statistical calculation can be anticipated.

8.5. Conclusions

Photofragment ion imaging has been applied to 193 nm photodissociation of vinyl bromide. The C-Br bond rupture predominantly occurs by rapid electronic relaxation from the optically-excited (π,π*) state to (n(Br) or π(Br), σ*(C-Br)) repulsive states.

Translational energy release is comparable between the Br and Br* channels, despite that the available energy is 10.5 kcal mol^{-1} smaller in the Br* channel. This suggests that the state leading to the $^2P_{1/2}$ is more repulsive along the C-Br stretching than that leading to $^2P_{3/2}$ at the crossing point with the (π,π*) state. Br atoms have exhibited no orbital alignment. Low translational energy components of Br and Br* were assigned to the dissociation of VBr from the ground state, although contributions of VBr from the secondary dissociation of C_2H_2Br radical is also suggested for the Br channel. The anisotropic distribution of low energy Br atoms indicates that the ground state VBr has a lifetime (1-5 ps) shorter than its rotational period (4.7 ps; T_{rot} = 20 K).

References

[1] R.J. Buenker, V. Bonacic-Koutecký, L. Pogliani, J. Chem. Phys. **73**, 1836 (1980).

[2] I. Ohmine, J. Chem. Phys. **83**, 2348 (1985).

[3] S. Satyapal, G.W. Johnston, R. Bersohn, I, Oref, J. Chem. Phys. **93**, 6398 (1990).

[4] B.A. Balko, J. Zhang, Y.T. Lee, J. Chem. Phys. **97**, 935 (1992).

[5] E.F. Cromwell, A. Stolow, M.J.J. Vrakking, Y.T. Lee, J. Chem. Phys. **97**, 4029 (1992).

[6] M.J. Berry, J. Chem. Phys. **61**, 3114 (1974).

[7] M. Umemoto, K. Seki, H. Shinohara, U. Nagashima, N. Nishi, M. Kinoshita, R. Shimada, J. Chem. Phys. **83**, 1657 (1985).

[8] Y. Mo, K. Tonokura, Y. Matsumi, M. Kawasaki, T. Sato, T. Arikawa, P.T.A. Reilly, Y. Xie, Y. Yang, Y. Huang, R.J. Gordon, J. Chem. Phys. **97**, 4815 (1992).

[9] P.T.A. Reilly, Y. Xie, R.J. Gordon, Chem. Phys. Lett. **178**, 511 (1991).

[10] G. He, Y. Yang, Y. Huang, R.J. Gordon, J. Phys. Chem. **97**, 2186 (1993).

[11] Y. Huang, Y. Yang, G. He, R.J. Gordon, J. Chem. Phys. **99**, 2752 (1993).

[12] K. Sato, Y. Shihira, S. Tsunashima, H. Umemoto, T. Takayanagi, K. Furukawa, S. Ohno, J. Chem. Phys. **99**, (1993) 1703.

[13] T. Suzuki, K. Tonokura, L.S. Bontuyan, N. Hashimoto, J. Phys. Chem. **98**, 13447 (1994).

[14] Y. Huang, G. He, Y. Yang, S. Hashimoto, R.J. Gordon, Chem. Phys. Lett. **229**, 621 (1994).

[15] Y. Huang, Y. Yang,G. He, S. Hashimoto, R.J. Gordon, J. Chem. Phys. **103**, 5476 (1995).

[16] P.W. Browning, D.C. Kitchen, M.F. Arendt, L.J. Butler, J. Phys. Chem. **100**, 7765 (1996).

[17] T.L. Myers, D.C. Kitchen, B. Hu, L.J. Butler, J. Chem. Phys. **104**, 5446 (1996).

[18] K. Tonokura, L.B. Daniels, T. Suzuki, K. Yamashita, J. Phys. Chem. A **101**, 7754 (1997).

[19] A.M. Wodtke, E.J. Hintsa, J. Somorjai, Y.T. Lee, Isr. J. Chem. **29**, 383 (1989).

[20] G.J. Mains, L.M. Raff, S.A. Abrash, J. Phys. Chem. **99**, 3532 (1995).

[21] S.A. Abrash, R.W. Zehner, G.J. Mains, L.M. Raff, J. Phys. Chem. **99**, 2959 (1995).

[22] R. D. Kay, L.M. Raff, J. Phys. Chem. A **101**, 1007 (1997).

[23] J.F. Riehl, K. Morokuma, J. Chem. Phys. **100**, 8976 (1994).

[24] D.W. Chandler, P.L. Houston, J. Chem. Phys. **87**, 1445 (1987).

[25] B.J. Whitaker, "Research in chemical kinetics, Vol. 1" eds. R.G. Hampton and G. Hancock (Elsevier, 1993).

[26] A.J.R. Heck, D.W. Chandler, Ann. Rev. Phys. Chem. **46**, 335 (1995).

[27] D. Proch, T. Trickl, Rev. Sci. Instrum. **60**, 713 (1989).

[28] D.H. Parker, A.T.J.B. Eppink, J. Chem. Phys. **107**, 2357 (1997).

[29] Z. Xu, B. Koplitz, C. Wittig, J. Phys. Chem. **92**, 5518 (1988).

[30] F. Magnotta, D.J. Nesbitt, S.R. Leone, Chem. Phys. Lett. **83**, 21 (1981).

[31] J. Rasure, D. Argiro, T. Sauer, C. Williams, Inter. J. Imaging Systems and Technology **2**, 183 (1990).

[32] Y. Mo, H. Katayanagi, M.C. Heaven, T. Suzuki, Phys. Rev. Lett. **77**, 830 (1996).

[33] T. Suzuki, H. Katayanagi, Y. Mo, K. Tonokura, Chem. Phys. Lett. **256,** 90 (1996).

[34] A.S. Bracker, H.M. Bevsek, F.C. Sailes, A.G. Suits, Y.T. Lee, O.S. Vasyutinskii, Phys. Rev. Lett. in press.

[35] R.N. Zare, Mol. Photochem. **4**, 1 (1972).

[36] B. J. Hueber, R. M. Martin, J. Phys. Chem. **72**, 3046 (1968).

[37] P. F. Zittel, D. D. Little, J. Chem. Phys. **71**, 713 (1979).

[38] J. Schander, B.R. Russell, J. Am. Chem. Soc. **98**, 6900 (1976).

[39] K. Yamashita, private communication.

[40] M. N. Glukhovtsev, R. B. Bach, J. Phys. Chem. A **101**, 3574 (1997).

[41] A. M. Mebel, Y.-T. Chen, S.-H. Lin, Chem. Phys. Lett. **275**, 19 (1997).

[42] K. M. Ervin, S. Gronert, S.E. Barlow, M.K. Gilles, A.G. Harrison, V.M. Bierbaum, C.H. DePuy, W.C. Lineberger, G.B. Ellison, J. Am. Chem. Soc. **112**, 5750 (1990).

[43] H.E. Hunziker, H. Kneppe, A.D. McLean, P. Siegbahn, H.R. Wendt, Can. J. Chem. **61**, 993 (1983).

[44] I. Barnes, V. Bastian, K. H. Becker, R. Overath, Z. Tong, Int. J. Chem. Kinet. **21**, 499 (1989).

[45] S. L. Laursen, G. C. Pimentel, J. Phys. Chem. **94**, 8175 (1990).

[46] K. D. de Varent, Ann. Soc. Sci. Bruxelles **84**, 277 (1970).

Table 8-1 Heats of formation and available energies for C-Br, C-H bond ruptures in 193 nm photodissociation of VBr.

Reaction	Products	ΔH_0 (E_{avl}) kcal/mol		References
		Br	Br*	
(a)	C_2H_3 (X) + Br	79.2(68.8)	89.7(58.3)	37
(b)	C_2H_3 (Ã) + Br	133.8(14.2)	144.3(3.7)	36,37
(c-1)	HCCH + Br + H	112.8(35.2)	123.3(24.7)	35,37
(c-2)	H_2CC + Br + H	160.2	170.7	35,37
(d)	H_2CCBr + H	100(48)		a
(e-1)	HCCBr + H + H	149.2		16,b
(e-2)	CCHBr + H + H	195.9		16,b

Assuming C-H bond energy of 100 kcal/mol.

D_0(H-H) = 104.1 kcal/mol (ΔH_0(H) = 52.07 kcal/mol).

The parentheses in the table show the available energy for each channels in the 193 nm photodissociation(*hn* = 148 kcal/mol).

Figures for Chapter 8

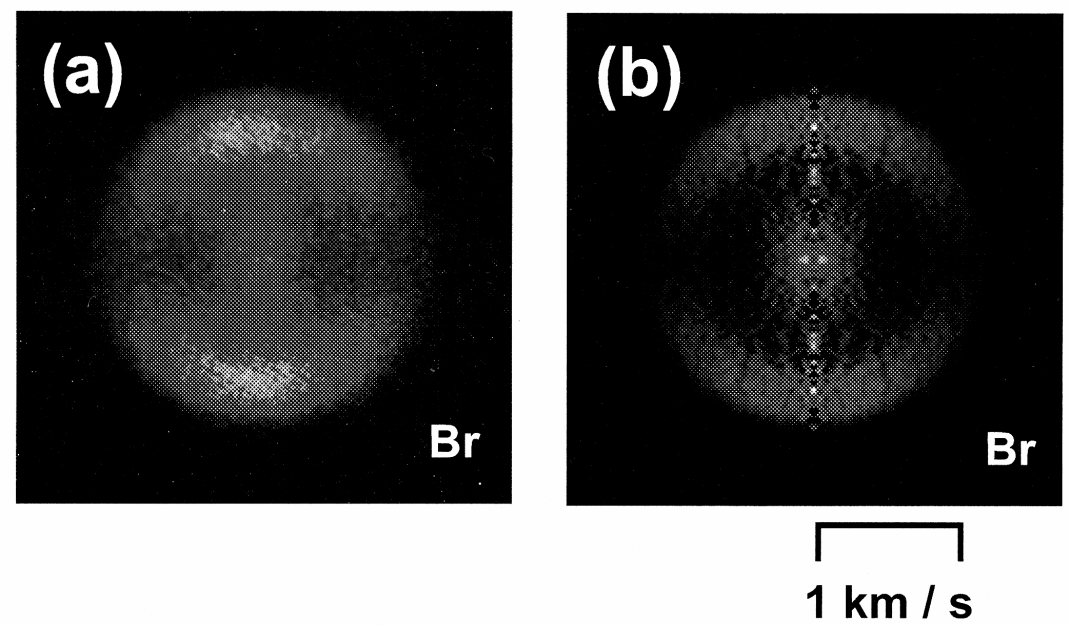

Fig.8-1
(a) The raw image of Br($^2P_{3/2}$) produced by 193 nm photodissociation of vinyl bromide and (b) its inverse Abel transform.

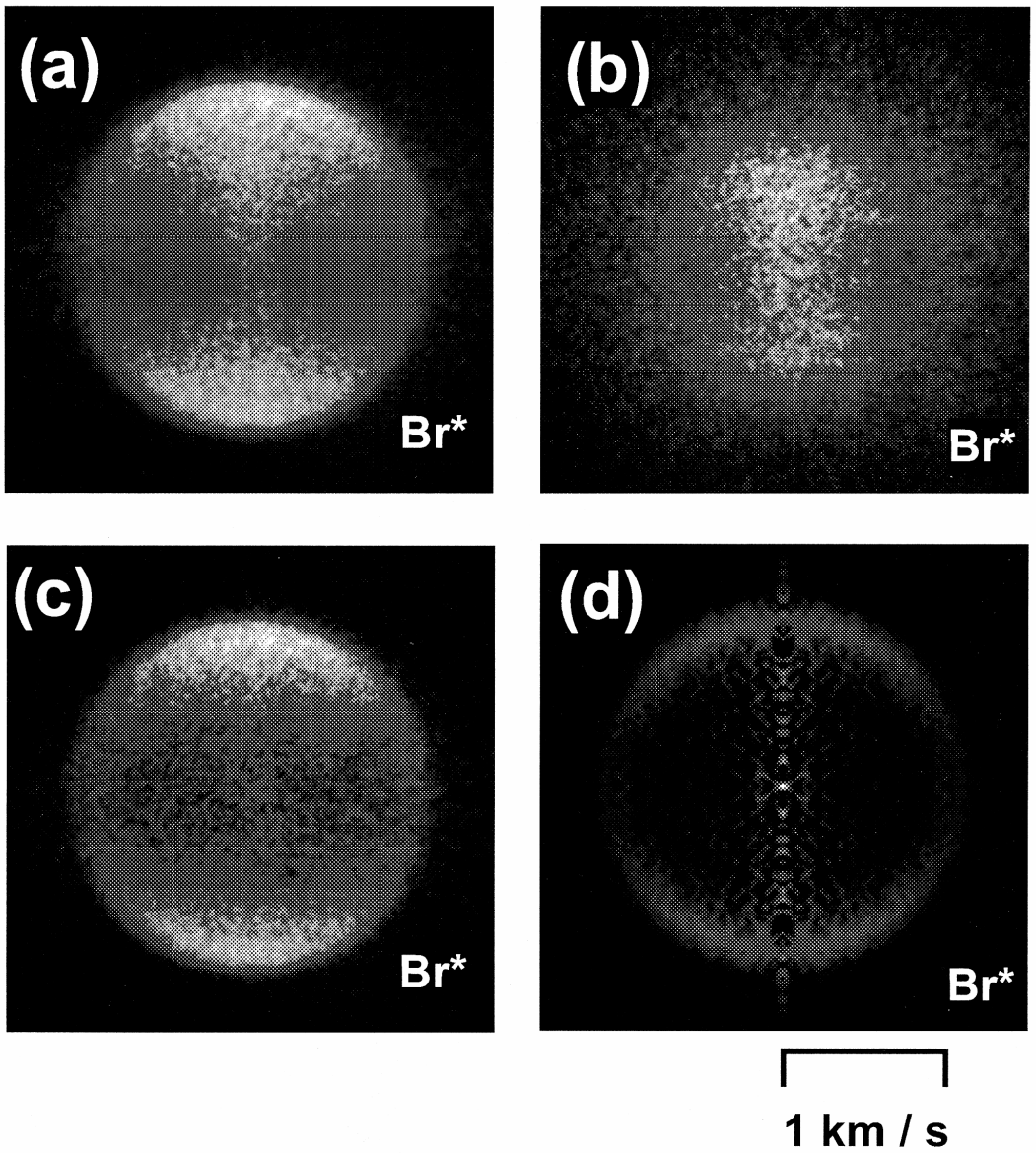

Fig. 8-2
(a) The raw image of Br*($^2P_{1/2}$) produced by 193 nm photodissociation of vinyl bromide observed with pump and probe laser beams.
(b) One-color signal produced solely by probe laser beam with the same laser power (50 μJ pulse^{-1}).
(c) The image of Br* produced by 193 nm photodissociation of vinyl bromide obtained by subtracting the background (b) from the original data (a).
(d) The inverse Abel transform of the image (c).

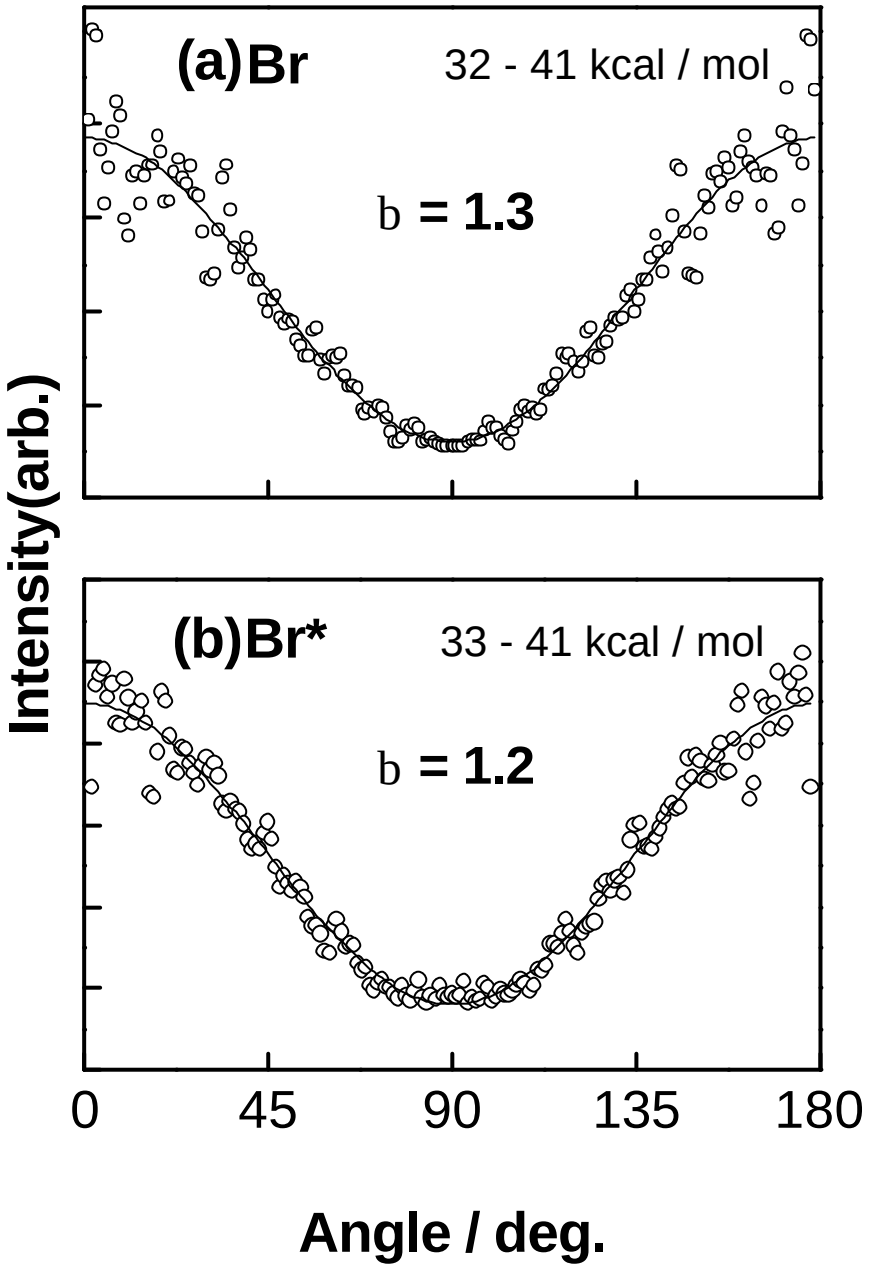

Fig. 8-3
(a) Angular distribution of Br($^2P_{3/2}$) at the center-of-mass translational energy release of 32 - 41 kcal mol^{-1}. Solid line shows the simulated curve assuming b = 1.3.
(b) Angular distribution of Br*($^2P_{1/2}$) at the center-of-mass translational energy release of 33 - 41 kcal mol^{-1}. Solid line shows the simulated curve assuming b = 1.2.

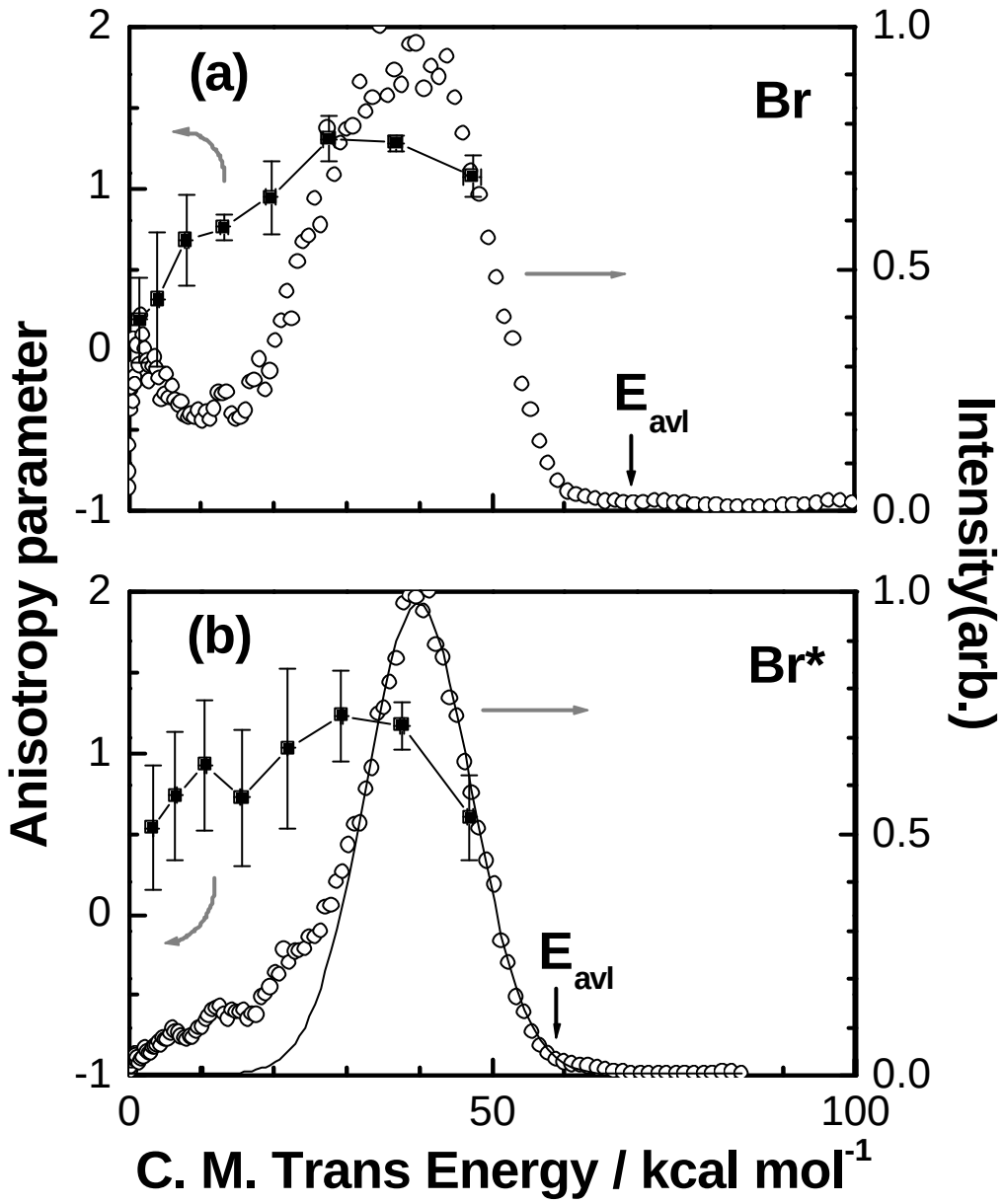

Fig. 8-4
Center-of-mass translational energy release, $P(E_T)$, and the variation of anisotropy parameter, $b(E_T)$, in (a) Br($^2P_{3/2}$) and (b) Br*($^2P_{1/2}$) channels. Solid line in (b) shows the fit of a Gaussian function.

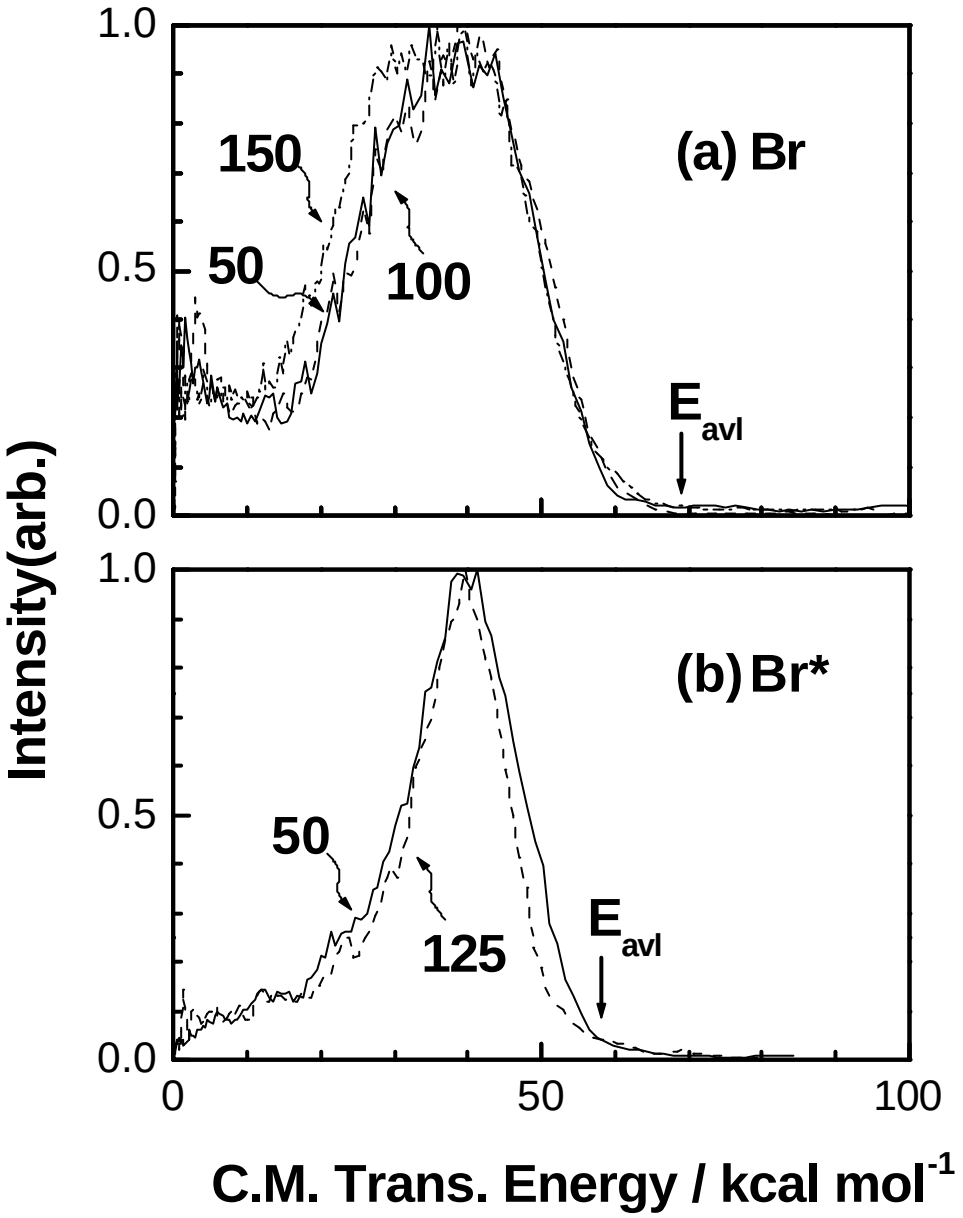

Fig. 8-5
The probe laser power dependence of the center-of-mass translational energy release, $P(E_T)$, for (a) $Br(^2P_{3/2})$ (b) $Br^*(^2P_{1/2})$ channels. The laser power used are indicated in the figure. The unuits are μJ $pulse^{-1}$.

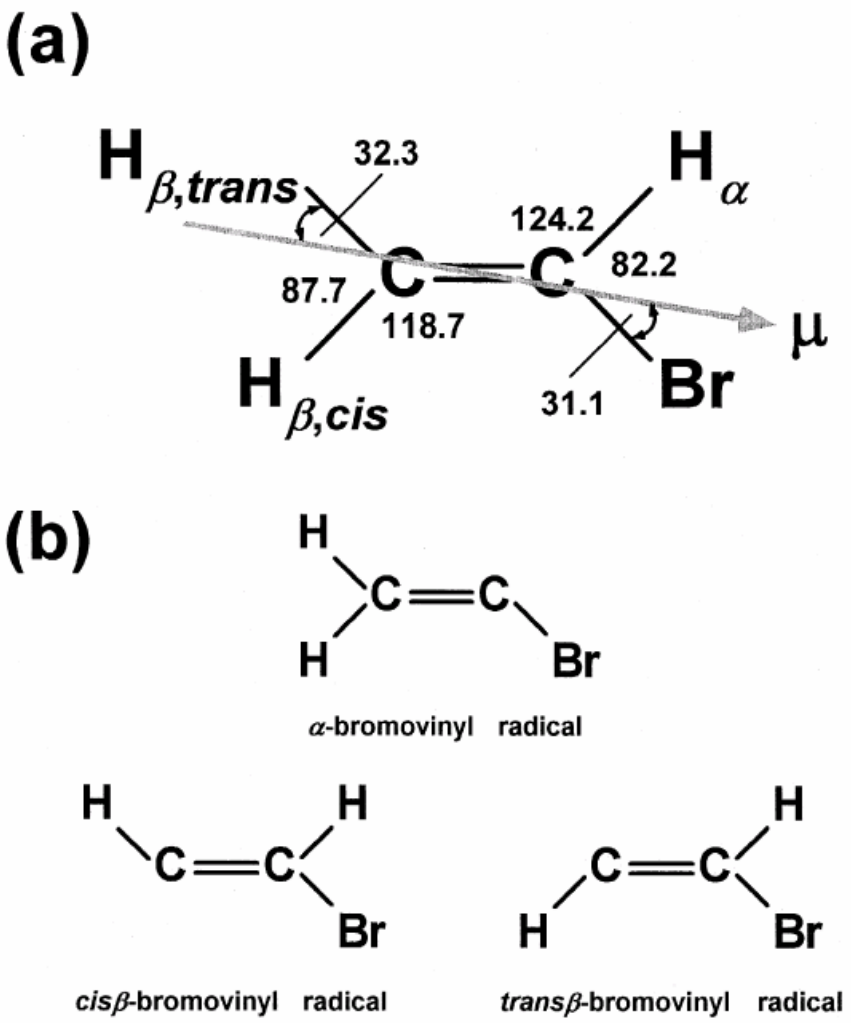

Fig. 8-6
(a) The geometry of VBr in the ground state and the transition dipole moment for π^*? π? transition.
(b) The nomenclature of bromo vinyl radicals used in the present paper. This is based on Ref. 17.

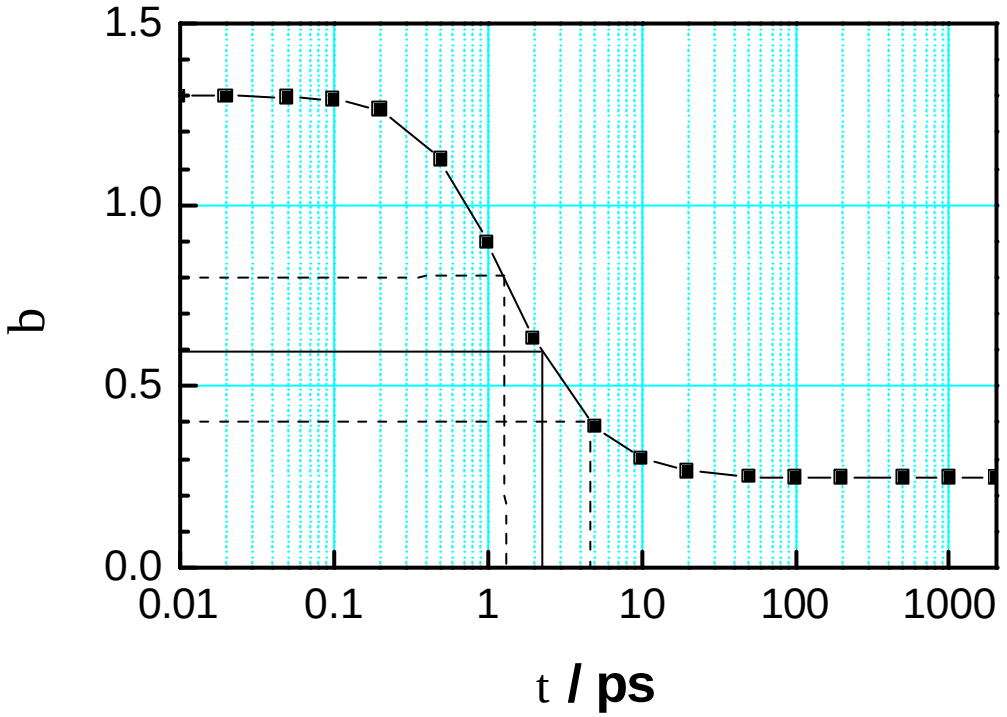

Fig. 8-7
Reduction of the anisotropy parameter due to the rotation of metastable VBr molecule. The rotational temperature of VBr was assumed to be 20 K.

Chapter 9

Concluding Remarks

In the Chapter 2, we applied the photoion imaging technique to elucidate the ultraviolet photodissociation dynamics of OCS. We found the bimodal translational energy distribution not only in the singlet $S(^1D_2)$ channel but also in the minor (<5%) triplet channel. This suggests the triplet sulfur atoms are produced by $2^1A'(^1\Delta)\leftarrow 1^1A'$(ground state) optical transition followed by intersystem crossing. The anisotropy parameters (b) were obtained for each translational energy components from the ion images, and they were positive for all components.

In the Chapter 3, we focus on the analysis of the electron orbital polarization of $S(^1D_2)$ atoms. We developed the forward convolution simulation program to extract the information of orbital polarization from ion images. The "true" anisotropy parameters and magnetic sublevel populations were b=1.8 and (m_J =0):(m_J =1):(m_J =2) = 0.6:0.14:0.06 for the low speed component, and b=0.7 and 0.48:0.24:0.02 for the high speed component. In this analysis, we employed two assumptions: the orbital alignment is cylindrically symmetric around the velocity vector and independent on the scattering angle of $S(^1D_2)$.

In the Chapter 4, In order to corroborate the contribution of the $1^1A''\leftarrow 1^1A'$ transition, we observed the excitation wavelength dependence of the $S(^1D_2)$ ion images. As a result, the low speed component originates from $2^1A'(^1\Delta)\leftarrow 1^1A'$(ground state) and the high-speed component from both A'←A' and A"←A' transitions. From these results, following two questions naturally rose: why do dissociations from the A' and A" states produce almost the same speed of S atoms? Why does only the A' state show the bimodal distribution? To answer these questions, the experimental results were compared with wavepacket calculations. It was discovered that the $2^1A'$ and $1^1A''$ potential energy surfaces are quite similar to each other, resulting in the same recoil velocity in the case of high-speed components. The low speed component was assigned to the non-adiabatic dissociation pathway via 2A' to 1A', where the process from 1A" to 1A' is forbidden without Coriolis interactions. The non-adiabatic transition probability was 0.35±0.02 from the $S(^1D_2)$ image at the 223 nm excitation.

In the Chapter 5, the "counterfragment" CO in the photodissociation of OCS→S+CO images were observed for each CO rotational state. The translational energy distributions of the CO fragments directly reflect the internal (bending vibrational) energy of the parent molecule OCS. The j(CO) population was obtained from the REMPI spectra of CO. Quantitative analysis revealed that the non-adiabatic transition in dissociation starting from OCS(010) was 0.21 that is similar to but slightly smaller than the value 0.34, from OCS(000).

The Chapter 6 was concerned with photoelectron imaging following (2+1) and (2+1') REMPI in the jet-cooled CO molecules. The photoelectron energy distribution emitted from $B(^1\Sigma^+)$ state of CO shows long vibrational progression up to $v^+=8$, i.e. vibrationally off-diagonal. The results suggest the 'superexcited' Rydberg states with an $A^2\Pi$ ion core plays an important role in the jet-cooled CO.

The experiments in the Chapter 7 were performed at the Brookhaven National Laboratory (New York, US) in Dr. Hall's group. The experimental method used in this research is FM transient absorption spectroscopy developed in his group. This method allows us to obtain absorption spectra of subtle amount of photofragments using modulated output of a ring laser as a probe light. The coincident CO rotational distribution with selected rotational levels of CH_2 produced from the 308 nm photodissociation of ketene (CH_2=CO) was estimated and found to differ from statistical predictions.

In the 193 nm photodissociation dynamics of hexa-atomic molecule, vinyl bromide (CH_2=CHBr), the fine structure branching ratio $[Br^*(^2P_{1/2})]/[Br(^2P_{3/2})]$ and translational energy distribution of each Br and Br^* fragments were measured by photoion imaging technique. The C-Br bond rupture occurs via two pathways: the direct dissociation on the (n(Br) or π(Br), σ^*(C-Br)) repulsive surfaces and dissociation from the ground state of VBr. The fine structure branching ratio was determined to be 0.06 ± 0.03.

We focused on the multi-surface photodissociation dynamics in this series of experimental researches. There exists, however, a challenging topic remains untouched: the effect of product matter wave interference between dissociation channels. This is because the effect appears in the orbital orientation [1-3] and to measure it requires highly differentiated experimental data. Existing experimental technique hardly be usable. Additionally, the theories of the interference effect have not been well organized yet [2,4].

The tomography, or slice imaging, to obtain entire 3D scattering distribution directly is one of the most powerful tools to elucidate the interference effect. Several groups including the group at IMS [5,6] have independently started construction of tomography equipment and more rigorous theory.

References

[1] T. P. Rakitzis, S. A. Kandel, A. J. Alexander, Z.-H. Kim, R. N. Zare, Science **281**, 1346 (1998).

[2] T. P. Rakitzis, R. N. Zare, J. Chem. Phys. **110**, 3341 (1999).

[3] T. P. Rakitzis, R. N. Zare, J. Chem. Phys. **110**, 3351 (1999).

[4] L. D. A. Siebbeles, M. Glass-Maujean, O. S. Vasyutinskii, J. A. Beswick, O. Roncero, J. Chem. Phys. **100**, 3610 (1994).

[5] C. R. Gebhardt, T. P. Rakitzis, P. C. Samartzis, V. Ladopoulos, T. N. Kitsopoulos, Rev. Sci. Instrum. **72**, 3848 (2001).

[6] K. Tonokura, T. Suzuki, Chem. Phys. Lett. **224**, 1 (1994).

謝辞　（in Japanese）

本研究を行うにあたり、指導教官の鈴木俊法助教授（現理化学研究所）には、研究全般に渡り多くのご指導、ご鞭撻をいただきました。また、先生の姿から、研究者としての人生の素晴らしさ、また、厳しさを学びました。心より感謝御礼申し上げます。

戸野倉賢一助手（現東京大学）ならびに高口博志助手（現理化学研究所）には、実験、理論の両面で基礎知識から具体的問題の議論まで、常に現場の視点からのご指導をいただきました。心より感謝御礼申し上げます。

本論文第４章の *ab initio* 波束動力学計算は、分子科学研究所（分子研）計算科学研究センター青柳睦教授（現九州大学）および南部伸孝助手との共同研究という形で行うことが出来ました。筆者にとって全く未知であった理論研究について、多くの貴重なご指導、ご協力をいただきました。心より感謝御礼申し上げます。

電子構造研究系の先生方、吉原經太郎教授（現北陸先端科学技術大学院大学）、花崎一郎教授、松本吉泰助教授（現総合研究大学院大学（総研大）先導科学研究科教授）、西信之教授、藤井雅明教授、ならびに佃達哉助教授には、研究室の枠を越えてご指導ご鞭撻を頂きました。心より感謝御礼申し上げます。

研究の過程で、当時博士研究員の、米蔵誠哲博士（現琉球大学）、下条竜夫博士（現分子研 UVSOR）、松本剛照博士（現姫路工業大学）ならびに、当時総研大の学生として在籍された、橋本伸久博士（現住友化学）、柴田武博士（現東芝）、坪内雅明博士（現理化学研究所）には、多くのご指導、ご協力をいただきました。皆様方との議論、交流を抜きにしては、本研究をまとめることは出来なかったと思います。ありがとうございました。

分子研では、日本の方々に加えて多くの外国人研究者との共同研究を行う機会を得ることができ、科学にとどまらず、視野の広い考え方を身につける上で、またとない環境を与えて頂きました。特に、光イオン化画像観測の理論および計算プログラムの基礎部分は、莫宇翔（Yuxiang Mo）教授（清華大学、中国）の開発によるものです。また、Michael C. Heaven 教授（Emory 大学、GA）には、S の軌道整列観測（第３章）等についてご指導いただきました。Cornelis A. de Lange 教授（Amsterdam 大学、オランダ）には、CO の光電子画像観測実験の基本的アイデアについてご指導いただき、実験の際も、現場で多くのアドバイスをいただきました。また、外国人研究員の李海洋（Haiyang Li）博士には、塩化アセチルの実験の際ご指導、ご協力いただきました。ありがとうございました。

James Muckerman 教授（Brookhaben National Laboratory（BNL） NY）、および Gregory E. Hall 教授（BNL）には、平成１０年度に、BNL に滞在して実験を行う機会を与えていただき、滞

在中は、研究面、生活面共に多くのご指導と助言をいただきました。また、実験では Mattew L. Costen 博士（現 Heriot-Watt 大学、UK）にご指導いただきました。ありがとうございました。

技官として分子研に採用されてから、この学位論文をまとめるまでに、筆者は９年４ヶ月の間、先生方、電子構造研究系の方々を始めとして、分子研の皆様にいろいろな面で大変お世話になりました。ありがとうございました。

最後になりましたが、研究生活を常に精神的に支え、また理解してくれた両親、家族、および古くからの友人に心より感謝いたします。